Exploring the phase space of medium induced QCD radiation with jets in ALICE at the LHC

A novel approach to the experimental study of QCD radiation in the Quark Gluon Plasma

Harry Arthur Andrews

A thesis submitted to
the University of Birmingham
for the degree of
Doctor of Philosophy

UNIVERSITY OF
BIRMINGHAM

Nuclear Physics Group
School of Physics and Astronomy
College of Engineering and Physical Sciences
University of Birmingham
July 2019

Abstract

Jets are back to back cascades of particles produced in the hard scattering of quarks and gluons. The pattern of cascade as these recoiling partons separate is governed by the properties of Quantum Chromo-Dynamics (QCD), the field theory for the strong nuclear force that binds together the quarks and gluons that make up the atomic nucleus. Studying jets from their production to their fragmentation gives insight into various unanswered aspects of QCD. Additionally, studying their modification in the presence of a strongly interacting deconfined medium of quarks and gluons produced in heavy-ion collisions, known as the Quark-Gluon Plasma (QGP), can help us to understand the properties of the strong nuclear force under the most extreme conditions akin to those believed to exist at the earliest stages of the universe or in the core of neutron stars.

In this thesis, novel approaches to studying jet substructure are presented. Measurements were performed using the ALICE detector at the CERN LHC on pp collisions with a centre-of-mass energy of $\sqrt{s} = 7$ TeV and Pb–Pb collisions at $\sqrt{s_{\mathrm{NN}}} = 2.76$ TeV. The results from Pb–Pb collisions are compared to those from pp collisions where significant differences in the momentum fraction between two subjets identified via grooming methods are observed. A dependence of this modification on the opening angle between the subjets is observed. Additionally, new measurements are performed on the number of splittings identified in jets using iterative declustering techniques.

Declaration of Author's Contribution

The work discussed in this thesis is entirely my own and unless otherwise stated, the results and figures presented were produced by me. It would, however, be remiss of me not to acknowledge the significant contribution that was made to this work from my colleagues within the ALICE collaboration and members of the wider theoretical and experimental community.

My work was mostly focussed upon two key areas that are presented in this document. The first and most significant was the jet grooming analysis performed on data collected by the ALICE collaboration focussing on the substructure observables z_{g}, R_{g} and n_{SD}; the latter of these observables being a completely novel measurement of jet substructure. This work resulted in the publication "*Exploration of jet substructure using iterative declustering in pp and Pb-Pb collisions at LHC energies*" [1] which was written by myself and Leticia Cunqueiro and a presentation at Quark Matter 2018 given by me. I was responsible for all of the analysis performed after initial data reconstruction as is discussed in Chapter 5. The second area is the development of the concept of the "*Lund Jet Plane*" and its potential applications to heavy-ion physics that is discussed in Chapter 3 (specifically Section 3.1). This work largely resulted from the 5^{th} Heavy Ion Jet Workshop and CERN TH institute in which the idea of using the Lund plane as a tool for representing the phase space of jet fragmentation in medium was discussed extensively; discussions in which I was a significant contributor. This workshop resulted in the publication "*Novel tools and observables for jet physics in heavy-ion collisions*" [2] where I was a significant contributing author, producing a large number of the plots presented in the paper. Whilst this work does not at present result in quantifiable measurements, it has been deemed a valuable contribution to the community and continues to be developed, justifying its inclusion in this thesis.

Additionally, as my service contribution to the experiment, I measured the performance of the three CORDE boards used in the ALICE Central Trigger Processor for calibration of the detector system with the central LHC clock.

Acknowledgements

During the course of this PhD I have had the chance to develop myself both as a person and as a professional far beyond what I believed myself capable. I owe this entirely to the people that I have had the pleasure to spend the last four years with. There are too many to mention everyone by name and any omissions that deserve mention are due to my own forgetfulness.

To everyone who has come and gone through E318 over the years: Tanya, Sam, Robin, Jack, Nima, Kae, Emzo, Tony, Stuart, Marianna, Jakub, Ollie, Hakan, Pedro, Beckie, Yi Ming, Angus, Ross and Simone, thank you for making the office such an enjoyable place to come in and work. I don't think that I will ever work anywhere that is so unproductive but also so fun. To the honorary members of the office, Neil, Chris and Ellie, thank you for making lunch times so entertaining. I still can't believe how much we were able to fit into a 30 minute lunch break at times...

To the other members of the Birmingham ALICE group: David Evans, Roman Lietava, Orlando Villalobos Baillie, Lee Barnby, Anton Jusko and Marian Krivda, thank you for your guidance throughout the course of my PhD and for making the office at CERN a very welcoming and friendly place to work.

To Peter and Leticia, my fantastic supervisors. I owe everything contained in these pages to your tireless effort, unrelenting patience and brilliant guidance. It has been an absolute pleasure to work with you both and to get to know you both as wonderful people and exemplary academics. Peter, I have always found our meetings to be incredibly insightful and the skills I have learned from you will stay with me for life, whether it's to think truly and critically about all aspects of research or how to survive on the top of a very windy mountain in the lake district, thank you. Leticia, the results presented in this thesis would have never

been possible were it not for you. There are no words that can quantify how grateful I am for your infinite patience with me over the course of my PhD and for your invaluable guidance and teachings. I have learnt more from you than I could have ever thought possible at the outset of this journey. I hope that one day you are able to find the time to get that German Shepherd.

To my family who I owe everything. Thank you for your eternal support. To Mum and Dad, without your belief in me I may well have given up when my teachers told me I wasn't good enough, you are the only mentors I have ever needed. To Rorie, I have no idea where I would be in life without you but I know it would be an immeasurably worse place. We have grown together and every good part of me, I owe to you. I can't wait for what lies ahead.

To my family and to Rorie, the very best of me.

Contents

1 Introduction **2**

1.1 The Standard Model 2

1.2 Quantum Chromodynamics 3

1.2.1 Coupling in QCD 5

1.2.2 Confinement 7

1.2.3 Asymptotic Freedom 7

1.3 The Quark Gluon Plasma 8

1.3.1 QGP in Colliders 10

2 Jets **16**

2.1 The Physics of Jets 16

2.1.1 Parton Distribution Functions 18

2.1.2 Fragmentation Functions 19

2.2 Jets in the Quark Gluon Plasma 22

2.2.1 Jet Quenching 25

2.2.2 Coherent Emitters 28

2.3 Jet Finding 30

2.3.1 Jet Clustering Algorithms 31

2.4 Theoretical Models 34

2.4.1 PYTHIA 34
2.4.2 POWHEG 35
2.4.3 JEWEL 35
2.4.4 The Hybrid Model 36

3 Jet Substructure **38**
3.1 The Lund Jet Plane 39
3.1.1 Reconstructing Jet Emissions 39
3.1.2 Filling the Lund Plane 41
3.1.3 Soft Drop Grooming 46
3.1.4 Projecting the Lund Plane 47
3.2 Substructure Observables 51
3.2.1 Momentum Fraction z_{g} 51
3.2.2 Groomed Radius R_{g} 52
3.2.3 Number of Splittings n_{SD} 55

4 Experiment **57**
4.1 The Large Hadron Collider 57
4.2 ALICE 59
4.2.1 Overview 59
4.2.2 Inner Tracking System 61
4.2.3 Time Projection Chamber 64
4.2.4 V0 65

5 Analysis **67**
5.1 Introduction 67
5.2 Data Selection 68
5.2.1 Datasets 68

5.2.2 Event Selection 69
5.2.3 Tracking 70
5.2.4 Centrality Determination 75
5.2.5 Jet Selection 76
5.3 Background Subtraction 79
5.3.1 Underlying Event Subtraction 79
5.3.2 Combinatorial Jets 82
5.4 Detector and Background Response 84
5.4.1 Constructing the Response 84
5.4.2 Embedding 86
5.4.3 Characterising the Response 88
5.5 Raw Results 92
5.5.1 Lund Planes 92
5.5.2 Jet Shapes 93
5.6 Bayesian Unfolding 95
5.7 Folding 106
5.8 Systematic Uncertainties 109
5.8.1 pp 110
5.8.2 Pb–Pb 113

6 Results and Discussion **119**

6.1 pp 119
6.1.1 Momentum Fraction z_{g} 120
6.1.2 Groomed Radius R_{g} 121
6.1.3 Number of Splittings n_{SD} 121
6.2 Pb–Pb 123
6.2.1 Momentum Fraction z_{g} 124

6.2.2 Groomed Radius R_{g} 127

6.2.3 Number of Splittings n_{SD} 128

Conclusion **131**

Future Work **134**

Appendices **134**

A Publication: Exploration of jet substructure using iterative declustering in pp and Pb–Pb collisions at LHC energies **135**

List of Figures

1.1 The ingredients of the standard model of particle physics [3]. 3

1.2 World average values for the strong coupling constant $\alpha_S(Q)$ [4]. 6

1.3 QCD Phase Diagram [9]. 9

1.4 Lattice QCD predictions for energy density as a function of temperature modelling a different number of quark flavours [12]. Figure adapted from calculations made in Ref. [13]. 10

1.5 Light-cone evolution diagram of a heavy-ion collision. The different temperature scales of evolution are indicated by T_{C} which indicates the critical temperature and T_{ch} and T_{fo}, the chemical freeze-out and thermal freeze-out temperatures respectively. The formation time of the QGP is shown as $\tau_0 \approx 1$ fm/c [14]. 11

2.1 Proton PDFs for two different selections of exchanged 4-momentum squared, μ^2 [81]. 19

2.2 Distribution of $F(z, p_{\mathrm{T,jet}})$ in bins of $p_{\mathrm{T,jet}}$ as measured by the ATLAS collaboration in pp collisions at $\sqrt{s} = 7$ TeV [82]. Data are shown as circles with predictions from AMBT1 PYTHIA shown as solid lines. 21

2.3 Energy loss Feynmann diagrams for collisional (left) and radiative (right) energy loss of a quark traversing a quark-gluon plasma with initial energy E losing ΔE energy to the medium. 24

2.4 Comparison of the nuclear modification factor for fully reconstructed anti-k_{T} jets ($R = 0.2$) with ALICE, ATLAS and CMS [91]. 26

2.5 Nuclear modification factor R_{AA} for π^0 as a function of p_{T} as measured by the PHENIX collaboration [106] for two different centrality ranges compared to calculations from 3 energy loss formalisms: Higher-Twist (HT), finite temperature field theory (AMY) and multiple soft gluon emission (ASW). 28

2.6 A schematic representation of a jet shower following angular ordering for a medium with $\Lambda_{\mathrm{med}} < r_{\perp}$ (left) and $\Lambda_{\mathrm{med}} > r_{\perp}$ (right). 29

2.7 Illustration for collinear safety where partons are represented by vertical lines whose height is proportional to their transverse momentum and the horizontal displacement represents their distribution in rapidity space [116]. 33

3.1 A schematic diagram of a simple $1 \rightarrow 2$ jet splitting (antenna) with kinematical variables: θ (angle of radiation) and z (momentum fraction). 40

3.2 Lund diagram representation of jet clustering history with three different primary emissions with varying formation times [2]. 41

3.3 Primary Lund plane for jets reconstructed in PYTHIA generated events at $\sqrt{s}$= 7 TeV. 42

3.4 Average Lund plane density ρ for jets reconstructed from Pythia simulated events reclustered with the C/A algorithm. 44

3.5 Primary Lund plane for anti$-k_{\mathrm{T}}$ $R = 0.4$ jets reconstructed in PYTHIA generated events at $\sqrt{s} = 5.02$ TeV using three different reclustering algorithms: Cambridge-Aachen (left), k_{T} (centre) and anti$-k_{\mathrm{T}}$ (right). 46

3.6 Lund plane for each splitting using Cambridge-Aachen reclustering on anti-k_{T}jets reconstructed from PYTHIA generated events. 48
3.7 X-axis projection of Lund diagrams from Fig.3.6. 49
3.8 Y-axis projection of Lund diagrams from Fig.3.6. 50
3.9 Distribution of z_{g} for jets reconstructed in PYTHIA 6 Perugia Tune 2011, PYTHIA 8 and PYTHIA + POWHEG generated events in the range $40 \leq p_{\mathrm{T,jet}}^{\mathrm{ch}} < 60$ GeV/c. 52
3.10 Ratios of z_{g} distributions for central Pb–Pb collisions and smeared pp collisions for a range of $p_{\mathrm{T,jet}}$ [151]. Calculations shown are from various jet quenching models [109, 154–157]. 53
3.11 Top: Trigger and recoil jet z_{g} distributions in the $p_{\mathrm{T,jet}}$ range 20-30 GeV/c and 10-20 GeV/c, respectively, for Au–Au collisions and smeared pp collisions as measured by RHIC [153]. Bottom: Ratio between the Au–Au and pp distributions with systematic uncertainties shown as shaded bands. 54
3.12 Distribution of R_{g} for jets reconstructed in PYTHIA 6 Perugia Tune 2011, PYTHIA 8 and PYTHIA + POWHEG generated events in the range $40 \leq p_{\mathrm{T,jet}}^{\mathrm{ch}} < 60$ GeV/c. 55
3.13 Distribution of n_{SD} for jets reconstructed in PYTHIA 6 Perugia Tune 2011, PYTHIA 8 and PYTHIA + POWHEG generated events in the range $40 \leq p_{\mathrm{T,jet}}^{\mathrm{ch}} < 60$ GeV/c. 56

4.1 Schematic of the CERN LHC accelerator complex [159]. 58
4.2 Schematic of the ALICE detector with sub-detectors labelled and inlay of ITS [47]. 60
4.3 Schematic layout of the ALICE Inner Tracking System [47]. 61
4.4 Photograph of the half-barrel of the ALICE Silicon Pixel Detector [47]. . . . 62

4.5 Photograph (left) and CAD design (right) of the ALICE Silicon Drift Detector System [47]. 63
4.6 The ALICE TPC field cage in 3D [47]. 65
4.7 Front view of V0A (left) and V0C (right) [47]. 66

5.1 PYTHIA6 Perugia 0 simulated jet transverse momentum spectra for each of the 10 $p_{\mathrm{T,hard}}$ bins. 69
5.2 Tracking efficiency of the ALICE TPC for primary particles in simulated pp and Pb–Pb collisions [174]. 71
5.3 Track azimuthal distribution for three components of hybrid track list for centrality class 0-10% for 2010 Pb–Pb collisions at $\sqrt{s_{\mathrm{NN}}}$= 2.76 TeV [176]. . 74
5.4 Reconstructed track kinematic spectra for tracks clustered into jets in pp collisions at $\sqrt{s}$ = 7 TeV and the centrality class 0-10% of Pb–Pb collisions at $\sqrt{s_{\mathrm{NN}}}$ = 2.76 TeV. 75
5.5 (left) An illustrative example of the correlation between final state observables N_{ch} and the Glauber calculated quantities (b, N_{part}) [20]. (right) Sum of V0 amplitude distribution with Glauber model fit and centrality class cuts. . . . 76
5.6 Reconstructed jet transverse momentum spectra for pp collisions at $\sqrt{s}$= 7 TeV. 77
5.7 Reconstructed $\eta_{jet}^{ch,rec}$ for pp collisions at $\sqrt{s}$= 7 TeV (left) and Pb–Pb collisions at $\sqrt{s_{\mathrm{NN}}}$= 2.76 TeV (right). 78
5.8 Reconstructed $\varphi_{jet}^{ch,rec}$ for pp collisions at $\sqrt{s}$= 7 TeV. 79
5.9 Reconstructed $\varphi_{jet}^{ch,rec}$ for Pb–Pb collisions at $\sqrt{s}$= 2.76 TeV: (top left) all datasets combined, (top right) LHC11h (good), (bottom left) LHC11h (semigood 1), (bottom right) LHC11h (semigood 2). 80
5.10 Average background density (ρ) as a function of event centrality calculated using $R = 0.2$ k_{T} clusters for Pb–Pb events at $\sqrt{s_{\mathrm{NN}}}$= 2.76 TeV. 81

5.11 Uncorrected jet spectra after background subtraction for $R = 0.2$ (left) and $R = 0.3$ (right) jets in central Pb–Pb collisions with no restriction on the leading hadron (inclusive, black circles), a leading hadron with at least $p_{\mathrm{T}} > 5$ GeV/c (green crosses) and $p_{\mathrm{T}} > 10$ GeV/c (red squares) [62]. 83

5.12 Detector (left) and embedding (right) response matrices for charged jet transverse momentum of jets generated using PYTHIA with detector effects modelled using GEANT 3. 86

5.13 Detector (left) and embedding (right) response matrices for z_{g}, R_{g} and n_{SD} for jets generated using PYTHIA with detector effects modelled using GEANT 3. 87

5.14 Jet energy shift for detector response of jets identified with anti-k_{T} clustering with $R = 0.4$ for a range of jet transverse momentum at particle level in simulated PYTHIA events at $\sqrt{s} = 7$ TeV. 89

5.15 (left) Jet energy shift for detector and underlying event response of jets identified with anti$-k_{\mathrm{T}}$ clustering with $R = 0.4$ for a range of jet transverse momentum at particle level in PYTHIA+embedding events at $\sqrt{s_{\mathrm{NN}}} = 2.76$ TeV. (right) Average jet energy shift for full range of jet transverse momentum for detector only and detector + underlying event responses. 90

5.16 Jet shape resolution distributions for z_{g} and R_{g} for detector and underlying event response of PYTHIA jets identified with anti$-k_{\mathrm{T}}$ clustering with $R = 0.4$ for a range of jet transverse momentum at particle level. 91

5.17 Average jet shape resolution of z_{g} and R_{g} in the full range of jet transverse momentum for jets reconstructed with anti$-k_{\mathrm{T}}$ clustering with $R = 0.4$ from PYTHIA simulations with detector effects applied and embedded in central Pb–Pb events. 92

5.18 Lund planes populated with splittings identified with recursive declustering of jets in pp (left) and Pb–Pb (right) collisions at $\sqrt{s} = 7$ TeV and $\sqrt{s_{\rm NN}} = 2.76$ TeV respectively. 93

5.19 Lund plane for jets identified in PYTHIA simulated events at $\sqrt{s} = 2.76$ TeV embedded into real, $0 - 10\%$ centrality, Pb–Pb events. 94

5.20 Raw distributions for $z_{\rm g}$, $R_{\rm g}$ and $n_{\rm SD}$ for jets reconstructed in the transverse momentum range $40 \leq p_{\rm T,jet}^{\rm ch} < 60$ GeV/c in pp collisions at $\sqrt{s} = 7$ TeV (left) and $80 \leq p_{\rm T,jet}^{\rm ch} < 120$ GeV/c in Pb–Pb collisions at $\sqrt{s_{\rm NN}} = 2.76$ TeV (right) using the ALICE detector. 96

5.21 Statistics for input into unfolding of two dimensional measured distributions in shape and $p_{\rm T,jet}^{\rm ch}$ for $z_{\rm g}$, $R_{\rm g}$ and $n_{\rm SD}$. 99

5.22 Kinematic efficiency correction factors to applied to unfolded solutions for $p_{\rm T,jet}^{\rm ch}$ spectrum (top left), $z_{\rm g}$ (top right) , $R_{\rm g}$ (bottom left) and $n_{\rm SD}$ (bottom right). 101

5.23 Unfolded distributions for $p_{\rm T,jet}^{\rm ch}$ spectrum (top left), $z_{\rm g}$ (top right), $R_{\rm g}$ (bottom left) and $n_{\rm SD}$ (bottom right) for $R = 0.4$ jets in pp collisions at $\sqrt{s} = 7$ TeV. For jet shape distributions, jets are selected in the range $40 \leq p_{\rm T,jet}^{\rm ch} < 60$ GeV/c. 102

5.24 Refolding tests for $p_{\rm T,jet}^{\rm ch}$ spectrum (top left), $z_{\rm g}$ (top right), $R_{\rm g}$ (bottom left) and $n_{\rm SD}$ (bottom right) for $R = 0.4$ jets in pp collisions at $\sqrt{s} = 7$ TeV. For jet shape distributions, jets are selected in the range $40 \leq p_{\rm T,jet}^{\rm ch} < 60$ GeV/c. 103

5.25 Closure tests in z_g and $p_{\rm T,jet}^{\rm ch}$for unfolding of z_g with pp data. 104

5.26 Closure tests in R_g and $p_{\rm T,jet}^{\rm ch}$for unfolding of R_g with pp data. 105

5.27 Closure tests in n_{SD} and $p_{\rm T,jet}^{\rm ch}$for unfolding of n_{SD} with pp data. 105

5.28 Pearson's coefficients for $p_{\rm T,jet}^{\rm ch}$, $z_{\rm g}$ (iteration 4), $R_{\rm g}$ (iteration 5) and $n_{\rm SD}$ (iteration 4) in the unfolded range of $40 \leq p_{\rm T,jet}^{\rm ch} < 60$ GeV/c. 107

5.29 Effects of folding for Hybrid Model predictions of the $p_{\mathrm{T,jet}}^{\mathrm{ch}}$ spectrum and shape distributions for z_{g}, R_{g} and n_{SD} performed using a response matrix constructed from embedded PYTHIA jets. 109

5.30 Effects of folding for JEWEL (with recoils) predictions of the $p_{\mathrm{T,jet}}^{\mathrm{ch}}$ spectrum and shape distributions for z_{g}, R_{g} and n_{SD} performed using a response matrix constructed from embedded PYTHIA jets. 110

5.31 Components of the systematic uncertainties in pp. 114

6.1 Fully corrected z_{g} distribution for $R = 0.4$ jets reconstructed in pp collisions at $\sqrt{s} = 7$ TeV using the ALICE detector in the range $40 \leq p_{\mathrm{T,jet}}^{\mathrm{ch}} < 60$ GeV/c with statistical and systematic uncertainties and compared to jets reconstructed from PYTHIA simulated events [1]. 120

6.2 Fully corrected R_{g} distribution for $R = 0.4$ jets reconstructed in pp collisions at $\sqrt{s}$= 7 TeV using the ALICE detector in the range $40 \leq p_{\mathrm{T,jet}}^{\mathrm{ch}} < 60$ GeV/c with statistical and systematic uncertainties and compared to jets reconstructed from PYTHIA simulated events. 122

6.3 Fully corrected n_{SD} distribution for $R = 0.4$ jets reconstructed in pp collisions at $\sqrt{s} = 7$ TeV using the ALICE detector in the range $40 \leq p_{\mathrm{T,jet}}^{\mathrm{ch}} <$ 60 GeV/c with statistical and systematic uncertainties and compared to jets reconstructed from PYTHIA simulated events [1]. 123

6.4 Distributions of z_{g} and corresponding ratios for Pb–Pb in the 0–10 % most central events and PYTHIA embedded jets in the range $80 \leq p_{\mathrm{T,jet}}^{\mathrm{ch}} < 120$ GeV/c with several cuts on the splitting opening angle [1]. Comparisons to two jet quenching models JEWEL and the Hybrid Model are also shown as curves. Error bars represent statistical uncertainties on all distributions and the shaded and hashed areas in the top half of the plots represent the systematic uncertainties attributed to the data and PYTHIA reference respectively. Combined errors (in quadrature) in the ratio panel shown as shaded areas. 125

6.5 Distribution of R_{g} and corresponding ratios for Pb–Pb in the 0–10 % most central events and PYTHIA embedded jets in the range $80 \leq p_{\mathrm{T,jet}}^{\mathrm{ch}} < 120$ GeV/c with comparisons to two jet quenching models, JEWEL and the Hybrid model. 128

6.6 Distribution of n_{SD} and corresponding ratios for Pb–Pb in the 0–10 % most central events and PYTHIA embedded jets in the range $80 \leq p_{\mathrm{T,jet}}^{\mathrm{ch}} < 120$ GeV/c with comparisons to two jet quenching models JEWEL and the Hybrid model [1]. 129

List of Tables

4.1 SSD system parameters [47]. 64

5.1 N_{part} for Pb–Pb collisions at $\sqrt{s_{\mathrm{NN}}} = 2.76$ TeV derived from a Glauber fit to the sum of V0 amplitudes [178]. 76

5.2 Average shift in observables due to underlying event and detector effects for jets in pp ($40 \leq p_{\mathrm{T,jet}}^{\mathrm{ch}} < 60$ GeV/c) and Pb–Pb ($80 \leq p_{\mathrm{T,jet}}^{\mathrm{ch}} < 120$ GeV/c) collisions. 90

5.3 Chosen unfolding iteration used for fully corrected measurement of z_{g}, R_{g} and n_{SD} in pp collisions at $\sqrt{s} = 7$ TeV. 105

5.4 Unfolding range modifications used to estimate the systematic uncertainty attributed to the ranges used in the unfolding procedure. 112

5.5 Relative systematic uncertainties on the measured jet shapes in pp collisions for three selected jet shape intervals in the jet $p_{\mathrm{T,jet}}^{\mathrm{ch}}$ range of 40–60 GeV/c. . 113

5.6 Relative systematic uncertainties on the measured jet shapes in pp collisions for three selected jet shape intervals in the jet $p_{\mathrm{T,jet}}^{\mathrm{ch}}$ range of 40–60 GeV/c. . 115

5.7 Relative systematic uncertainties on the measured jet shapes in pp collisions for three selected jet shape intervals in the jet $p_{\mathrm{T,jet}}^{\mathrm{ch}}$ range of 40–60 GeV/c. . 115

5.8 Relative systematic uncertainties on the measured jet shapes in Pb–Pb collisions for three selected jet shape intervals in the jet $p_{\mathrm{T,jet}}^{\mathrm{ch}}$ range of 80–120 GeV/c. 117

5.9 Relative systematic uncertainties on R_{g} and n_{SD} in Pb-Pb collisions for three selected jet shape intervals in the jet $p_{\mathrm{T,jet}}^{\mathrm{ch}}$ range of 80–120 GeV/c. 118

6.1 Fraction of jets that pass the soft drop condition $z_{\mathrm{cut}} = 0.1$ and $\beta = 0$ in the specified range of angular separation and in the transverse momentum range $40 \leq p_{\mathrm{T,jet}}^{\mathrm{ch}} < 60\,\mathrm{GeV}/c$ for pp collisions and $80 \leq p_{\mathrm{T,jet}}^{\mathrm{ch}} < 120\,\mathrm{GeV}/c$ for Pb–Pb collisions. Uncertainties on the data are written as statistical(systematic). 130

Chapter 1

Introduction

1.1 The Standard Model

The standard model of particle physics is the theory describing all fundamental observable particles in the universe and their interactions with each other. There are 17 of these fundamental particles and Fig. 1.1 shows how they are separated into different families. The particles are separated into two broad categories, *fermions* (spin-1/2) which make up all the matter that we observe around us and the *bosons* (integer spin) which are the mediators of the forces. The four spin-1 vector bosons are each associated with one of the fundamental forces: the electromagnetic force (photon), weak nuclear force ($W^{\pm}/Z^{0}$) and strong nuclear force (gluon). Each of these forces are mediated in matter interactions via the exchange of their corresponding force carrier particles and each has an associated field theory that mathematically describes them. Of these forces, the least well constrained by far is the strong nuclear force, described by the field theory of Quantum Chromodynamics (QCD). This thesis aims to address some of the less well constrained aspects of QCD in vacuum as well as the extreme conditions of heavy ion collisions. The rest of this chapter will introduce some of the fundamental concepts that are central to the work presented.

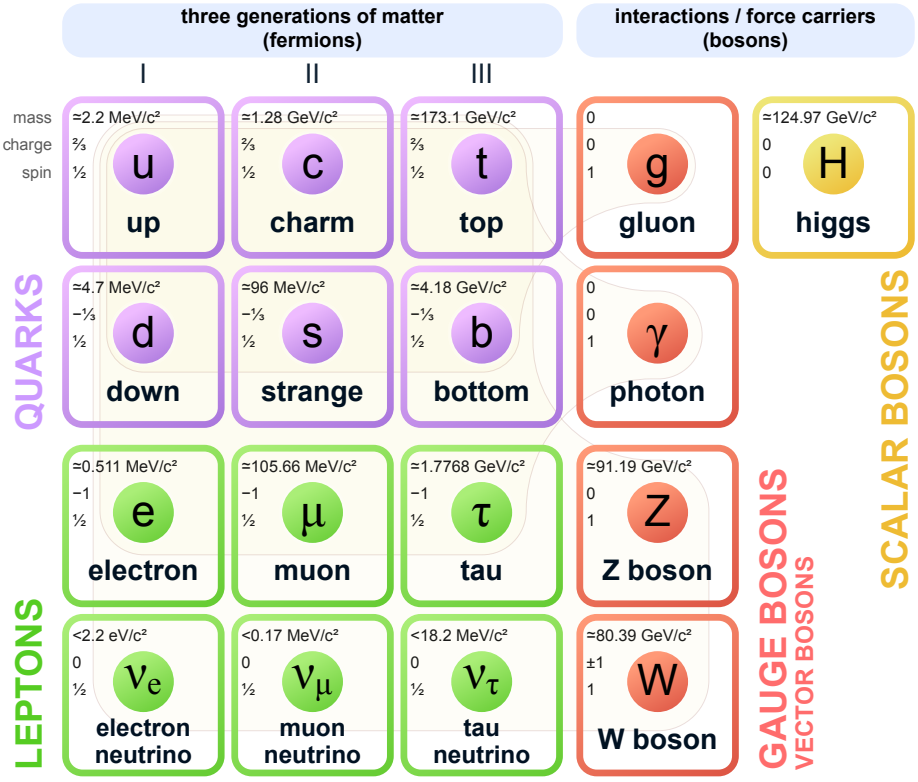

Figure 1.1: The ingredients of the standard model of particle physics [3].

1.2 Quantum Chromodynamics

Quantum Chromodynamics (QCD) is a non-abelian gauge field theory that describes the strong interaction mediated between coloured objects (quarks and gluons). QCD is an SU(3) group theory which means the Dirac equation is invariant under local $SU(3)_C$ transformations of the free quark wave function:

$$(i\gamma^\mu \partial_\mu - m)\Psi = 0, \tag{1.1}$$

$$\Psi' = e^{i\frac{g_s}{2}\lambda_j \phi_j(x)}\Psi, \tag{1.2}$$

where Ψ' is the gauge transform of the free quark wave function, Ψ, which is the product of the ordinary Dirac wave function and the colour wave function

$$\Psi = \psi(x)\chi_{\mathrm{C}}. \tag{1.3}$$

The colour charge component has three orthogonal basis states (namely, red, green and blue) which are represented by:

$$\chi_{\mathrm{R}} = \begin{pmatrix} 1 \\ 0 \\ 0 \end{pmatrix}, \ \chi_{\mathrm{G}} = \begin{pmatrix} 0 \\ 1 \\ 0 \end{pmatrix}, \ \chi_{\mathrm{B}} = \begin{pmatrix} 0 \\ 0 \\ 1 \end{pmatrix}. \tag{1.4}$$

After introducing the gauge fields G^{μ}_{j} in the local $\mathrm{SU(3)_C}$ transformation, the Lagrangian for QCD can be shown to be:

$$\mathcal{L}_{\mathrm{QCD}} = \bar{\Psi}(i\gamma_{\mu}\mathcal{D}^{\mu} - m)\Psi - \frac{1}{4}F_{\mathrm{j},\mu\nu}F^{\mu\nu}_{\mathrm{j}}, \tag{1.5}$$

where the field strength tensor is given by

$$F^{\mu\nu}_{\mathrm{j}} = \partial^{\mu}G^{\nu}_{\mathrm{j}} - \partial^{\nu}G^{\mu}_{\mathrm{j}} - g_{\mathrm{s}}f_{\mathrm{jkl}}G^{\mu}_{\mathrm{k}}G^{\nu}_{\mathrm{l}}. \tag{1.6}$$

The final term in the QCD field strength tensor arises due to the non-abelian nature of the gauge theory and leads to the extremely significant property of the theory that the gauge bosons have self-interaction terms that arise when squaring the field strength tensor in the QCD lagrangian.

The simplest form of this self interaction can be understood by considering the three point interaction (trilinear coupling) which is proportional to the structure constants f_{jkl} (where j,k and l run over the vector bosons) and the coupling constant g_{s}. The structure constants of the gauge theory are defined by

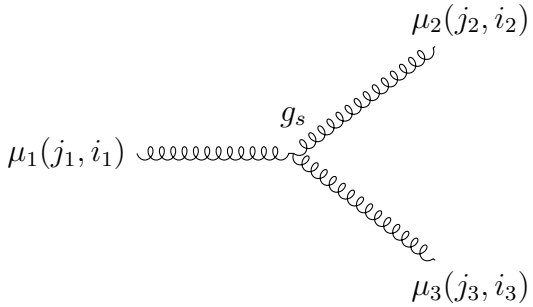

$$\left[\lambda_{\mathrm{j}}, \lambda_{\mathrm{k}}\right] = 2i \sum_{l=1}^{8} f_{\mathrm{jkl}} \lambda_{\mathrm{l}} \tag{1.7}$$

For an abelian group, the generators λ_μ commute so these terms vanish and hence the abelian U(1) theory of Quantum ElectroDynamics (QED) sees no self interaction terms between the gauge bosons (photons). However, for the non-abelian SU(3) theory of QCD there are $N_{\mathrm{C}}^2 - 1 = 8$ generators that do not commute and the consequence is self coupling between the gauge bosons and so the gluons must carry a colour charge.

1.2.1 Coupling in QCD

As with all quantum field theories of the standard model, the cross sections of physical processes are calculated in perturbation theory where higher-order processes (additional vertices) contribute with correspondingly higher-orders of the coupling constant α. In general, these higher-order terms can be ignored because the couplings are generally small. The self-coupling nature of gluons in QCD, however, means that higher-order terms cannot be neglected and the calculations become divergent. Despite the name coupling constant, the coupling between two strongly interacting objects is not, in fact, constant. The coupling depends on the exchanged four momentum (or equivalently the distance of the interaction) and is often referred to as a running coupling which can be obtained via renormalisation as:

$$\alpha_s(Q^2) = \frac{12\pi}{(11N_C - 2N_f)log\frac{Q^2}{\Lambda^2_{QCD}}}, \tag{1.8}$$

where $N_C = 3$ is the number of colour charges, N_f is the number of quark flavours accessible, defined as the number of quarks with mass less than the energy scale of the interaction, and $\Lambda_{QCD} \approx 1$ GeV is the QCD scale parameter. The running of the strong coupling constant, α_S, is shown in Fig. 1.2. From this figure, it can be seen that α_S gets large at small momentum transfer scales which leads to the breakdown of perturbation theory for describing strong nuclear interactions.

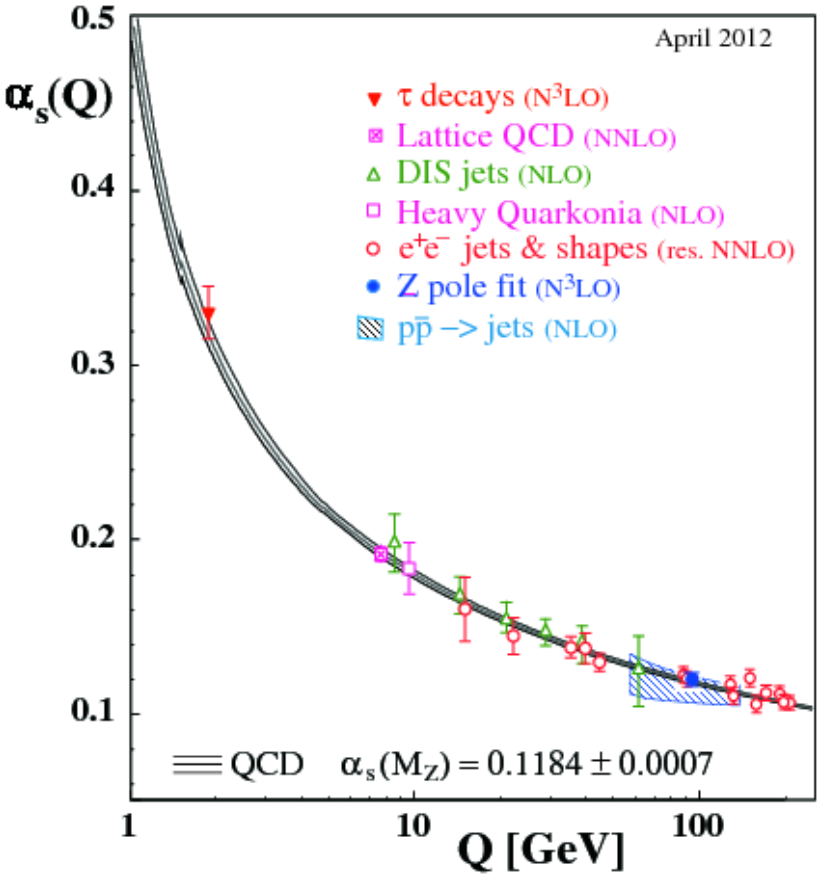

Figure 1.2: World average values for the strong coupling constant $\alpha_S(Q)$ [4].

The dependence of $\alpha_s(Q)$ on momentum transfer (or energy) gives rise to two very important characteristics of the strong force: *confinement* and *asymptotic freedom*.

1.2.2 Confinement

From Fig. 1.2, it can be seen that at decreasing values of momentum transfer the value of α_s increases logarithmically; this relationship can also be read from equation 1.8 where the value of α_s increases as Q^2 approaches Λ^2_{QCD}. Due to the Heisenberg Uncertainty Principle, low momentum transfers can be thought of as corresponding to large distances and so the strength of the strong coupling constant can be thought of as increasing at larger interaction distances. This increasing strength of interaction between coloured objects is a consequence of the self-coupling of gluons and leads to the property of confinement. Confinement refers to the fact that coloured objects cannot be observed as free objects in nature and instead are forced to be bound in colourless hadrons. If one were to separate two quarks that are bound together, the increasing field energy between the two objects would reach the point where it becomes energetically favourable to create a real quark anti-quark pair which will bind to the two separated quarks thereby satisfying the requirement that quarks are bound in colourless states.

1.2.3 Asymptotic Freedom

Another consequence of the running coupling of QCD is asymptotic freedom. This means that at either very short distances, or equivalently, very large exchanges of momentum, α_s tends to zero. This means at sufficiently high energies, quarks behave as free particles.

Asymptotic freedom was discovered simultaneously in 1973 by both David Gross and Frank Wilczek [5] and David Politzer [6]. The asymptotic nature of QCD is shown mathematically by calculating the $\beta-$function for a Yang-Mills theory which shows that (for as many as 16 triplets of quarks) strong coupling has a negative dependence on the energy scale. In quantum field theory the $\beta-$function describes the dependence of the coupling strength of a certain field on the energy of the physical process that is described by that theory. The

negative dependence observed in QCD arises from the contribution of gluon anti-screening to the colour magnetic permeability μ.

In QED, screening arises when vacuum fluctuations between two test charges create fermion anti-fermion pairs that are polarised and "screen" the charge observed by each respective test charge and the other. As the distance is increased (or equivalently the momentum transfer is decreased) the observed charge is decreased.

In QCD, there is a conflicting contribution to the screening process which comes from the gluon self-interaction property. The self interaction of gluons leads to gluon loops that arise from vacuum fluctuations like the fermion anti-fermion pairs. The gluon loops contribute an anti-screening effect. The anti-screening arises because the gluons act as colour magnetic dipoles that align themselves parallel to an applied external field which increases the magnitude of μ to above unity [7].

1.3 The Quark Gluon Plasma

The asymptotically free nature of QCD can be taken to the extreme and, at sufficiently high energies, the attractive interaction between coloured objects will cease to exist and the charges will be free to exist deconfined from their bound hadronic states. A system of such high temperature and density would lead to hadronic matter undergong a phase transition and "melting" into a deconfined state of coloured matter known as the Quark Gluon Plasma (QGP). This state of matter was first hypothesised by Collins and Perry in 1975 [8]. It is theorised that in the early stages after the big bang (until approximately $1\mu s$) all matter in the universe existed in a Quark Gluon Plasma phase at extremely high temperature and low net baryon density as shown in Fig. 1.3. The Quark Gluon Plasma is also expected to exist in the very dense cores of neutron stars.

Experimentally, a phase transition can occur in a bulk system of QCD matter if it is

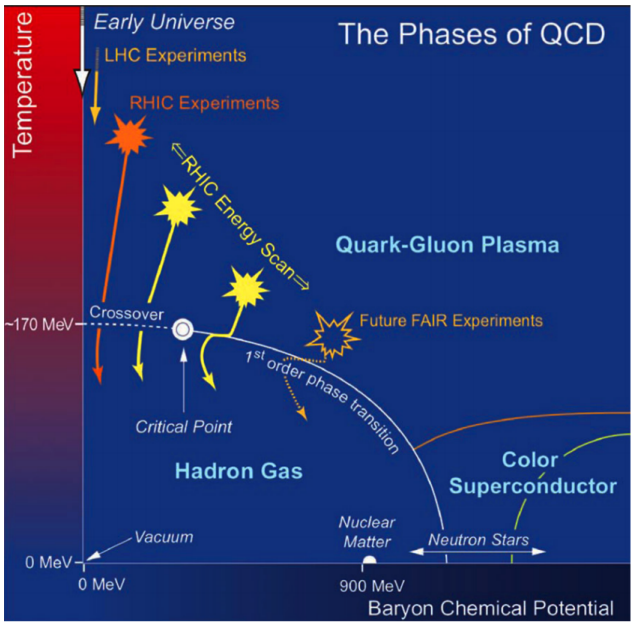

Figure 1.3: QCD Phase Diagram [9].

produced at sufficiently high energy densities. Such a system can be produced in relativistic collisions of heavy nuclei containing many constituent nucleons. In these collisions, the average interaction energy between the colliding nucleons is relatively low and not sufficient to reach the asymptotic limit of QCD. Instead, the phase transition is permitted due to a process known as Debye Screening.

Debye Screening

Debye screening refers to the process by which the net effect of charge carriers is screened at large distances in a dense, charged medium due to the charges between them. This means that the effective range of a test charge is limited to a characteristic length (the Debye screening radius), r_{D}. This process occurs in both electromagnetic plasmas in QED and the QGP for QCD. As the temperature and density of a colour charged system increase, the Debye radius decreases. If the temperature of the system is increased to a sufficiently high level, the Debye radius can fall below the binding radius of valence quarks. This leads to nucleons becoming unbound. The critical temperature at which this phase transition occurs, T_{C}, can

be calculated by lattice theory and simulations. Using 2 and 3 flavour QCD, transition temperatures of approximately $T_C \approx 170$ and 150 MeV are predicted respectively [10, 11]. Figure 1.4 shows the lattice QCD predictions for energy density, ϵ, as a function of system temperature T. At the stated temperature of 170 MeV, the predictions show a very sudden change in energy density, which indicates a phase change from a hadronic gas to a deconfined QCD plasma.

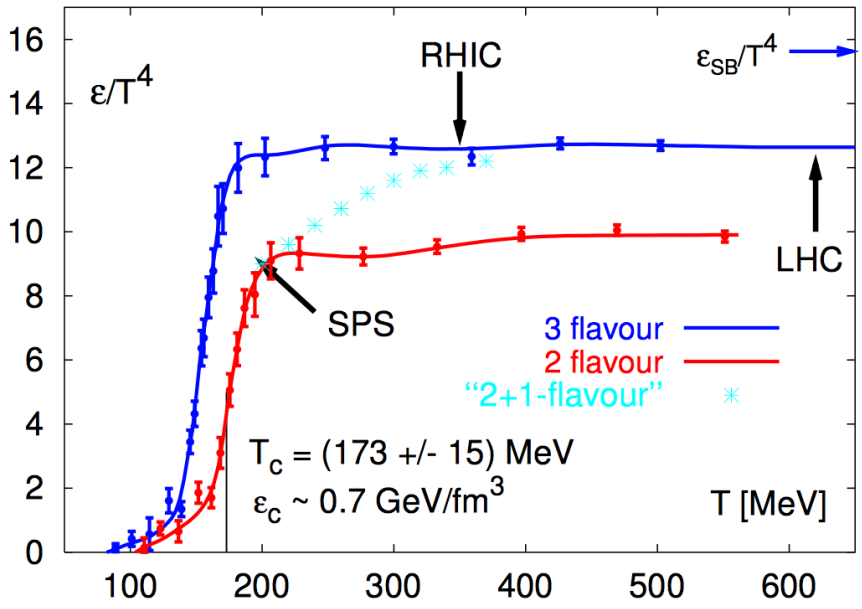

Figure 1.4: Lattice QCD predictions for energy density as a function of temperature modelling a different number of quark flavours [12]. Figure adapted from calculations made in Ref. [13].

1.3.1 QGP in Colliders

After the QGP was first hypothesised, experimentalists set out to study whether or not it could physically be produced. Any such medium, were it to be produced, would only exist for a very brief amount of time before undergoing a phase transition back to normal hadronic matter. The light cone evolution of this process is shown in Fig. 1.5. Due to its short lived nature, the production of a QGP can only be inferred from observations of

certain experimental *signatures* that indicate a phase transition has occurred. The two most prominent of these signatures are *strangeness enhancement* and *charmonium suppression*.

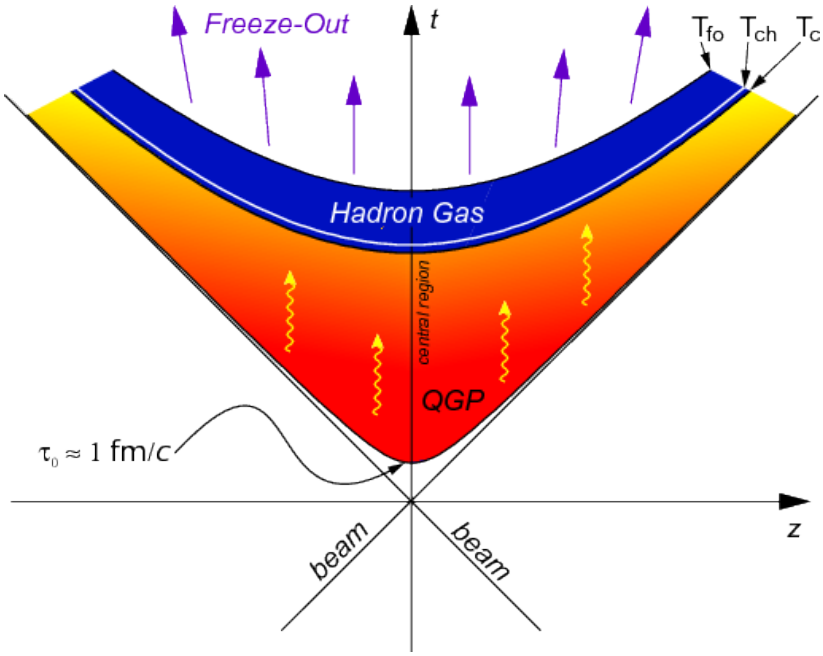

Figure 1.5: Light-cone evolution diagram of a heavy-ion collision. The different temperature scales of evolution are indicated by T_{C} which indicates the critical temperature and T_{ch} and T_{fo}, the chemical freeze-out and thermal freeze-out temperatures respectively. The formation time of the QGP is shown as $\tau_0 \approx 1$ fm/c [14].

Strangeness enhancement was one of the first proposed signatures of the formation of a QGP. From Lattice QCD simulations, the transition temperature for the QGP is expected to be approximately $T_C = 160$ MeV, which is of the same order as the mass of the strange quark [15]. In 1982, Rafelski and Muller predicted that this overlap of scales would lead to an increase of the gluon fusion production rates of strange quarks [16]. This increased thermal production of strangeness was predicted to lead, in particular, to an enhanced abundance of rare, strange baryons such as Λ, Ω and Ξ.

Unlike strangeness production, charm particle production is not expected to be modified by thermal production in the QGP. This is because the charm quark mass is much greater than the average plasma temperatures expected in heavy-ion collisions. However, the probability

of $c\bar{c}$ pairs forming charmonium states in the QGP is affected by the Debye screening radius of the plasma. In a denser medium, pairs of charm quarks are screened by the colour charges between them and this leads to a decrease in the rate of charmonium production in the QGP. This suppression of charmonium was first proposed by Matsui and Satz in 1986 [17].

These two initial signatures of the QGP phase transition link to different aspects of the plasma. Strangeness is enhanced due to the creation of copious thermal gluons whilst charm production remains unchanged but charmonium is suppressed due to screening effects linked to the density of the medium. Of course, any level of suppression or enhancement is defined relative to some reference. In heavy-ion collisions, this reference is taken to be pp collisions as the volume of this collision system is expected to be too small for QGP creation[1]. Scaling must be performed on pp collisions in order to compare particle production rates with those observed in heavy-ion collisions. For soft processes, such as strangeness production, the scaling parameter is the volume which is taken as total charged particle multiplicity. Charmonium production is considered a hard process which originates from individual scatterings. The scaling parameter for these processes is the number of binary collisions (estimated using the Glauber Model [20]).

First attempts to create a Quark Gluon Plasma in the lab were made in the 1980s after upgrades were performed to the Alternating Gradient Synchrotron (AGS) at the Brookhaven National Laboratory (BNL) and the Super Proton Synchrotron (SPS) at CERN to allow them to perform fixed target experiments with beams of heavy ions. By the early 1990s, experiments performed at these facilities began to observe evidence of the QGP phase transition. Observations of the enhancement of strange baryons in fixed target experiments at SPS offered the first evidence for this phase transition [21–23]. These observations were confirmed when SPS entered the second phase of its heavy-ion programme [24–27] along with the first

[1]It is the topic of some debate as to whether QGP phase transitions have been observed in high-multiplicity small systems, with recent measurements observing an enhancement of strangeness production in high multiplicity pp and p–Pb collisions [18, 19].

observations of the suppression of charmonium in heavy-ion collisions [28, 29]. These results collectively constituted the first evidence that a phase transition to a deconfined state of quarks and gluons was possible to achieve in collisions of heavy nuclei.

The next phase in the study of the QGP came with the construction of the Relativistic Heavy Ion Collider (RHIC), the worlds first collider of heavy nuclei. Initially, RHIC delivered heavy-ion collisions to four experiments, PHOBOS, BRAHMS, PHENIX and STAR. Observing Au-Au collisions at centre-of-mass energies between $\sqrt{s_{\mathrm{NN}}} = 130 - 200$ GeV, these four experiments created a wealth of new data in the search for QGP signatures. Building on the measurements performed at SPS, the RHIC experiments were able to confirm that, indeed, a deconfined system of quarks and gluons is produced in heavy-ion collisions at sufficiently high energies [30–36].

In addition to studying the already observed signatures of the QGP phase transition, the higher collision energy of RHIC meant that the experiments were able to study the effects of the medium in more detail with new observables. In particular, one of the strong areas of focus for these studies was the production of high$-p_{\mathrm{T}}$ charged hadrons. Measurements of the yield of inclusive high$-p_{\mathrm{T}}$ charged hadrons in the most central Au–Au collisions performed by the experiments at RHIC showed that they are significantly suppressed relative to pp collisions at the same beam energies [37–41]. These observations provide further evidence that a dense, strongly interacting medium is formed in central A–A collisions and that the production of high$-p_{\mathrm{T}}$ particles that traverse it is significantly modified. Another significant observation made from these new datasets was the fact that the anisotropic flow of charged particles resulting from central heavy-ion collisions agreed quantitatively for the first time with predictions from ideal fluid dynamics [42]. Anisotropies in the transverse momentum distribution of final state particles were first predicted as an unambiguous signature of collective behaviour by Ollitrault in 1992 [43]. These observations created a major shift in the understanding of the QGP within the community, showing that the medium behaved as a

strongly-coupled plasma that flowed like a liquid as opposed to a hot gas of colour charged particles as previously understood.

By this stage in the time line of the study of the QGP, it became clear that there was overwhelming evidence that the deconfined state of quarks and gluons did exist and was producible under laboratory conditions and the four RHIC experiments published white papers summarising their discoveries and highlighting open questions [30–33]. Therefore, focus began to shift towards understanding more about this new state of matter and how it behaved.

Since 2010, the Large Hadron Collider (LHC) at CERN has delivered the highest energy beams achieved to date [44–46]. The LHC consists of four experiments situated at the four collision points around the ring, ALICE, ATLAS, CMS and LHCb [47–50]. The ALICE experiment is the only one of the four to be optimised for studying heavy-ion collisions. A detailed description of the ALICE detector can be found in Chapter 4. Initially, the LHC collided lead nuclei at a centre-of-mass energy of $\sqrt{s_{\mathrm{NN}}} = 2.76$ TeV and measurements performed by ALICE and CMS provided further evidence of the QGP phase transition with observations of charmonium suppression [51, 52] and strangeness enhancement [53, 54]. However, a strong area of focus for these experiments has been that of jets and jet substructure. Advancements in jet clustering techniques [55, 56] meant that the studies of the yield of high$-p_{\mathrm{T}}$ hadrons performed at RHIC could be extended by measuring jets of hadrons. Jets are particularly useful probes of the QGP medium because their formation time is very small – shorter than the expected formation time of the medium itself. This means that they are sensitive to all the stages of the QGP evolution. The suppression of jets in Pb–Pb collisions has been extensively studied by the ALICE, CMS and ATLAS collaborations [57–67] and these measurements contribute significantly to furthering our understanding of the dense nuclear medium created in central heavy-ion collisions.

In recent years, jet substructure has emerged as a powerful tool for studying the inter-

actions between high$-p_{\mathrm{T}}$ particles and the QGP. By studying jet substructure and its modification in heavy-ion collisions relative to pp, it is possible to elucidate information about the underlying mechanisms contributing the energy loss for jets and high$-p_{\mathrm{T}}$ particles that is observed. A set of observables known as *jet shapes*, which relate to certain aspects of the substructure of jets, have been measured by experiments at the LHC [68–71]. Comparing these measurements to theoretical predictions enables the determination of the dynamical properties of the medium such as the medium transport parameter $\hat{q}$ and opacity.

Studying the substructure of jets is the focus of the work presented in this thesis. Recursive and grooming techniques, primarily developed for the measurement of jet substructure in high energy hadron collisions for QCD studies and searches for Beyond the Standard Model (BSM) physics [72–74], are explored. Additionally, a novel approach to studying the phase space of the QCD radiation of jets is presented.

The thesis is organised as follows. Chapter 2 discusses the details of jets and their production in high energy hadron collisions as well as their subsequent modification in heavy-ion collisions. Chapter 3 covers some new ideas about how studying their substructure may shed light on the currently poorly understood concept of jet energy loss in the QGP. The ALICE experiment, used to study these high energy collisions, will be discussed in Chapter 4 with the analysis procedure covered in detail in Chapter 5. Chapter 6 presents the final results and discussion of the entire thesis before some concluding remarks and proposals for future work. Appendix A contains the publication that resulted directly from the work presented in this thesis.

Chapter 2

Jets

2.1 The Physics of Jets

A jet is defined as collimated energy flow formed from successive gluonic emissions off of an initial high energy parton. A jet can be thought of as being produced in three distinct stages, separated by their characteristic energy scales. The first stage, which occurs at the largest energy scale, involves the interaction of a small number of primary partons exchanging a large momentum transfer-squared, Q^2. Experimentally, jets are produced by colliding together hadrons or leptons at high energies which subsequently undergo hard sub-processes such as $q\bar{q} \rightarrow q\bar{q}$ or $e^+e^- \rightarrow q\bar{q}$. The second scale of interest is the multi-parton cascade shower that occurs over the time scale from the initial hard scattering to some showering cutoff scale, t_0. At this scale, gluons are radiated off the initial traversing parton and subsequently decay into quark antiquark pairs or radiate additional gluons. This cascade of emissions leads to a shower of partons aligned to the direction of the initial radiator due to the collinear enhancements of the QCD matrix elements. As the virtualities of the partons reaches the somewhat arbitrarily defined showering cutoff scale[1], a non-perturbative process known as

[1]The showering cut off scale should be small but much greater than the intrinsic scale Λ^2_{QCD} so as to satisfy the requirement that a perturbative description of QCD is sustained down to this scale.

hadronisation occurs. This is the last of the three distinct stages of jet evolution whereby the resultant set of partons combine to form a set of final state hadrons. The process of hadronisation occurs at scales where non-perturbative effects cannot be neglected and is therefore very difficult to model theoretically. Details of how different models simulate this process are described in Section 2.4. The resulting collection of final state particles is defined as a jet and these jets form the basis of the analysis performed in this work.

Jets have been studied extensively for the past five decades at high energy colliders and work performed by a large number of experiments has laid the groundwork of understanding in jets and their associated physics that allows for analyses such as that which is carried out here. In the modern day, jets are more relevant than ever and their production at LHC energies is far greater than in any preceding experiments with a significantly increased cross section for hard processes. The jet cross section can be calculated using the pQCD factorisation theorem [75]. Factorisation allows us to separate out the contributions from the non-perturbative initial and final states governed by the Parton Distribution Functions (PDFs) and Fragmentation Functions (FFs), respectively, from the perturbative high-Q^2 scattering that can be calculated in QCD. One may represent the perturbative component of the jet production cross section as $d\sigma^{ab\to c+X}(x_1, x_2)$, which is the cross section for producing parton c via the scattering of partons a and b with momentum fraction x_1 and x_2 respectively. Then the factorisation of hard processes in QCD leads to the cross section for jet or single hadron production in pp collisions to take the form

$$d\sigma^{pp\to h/jet+X} \propto f_a(x_1, Q^2) \otimes f_b(x_2, Q^2) \otimes d\sigma^{ab\to c+X}(x_1, x_2) \otimes D_c^{h/jet}(z, \mu^2), \tag{2.1}$$

where the initial state non-perturbative terms $f_{a,b}(x_{1,2}, Q^2)$ are the PDFs which are interpreted as the probability of finding parton of type a in a hadron carrying a fraction of the

hadron momentum, x_1, and $D_c^{h/jet}(z, \mu^2)$ is the FF which represents the probability that parton c fragments into a hadron h or jet with fractional momentum $z = p_{\mathrm{h/jet}}/p_c$.

2.1.1 Parton Distribution Functions

When colliding protons using high energy particle colliders, the constituent partons, on average, exchange sufficiently high energy (Q^2) to resolve the partonic structure of the other proton. This resolving power of the partons means that the resulting interactions from the collisions are dependent on the distribution of partons in the participating hadrons. The PDFs represent the probability of a given partonic constituent carrying a certain fraction of the overall hadron momentum. They are non-perturbative and must be evaluated experimentally. Typically the PDFs are determined using data from Deep Inelastic Scattering (DIS) experiments which involve scattering electrons off protons or nuclei [76]. The PDFs are measured at a certain energy scale indicated by the Q^2 argument in equation 2.1 and are non-perturbative. However, their evolution to different energies can be performed using the DGLAP evolution equations which employ perturbative techniques [77–79]. Figure 2.1 shows the proton PDFs at two different energy scales and it can be seen that the structure of the proton changes as the energy of the resolving particle is increased. The PDFs are determined using global fits to a wide range of available hard scattering data, including those from DIS experiments. Parton distributions have been studied extensively for the past 30 years and as more data has become available the global fits have been performed to increasingly higher accuracy at LO, NLO and NNLO (see Ref. [80] and references therein).

At higher energy, the proton is seen to be made up of an increasing number of low energy gluons. This can be explained by considering the resolving power of a higher energy probe. If the interaction energy of a probe is increased then, from the Heisenberg uncertainty principle, it is able to resolve shorter distances. If these distances are sufficiently small, the probe may begin to *see* the low energy gluons being exchanged by the bound quarks and so will resolve a

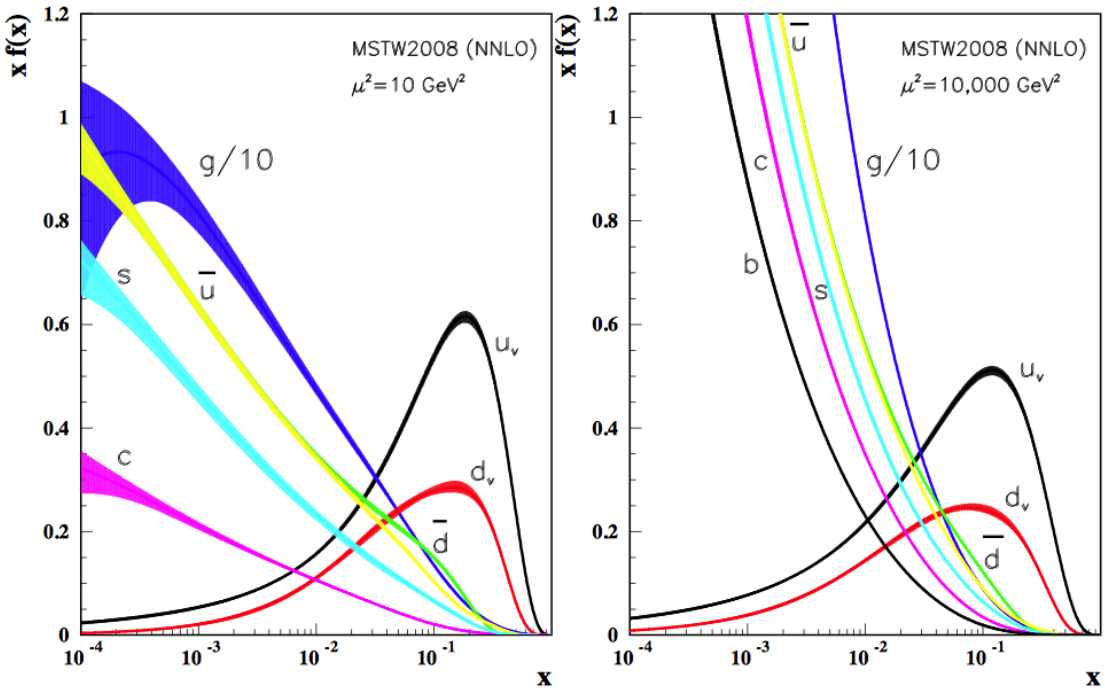

Figure 2.1: Proton PDFs for two different selections of exchanged 4-momentum squared, μ^2 [81].

more gluonic proton than a probe that is lower in energy and hence only able to resolve on the length scale of the valence quarks. At LHC energies, the dominant process by which jets are produced is gluon fusion due to the increased gluon density of the colliding protons. Having a set of highly accurate PDFs means that one of the two non-perturbative components of the factorised jet and single parton cross section is extremely well constrained. This is a very important ingredient in understanding jet production in the energy regime of the LHC.

2.1.2 Fragmentation Functions

Fragmentation Functions make up the non-perturbative final state component of the factorised single hadron or jet cross sections. The fragmentation functions are generally denoted by $D_i^h(z, Q)$ and are defined as the probability of forming a hadron, h, that carries a fraction z of the overall initial parton, i, momentum at the energy scale Q. The fragmentation

functions describe the production of a jet from the point of initial hard scattering through to the energy scales of partonic showering and non-perturbative hadronisation discussed in section 2.1. As they must describe the process of hadronisation, the fragmentation functions are clearly non-perturbative. However, as with the PDFs, their energy dependence can be evaluated perturbatively as long as Q is large.

Figure 2.2 shows the distribution for the fragmentation observable $F(z, p_{\mathrm{T,jet}})$ measured in pp collisions at $\sqrt{s} = 7$ TeV by the ATLAS collaboration [82]. The observable is defined as

$$F(z, p_{\mathrm{T,jet}}) = \frac{1}{N_{\mathrm{jet}}} \frac{dN_{\mathrm{ch}}}{dz}, \tag{2.2}$$

where the $1/N_{\mathrm{jet}}$ is the normalisation to the number of jets, N_{ch} is the number of charged particles in the jet and z is defined as

$$z = \frac{\mathbf{p}_{\mathrm{jet}} \cdot \mathbf{p}_{\mathrm{ch}}}{|\mathbf{p}_{\mathrm{jet}}|^{\mathbf{2}}}. \tag{2.3}$$

$F(z, p_{\mathrm{T,jet}})$ is a sum over all the fragmentation functions, $D_i^h(z, Q)$, for each parton species, i, weighted by their production rate from hard scattering processes. The distributions of the data agree well with the predictions from the PYTHIA Monte Carlo event generator across the full range of $p_{\mathrm{T,jet}}$. The PYTHIA event generator and its approach to modelling the non-perturbative process of hadronisation are discussed in more detail in Section 2.4.1.

The stage of jet evolution described by the fragmentation functions is the premise for the field of jet substructure studies and the work conducted in this thesis. The perturbative scales of the partonic showering of the jet are widely understood to be goverened by the QCD splitting functions which are contained within the DGLAP evolution equations. The splitting functions of QCD describe the probability of a single parton with momentum x splitting into a pair of partons with a share of the inital momentum zx and $(1 - z)x$, respectively. To

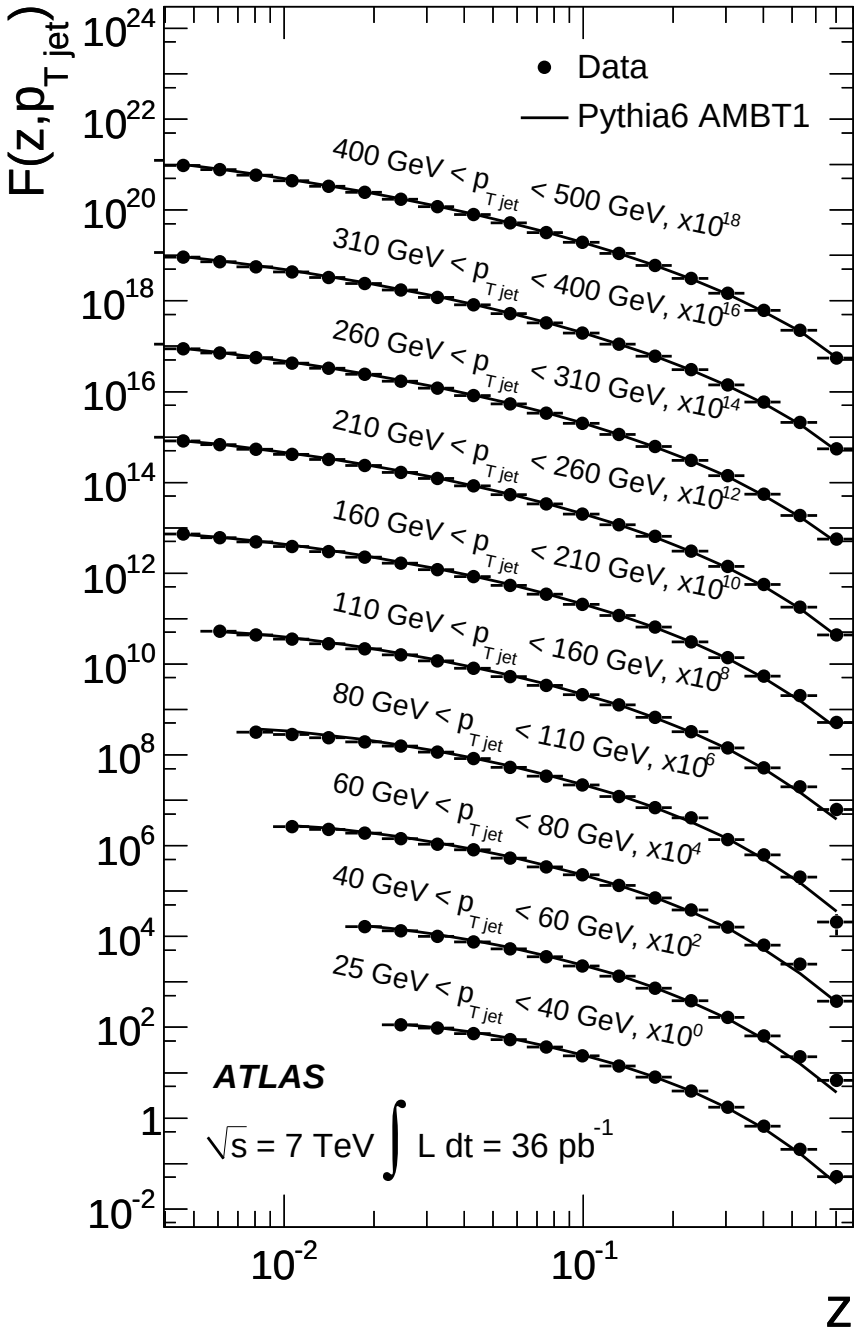

Figure 2.2: Distribution of $F(z, p_{\mathrm{T,jet}})$ in bins of $p_{\mathrm{T,jet}}$ as measured by the ATLAS collaboration in pp collisions at $\sqrt{s} = 7$ TeV [82]. Data are shown as circles with predictions from AMBT1 PYTHIA shown as solid lines.

leading order the QCD splitting functions are given as

$$P_{q\to qg}(z) = C_F\Big[\frac{1+z^2}{1-z}\Big], \tag{2.4}$$

$$P_{q\to gq} = P_{q\to qg}(1-z) = C_F\frac{1+(1-z)^2}{z}, \tag{2.5}$$

$$P_{g\to q\bar{q}}(z) = T_R[z^2+(1-z)^2], \tag{2.6}$$

$$P_{g\to g}(z) = 2C_A\Big[\frac{z}{1-z}+\frac{1-z}{z}+z(1-z)\Big], \tag{2.7}$$

where $C_F = \frac{4}{3}$, $C_A = N_c = 3$ and $T_R = \frac{1}{2}$ are the QCD structure constants. By studying jet substructure using the methods detailed in Chapter 3, it is possible to measure observables that are closely linked to these fundamental QCD equations.

2.2 Jets in the Quark Gluon Plasma

Jets are not only useful objects for probing the fundamentals of QCD in environments generated in pp or e^+e^- collisions, but also have far reaching applications in the field of heavy-ion collisions. Jets are produced on time-scales much smaller than that of the formation time of the QGP and as such they make excellent probes that offer access to all stages of the evolution of the strongly interacting, deconfined medium. With the exception of the slight modification of the nuclear Parton Distribution Functions (nPDFs) relative to the proton PDFs, the production of jets in heavy-ion collisions is expected to be equivalent to that of a superposition of many pp collisions. Studying how the subsequent evolution of jets is modified in the presence of the QGP formed in such collisions can offer significant insight to understanding the fundamental properties of the medium and the QCD processes taking

place.

The suppression of high$-p_{\mathrm{T}}$ hadrons and jets observed in heavy-ion collisions relative to pp collisions [57–67, 83–85] is attributed to energy loss that occurs as the jet propagates through the medium. This energy loss can occur via *collisional* and *radiative* processes which reduce the energy of the traversing parton via *elastic* and *inelastic* scatterings, respectively [86]. A parton traversing a QGP can be treated as analagous to an electrically charged particle traversing a QED plasma; this approach is often taken when attempting to model partonic energy loss in the medium. The energy loss experienced by a particle traversing a medium depends on several well defined parameters

- the *mean free path* $\lambda = 1/(\rho\sigma)$, where ρ is the medium density and σ is the integrated cross section for particle-medium interactions.
- the *opacity* $N = L/\lambda$ which is defined as the number of scatterings of the parton by a medium of length L.
- the *Debye mass* $m_D(T) \sim gT$ which characterises the typical momentum exchange with the medium in a given interaction and depends on the medium temperature T and the strong coupling parameter g.
- the *transport coefficient* $\hat{q} \equiv m_D^2/\lambda$ which defines the "scattering power" of the medium as the average transverse momentum squared exchanged per unit of path length.

Collisional energy loss

First estimated by Bjorken in 1982 [87], the collisional energy loss of a particle traversing a medium arises through elastic scatterings with the constituents within the plasma. This process is the dominant method of energy loss for low momentum particles and the average energy loss per scattering for a medium of temperature T is given approximately as

$$\langle \Delta E_{coll}^{1scat} \rangle \approx \frac{1}{\sigma T} \int_{m_D^2}^{t_{max}} t \frac{d\sigma}{dt} dt, \tag{2.8}$$

where the differential cross section $d\sigma/dt$ is given with respect to momentum transfer squared $t = Q^2$ [86]. This method of energy loss is shown for a quark propagating the quark-gluon plasma and exchanging energy ΔE with the medium on the left of Fig. 2.3.

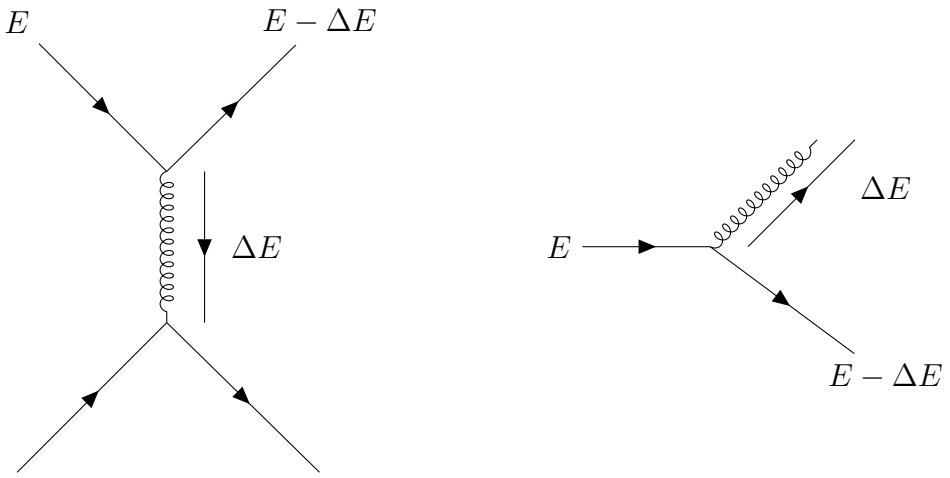

Figure 2.3: Energy loss Feynmann diagrams for collisional (left) and radiative (right) energy loss of a quark traversing a quark-gluon plasma with initial energy E losing ΔE energy to the medium.

Radiative Energy Loss

The second method of energy loss in the QGP is radiative energy loss, where energy is carried away from the traversing parton via inelastic scatterings with the medium. Figure 2.3 (right) shows how this process occurs for a traversing quark radiating a gluon induced by the medium. This method of energy loss is the dominant process for high energy particles in a plasma. In general, for a charge traversing a medium, the energy radiated by a photon or gluon is given by the Bremsstrahlung spectrum

$$\Delta E_{rad}^{1scat} = \int^{E} \omega \frac{dI_{rad}}{d\omega} d\omega \tag{2.9}$$

where ω is the energy of the radiated photon or gluon and I_{rad} is the radiation intensity. The Bremsstrahlung spectrum is calculated differently for media with lengths much smaller and much larger than the mean free path. These regimes are known as the Bethe-Heitler (BH) regime [88] ($L \ll \lambda$) and the Landau-Pomeranchuk-Migdal (LPM) regime [89, 90] ($L \gg \lambda$). These regimes are separated due to the fact that in general, for a thin medium (BH regime), the traversing particle experiences at most a single inelastic scatter with the medium whereas in a thick medium (LPM regime) there are $N = L/\lambda$ scatterings which is defined as the opacity of the medium. In the LPM regime, the Bremsstrahlung spectrum is not simply N times the BH spectrum due to the LPM effect which in QED describes the fact that neighbouring scattering centres in the medium interfere coherently due to the finite formation time of a photon and therefore act as a single scattering centre as opposed to several.

2.2.1 Jet Quenching

The two energy loss mechanisms for a charge propagating through a plasma lead to the phenomenon known as *jet quenching*. Jet quenching is observed in experiment by performing measurements of the nuclear modification factor (R_{AA}) which is defined as the ratio of jet yields in A–A collisions relative to pp collisions scaled by the number of binary collisions. The number of binary collisions is estimated from the event multiplicities using the Glauber Model [20]. Figure 2.4 shows the distributions of R_{AA} as measured by ALICE, CMS and ATLAS for $R = 0.2$ jets in Pb–Pb collisions at $\sqrt{s_{\mathrm{NN}}} = 2.76$ TeV. It can be seen from the distributions that jets are suppressed by up to a factor of 5 in Pb–Pb collisions relative to pp. This suggests that jets lose a significant fraction of their energy as they travel through the QGP.

Theoretically, there are several different approaches taken to model the process of jet quenching in the quark-gluon plasma. These models build on the idealised energy-loss equa-

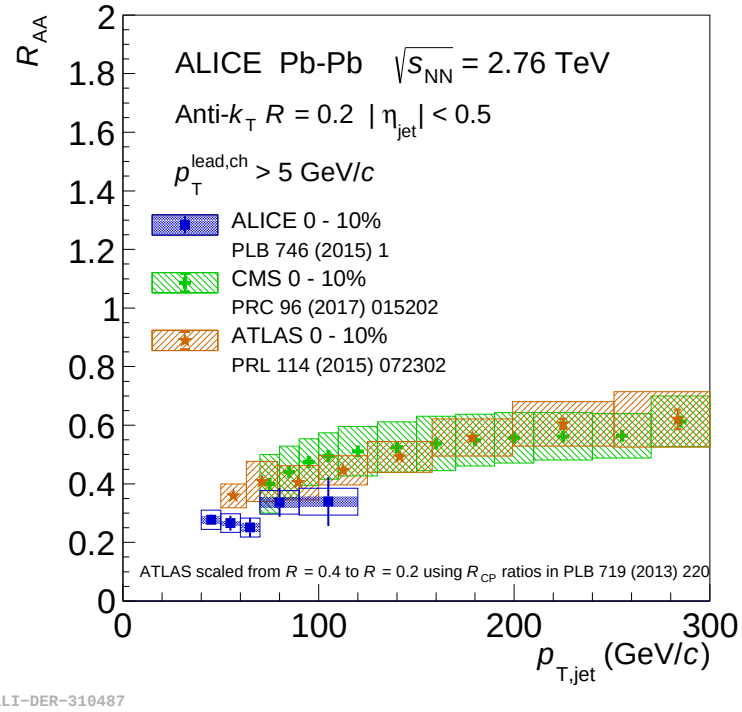

Figure 2.4: Comparison of the nuclear modification factor for fully reconstructed anti-k_T jets ($R = 0.2$) with ALICE, ATLAS and CMS [91].

tions, Eq. 2.8 and Eq. 2.9, that describe the energy loss of an infinite-energy parton traversing a non-expanding QGP treated as an ideal gas to the more realistic QGP formed in heavy-ion collisions. There are four main pQCD formalisms for describing the energy loss of a parton propagating through a QGP and all are based on a pQCD factorised approach. The models differ mostly in their treatment of the relevant scales of the scatterings such as parton energy, E, typical momentum exchange, m_D, and the size and expansion of the medium. The first of these formalisms is the BDMPS-Z approach, named after the original authors [92–96]. The BDMPS-Z model takes a path integral approach to the opacity expansion of the medium and describes the energy loss as a consequence of many soft scatterings off multiple scattering centres in the medium. The second formalism, which again attempts to describe the partonic energy loss by computing the radiated gluon spectrum, is the GLV model [97–101]. The main difference between the GLV and BDMPS-Z formalisms is that GLV begins from the spec-

trum of single-hard radiation and expands to a finite number of collisions using Feynmann diagrams [99]. This is an approach to modelling a "thin" plasma that is only a few mean free paths thick leading to the finite number of collisions.

The two other main formalisms aim to determine the final distribution of partons traversing the QGP directly. The Higher-Twist (HT) approximation [102] does this by applying corrections to the leading-twist cross sections that are enhanced by the medium length, L. Finally, AMY [103–105] uses a finite temperature field theory approach to compute modified fragmentation functions by convolving the vacuum FF with the hard parton upon its exit from the medium after medium induced scatterings of the order gT.[2]

These different jet quenching formalisms have all made successful comparisons to experimental data, Fig. 2.5 shows the calculations from three of these parton energy loss formalisms for π^0 suppression compared to data obtained with PHENIX in Au–Au collisions at $\sqrt{s_{\mathrm{NN}}} = 200$ GeV [106, 107]. The theoretical calculations also employ a 3D hydrodynamical evolution of the medium density.

Extensive comparisons of these theoretical models and experimental data are however hard to come by. This is because modelling the full process of jet quenching is a complex and multi-stage problem involving many competing components from the initial jet production to the time evolution of the medium and the jet fragmentation. Due to these many competing processes it is extremely difficult to isolate differences between the parton energy loss formalisms and elucidate the fundamental mechanisms of jet quenching. This is where the work conducted in this thesis aims to help address the current difficulties faced when attempting to extract information about the underlying physics processes of partonic energy loss in a colour charged medium. It is proposed that by studying the substructure of jets using novel recursive declustering techniques, as discussed in the following chapters, one is able to better differentiate between specific energy loss formalisms.

[2]For QCD, g is understood to be the strong coupling g_s, while for a QED plasma, g is taken to be the electric charge, e.

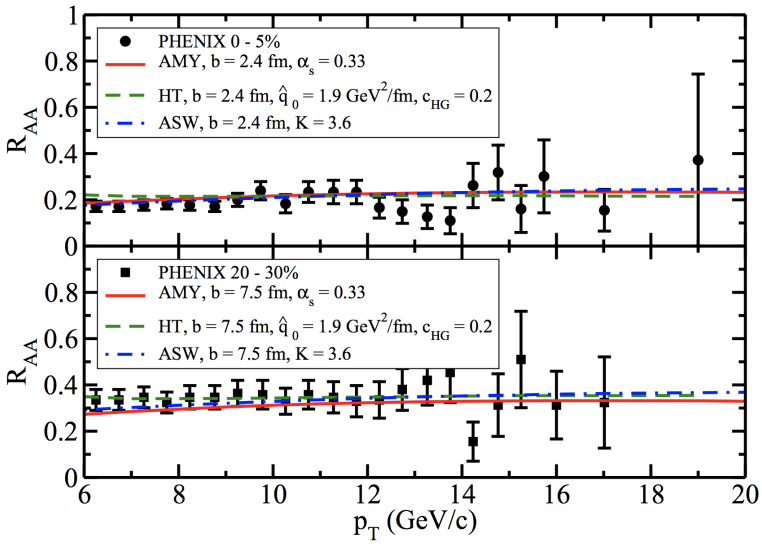

Figure 2.5: Nuclear modification factor R_{AA} for π^0 as a function of p_{T} as measured by the PHENIX collaboration [106] for two different centrality ranges compared to calculations from 3 energy loss formalisms: Higher-Twist (HT), finite temperature field theory (AMY) and multiple soft gluon emission (ASW).

2.2.2 Coherent Emitters

For a parton travelling through a strongly-interacting deconfined medium, the scattering sites with which it interacts can be separated by distances that are shorter than that of the wavelength of the radiated gluon. When this happens, the individual scattering sites cannot be treated independently and the quantum interference between them leads to a suppression of the gluon radiation spectrum, this is known as the previously mentioned LPM effect which was originally proposed for QED plasmas. Interference effects arise in another form when considering the fragmentation of a jet and this is related to *antenna radiation*, the soft gluon radiation from a pair of colour correlated partons [108–110].

In vacuum, the process of multiple gluon emissions is governed by the effects of colour coherence. These effects can be best understood by considering a simple antenna of high energy partons separated by some opening angle Θ. Considering a pair of such partons radiating a gluon, they will have a transverse separation of $r_\perp = \Theta\, t_f$ at the time of formation of the gluon t_f, as shown in Fig. 2.6. The finite formation times of the emitted gluons

underpins both the coherence effects from the LPM effect. In vacuum, the antenna radiation is related to the emitted gluon kinematics by $t_f \sim 1/\theta^2\omega$ and in medium by $\tau_f \sim 2\omega/k_\perp^2$, where $k_\perp$ and θ are the transverse momentum and angle relative to the emitter and ω is the overall energy. The energy of the gluon determines its ability to independently resolve the separate prongs of the antenna and is related to its transverse momentum by $\lambda_\perp \sim 1/k_\perp$. A gluon radiated with $\lambda_\perp > r_\perp$ will not be able to resolve the separate branches of the antenna and the two prongs will radiate the gluon coherently meaning the gluon is only sensitive to their combined charge. For a gluon with $\lambda_\perp < r_\perp$ the individual components of the antenna can be resolved and the gluon will be radiated from a single prong. This relation of gluon energy to the resolving power of the antenna axis can be simply linked to the angular distribution of radiated gluons. For gluons radiated at angles $\theta < \Theta$ the individual charges are resolved whereas gluons radiated with $\theta > \Theta$ only observe the the colour dipole as a single charge and this leads to the phenomenon known as *angular ordering* [111].

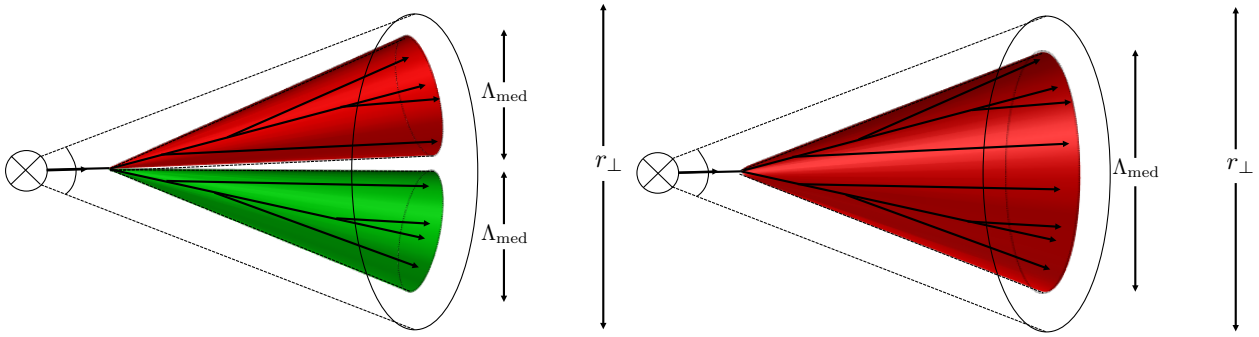

Figure 2.6: A schematic representation of a jet shower following angular ordering for a medium with $\Lambda_{\text{med}} < r_\perp$ (left) and $\Lambda_{\text{med}} > r_\perp$ (right).

When considering a jet fragmenting in a colour-charged strongly-interacting medium, there is the effect of the medium's ability to resolve the inner structure of the jet in addition to the coherence effects that occur in vacuum. There is a characteristic length scale over which the medium is able to resolve independent colour charges, this is denoted as Λ_{med}. This medium length scale is related to the properties of the medium by $\Lambda_{\text{med}} \equiv 1/\sqrt{\hat{q}L}$

and leads to a characteristic angle θ_c, below which the medium is unable to resolve the internal structure of the jet and sees it as a single emitter [109]. For a jet with an opening angle $\Theta_{\text{jet}} \ll \theta_c$ resulting from the first splitting (the largest angle in the shower due to angular ordering) the jet is not resolved by the medium (Fig. 2.6 right). By losing energy as a single emitter, the jet radiates as in vacuum so the fragmentation and substructure is identical to a jet that evolved outside of the medium. For the medium induced radiation, this occurs as if radiated off of the initial parton and hence the medium induced energy loss is directly proportional to the colour charge of the jet initiator. For a jet with an initial splitting $\Theta_{\text{jet}} \ll \theta_c$ (Fig. 2.6 left) the medium will resolve separate parts of the jet and will induce radiation off each prong of the antenna and possibly subsequent legs of the jet shower. When the individual components of the jet are resolved by the medium, the standard angular ordered fragmentation that is observed in vacuum will be broken in the subsequent evolution of the jet and the jet will lose more energy as a whole as additional medium induced energy loss occurs. The formation time of the splittings also affects the ability of the medium to resolve the different components of the jet. Splittings with a formation time longer than that of the lifetime of the medium will fully form outside the medium and hence will not radiate medium induced gluons, even if the angle of the splitting was above the critical angle θ_c.

Studying the effects of colour coherence has been the subject of many recent efforts by the experimental [112] and theoretical [2] communities and serves as a motivation for the studies performed in this work.

2.3 Jet Finding

Experimentally, one does not have access to all of the information needed to perfectly identify all particles corresponding to a single jet. Jets must be reconstructed using the information as measured by the detectors and the method of reconstruction must be clearly defined and

consistent so that one measurement can be compared to others as well as theoretical predictions. The methods by which jets are reconstructed in experiment are known collectively as jet clustering algorithms.

2.3.1 Jet Clustering Algorithms

Jet clustering algorithms offer a method by which final state hadrons, that are measured by the detectors at particle colliders, can be combined to reconstruct the initial kinematic information of the primary parton. Once event reconstruction has been performed, jets can be reconstructed using a variety of jet clustering algorithms. For the analysis performed in this thesis, charged jets, which take reconstructed tracks as input to jet clustering, are analysed. By using the reconstructed tracks as inputs defined by their $\eta - \varphi$ coordinates and 4-momenta, one can cluster potential jet candidates by following a prescribed set of rules. These rules, known collectively as algorithms, define the ordering in which tracks are combined in order to identify possible jets. The algorithm, which defines which particles are recombined, together with the choice of recombination scheme, specify a jet definition. A physical result should be independent on ones choice of jet definition.

Whilst there are a variety of different algorithms that can be used to reconstruct jets, the vast majority of jet finding is performed using a subset of algorithms known as *sequential recombination algorithms*. These algorithms take a "bottom-up" approach, meaning that they start with the individual input tracks and sequentially undo the QCD splittings via recombination. The most commonly used sequential recombination algorithms are the three variations of the generalised k_{T} algorithm: k_{T}, anti-k_{T} and Cambridge-Aachen [55, 56, 113, 114].

Generalised k_{T} Algorithm

The generalised k_{T} algorithm calculates the distance between all input particles based on:

$$d_{\mathrm{i,j}} = \min(p_{\mathrm{T,i}}^{2\alpha}, p_{\mathrm{T,j}}^{2\alpha})\frac{\Delta R_{\mathrm{i,j}}^2}{R^2}, \qquad d_{\mathrm{i,B}} = p_{\mathrm{T,i}}^{2\alpha}, \tag{2.10}$$

where $d_{\mathrm{i,j}}$ is the distance between particles i and j and R is the jet clustering radius. The parameter α defines the ordering of the clustering. With $\alpha = 1$ the clustering starts by clustering the softest particles first (k_{T}), α = -1 clusters the hardest constituents first (anti-k_{T}) and $\alpha = 0$ only considers the angular separation of the tracks (Cambridge-Aachen). The quantity $d_{\mathrm{i,B}}$ is referred to as the "beam distance". The three algorithms then follow the same prescription:

1. Find the smallest of $d_{\mathrm{i,j}}$ and $d_{\mathrm{i,B}}$
2. if $d_{\mathrm{i,j}}$ recombine i and j using the given recombination scheme
3. if $d_{\mathrm{i,B}}$ call i a jet and remove it from the list of input particles
4. repeat from the step 1. until all particles are clustered into jets

Infrared-Collinear Safety

An important aspect of jet reconstruction is the concept of infrared and collinear (IRC) safety. IRC safety refers to the invariance of an object with respect to the event modifications of additional collinear splittings and infrared emissions. An example of an observable that is not IRC safe would be the number of jets in an event, because additional emissions of soft (infrared) particles close to the beam axis would lead to an increase in the total number of jets reconstructed. However if one imposes a minimum transverse momentum cut on the reconstructed jet candidates then the number of jets becomes IRC safe; the soft

"jets" reconstructed close to the beam axis won't pass any reasonable transverse momentum threshold.

IRC safety is important because without it one loses real-virtual cancellation in NLO/NNLO QCD calculations and this causes calculations to diverge [115]. Figure. 2.7 shows how two different methods of labelling the same set of particles into jets can produce a collinear safe and a collinear unsafe set of jets, respectively. In the collinear safe case, the radiation of an additional collinear gluon does not change the jet that is clustered. In the unsafe case, the soft presence of the collinear gluon leads to two different jets being clustered. A clustering algorithm that produces different results when such gluons are radiated will result in a collinear unsafe population of jets. For any observable to be reliable and comparable to theory, the calculations require it to be IRC safe. The sequential recombination jet clustering algorithms used in this analysis produce a collection of IRC safe jets.

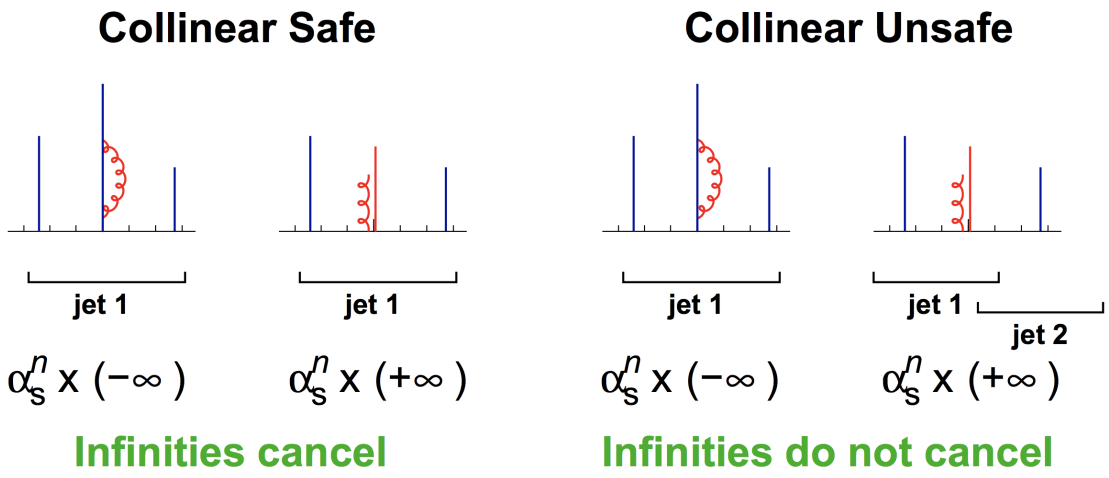

Figure 2.7: Illustration for collinear safety where partons are represented by vertical lines whose height is proportional to their transverse momentum and the horizontal displacement represents their distribution in rapidity space [116].

2.4 Theoretical Models

2.4.1 PYTHIA

PYTHIA is a high-energy physics event generator that models the entire event from initial particle interactions from the two incoming hadrons to the final state of outgoing particles. Using a variety of analytical results and various QCD-based models, PYTHIA is used to simulate a wide range of physics including hard processes, partonic showers, fragmentation and hadronisation. In this analysis, two different versions of PYTHIA are used. PYTHIA 6.4 [117] is the older version based on Fortran code with systematic tunes to LHC data available [118]. It is used for embedding into real Pb–Pb events (Perguia 0 tune) and for comparisons to the unfolded pp data (Perugia 2011 tune). PYTHIA 8 [119] is a more modern version of the PYTHIA program written in C++ that is used also to compare the unfolded pp data without any specific tunes.

PYTHIA is optimised for modelling hard processes with one or two final-state objects. For the generations used in these studies the *QCD jets* configuration was used which includes all partonic $2 \rightarrow 2$ scattering processes with no higher-order loop corrections applied. The partonic showering of jets in PYTHIA is virtuality-ordered, modelled using splitting kernels $P_a \rightarrow bc(z)$ which define the fraction of momentum carried by the daughter b from parent parton a. The hadronisation process in PYTHIA is calculated using the Lund string fragmentation model [120, 121] as default. In the Lund string model the fragmentation proceeds from the stretching of a colour flux tube connecting a quark and antiquark ($q_1\bar{q}_1$) that are travelling apart from each other. As the potential energy in the string increases with the separation it becomes energetically favourable to generate a new quark-antiquark pair that bind with the original pair to form two mesons ($q_1\bar{q}_2 + \bar{q}_1 q_2$). This process proceeds generating new quark and antiquark pairs until the energy of the outgoing hadrons is low enough that the constituents no longer attempt to separate. It is also possible that a diquark-antidiquark pair

is produced in the string fragmentation process leading to the creation of baryon-antibaryon pairs. The fragmentation stage of the hadronisation process often results in a large number of unstable particles that subsequently decay. This decay process is modelled by PYTHIA by including the proper mass distributions and decay properties of possible final state hadrons.

2.4.2 POWHEG

For more precise comparisons of jet observables in pp collisions NLO corrections can be applied to the scattering processes using a framework such as POWHEG-BOX [122]. This framework is a method of matching NLO calculations of the initial hard process to the parton shower of a given Monte Carlo generator using the POWHEG method [123, 124]. The implementation of the POWHEG-BOX framework for this work was performed using code kindly made available by Savatore Aiola [125]. For the comparison to the pp measurements performed in this analysis, the NLO calculations were passed to PYTHIA 6 Perguia 2011 for the subsequent generation of the parton shower, hadronisation and final state particle decays.

2.4.3 JEWEL

The measurements performed on Pb–Pb data in this thesis are compared to two different medium induced jet energy loss models. The first of these models is the JEts With Energy Loss (JEWEL) Monte Carlo generator [126, 127]. JEWEL starts by taking di-jets produced from hard scatterings and initial state parton showering simulated by PYTHIA 6.4 [117]. The medium modified parton shower is then generated by simulating collisional and radiative energy loss via interactions with the medium scattering centres. The result of the modified shower is then passed back to PYTHIA to perform the hadronisation process using the Lund string model. The medium thermalised partons that are used as scattering centres for the jet can either be discarded or propagated to the end of the parton shower. This is

referred to as "recoils off" or "recoils on" respectively within the JEWEL framework. It is expected that these medium recoil particles will have an impact on the final distribution of jet substructure observables and thus their inclusion is recommended [128]. The recoil particles are propagated to the hadronisation stage without any further interactions with the medium as default due to the fact their interactions with the medium are expected to be much softer than the jet-medium interactions and so the perturbative description used by JEWEL may not be appropriate. When JEWEL is run with recoils on then an additional background subtraction is performed to remove the thermal component of the medium particles. The default method for this subtraction is the "4MomSub" procedure. The JEWEL samples used for comparison in these studies were provided by Marco Van Leeuwen [129] with an initial medium formation time of $\tau_i = 0.6$ fm/c and initial temperature of 360 MeV.

2.4.4 The Hybrid Model

The Hybrid Model [130–133] is the second jet energy loss model used for comparison in this work. As the name suggests, it takes a hybrid approach to modelling jet energy loss in the presence of deconfined colour charged medium. The hard processes, including the initial hard scattering and subsequent partonic branching, are treated perturbatively using the DGLAP evolution equations. The splittings are assumed to be unmodified by the presence of the medium as the exchanges of momentum between the jet and the medium are assumed to be of the order of the medium temperature, T, and thus do not significantly modify the leading parton virtuality. The partonic splittings are left unmodified also due to the fact that the splittings occur over distance scales smaller than the resolving power of the medium. For partons travelling through the plasma, energy loss is calculated using a dual gravitational approach that models the soft interactions as falling "strings" that transport the energy away from the parton to the plasma. The rate of energy loss of these partons is calculated based on a light quark propagating a finite slab (thickness x) of strongly coupled $N = 4$

supersymmetric Yang-Mills plasma [130, 134] and takes the form:

$$\frac{1}{E_{\text{in}}}\frac{dE}{dx} = -\frac{4}{\pi}\frac{x^2}{x_{stop}^2}\frac{1}{\sqrt{x_{stop}^2 - x^2}}, \tag{2.11}$$

where E_{in} is the initial parton energy at the point it enters the plasma and x_{stop} is the stopping distance of the parton. This expression holds as long as $1/(\pi T) \ll x < x_{stop}$, that is that the medium is thick enough that the initial transients may be neglected but thin enough so that the parton survives to the other side of the medium. The stopping distance of the parton is derived in Refs. [135, 136] and is given by

$$x_{stop} = \frac{1}{2\kappa_{sc}}\frac{E_{in}^{1/3}}{T^{4/3}}, \tag{2.12}$$

where κ_{sc} is a dimensionless constant and a free parameter in the model.

Simulations performed for comparison to the measurements shown in this work were provided by Daniel Pablos [137]. The simulations were performed with two values of medium transition temperature $T_{\text{c}} = 145$ MeV and $T_{\text{c}} = 170$ MeV and a band is produced showing the range. Events were simulated with an event centrality of $0 - 10\%$ to replicate the data.

Chapter 3

Jet Substructure

The preceding chapter discussed the general concepts of jets from their production in the cleanest of collision environments to their modification due to the medium in the presence of the complex environment of heavy-ion collisions. Now a more detailed discussion focussing on the methods deployed in this thesis will be presented.

In recent years, the focus of the experimental and theoretical communities in heavy-ion jet physics has shifted towards trying to understand how the substructure of jets is modified due to the presence of the QGP. In order to study such modifications a variety of observables have been developed and adopted from other high energy physics studies that could be sensitive to interactions of the jet with the medium, these observables are known collectively as *jet shapes*. These jet substructure studies have been performed extensively both theoretically [128, 132, 138–141] and experimentally [68, 69, 71, 142–145].

In this work a different approach will be taken to studying the internal structure of jets that largely derives from collaborative work performed by the author at the 5^{th} Heavy Ion Workshop and CERN TH Institute at CERN in 2017 [2]. This approach starts from a "map" of the splittings of a jet in their kinematic phase space as a qualitative representation of the jet fragmentation. The tool used to construct this map of splittings is known as the *Lund*

jet plane. The method by which this plane is constructed and how it can be used to study fundamental components of jets are detailed in the following sections.

3.1 The Lund Jet Plane

3.1.1 Reconstructing Jet Emissions

The Lund jet diagram is a method of representing the phase space of jets and exists in different forms. The plane is often constructed of variables that exist in the logarithmic phase space due to the soft $(1/z)$ and collinear $(1/\theta)$ divergences of the QCD splittings which have the differential probability in vacuum given by:

$$dP = 2\frac{\alpha_s C_i}{\pi}\mathrm{dlog(z}\theta)\mathrm{dlog}\frac{1}{\theta}, \tag{3.1}$$

where α_s is the strong coupling constant, C_i is the colour representation ($C_\mathrm{i} = C_\mathrm{F}$ for quark and $C_\mathrm{i} = N_\mathrm{c}$ for gluon splittings, respectively) and z (momentum fraction) and θ (angle) are the kinematics of the splitting as shown in Fig. 3.1. The momentum fraction z is defined as

$$z = \frac{min(p_{\mathrm{T},1}, p_{\mathrm{T},2})}{p_{\mathrm{T},1} + p_{\mathrm{T},2}}. \tag{3.2}$$

Figure 3.2 shows the form of Lund diagram that is considered in this section. The $y-$axis is the logarithm of the product of the two splittings parameters $(z\theta)$ and the $x-$axis is the logarithm of the reciprocal of the splitting angle $(1/\theta)$. The label on the $y-$axis, $\ln R$, shows the maximum allowed value that splittings may populate due to the fact that they must be contained within the jet radius, R. Similarly, along the $x-$axis, the minimum allowed value is set to $\ln\frac{1}{R}$. The region in which splittings are allowed to populate is also constrained by a straight diagonal line labelled $z = 1$. This line represents the limit where 100% of the jet momentum is carried by the emitted gluon and therefore no entries can populate the

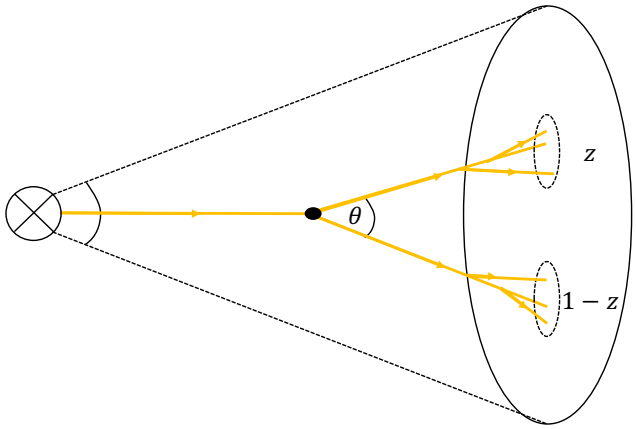

Figure 3.1: A schematic diagram of a simple 1→ 2 jet splitting (antenna) with kinematical variables: θ (angle of radiation) and z (momentum fraction).

plane above this line. The diagram shows the location of three different splittings with three different formation times. The formation time is the characteristic time-scale of the splitting and is related to the finite energy resolution $t_{\mathrm{f}} \approx \Delta E^{-1}$ from the Heisenberg uncertainty principle. The formation time for splittings in vacuum is defined explicitly as

$$t_{\mathrm{f}} = \frac{2z(1-z)p_{\mathrm{T}}}{k_{\mathrm{T}}^2} = \frac{2p_{\mathrm{T}}}{M^2}, \tag{3.3}$$

where $k_{\mathrm{T}} = z(1-z)p_{\mathrm{T}}\theta$ is the relative transverse momentum of the antenna in the small angle limit and M is the antenna invariant mass which is given by

$$M^2 = z(1-z)p_{\mathrm{T}}^2\theta^2 \tag{3.4}$$

where p_{T} here refers to the total transverse momentum of the antenna.

Due to the restrictions imposed by the finite formation times of splittings the gluon emissions in vacuum are strictly angular ordered. Therefore, if the jet constituents are clustered using an angular ordered, sequential method (such as the CA algorithm), the clustering history should be related directly to the time evolution of the jet splittings. By unwinding the clustering process one stage at a time, the kinematic information at each stage can be used

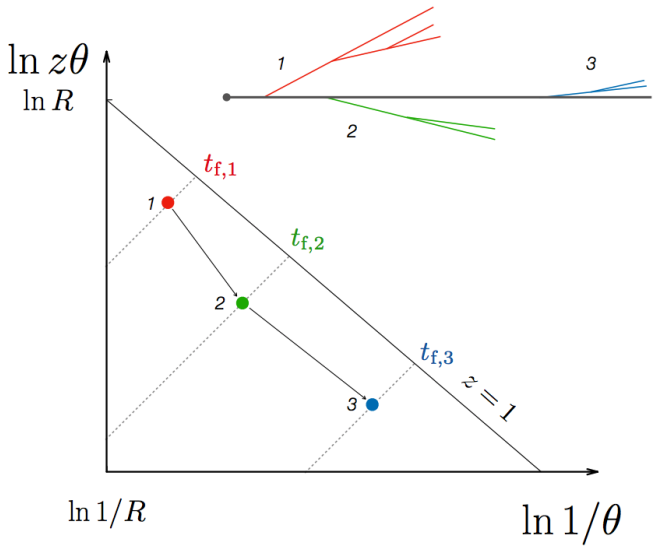

Figure 3.2: Lund diagram representation of jet clustering history with three different primary emissions with varying formation times [2].

to fill the Lund plane as shown in Fig. 3.2.

3.1.2 Filling the Lund Plane

To populate the plane and connect theory to experimental observables one requires a consistent definition of a "jet" and a prescription for how the history of the evolution is defined. This is done using the jet definition procedures outlined in Section 2.3 where the anti$-k_{\mathrm{T}}$ algorithm is used to first reconstruct jets in the event. Then the jet can be reclustered using a different algorithm depending on the aspect of jet substructure under investigation. In this thesis, and for the majority of jet substructure studies, the Cambridge-Aachen algorithm is used to recluster the jet as it defines the jet based on its angular scale and this offers a close connection to angular ordering of typical QCD branching. The entries in the Lund Plane are recorded as follows:

1. Reclustering sequence unwound to previous step to obtain two branches

2. Momentum fraction of the pair of branches is calculated from equation 3.2

3. Softer branch discarded

4. Continue from step 1. using the remaining, harder, branch and repeat until no more branches remain.

An example of how the Lund plane is populated using PYTHIA simulated events and Cambridge-Aachen reclustering is shown in Fig. 3.3. In order to satisfy infrared and collinear safety, the Lund plane should be normalised to the total number of jets.

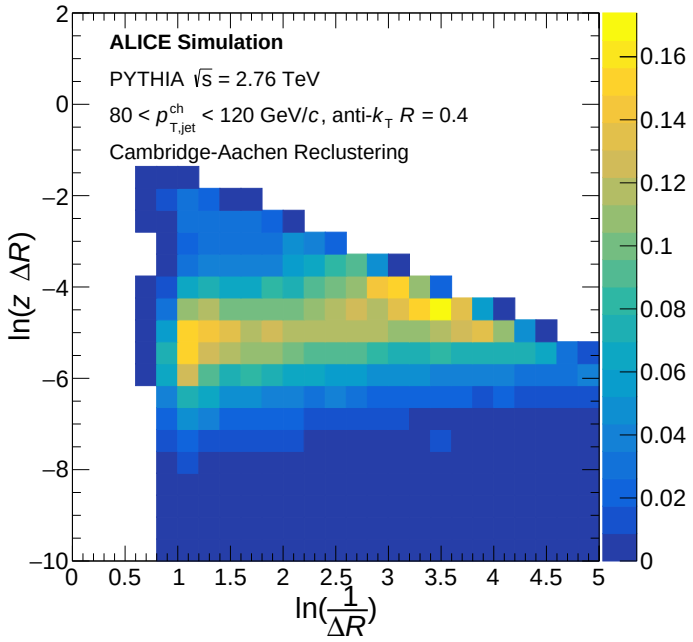

Figure 3.3: Primary Lund plane for jets reconstructed in PYTHIA generated events at $\sqrt{s}$= 7 TeV.

Studying the density of entries in the Lund plane is the easiest way to explore this phase space and the density in the $ln(k_t) - ln(1/\theta)$ plane can be denoted

$$\rho(\theta, k_t) = \frac{1}{N_{\text{jet}}} \frac{dn_{emission}}{d\ln(k_t) d\ln(1/\theta)} \qquad k_t = p_{T,2}\theta, \tag{3.5}$$

where k_t directly relates to the scale of the splitting process and gives a clear separation of regions of phase space that can be modelled with perturbative calculations and those that cannot. The expected density of entries in the Lund plane for quark initiated jets to leading order in perturbative QCD is expected to be

$$\rho \approx \frac{\alpha_s(k_t)C_F}{\pi}\bar{z}(p_{gq}(\bar{z}) + p_{gq}(1-\bar{z})), \qquad z = \frac{k_t}{p_{\mathrm{T,jet}}\theta} \qquad (\theta \ll 1), \tag{3.6}$$

where $C_{\mathrm{F}} = \frac{4}{3}$, $p_{gq} = \frac{1+(1-z)^2}{z}$ $(0 < z < 1)$ [146]. $\bar{z}$ is the effective momentum fraction, and, for single emissions, is equivalent to z of 3.2. When $\bar{z} \ll 1$ the density of primary Lund emissions becomes

$$\rho \approx \frac{\alpha_s(k_t)C_{\mathrm{F}}}{\pi} \qquad (\theta \ll 1, \bar{z} \ll 1) \tag{3.7}$$

which depends only on the strong coupling $\alpha_s(k_t)$.

Figure 3.4 shows how the Lund plane is populated with these useful axes. The plane is shown in different ranges of $p^{\mathrm{ch}}_{\mathrm{T,jet}}$ and a strong band of high probability is observed below $ln(k_{\mathrm{t}}) = 0$ GeV. In this region the density of coverage of the Lund plane cannot be well described by pQCD and the density shown in equation 3.5 no longer well describes the density. In order to be able to reliably compare experimental measurement to theoretical prediction, the region of the diagram above $ln(k_{\mathrm{t}}) = 0$ GeV should be explored.

A dependence on $p^{\mathrm{ch}}_{\mathrm{T,jet}}$ is observed between the plots in Fig. 3.4 where it can be seen that the splittings are distributed at larger angles for jets with lower $p^{\mathrm{ch}}_{\mathrm{T,jet}}$. As the transverse momentum of the jet increases the splittings become more collimated which is shown by the increase in density coverage of the Lund planes at large values on the $ln(1/\theta)$ axis. This collimation of more energetic jets fits qualitatively with our understanding of how high transverse momentum jets fragment.

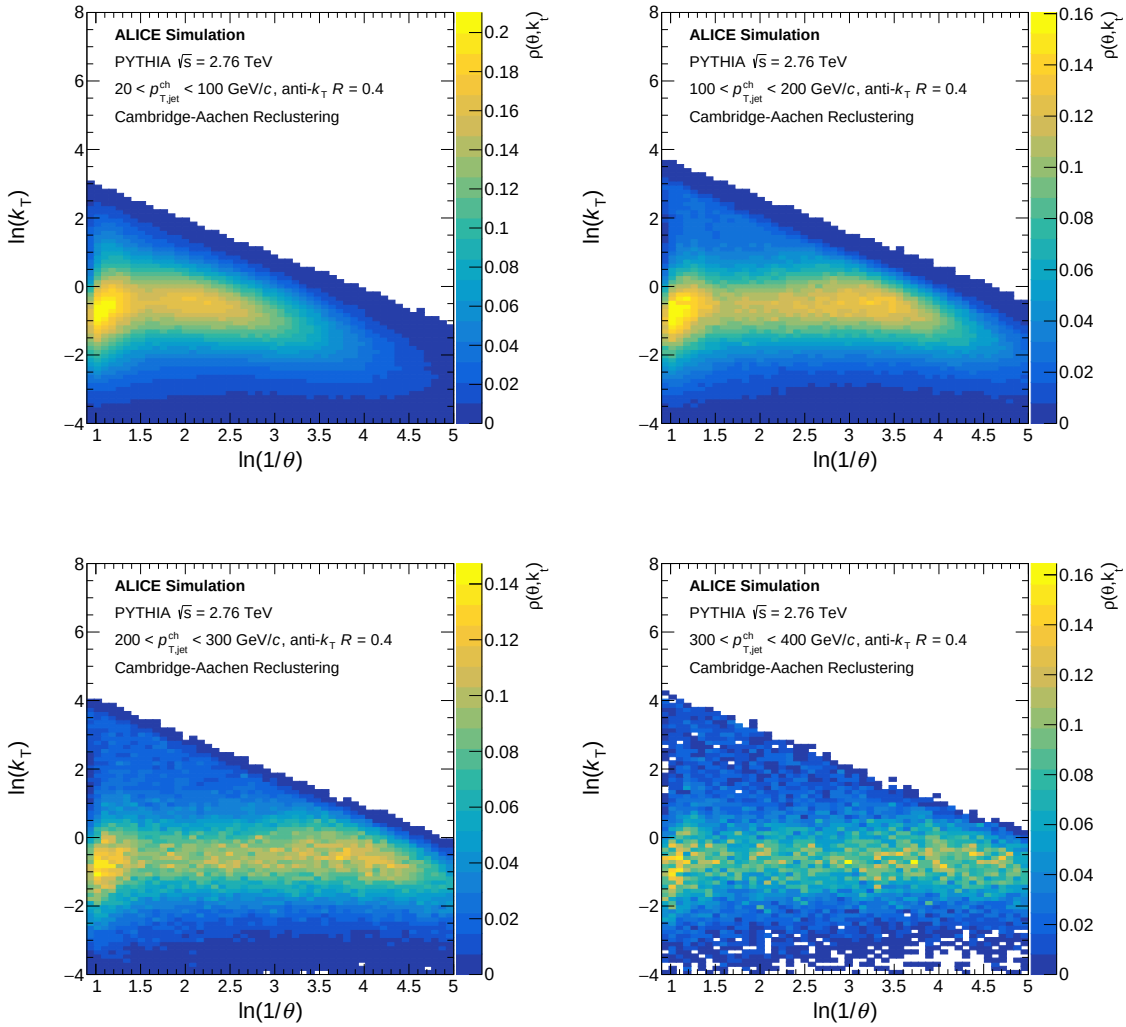

Figure 3.4: Average Lund plane density ρ for jets reconstructed from Pythia simulated events reclustered with the C/A algorithm.

Reclustering Algorithms

From this point on, the Lund plane will be represented using the axis as shown in Fig. 3.2. This representation was first proposed as a method for discriminating between possible energy loss formalisms as energy loss via many low energy emissions should populate different regions of the plane compared to Molière-like scattering [147] as discussed in Ref. [2].

Another modification that can be used to study different aspects of jet substructure

using the Lund plane is to change the clustering algorithm used. Using the k_{T} and anti$-k_{\mathrm{T}}$ algorithms to cluster the jet constituents will change the ordering of the hierarchical tree of the jet. If the k_{T} algorithm is used the clustering defines the jet on its k_{T} scale, which, if one considers Eq. 3.3, would be a useful method of ordering the evolution of the splittings. However, the k_{T} algorithm is very sensitive to local clusters of soft particles due to the fact that it starts by clustering together these soft particles and in the presence of the underlying event of heavy ion collisions the hierarchical tree will be significantly distorted by combinatorial background. The anti$-k_{\mathrm{T}}$ algorithm will cluster the jet around the hardest branch (referred to as the jet core) and will lose all connection to QCD branching history and hence offers very little applicability to jet substructure studies.

The Lund planes constructed using the three different algorithms are shown in Fig. 3.5 for jets reconstructed from PYTHIA8 generated events. The Lund plane is populated using all splittings as it is not possible to only identify radiation off the primary emitter; this is equivalent to collapsing all subsequent emission Lund planes on to the primary plane. Due to the fact that the splitting kernel is invariant on the emitter this generalisation is possible. The jets are reconstructed first using the anti-k_{T} algorithm with a resolution parameter of $R = 0.4$ and a transverse momentum threshold of $p_{\mathrm{T,jet}}^{\mathrm{ch}} > 200$ GeV/c and then reclustered using the stated algorithm. The three different reclustering algorithms show very different features in the Lund plane with a reasonably uniform distribution for Cambridge-Aachen reclustering that is enhanced at large angles and intermediate $z\theta$ and again at narrow angles and very large z. The observable z runs along the positive diagonal of the Lund plane when the axes $ln(z\theta)ln(1/\theta)$ are used, therefore the entries along the upper right boundary of the Lund plane represent the most symmetric splittings ($z = 0.5$). There are enhanced features at large angles which can be attributed to the presence of the PYTHIA underlying event that has not been subtracted. The population of splittings is not uniform when using k_{T} or anti$-k_{\mathrm{T}}$ reclustering with a strong enhancement of splittings that are more symmetric in

momentum balance ($z \approx 0.5$) or at larger angles respectively.

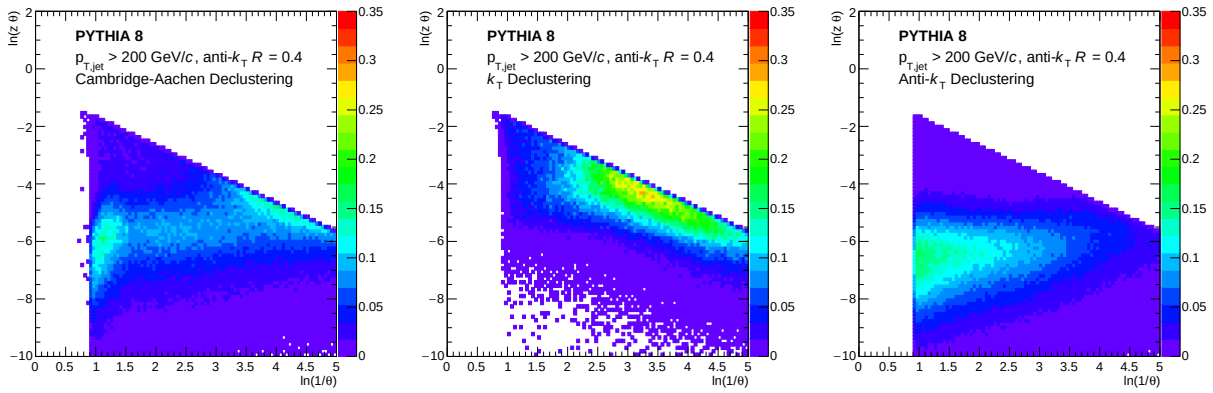

Figure 3.5: Primary Lund plane for anti$-k_{\mathrm{T}}$ $R = 0.4$ jets reconstructed in PYTHIA generated events at $\sqrt{s} = 5.02$ TeV using three different reclustering algorithms: Cambridge-Aachen (left), k_{T} (centre) and anti$-k_{\mathrm{T}}$ (right).

3.1.3 Soft Drop Grooming

The Lund plane is filled with splittings in the jet evolution across all scales. Theoretically it is difficult to calculate processes in regions of this phase space where the scale is small and hence the strong coupling constant is large. It is therefore desirable to "select" specific regions of this phase space that can be measured experimentally and permit theoretical computation. The method of grooming that is used in this work is that of the Soft Drop algorithm [148]. The Soft Drop algorithm is a variation on the modified Mass Drop Tagger (mMDT) [149, 150] which iteratively unwinds the jet clustering history and compares the kinematic information of the two subjets at each stage of this declustering. The Soft Drop algorithm starts by reclustering the jet using a desired algorithm, most commonly Cambridge-Aachen. The reclustered jet is then unwound one step in it's clustering history and the momentum fraction of the branch is calculated using Eq. 3.2 and compared to the Soft Drop grooming condition

$$z > z_{\mathrm{cut}} \left(\frac{\Delta R_{12}}{R_0}\right)^{\beta}, \tag{3.8}$$

where z_{cut} is a cut off defined by the user, ΔR_{12} is the angular separation of the two subjets, R_0 is the radius of the jet and β is the angular exponent used to control the sensitivity to large angle radiation. A large value of β will favour grooming away wide angle radiation whilst a value of β below 0 will leave more wide angled radiation ungroomed. If the pair of subjets identified at this stage of declustering do not pass this requirement then the softer (lower p_{T}) of the two subjets is discarded and the declustering is continued following the harder branch. This procedure continues until a pair of subjets that do satisfy Eq. 3.8 are identified. The default grooming parameters in Soft Drop are $z_{\text{cut}} = 0.1$ and $\beta = 0$ and these are the parameters used in the majority of this analysis. When the angular exponent is set to $\beta = 0$ the Soft Drop condition replicates the mMDT algorithm.

3.1.4 Projecting the Lund Plane

The Lund plane can also be used to map out the splittings at each stage of the declustering separately. Figure 3.6 shows how the Lund map evolves for PYTHIA jets as the splitting number is incremented. It can be seen clearly that the kinematics of the splitting evolve as the declustering iterates through the history of the jet. The angular-ordered nature of the Cambridge-Aachen algorithm can be seen as the splitting number is increased. As the number in the jet delcustering tree is increased, the splittings move to narrow angles (larger values of $ln(\frac{1}{\Delta R})$). These later splittings in the tree correspond to the first splittings as the declustering works backwards through the angular-ordered cluster. Figure 3.7 shows the x-axis projection of the Lund planes shown in Fig. 3.6 and these show how the splittings move from large angles to more narrow angles as the jet is iteratively declustered.

The red line in Fig. 3.6 shows the region of phase space extracted using the Soft Drop cut of $z_{cut} = 0.1$ with all splittings below the line being groomed away and only those above the line ($0.1 \leq z \leq 0.5$) accepted. The Lund diagrams show that the majority of early splittings are relatively soft and would be groomed away. It is not until about $n_{split} \approx 4$ that a large

number of splittings will satisfy the Soft Drop grooming requirements.

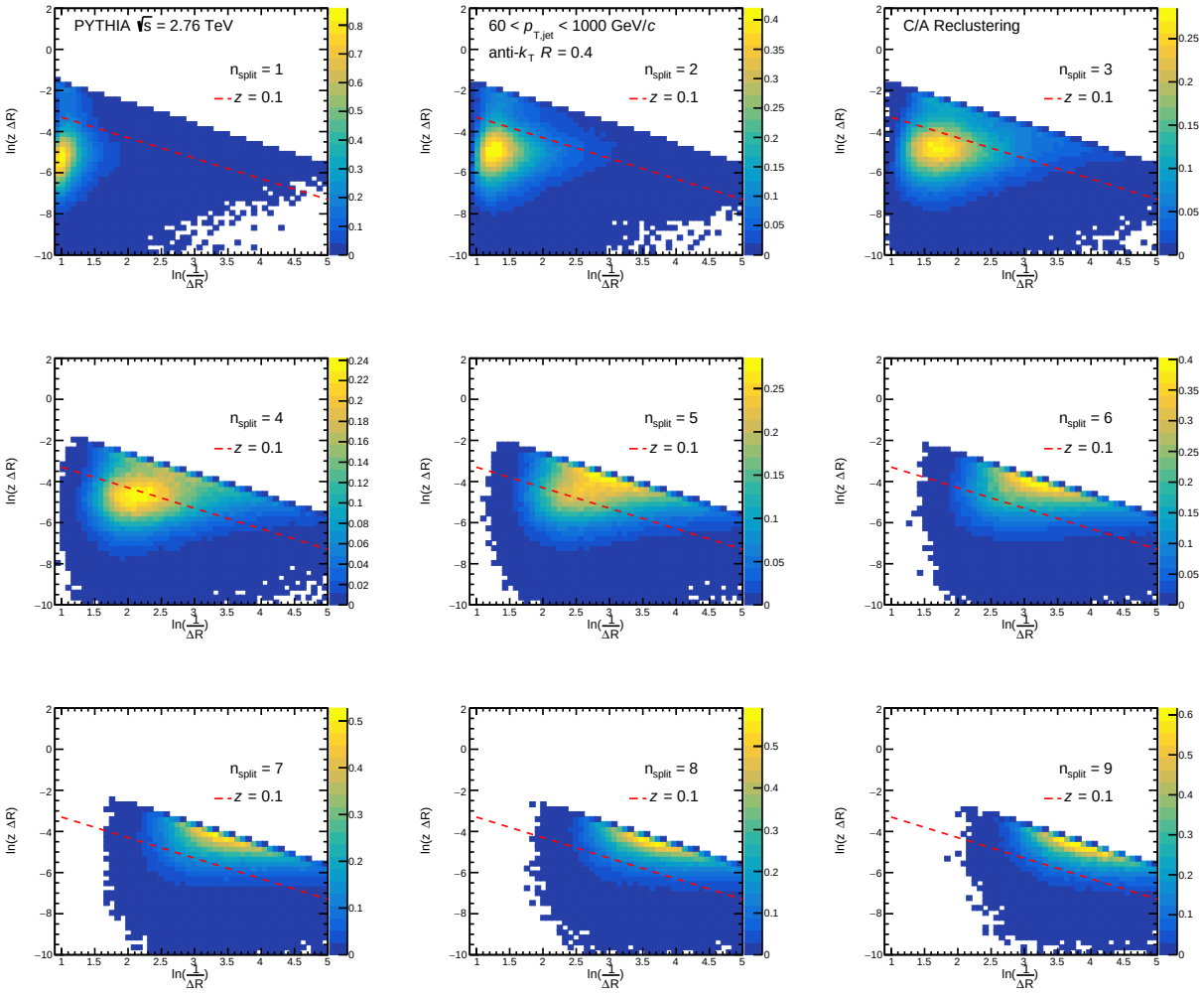

Figure 3.6: Lund plane for each splitting using Cambridge-Aachen reclustering on anti-k_{T}jets reconstructed from PYTHIA generated events.

There are several observables that are studied in jet substructure that can be thought of as projections of this Lund plane. Measurements of the momentum fraction, z, have shown evidence for the modification of splittings in medium [151] and this will be studied extensively in this work. The angle at which the splitting happens is also the linearised projection of the x-axis shown in Fig. 3.7 and is an observable that can be identified, along with z, by using the Soft Drop grooming algorithm. A third, more novel measurement, is to count

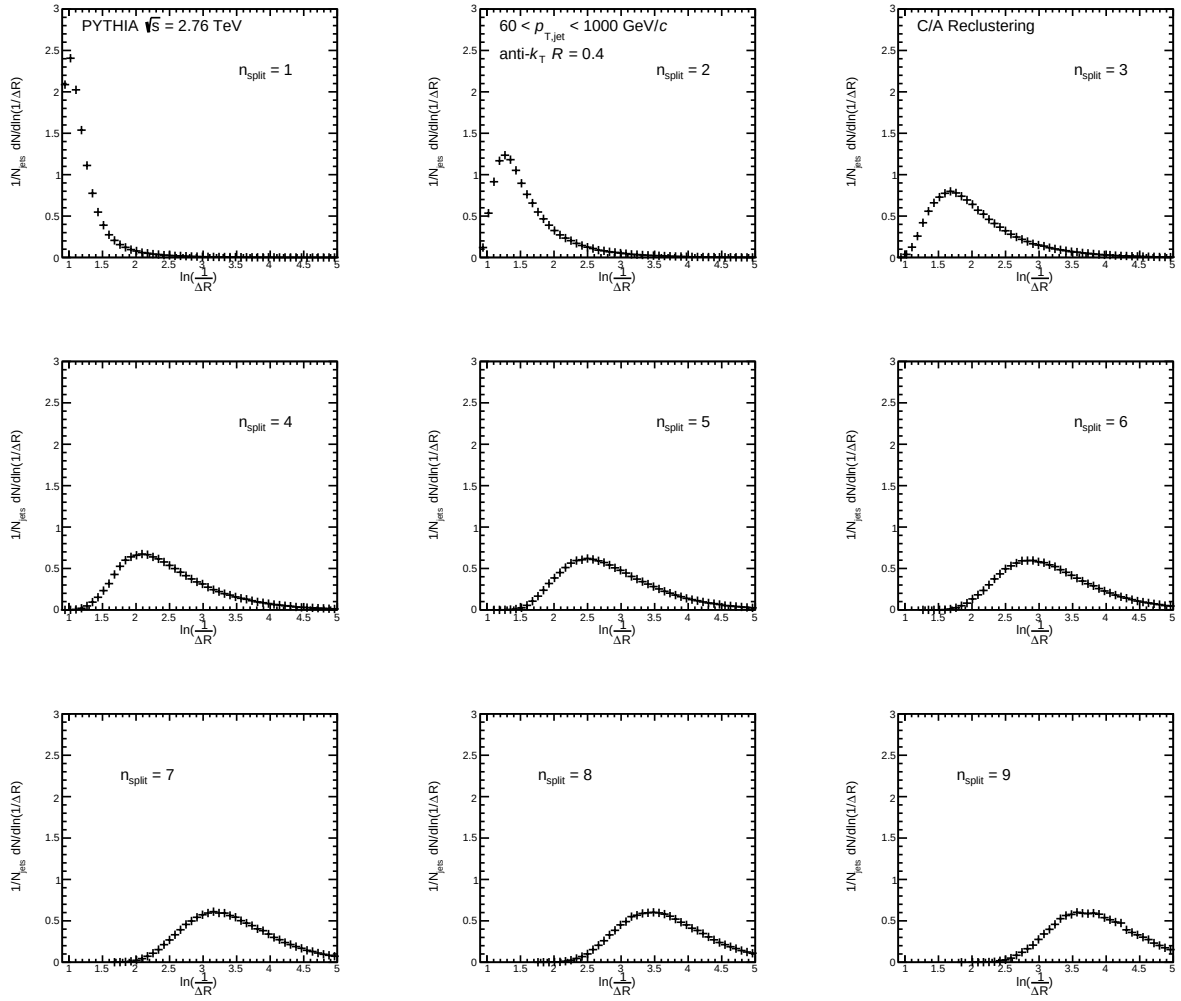

Figure 3.7: X-axis projection of Lund diagrams from Fig.3.6.

the total number of splittings that pass the Soft Drop grooming algorithm in the iterative declustering of the jet. This observable can be related to the total number of semi-hard splittings that occur in the jet evolution which could offer very useful insight into the role of medium-induced radiation as well as the degrees of freedom seen by the jet probe. An important point to consider, with an observable such as the number of antennae produced by the declustering, is infrared and collinear safety. It is clear that simply counting the number of stages involved in the clustering is not IRC safe as an additional infinitesimally soft emission will change the total number of splittings. However, by imposing a cut on the

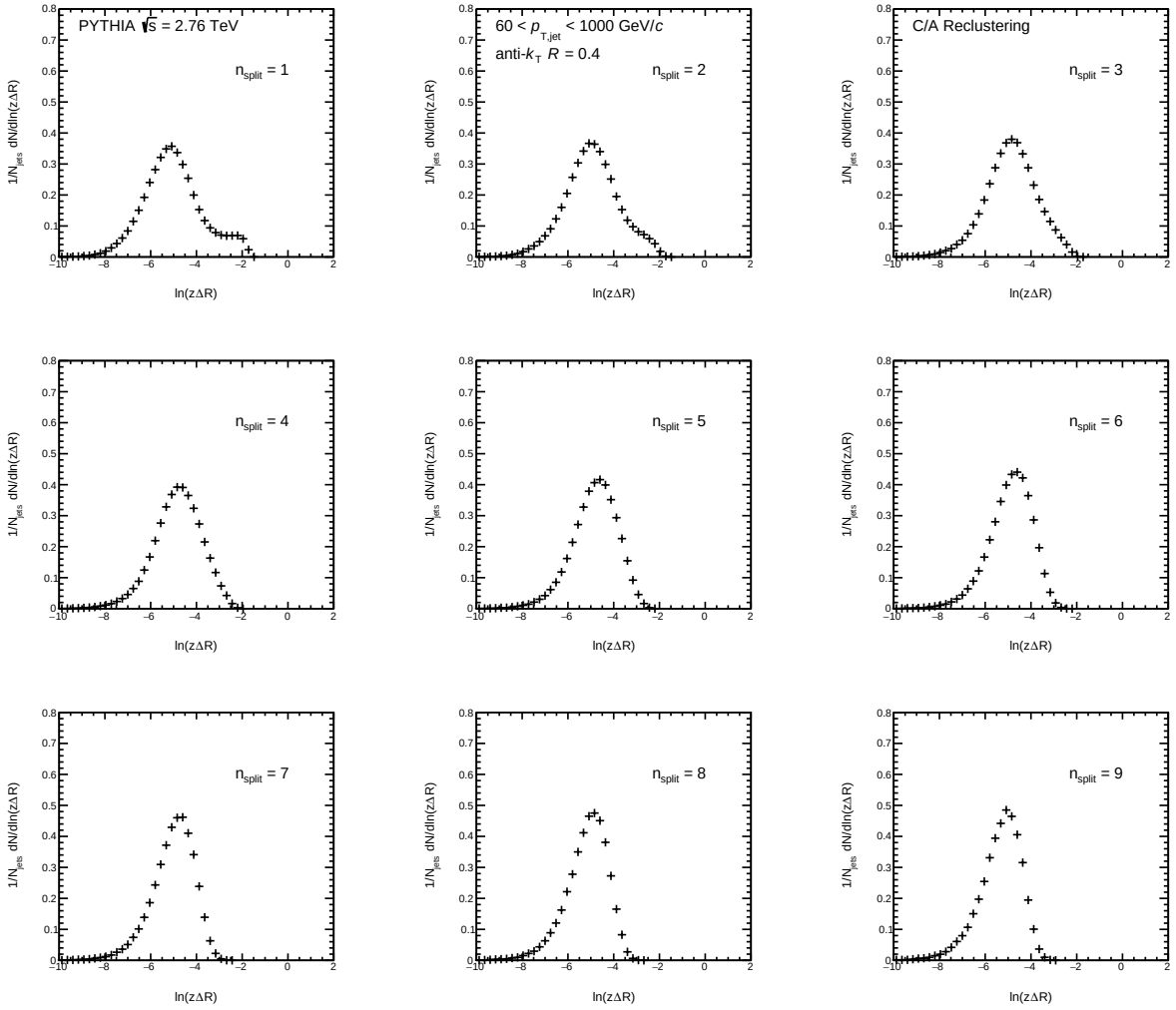

Figure 3.8: Y-axis projection of Lund diagrams from Fig.3.6.

k_{T} scale, i.e considering a selected region of the Lund plane, infrared and collinear safety can be recovered. As mentioned above, the region of the phase space that is selected by the Soft Drop grooming condition of $z_{\mathrm{cut}} = 0.1$ is constrained above the dashed red line in Fig. 3.6.

3.2 Substructure Observables

3.2.1 Momentum Fraction z_{g}

The first substructure observable measured is the groomed momentum fraction z_{g} of subjets identified using the Soft Drop grooming procedure outlined above. The subscript g refers to the observable for groomed jets whereas z with no subscript simply refers to the momentum fraction of any pair of subjets. Figure 3.9 shows the distribution of z_{g}, the measured momentum fraction of the first splitting that passes the Soft Drop grooming cut, for jets clustered in PYTHIA 6 Perugia Tune 2011, PYTHIA 8 and PYTHIA + POWHEG generated events. The distribution of z_{g} is unmodified by the NLO corrections applied by POWHEG which shows that z_{g} is not sensitive to next-to-leading order processes. It has been shown that this observable is closely linked to the QCD splitting functions (see Section 2.1.2) and predictions from Monte Carlo generators well reproduce the distribution obtained from analytical calculations performed from first principle QCD techniques [152].

The measurement of z_{g} has been performed in Au–Au collisions by the STAR collaboration at RHIC [153] and Pb–Pb collisions by the CMS collaboration at the LHC [151].

The distribution of z_{g} as measured by CMS is shown in Fig. 3.10. A significant modification of the distribution was observed in the CMS measurement between central Pb–Pb and pp collisions. The modification shows a suppression of the most symmetric splittings in central Pb–Pb collisions and a small enhancement of splittings at $z_{\mathrm{g}} \approx 0.1$; because of the steeply falling nature of the z_{g} distribution as shown in Fig. 3.9 a small enhancement of asymmetric splittings leads to a strong suppression of the less probable symmetric splittings.

The measurement performed by the STAR collaboration uses a trigger and recoil jet approach [153]. In this method, the fact that jets are produced in back-to-back pairs is exploited and a trigger jet is used to look for a corresponding recoil jet in the opposite direction. Measuring jets in this way is an effective method of removing the contribution from

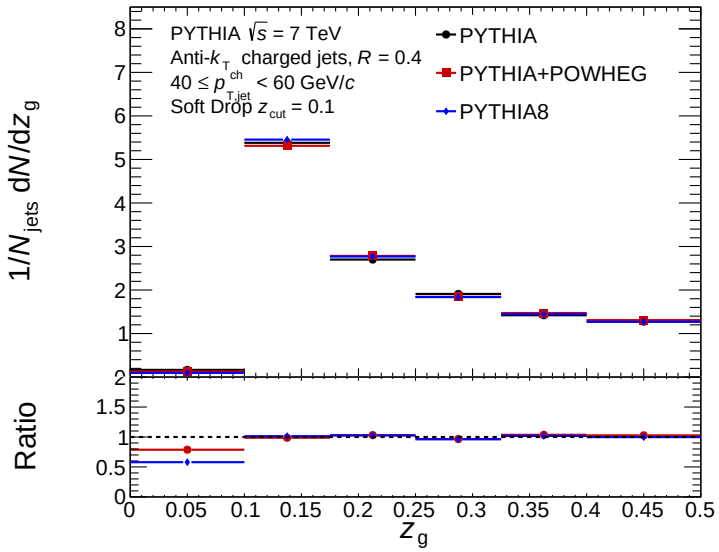

Figure 3.9: Distribution of z_{g} for jets reconstructed in PYTHIA 6 Perugia Tune 2011, PYTHIA 8 and PYTHIA + POWHEG generated events in the range $40 \leq p_{\mathrm{T,jet}}^{\mathrm{ch}} < 60$ GeV/c.

combinatorial jets. Contrastingly, this measurement observes no significant modification of the z_{g} distribution for either trigger or recoil jet populations relative to the pp baseline. This differing result provides good motivation for a study of the jet splitting momentum fraction in ALICE. The kinematic regime studied by CMS with a minimum jet transverse momentum of 140 GeV/c is significantly higher than that of STAR where the maximum considered is 30 GeV/c. ALICE can operate between these two energy ranges and results will be presented in the ranges $40 - 60$ GeV/c and $80 - 120$ GeV/c in pp and Pb–Pb collisions, respectively. Studying this intermediate kinematic region may provide insight into the transition between the two observations.

3.2.2 Groomed Radius R_{g}

In Fig. 3.12 the simulated distribution of the angle R_{g} of the first splitting that satisfies the Soft Drop grooming conditions is shown. As with Fig. 3.9 the distributions for PYTHIA6, PYTHIA 8 and PYTHIA + POWHEG are shown. There is a more significant difference

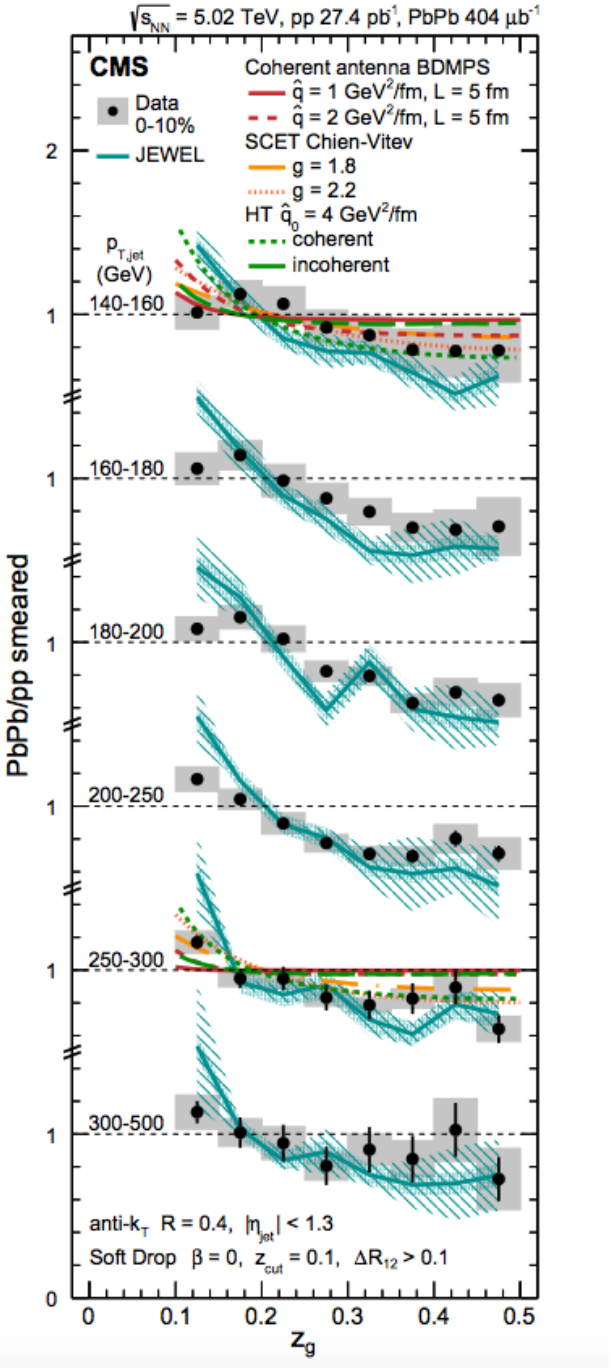

Figure 3.10: Ratios of z_g distributions for central Pb–Pb collisions and smeared pp collisions for a range of $p_{T,jet}$ [151]. Calculations shown are from various jet quenching models [109, 154–157].

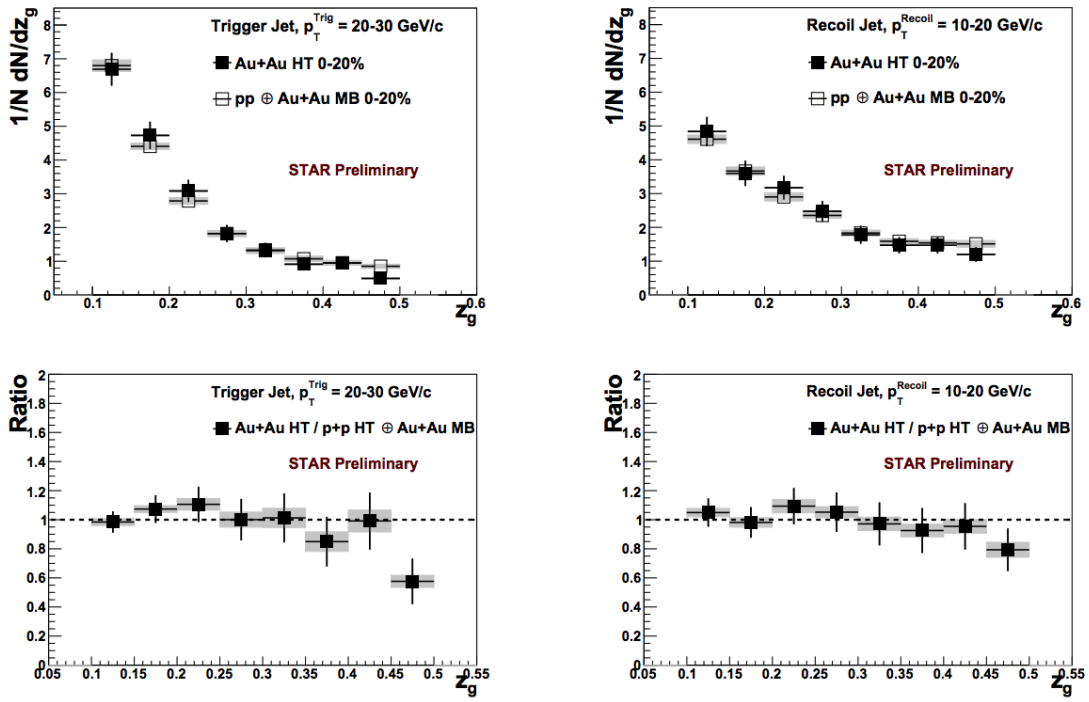

Figure 3.11: Top: Trigger and recoil jet z_{g} distributions in the $p_{\mathrm{T,jet}}$ range 20-30 GeV/c and 10-20 GeV/c, respectively, for Au–Au collisions and smeared pp collisions as measured by RHIC [153]. Bottom: Ratio between the Au–Au and pp distributions with systematic uncertainties shown as shaded bands.

between the generators compared to the z_{g} distribution with PYTHIA 8 and PYTHIA + POWHEG both producing a distribution which is shifted to larger angles relative to PYTHIA 6.

The angular distribution of groomed subjets is directly connected to the QCD splittings in the same way as z_{g}. However, measurements of this distribution have not been reported in previous studies of groomed jet substructure. The angular separation of splittings is an important difference between the two previous measurements of z_{g}. In the CMS measurement, a minimum splitting aperture of $\Delta R > 0.1$ was imposed which modifies the sample of splittings studied.

Studying the distribution of R_{g} will help improve our understanding of the distribution of jet splittings in phase space. It is also important to fully understand the distribution when

one wants to investigate the z_g distribution differentially in splitting angle as is done in this work.

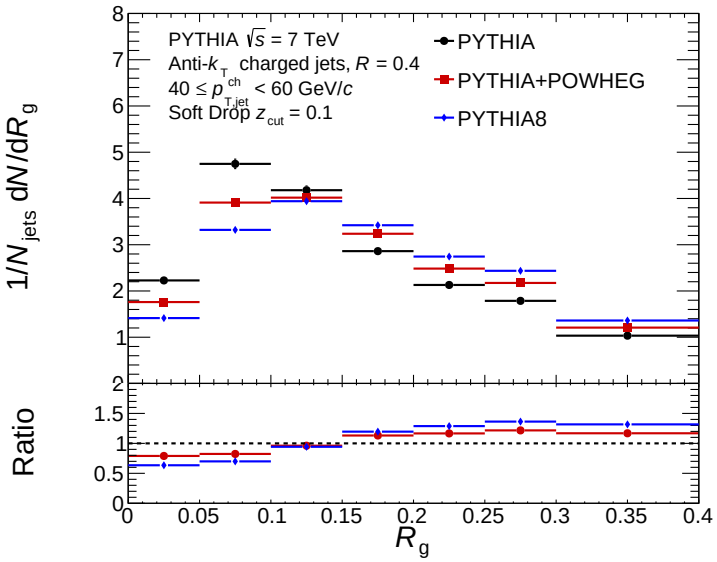

Figure 3.12: Distribution of R_g for jets reconstructed in PYTHIA 6 Perugia Tune 2011, PYTHIA 8 and PYTHIA + POWHEG generated events in the range $40 \leq p_{\mathrm{T,jet}}^{\mathrm{ch}} < 60$ GeV/c.

3.2.3 Number of Splittings n_{SD}

A third observable that relates to the fragmentation pattern of jets is the number of splittings in the declustered jet tree. Specifically, the observable used, n_{SD}, is a measure of the number of splittings that satisfy the specified Soft Drop grooming conditions. In practice, the observable is measured by adopting the same grooming procedure used to identify the first splitting that satisfies the Soft Drop grooming conditions as with z_g and R_g. Once the first "semi-hard" splitting is identified, rather than stopping the declustering, the sequence is iterated further, following the harder branch at all stages. Meanwhile, the number of splittings that are above the grooming threshold are counted until only a single particle remains. The total number of splittings that satisfied the Soft Drop threshold is taken as n_{SD}. By counting the number of antenna in the iterative declustering of a jet, it is possible to study the effect of the

additional, medium-induced, gluon radiation that is expected to take place in the presence of the QGP. Any additional radiation that occurs where a significant fraction of the original parton momentum is transferred away is expected to increase the total number of branches identified above the grooming threshold in the iterative declustering of the jet. Studying this observable congruently with the other grooming observables already discussed may help provide additional discriminating power in discerning the mechanisms by which energetic partons exchange energy with the strongly interacting deconfined medium. An example of the distribution of n_{SD} is shown in Fig. 3.13 for PYTHIA simulated events using PYTHIA 6 and PYTHIA 8 as well as simulations with NLO corrections applied via the POWHEG method.

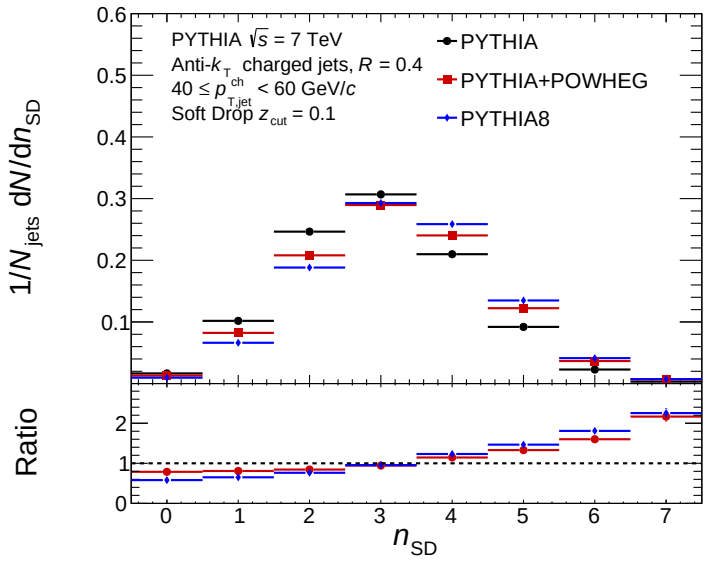

Figure 3.13: Distribution of n_{SD} for jets reconstructed in PYTHIA 6 Perugia Tune 2011, PYTHIA 8 and PYTHIA + POWHEG generated events in the range $40 \leq p_{\mathrm{T,jet}}^{\mathrm{ch}} < 60$ GeV/c.

The distribution of n_{SD} shows that approximately 3 semi–hard splittings occur on average in the jet evolution for the Monte Carlo models presented. The distribution is relatively broad with an increase at larger values of n_{SD} observed for PYTHIA + POWHEG and PYTHIA8 relative to PYTHIA 6.

Chapter 4

Experiment

4.1 The Large Hadron Collider

Based at the European Organisation for Nuclear Research (CERN), up to 175 m underneath the Swiss-French border and measuring 26.7 km in circumference is the world's largest and most powerful particle accelerator, the Large Hadron Collider (LHC). The LHC is constructed of a pair of synchrotron rings, encapsulated in superconducting magnets with the primary aim of accelerating hadrons to energies at the frontier of current capabilities. The LHC operated in its initial stage (run 1) at energies of 3.5 TeV per beam for proton-proton collisions ($\sqrt{s} = 7$ TeV) between 2010 and 2013. In the same time period it also collided lead nuclei together with beam energies per nucleon of 1.88 TeV ($\sqrt{s_{\mathrm{NN}}} = 2.76$ TeV). For the two years following 2013, collisions were stopped to allow for upgrades to be performed on the accelerator and experiments (LS1) before data taking began again in 2015 with new collision energies of up to $\sqrt{s} = 13$ TeV in pp collisions and $\sqrt{s_{\mathrm{NN}}} = 5.02$ TeV in Pb–Pb collisions

The acceleration of the beams is a sequential process that uses a combination of Linear Accelerators (LINACS) and smaller accelerator rings before injecting the beams into the LHC ring (see figure 4.1). In pp collisions the protons are obtained by ionising hydrogen

atoms by stripping them of their electrons prior to the initial stage of acceleration where the Radio Frequency Quadrupole (QRF) accelerates them to energies of 750 keV. LINAC2 is then used to increase the energy of the beams to 50 MeV before they are injected into the Proton Synchrotron Booster (PSB), the first circular accelerator stage. The protons are then fed into the larger Proton Synchrotron which accelerates them up to 25 GeV and subsequently the Super Proton Synchrotron (SPS) which increases the energy to 450 GeV prior to injection into the LHC ring. The final ramping up of beam energies occurs in the LHC itself where the beams circulate the 26.7 km ring up to the specified experimental beam energies. The beams are steered using 8.33 T magnetic fields from dipole magnets and focused using quadrupole magnets. The beams are accelerated in the straight segments of the ring using 400 MHz radio frequency cavities [158]. In pp collisions the beams contain up to 2808 bunches with a minimum bunch separation of 25 ns.

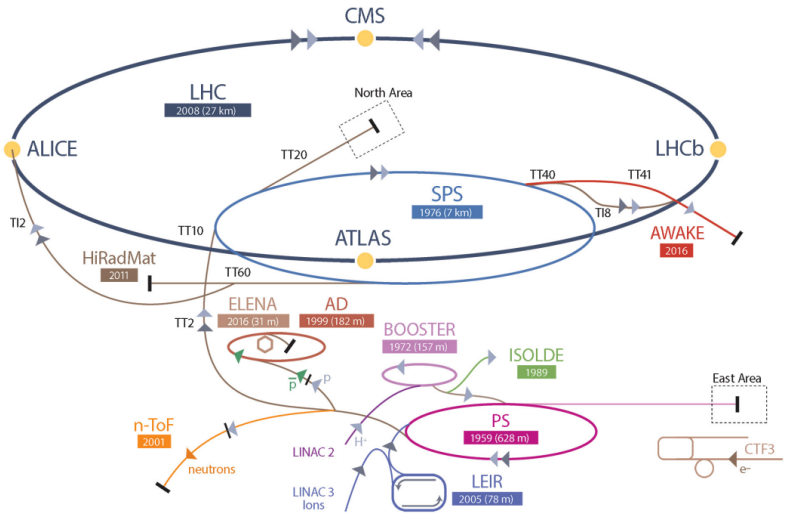

Figure 4.1: Schematic of the CERN LHC accelerator complex [159].

At four points around the ring the two synchrotron beam pipes cross over to produce collision points. At each these collision points is a different detector system that is set up to study the results of the collisions. The four detectors are each optimised for specific physics

investigations with the CMS and ATLAS detectors, which are multi-purpose detectors, optimised to study the pp collisions in searches for extremely rare processes both within the standard model and beyond. LHCb is a forward detector that is designed to study the physics of b quarks in an attempt to measure the parameters of CP violation. The ALICE detector is the only detector optimised for studying the physics of heavy-ion collisions with excellent tracking capabilities in order to analyse the extremely high multiplicity environment of heavy-ion collisions.

For heavy-ion collisions the LHC accelerates lead nuclei by first heating lead atoms to form a vapour which is ionised and then accelerated using LINAC3 before being injected into the the Low Energy Ion Ring (LEIR). After being accelerated by LEIR the ion bunches are injected into the PS where the rest of the acceleration process is the same as described for protons.

4.2 ALICE

4.2.1 Overview

ALICE (A Large Ion Collider Experiement) is one of the four experiments based at the interaction points of the LHC. It was commissioned chiefly to study the physics of heavy ion collisions and the physics of QCD. The detector was originally constructed of 18 sub-detectors which were specially designed to measure specific aspects of the collisions. The layout of the detector is shown in Fig. 4.2. The central barrel of the detector consists of the primary tracking detectors as well as the High Momentum Particle Identification (HMPID) system [160] and calorimeters [161]. It is housed inside a large solenoid magnet with a magnetic field strength of 0.5 T. The detector also consists of a forward muon arm which is tasked with the tracking and measurement of muons.

ALICE was designed to study the very high multiplicity environment of Pb–Pb colli-

sions with an anticipated pseudorapidity density at mid-rapidity of $\frac{dN}{d\eta} = 2000 - 8000$, at LHC collision energies [47] [1]. This estimate was revealed to be a significant overestimate with extrapolations from measurements at the Relativistic Heavy Ion Collider (RHIC) at Brookhaven National Lab (BNL) indicating much lower values of $\frac{dN}{d\eta} = 1500 - 4000$ and the first measurements of the $0 - 5\%$ most central Pb–Pb collisions at $\sqrt{s_{NN}}$= 2.76 TeV measuring multiplicities of $\frac{dN}{d\eta} = 1601 \pm 60$ [162]. These particle multiplicities are well within the design capabilities of the ALICE detector.

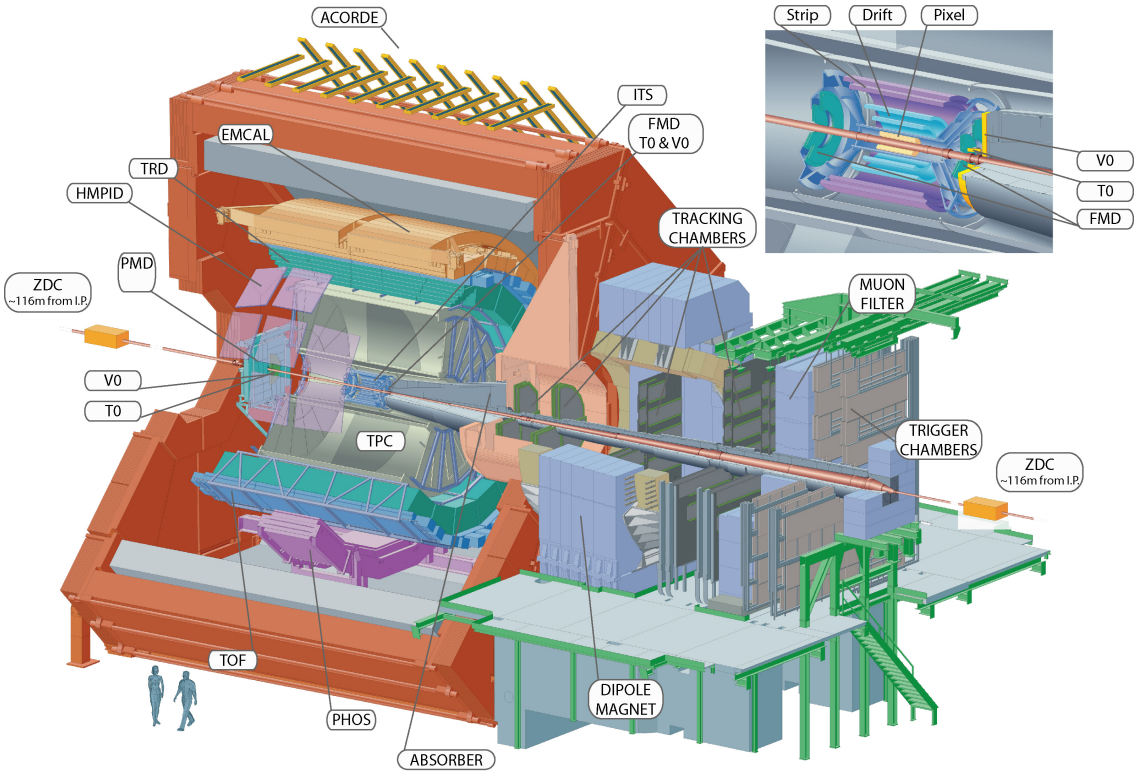

Figure 4.2: Schematic of the ALICE detector with sub-detectors labelled and inlay of ITS [47].

For a complete description of the detector the reader is referred to [47]. For the analysis detailed in this thesis only a small number of the detectors are used and these are described in more detail below.

[1] Note that the terms particle multiplicity and pseudorapidity density may be used interchangeably.

4.2.2 Inner Tracking System

The ALICE Inner Tracking System (ITS) [163, 164] is the closest detector to the beam pipe. Due to its proximity to the interaction point the ITS has to process the highest particle densities of all of the detectors. In order to process this high multiplicity environment, it is constructed of six cylindrical layers of silicon detectors coaxially placed around the beam pipe. The layers all span a pseudorapidity range of $|\eta| < 0.9$ for vertices located within $z = \pm 60$ mm of the nominal interaction point. The first layer is located at a radius of 39 mm and the outermost layer is positioned at 430 mm. The first two layers, where track densities of 90 cm^{-2} are expected, are made of Silicon Pixel Detectors (SPD), the middle two layers are made of Silicon Drift Detectors (SDD) and the outermost layers, where track densities are expected to have fallen to one particle per cm^2, are made of double-sided Silicon micro-Strip Detectors (SSD). A schematic of the layout of the ALICE ITS is shown in Fig. 4.3.

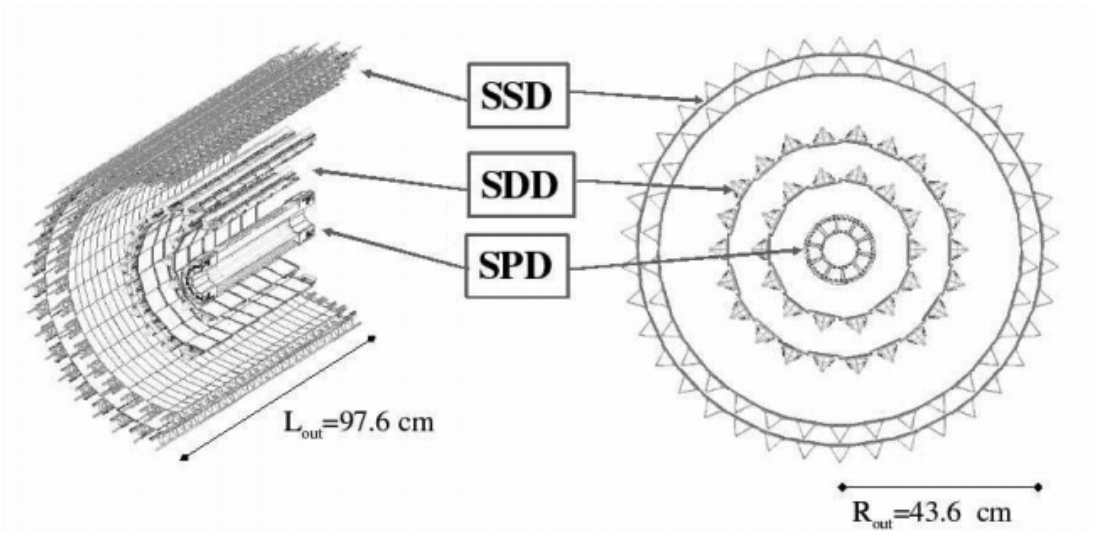

Figure 4.3: Schematic layout of the ALICE Inner Tracking System [47].

Silicon Pixel Detector

The two layers of SPDs make up the innermost part of the ITS as they have sufficient granularity for good two-particle separation in the large particle density environment of heavy-ion collisions where track densities can be as high as 90 cm^{-2}. A photograph of half of the barrel of the ALICE SPD is shown in Fig. 4.4. In order to achieve this granularity the detectors are made up of 9×10^6 pixels which are each 50×425 μm^2. The first layer of the detector has a pseudo-rapidity coverage of $|\eta| < 1.75$ [163].

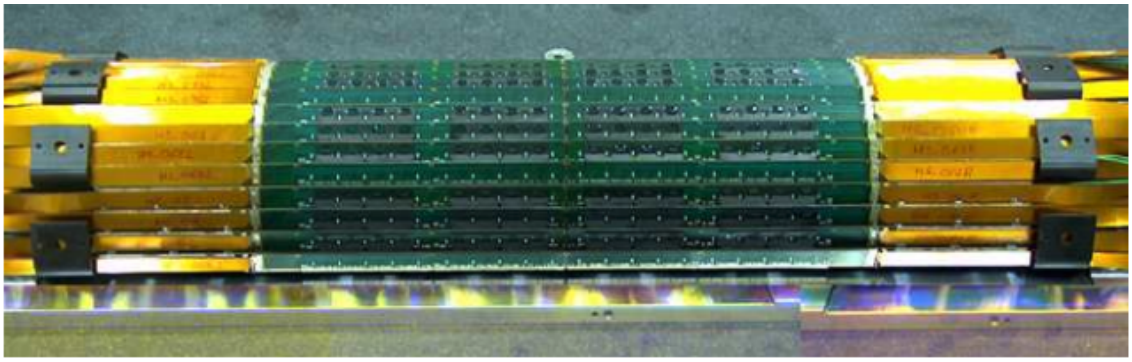

Figure 4.4: Photograph of the half-barrel of the ALICE Silicon Pixel Detector [47].

Silicon Drift Detector

Much like the SPDs in the first two layers of the ITS, the third and fourth layers are designed to process very high track-density environments with high resolution. Therefore the middle two layers are constructed using Silicon Drift Detectors (SDDs). The first layer, which is located at a radius of 15 cm is designed to reconstruct track densities of 7.2 cm^{-2} and the second layer at 24 cm is designed for track densities of 2.7 cm^{-2}. The detector is constructed of 300μm thick wafers with an active area of 7.02×7.53 cm^2. The electron-hole pairs released by ionising radiation in the SDD drift towards the ends of the wafer to an array of collecting anodes under the influence of an applied electric field. The first coordinate of the crossing point is determined by taking the centroid of the charge distribution across the

anodes and the second is reconstructed by calculating the drift time difference to each set of anodes using the electron mobility, μ_e, to calculate the drift velocity $v = \mu_e E$, where E is the applied electric field [165]. The active area of each wafer is separated into two adjacent 35 mm drift regions with 256 collecting anodes each. The spatial resolution of the SDD ranges from approximately 20 μm up to about 50 μm for hits with the shortest drift distances. A photograph as well as a CAD drawing of the SDD and mechanical support are shown in Fig. 4.5

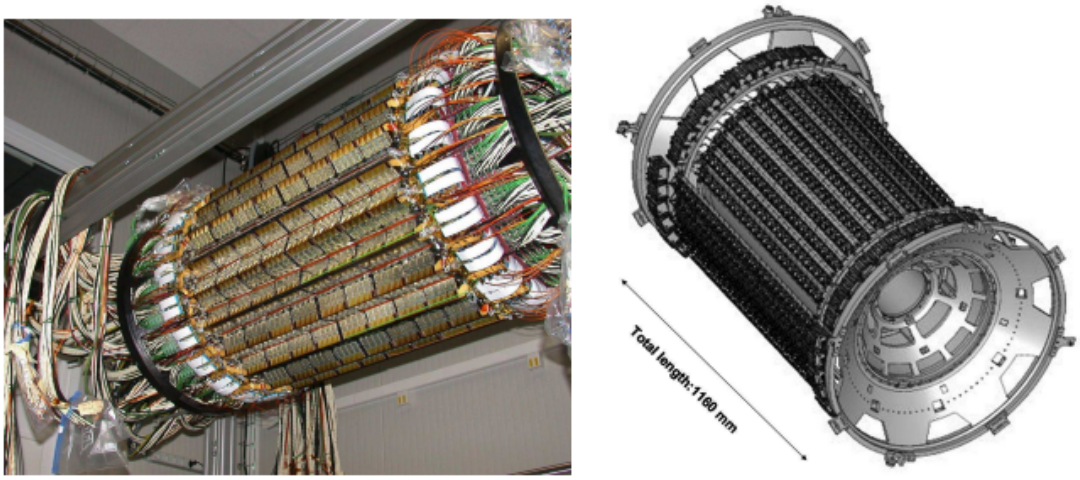

Figure 4.5: Photograph (left) and CAD design (right) of the ALICE Silicon Drift Detector System [47].

Silicon Strip Detector

The Silicon Strip Detector of the ALICE ITS consists of 1698 modules, each composed of a 1536 strip double-sided silicon sensor to make up over 2.6 millions readout channels. The system parameters of the SSD are shown in Table 4.1. Being the outermost layer of the ITS the SSD is crucial for matching tracks from the TPC to the ITS. In addition to this they also provide important $\mathrm{d}E/\mathrm{d}x$ information for low-momentum particle identification. The spatial resolution of the SSD has been measured to be better than 20 μm in the $r\varphi$ direction [47].

Component Layer	Layer 5	Layer 6
Radius	378 and 384 mm	428 and 424 mm
Sensitive Area	2.2m^2	2.8m^2
Number of ladders	34	38
Modules/Ladder	22	25
Total Modules	748	950
Total Weight	1.24kN	

Table 4.1: SSD system parameters [47].

4.2.3 Time Projection Chamber

Arguably the most important detector system used in this analysis is the Time Projection Chamber (TPC) [166]. The primary purpose of the TPC is to reconstruct the trajectory and measure the momentum of charged particles. It is optimised to achieve good two-particle separation, particle identification and vertex determination. The TPC spans a pseudo-rapidity of $|\eta| < 0.9$ for particles with full radial track length. The ALICE TPC was designed with the previously mentioned predicted particle multiplicities of up to $\frac{\mathrm{dN_{ch}}}{\mathrm{d}\eta} = 8000$, which equates to approximately 20000 charged primary and secondary tracks in acceptance.

The TPC is located within the inner barrel component of the ALICE detector at a radius of about 85 cm out to a radius of 250 cm and covers a distance of 500 cm along the beam pipe. Filled with 90 m^3 of a $Ne/CO_2/N_2$ gas mixture, the TPC is made up of a large cylindrical field cage as shown in Fig. 4.6. Primary electrons are transported up to 2.5 m to one of the end plates where multi-wire proportional chambers with cathode pad readout are mounted onto 18 trapezoidal sectors separated by small "dead-zones". The TPC has a drift velocity of 2.7 cm/μs with a maximum drift time of 92 μs. This relatively long drift time is the limiting factor in the maximum collision rate that can be measured by ALICE. The field cage shown in Fig. 4.6 is used to provide a highly uniform electrostatic field in the gas volume and is operated at high voltage gradients of approximately 400 V/cm with a high voltage of 100 kV provided to the central electrode.

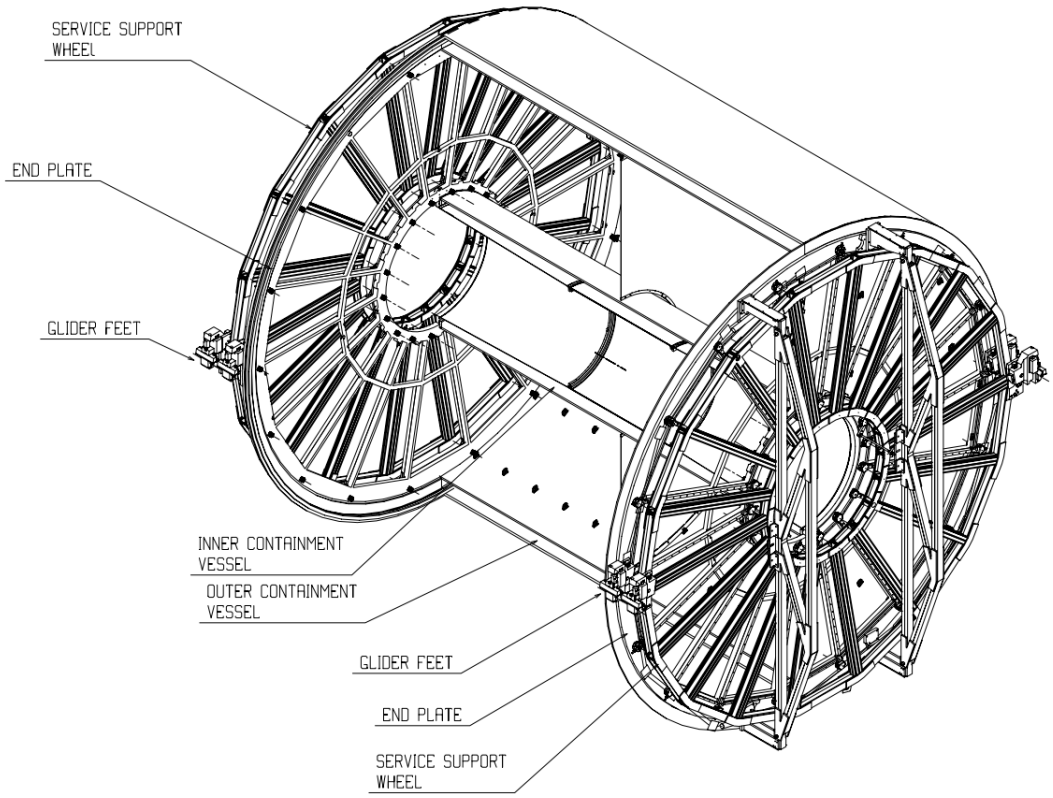

Figure 4.6: The ALICE TPC field cage in 3D [47].

The gas mixture which fills the TPC is optimised for drift speed and low diffusion. The Ne/CO_2 mixture has a very strong drift velocity dependence on gas temperature and hence, in order to achieve a constant drift velocity, the TPC system aims to achieve a thermal stability of $\Delta T \leq 0.1$ K. In order to achieve such thermal uniformity, an elaborate system of heat screens and cooling circuits is used [47].

4.2.4 V0

Another detector system that is used frequently in this analysis is the V0 detector [167]. The V0 detector is comprised of two arrays of scintillating detectors placed on either side of the ALICE interaction point called V0A and V0C. Whereas the previous detector systems are primarily used for charge particle tracking, the V0 system serves a different purpose. The

V0 detector is used for triggering in the case on minimum-bias (MB), multiplicity (MT), semi-central (CT1) and central (CT2) triggers as well as centrality estimation for Pb–Pb collisions.

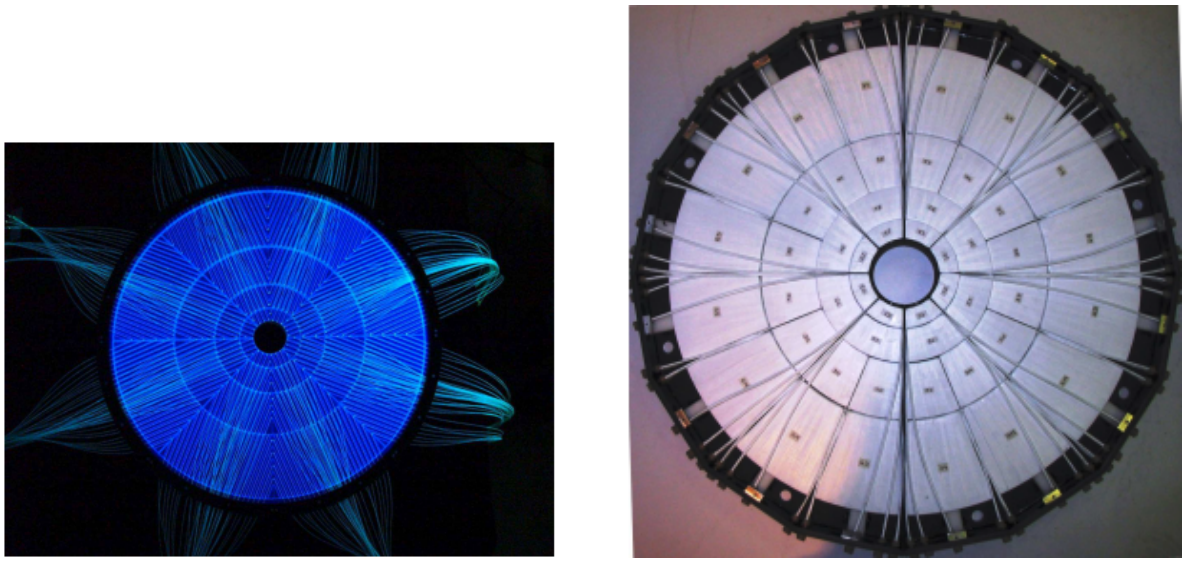

Figure 4.7: Front view of V0A (left) and V0C (right) [47].

The centrality of an event is determined by summing the energy measured by both the V0A and V0C. This energy directly relates to the number of primary particles created in the collision, which, using the glauber model, can be related to the centrality of a collision.

Chapter 5

Analysis

5.1 Introduction

In this chapter the measurement of jet substructure using Soft Drop and recursive techniques in pp at $\sqrt{s} = 7$ TeV and Pb–Pb collisions at $\sqrt{s_{\mathrm{NN}}} = 2.76$ TeV will be discussed. The measurement details for the two collision systems will be covered in parallel where possible. Section 5.2 describes the process of event selection applied to the two collision systems as well as tracking, jet reconstruction and selection and centrality determination in Pb–Pb events. The process of background subtraction and discussion of the problems with the underlying event are addressed in Section 5.3, whilst in Section 5.4 the jet response to detector and background effects is quantified. The raw (uncorrected) jet observables are presented in Section 5.5 before the processes of unfolding and folding are discussed in Sections 5.6 and 5.7. The systematic uncertainties are covered in detail in Section 5.8.

5.2 Data Selection

5.2.1 Datasets

The data used for this analysis were acquired during two different data taking periods for the two collision systems studied. The pp collisions analysed were taken in 2010 and are separated into two datasets LHC10d and LHC10e. These collisions were measured at $\sqrt{s} = 7$ TeV and the datasets comprise approximately 1.5×10^8 events and were recorded with a Minimum Bias (MB) trigger.

The Pb–Pb analysis was performed on data recorded by the ALICE detector in 2011 when the LHC delivered the second run of Pb–Pb collisions at a collision energy of $\sqrt{s_{\mathrm{NN}}} = 2.76$ TeV. The data are separated into three different datasets: one "good" set and "two semi-good" sets which combined make up the LHC11h dataset. The two semi-good sets are defined as such due to faulty TPC sectors in each of the sets. Extra offline cuts have to be applied to ensure these sectors are totally excluded from the analysis (section 5.2.5). The datasets comprise approximately 1.9×10^7 events and were recorded with a central (CENT) trigger.

In addition to data recorded by the ALICE detector, this analysis utilises sophisticated Monte Carlo generators to simulate collisions for comparison to data. PYTHIA simulated events are used to characterise the detector effects needed to correct the pp data. The detector effects are modelled using GEANT 3 [168] ALICE simulations and PYTHIA6 Perugia 0 simulated events which are generated in 10 $p_{\mathrm{T,hard}}$ bins with bin edges: [5, 11, 21, 36, 57, 84, 117, 152, 191, 234+] GeV/c. The $p_{\mathrm{T,hard}}$ bins refer to the limits imposed on kinematics of the hard process ($2 \rightarrow 2$ scattering) in the simulated event. Figure 5.1 shows the charged jet transverse momentum ($p_{\mathrm{T,jet}}^{\mathrm{ch}}$) distributions for each $p_{\mathrm{T,hard}}$ bin. The $p_{\mathrm{T,hard}}$ bins are merged using event weights calculated for each corresponding bin. The detector simulations are anchored to individual data-taking runs to best replicate the performance of the ALICE detector in the specified run period.

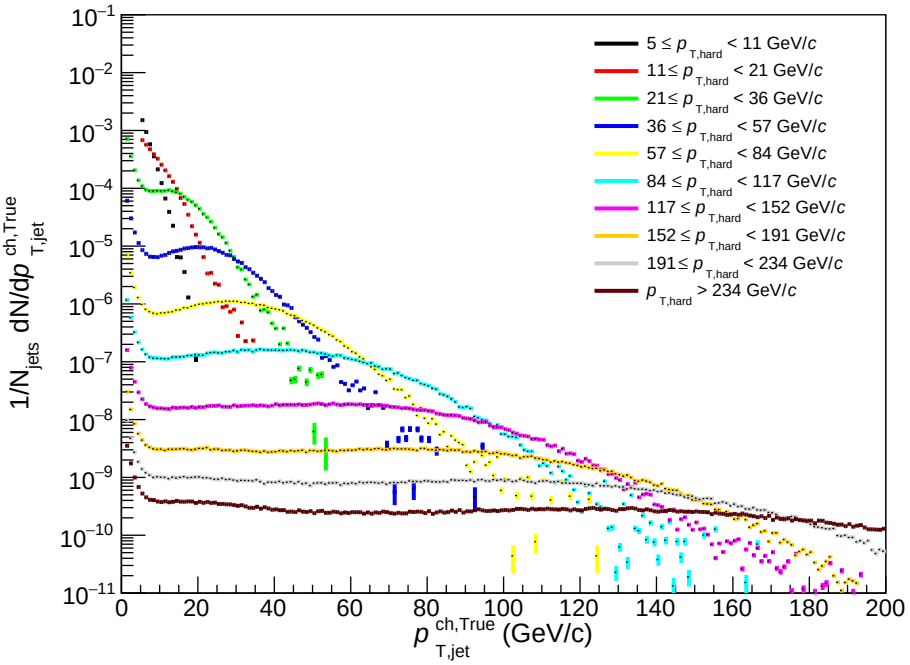

Figure 5.1: PYTHIA6 Perugia 0 simulated jet transverse momentum spectra for each of the 10 $p_{\mathrm{T,hard}}$ bins.

For Pb–Pb collisions, as well as applying detector effects, the simulated events are embedded into real $0-10\%$ centrality Pb–Pb events in order to fully replicate the effects of the underlying event. The embedded PYTHIA events are then used as a "vacuum" reference for comparison to the Pb–Pb data. The simulated events that are embedded are generated in the same $p_{\mathrm{T,hard}}$ bins and again have detector effects applied associated with the specific run period.

5.2.2 Event Selection

The events were selected initially by using online triggering implemented by the ALICE Central Trigger Processor (CTP) [169]. In pp collisions the data were measured using a minimum bias trigger which requires a hit in either of the VZERO detectors or the SPD giving approximately 85% triggering efficiency [170]. For the Pb–Pb collisions a central

trigger was used. The central trigger has an additional requirement on the sum of the signal amplitudes of the V0 detectors being above some threshold [171].

Data were analysed from runs registered as "good" where all sub-detectors were functioning and only runs with a uniform azimuthal distribution of charged tracks were used. In the event reconstruction a maximum primary vertex displacement $|V_z| < 10\,\mathrm{cm}$ from the nominal interaction point was applied for optimal reconstruction.

5.2.3 Tracking

Track Reconstruction

The tracking process performed with the ALICE detector is a multi-stage procedure that primarily uses information from the TPC and the ITS [172, 173]. Before the tracking procedure is performed a process known as "clusterisation" is performed which combines position, time and amplitude information of signals acquired by the detectors. The tracking starts from the outermost clusters measured by the TPC by generating track seeds from either two seeds and the vertex point or three clusters without the vertex constraint. These seeds are then propagated inwards to the nearest clusters that fulfil proximity cuts and quality cuts are used to ensure that the number of TPC clusters shared by multiple tracks is low and tracks contain a sufficient number of clusters each (at least 20 out of a maximum 159). To ensure tracks do not share too many clusters, any pair of tracks that share a fraction of clusters above a certain limit (between 25% and 50%) are compared and the track that is considered worse quality by a parameter based on cluster density, number of clusters and momentum is discarded. Once this first stage of tracking is completed the resulting tracks make up the TPC-only track lists. A preliminary particle identification is performed on this track list (using $\mathrm{d}E/\mathrm{d}x$) and a most-probable-mass assignment is used in order to apply ionisation energy loss corrections due to the interactions with the tracking detectors. Figure 5.2 shows the

tracking efficiency for the TPC where the efficiency is calculated by taking the ratio of the reconstructed tracks and generated primary particles in simulations; the tracking efficiency is shown as a function of primary particle transverse momentum.

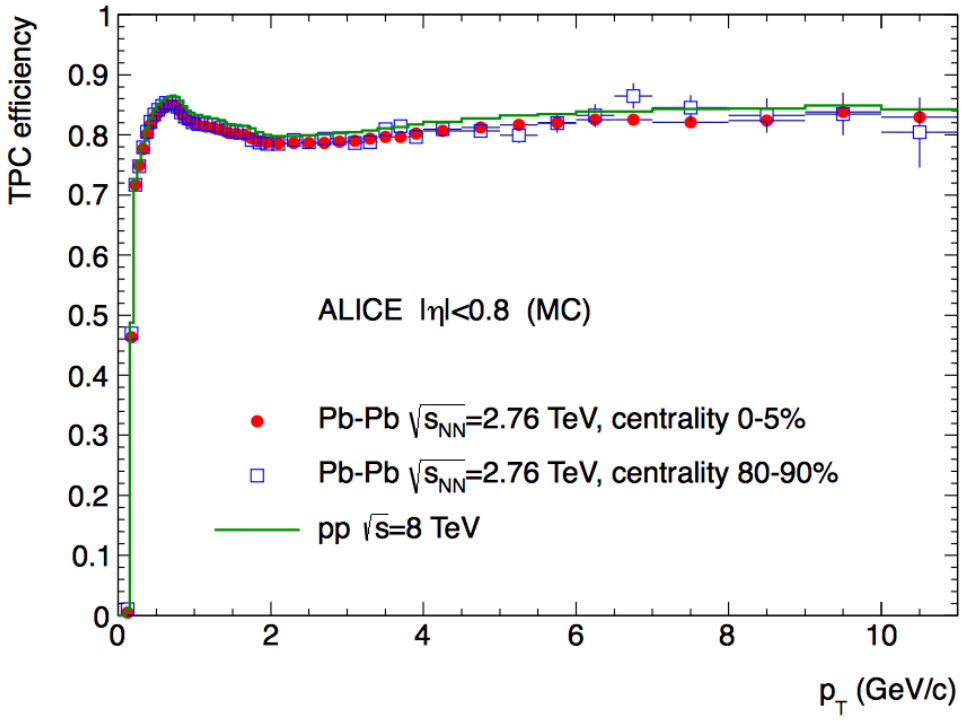

Figure 5.2: Tracking efficiency of the ALICE TPC for primary particles in simulated pp and Pb–Pb collisions [174].

The tracks reconstructed from the TPC clusters are then propagated to the outermost layer of the ITS and become the seeds for the tracking process in the ITS. As with the TPC tracking, the seeds are propagated inwards using clusters that satisfy proximity cuts. At each layer of the ITS the seeds are updated using the tracking result of the previous layer. The Kalman Filter technique [175] is used to refit the track candidates and assign a value of χ^2 for that track fit. Seeds without an update in a particular layer of the ITS are still used for track finding by having a systematic increase in their χ^2 value (unless the extrapolation occurs in the dead-zone of a layer in which case there are no clusters expected). After this process each TPC track has a corresponding tree of potential connecting tracks through the

ITS. As with the TPC, the seeding is performed twice, once with a vertex constraint and once without but with an additional seed. Once the candidate tracks are constructed they are ordered in terms of their χ^2. After checking for and resolving shared clusters between track candidates the one with the lowest χ^2 is added to the reconstructed event.

Any ITS clusters that are not used in the ITS-TPC track reconstruction are used for a standalone ITS reconstruction. This tracking is performed from the innermost ITS layers and is propagated outward. Once this process is propagated to the outermost layer the ITS track candidates are refitted using a Kalman filter technique and the track with the best χ^2 is used. This ITS only tracking is performed due to the low track identification efficiency of the TPC at transverse momenta below 500 MeV/c that is shown in figure 5.2. Performing this additional process allows reconstruction of particles with transverse momenta down to as low as 80 MeV/c.

After an outward propagation of tracks from the point of closest approach to the preliminary interaction vertex out to the detectors beyond the TPC using the Kalman Filter refitting a final inward propagation of all tracks is performed. This final stage propagates tracks inwards from the outer radius of the TPC and refits the tracks in both the TPC and ITS to determine the final position, direction, inverse curvature and covariance matrix for each track.

Hybrid Tracks

For some run periods during the 2010 Pb–Pb data taking period, some modules of the SPD were switched off due to problems with the ITS cooling system. The result of having these sectors switched off is inefficient regions for common track reconstruction. In order to ensure a uniform track distribution in the (η, φ) plane a hybrid approach is taken. The hybrid track list consists of a combination of:

- **global tracks**: global tracks identified in the process outlined in Section 5.2.3 with SPD hits and ITS refit
- **complementary tracks** (constrained to primary vertex to improve momentum resolution):
  - global tracks without SPD hit but with an ITS refit
  - global tracks without ITS refit or SPD hit.

The complementary tracks are constrained to the primary vertex in order to improve their transverse momentum resolution. The azimuthal distributions of the three types of tracks that are combined to make up the hybrid track list is shown in figure 5.3. The figure also shows the sum of the individual track sets which displays a clear homogeneous distribution in the azimuth. The good global tracks that are reconstructed with SPD hits and ITS refit have good transverse momentum resolution. Combining these tracks with the complementary tracks lowers the average transverse momentum resolution of the track list but this is accepted in favour of an overall homogeneous tracking efficiency.

Track Distributions

Several kinematic and fiducial cuts are applied to the track lists prior to jet finding. A minimum track transverse momentum of 150 MeV/c was applied to all tracks in both pp and Pb–Pb collisions and any jets containing tracks with $p_{\mathrm{T,track}}^{\mathrm{ch}} > 100\mathrm{GeV}/c$ are tagged and rejected after jet finding. For the LHC10h dataset (Pb–Pb) analysed there is $|\eta| < 0.9$ cut applied prior to primary vertex constraints being added to the complementary tracks. Applying the vertex constraint can modify the track momentum, η and ϕ so some tracks may be reconstructed outside the nominal η range (-0.9,0.9). Therefore an additional cut has to be applied to the accepted tracks to ensure only tracks within the fiducial η range of the tracking detectors are used. The final reconstructed track kinematic spectra and η

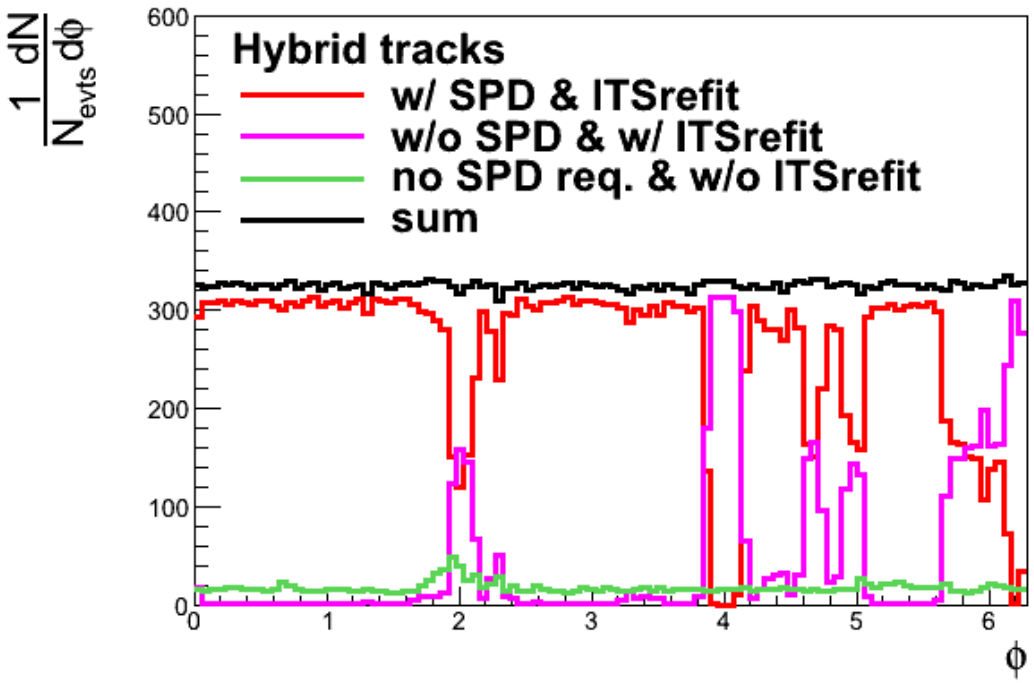

Figure 5.3: Track azimuthal distribution for three components of hybrid track list for centrality class 0-10% for 2010 Pb–Pb collisions at $\sqrt{s_{\mathrm{NN}}}$= 2.76 TeV [176].

distribution for tracks that are clustered into jets are shown in Fig. 5.4 for both pp and Pb–Pb collisions. The spectrum of the tracks reconstructed in pp collisions is much harder than in Pb–Pb collisions. This is due to the presence of the significant underlying event in Pb–Pb collisions which contributes a large number of soft particles to the jets. The η spectra also differ between the two collision systems with the pp distribution falling at larger values of $|\eta|$. This occurs because of the requirement that the jets are fully contained within the range ($|\eta| < 0.9$) of the TPC meaning tracks at the edge of the TPC acceptance contribute to fewer jets than those in the central region. This effect is not observed in the Pb–Pb spectra where instead the distribution appears inverted. This is due to the presence of small-area *combinatorial jets* (section 5.3.2) that accumulate at the border of the TPC acceptance. The large number of these fake jets that are comprised of uncorrelated particles from the underlying event leads to the enhancement of tracks at the edges of the η acceptance that is

observed. Combinatorial jets are corrected for using the background subtraction techniques discussed in Section 5.3.

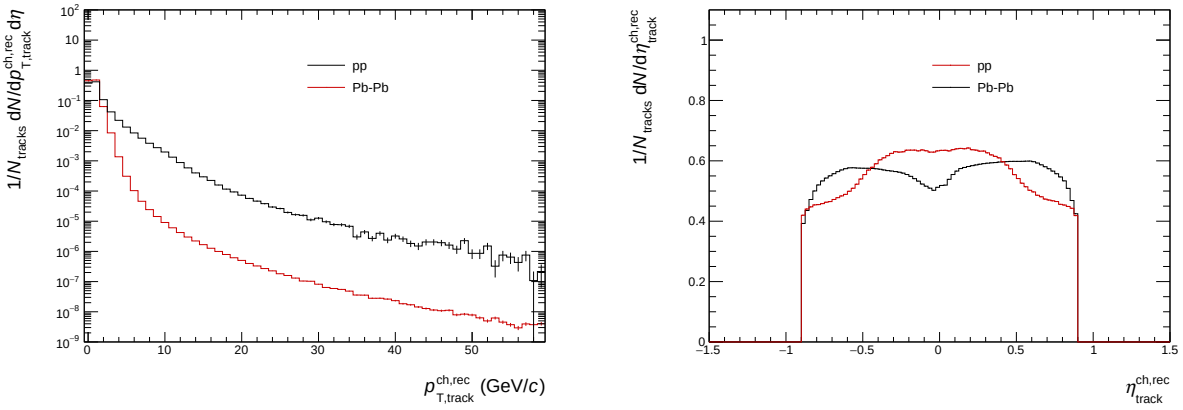

Figure 5.4: Reconstructed track kinematic spectra for tracks clustered into jets in pp collisions at $\sqrt{s} = 7$ TeV and the centrality class 0-10% of Pb–Pb collisions at $\sqrt{s_{\text{NN}}} = 2.76$ TeV.

5.2.4 Centrality Determination

In Pb–Pb collisions the events are assigned an event centrality which is related to the overlap of the two colliding nuclei, the impact parameter (b). As the centrality can not be directly measured it must be inferred; this is done by measuring the average charged-particle multiplicity in the ALICE V0 detector (N_{ch}). A measurement of N_{ch} can then be related to the impact parameter, number of collision participants, N_{part}, and by extension the event centrality, using the Glauber Model [20, 177]. The Glauber model uses the assumption that the event particle multiplicity is monotonically related to the impact parameter, b. Centrality classes are defined in order to link the experimental observables to the initial state quantities. The classes are assigned to both the experimental distributions and the Glauber model calculations and the mean values of each distribution are connected.

Figure 5.5 (left) shows an illustrative example for the correlation between the initial state parameters and the measured final state observable N_{ch}; the illustration shows how the cen-

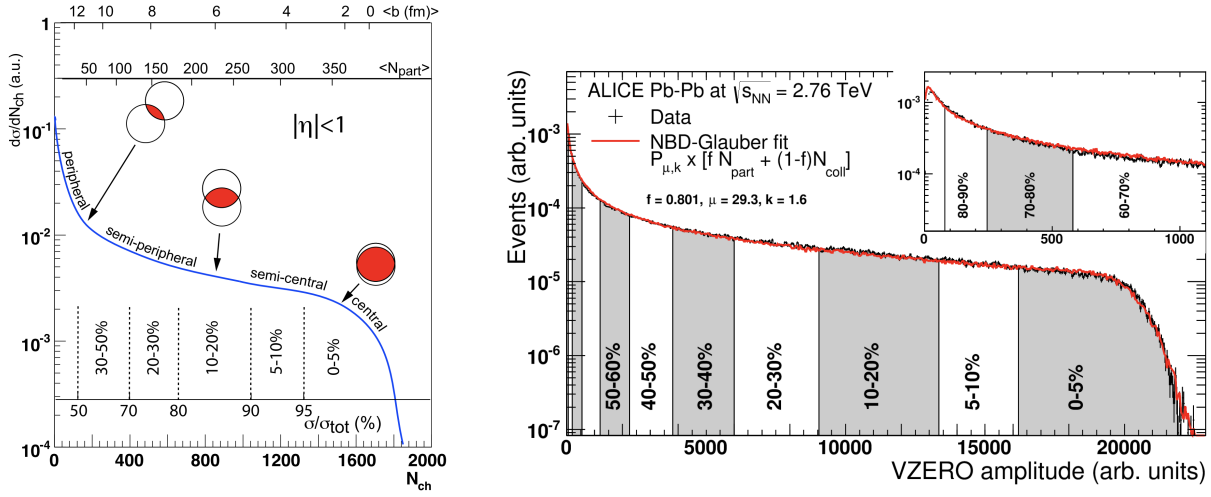

Figure 5.5: (left) An illustrative example of the correlation between final state observables N_{ch} and the Glauber calculated quantities (b, N_{part}) [20]. (right) Sum of V0 amplitude distribution with Glauber model fit and centrality class cuts.

Centrality	$\langle N_{\mathrm{part}} \rangle$	RMS
0-5%	382	17
5-10%	329.7	18
10-20%	260.5	27
20-40%	157.8	35
40-60%	69.13	22
60-80%	22.64	12

Table 5.1: N_{part} for Pb–Pb collisions at $\sqrt{s_{\mathrm{NN}}} = 2.76$ TeV derived from a Glauber fit to the sum of V0 amplitudes [178].

trality classes are applied to both the phenomenological calculations and the measured data. On the right hand side of figure 5.5 the sum of amplitudes of the ALICE V0 subdetectors is shown with an applied Glauber fit and the corresponding centrality classes. Table 5.1 shows the mean values of N_{part}, calculated using the Glauber model, for the experimentally measured centrality classes calculated for Pb–Pb collisions at $\sqrt{s_{\mathrm{NN}}} = 2.76$ TeV.

5.2.5 Jet Selection

Charged jets were reconstructed with FastJet 3.2.1 [179], using the anti$-k_{\mathrm{T}}$ algorithm and the E-scheme recombination scheme. For this analysis a jet resolution parameter of $R = 0.4$

was used for both collision systems. The inputs to jet clustering were charged tracks with a minimum track transverse momentum cut of $p^{ch}_{\mathrm{T,track}} = 150$ MeV/c.

There was a minimum transverse momentum threshold applied to all jet candidates of $p^{\mathrm{ch}}_{\mathrm{T,jet}} = 10$ GeV/c for pp collisions and $p^{\mathrm{ch}}_{\mathrm{T,jet}} = 20$ GeV/c in Pb–Pb collisions. A pseudo-rapidity restriction of $|\eta^{ch}_{jet}| < 0.5$ was applied to the jet populations to ensure they were fully contained within the fiducial volume of the ALICE tracking system. Additionally, in the case of the semi-good Pb–Pb datasets there was the restriction that the φ coordinate of the jets must be more than 0.4 away from the edge of the malfunctioning TPC sectors. The uncorrected transverse momentum distributions for jets reconstructed in pp collisions at $\sqrt{s} = 7$ TeV and Pb–Pb collisions at $\sqrt{s_{\mathrm{NN}}} = 2.76$ TeV are shown in Fig. 5.6.

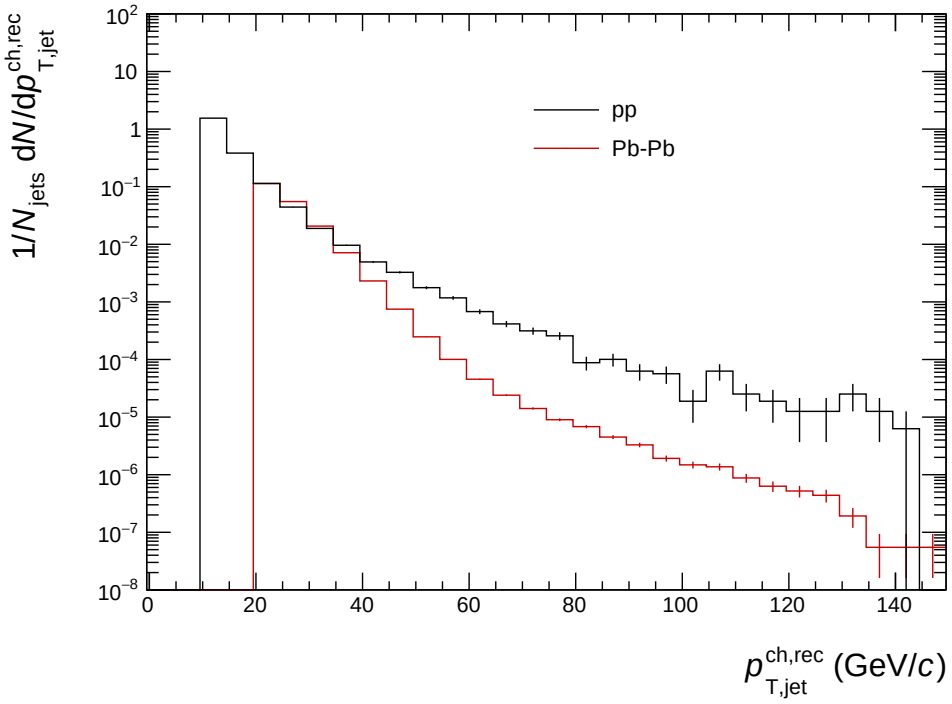

Figure 5.6: Reconstructed jet transverse momentum spectra for pp collisions at $\sqrt{s}$= 7 TeV.

The reconstructed $\eta^{ch,rec}_{jet}$ distributions are shown in Fig. 5.7 and the $\varphi^{ch,rec}_{jet}$ distributions for pp and Pb–Pb collisions are shown in figures 5.8 and 5.9, respectively. Jets are expected

to be produced approximately uniformly in η and φ. For pp collisions, the φ distribution shows clear peaks which arise at the boundaries of the 18 sectors of the TPC. In figure 5.9 the φ distributions for the Pb–Pb datasets are presented. The distribution is non-uniform across the full range of the azimuth which highlights the irregularities and inhomogeneities of the ALICE tracking system. These irregularities are exaggerated by the very dense environments of heavy-ion collisions and clustering the particles into jets further enhances this. Figure 5.9 highlights the importance of correcting for detector effects as done in this analysis by demonstrating the potential modification that can occur to observables in reconstruction.

The bottom two distributions in figure 5.9 show the φ distributions for the two semi-good datasets and the effect of removing the jets which overlap with two non-functioning TPC sectors can be clearly seen by a lack of entries in the respective φ ranges. As this analysis is focussed on charged jets the η range is dictated by the fiducial cuts of the TPC meaning the η range for charged tracks is $|\eta|$ <0.9 and $|\eta| < 0.5$ for $R = 0.4$ jets and full coverage in φ.

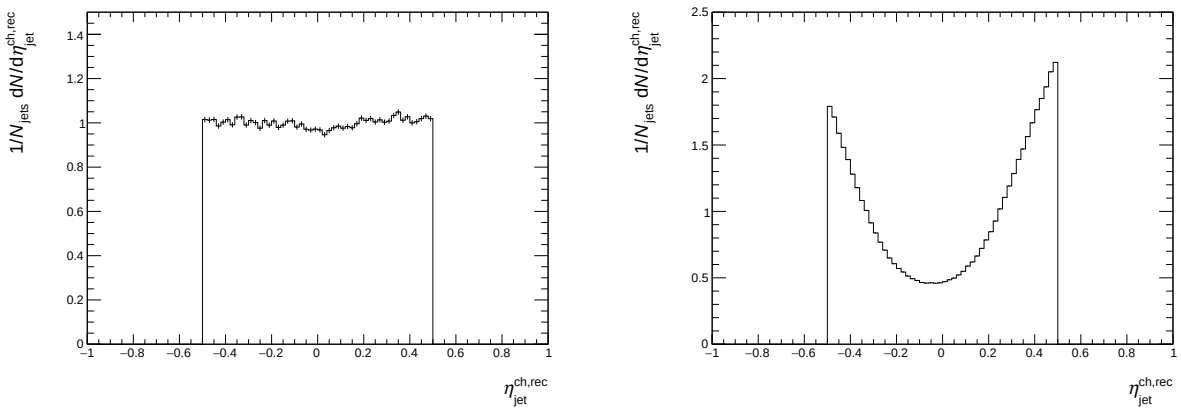

Figure 5.7: Reconstructed $\eta_{jet}^{ch,rec}$ for pp collisions at $\sqrt{s}$= 7 TeV (left) and Pb–Pb collisions at $\sqrt{s_{\mathrm{NN}}}$= 2.76 TeV (right).

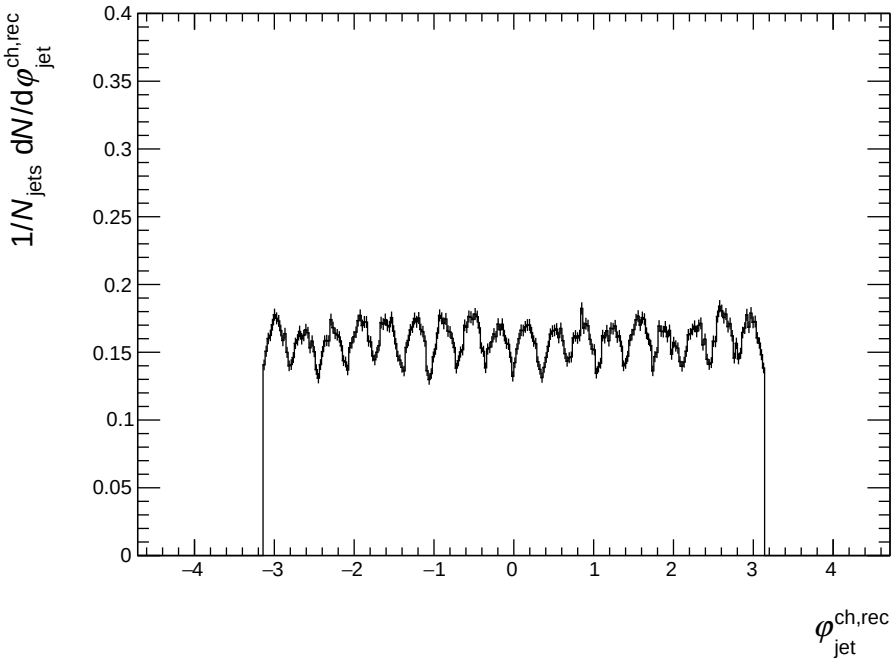

Figure 5.8: Reconstructed $\varphi_{jet}^{ch,rec}$ for pp collisions at $\sqrt{s}$= 7 TeV.

5.3 Background Subtraction

The measurements of jet observables are performed on a reconstructed jet population. These measurements can be significantly modified by additional processes that occur in the collisions, referred to as the underlying event, as well as detector effects and inefficiencies. In order to make meaningful comparisons to measurements performed by other experiments or theoretical predictions, these background effects need to be corrected for. This section discusses the method for correcting the underlying event whilst the Bayesian approach to correcting for detector effects is discussed in Section 5.6.

5.3.1 Underlying Event Subtraction

In pp collisons, the contribution from the underlying event is expected to be negligible so no subtraction is applied. For Pb–Pb collisions, the constituent subtraction method was

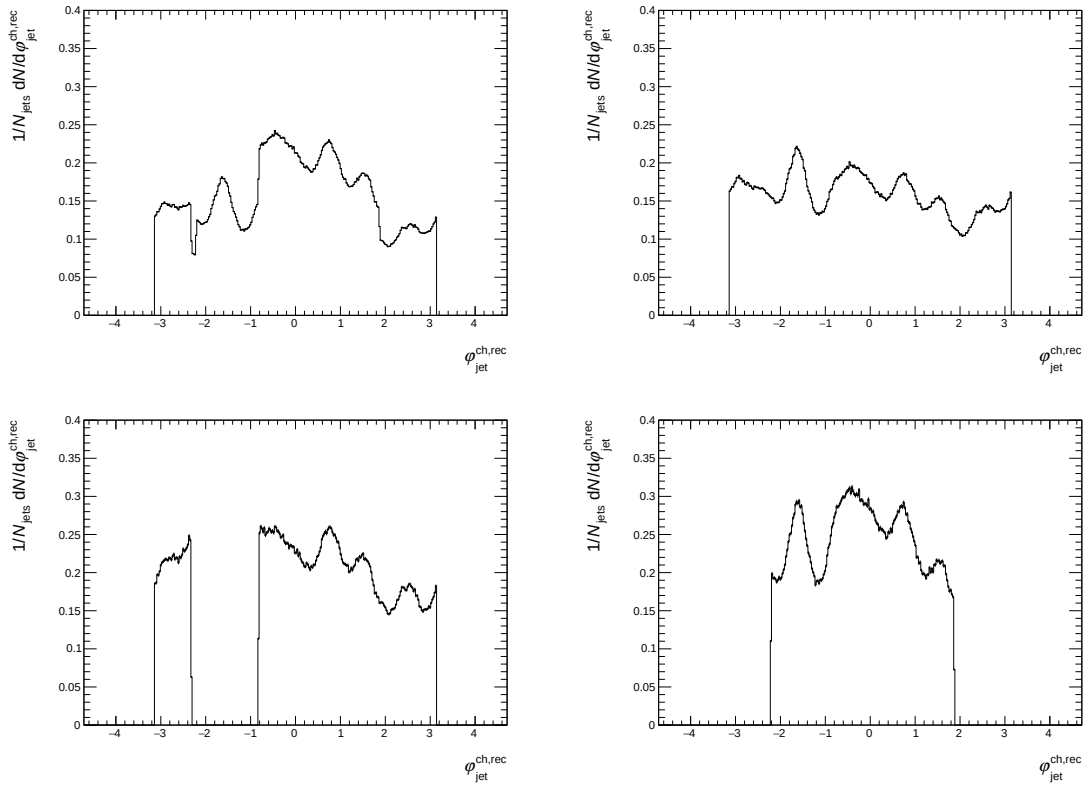

Figure 5.9: Reconstructed $\varphi_{jet}^{ch,rec}$ for Pb–Pb collisions at $\sqrt{s}$= 2.76 TeV: (top left) all datasets combined, (top right) LHC11h (good), (bottom left) LHC11h (semigood 1), (bottom right) LHC11h (semigood 2).

used [180]. The constituent subtraction method corrects at the track level of the jets by modifying their transverse momentum in an attempt to remove as much of the contribution from uncorrelated tracks as possible. Correcting at the individual constituent level is required when studying jet substructure.

In order to remove the contribution from the underlying event the average background p_{T}-density must first be calculated. This is done by clustering the event into k_{T} clusters with a resolution parameter of $R = 0.2$ and, after excluding the two highest transverse momentum clusters to remove the contribution from true hard scatterings, calculating the average background density as:

$$\rho = \text{median}\left[\left\{\frac{p_{\mathrm{T},j}}{A_j}\right\}\right], \tag{5.1}$$

where $p_{\mathrm{T},j}$ and A_j are the transverse momentum and area of the j^{th} k_{T} cluster. The median is used to further reduce sensitivity to outliers originating from fragments of jets originating from hard scatterings. Figure 5.10 shows the distribution of ρ as a function of centrality and it shows how the average background density decreases as the overlap of the colliding nuclei decreases.

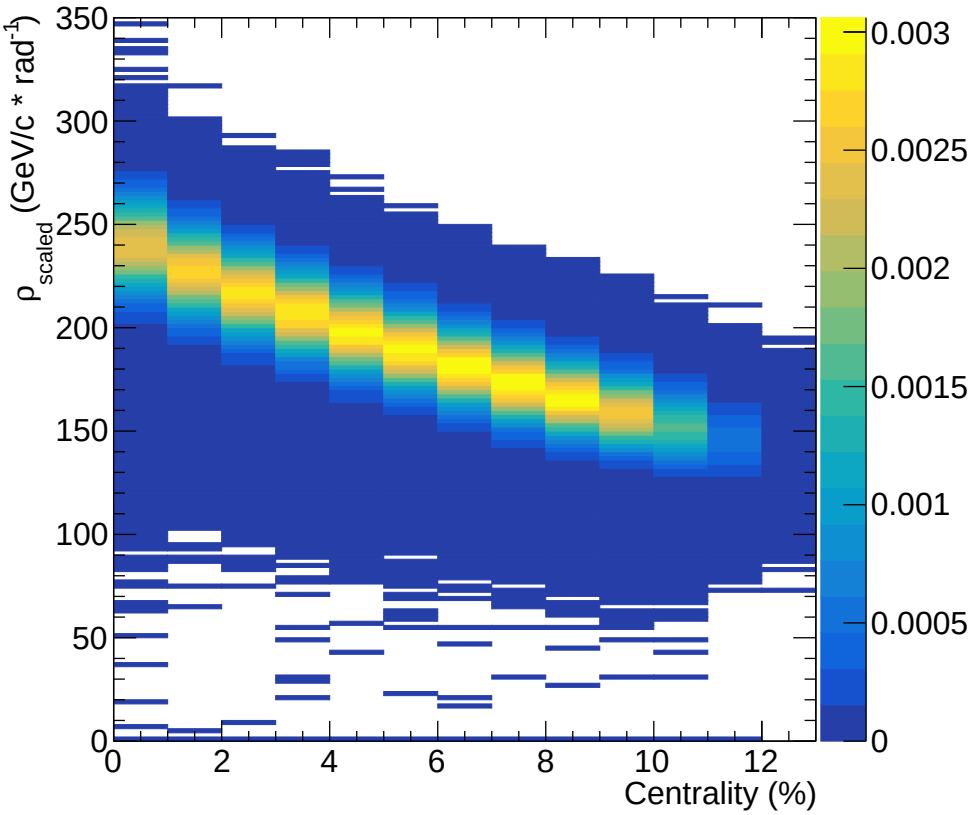

Figure 5.10: Average background density (ρ) as a function of event centrality calculated using $R = 0.2$ k_{T} clusters for Pb–Pb events at $\sqrt{s_{\mathrm{NN}}}$= 2.76 TeV.

To apply the subtraction the event is filled uniformly with *ghost particles* [179] within the

detector acceptance each assigned an area of 0.01 in $(\eta-\varphi)$ space for this analysis. The ghosts are clustered in the same way as reconstructed tracks in the jet finding procedure but do not modify the process due to being assigned negligible initial momentum. After jet finding, each ghost particle is assigned a transverse momentum given by $p_{\mathrm{T,g}} = A_{\mathrm{g}}\rho$ and a mass of $m_{\mathrm{g}} = A_{\mathrm{g}}\rho_{\mathrm{m}}$. The subtraction procedure begins by calculating the distance between each jet constituent and each ghost particle and storing them in a list. The ghost-constituent pairs are then ordered by their separation and the subtraction is applied in order of angular separation. The transverse momenta of the first pair are compared and if the ghost transverse momentum is lower than that of the real jet constituent the ghost is removed from the event and $p_{\mathrm{T,g}}$ is subtracted from the real jet constituent. The ghost-constituent list is then updated and the next closest pair is considered and the subtraction is applied again. If the ghost transverse momentum exceeds that of any constituent to which it is being compared then the transverse momentum of the constituent is subtracted from the transverse momentum of the ghost and the constituent transverse momentum is set to zero and the list is updated.

After all of the ghost particles clustered in a jet are removed then the jet shapes are calculated using the updated list of modified tracks.

5.3.2 Combinatorial Jets

In addition to the modification of real jets by the presence of a substantial underlying event, fluctuations in the background can lead to clusters of particles that have a large amount of transverse momentum despite being uncorrelated. These clusters that pass the jet cuts are known as *combinatorial jets*. These combinatorial jets can still have a significant amount of transverse momentum even after the process of constituent subtraction and can enter the jet population being studied. To ensure that the studied jet population is as free of combinatorial jets as possible one can impose a higher restriction on the minimum jet transverse momentum. Figure 5.11 shows the $p_{\mathrm{T,jet}}^{\mathrm{ch}}$ distribution for inclusive jets ($R = 0.2$ and $R = 0.3$) and for jets

with a leading hadron with at least $p_{\mathrm{T}} > 5$ GeV/c and $p_{\mathrm{T}} > 10$ GeV/c. These spectra are produced from the same jet populations and it can be seen that at low jet momenta the inclusive spectrum is significantly enhanced relative to the two spectra with the leading hadron requirement. Jets that contain a leading hadron with a large amount of transverse momentum are much more likely to originate from a hard-scattering process and hence be real jets. It can be seen from Fig. 5.11 that at higher transverse momentum the spectra begin to overlap which suggests that the inclusive jet population in this region is made up of a larger fraction of real jets. Increasing the jet radius increases the chance of capturing more of a background fluctuation in the catchment area of a jet and this leads to an increase in the transverse momentum of combinatorial jets. This can be seen in Fig. 5.11 where the spectra fully overlap by about $p_{\mathrm{T,jet}} \approx 60$ GeV/c for $R = 0.2$ jets (left) whereas for $R = 0.3$ jets it is not until $p_{\mathrm{T,jet}} \approx 80$ GeV/c. As this analysis is performed on $R = 0.4$ jets, the transverse momentum region studied in Pb–Pb collisions was chosen to be $80 \leq p_{\mathrm{T,jet}}^{\mathrm{ch}} < 120$ GeV/c.

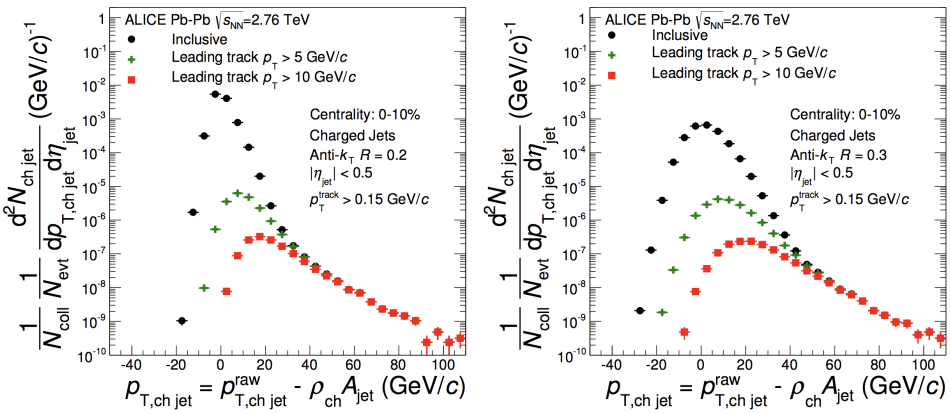

Figure 5.11: Uncorrected jet spectra after background subtraction for $R = 0.2$ (left) and $R = 0.3$ (right) jets in central Pb–Pb collisions with no restriction on the leading hadron (inclusive, black circles), a leading hadron with at least $p_{\mathrm{T}} > 5$ GeV/c (green crosses) and $p_{\mathrm{T}} > 10$ GeV/c (red squares) [62].

5.4 Detector and Background Response

Measurements of observables performed on data are done at the reconstructed level. In order to make meaningful comparisons to predictions from either analytical calculations of theoretical models either the measurements must be corrected to the "truth" level (sometimes referred to as "particle" level) or the predictions need to be smeared to the reconstructed level. This section will discuss the methods of performing this correction, known as *unfolding*, and smearing, known as *folding*. The data in pp collisions are unfolded and compared to particle level predictions from Monte Carlo generators whilst the data in Pb–Pb collisions are kept at the reconstructed level and the predictions from generators are folded and compared to the data. The mapping of particle level to reconstructed level is done using a *response matrix* which is a $2n$-dimensional matrix where n is the number of observables that one wishes to map concurrently for each jet.

5.4.1 Constructing the Response

In order to unfold the measurements in pp collisions and smear model comparisons for the Pb–Pb measurements a detailed understanding of the detector effects and underlying event fluctuations on the measurement is required. The dominant detector effect contributing to a modification in the observables of jet substructure is the track reconstruction efficiency. This effect, along with all other detector effects, is well modelled using the GEANT 3 simulation package. GEANT uses a very detailed description of the ALICE experimental setup to simulate the effects of the detectors and material budget on the events that are measured. In order to quantify these effects, events are generated using PYTHIA and then ran through the GEANT software where the smearing of the events due to the detector effects is performed. Full event reconstruction is then performed on the smeared events. In addition to this process, for Pb–Pb collisions the detector smeared events are then embedded into real, centrality class

0-10%, Pb–Pb events; a brief description of the embedding procedure is given in Section 5.4.2.

In the case of this analysis, where individual jets are analysed, a matching procedure is performed between the smeared and generated events, where jets that are reconstructed in the smeared events are matched to their corresponding jet in the generator level event. This matching is performed by using the geometrical comparison of the jets and pairing the jets which are separated by the smallest distance in $\eta - \varphi$ space.

Once the jets have been matched between the smeared and generator level, observables can be calculated on both sets of jets and a response matrix can be constructed. A response matrix has two axes, a "true" axis representing the measurement on the generator level jet and a "reconstructed" axis where the measurement on the smeared event jet is entered. The response matrix is filled jet-by-jet and an example matrix is shown in Fig. 5.12 for the jet spectra of PYTHIA and PYTHIA embedded jets . The degree of smearing due to detector effects is represented by the width of the diagonal element of the response; a clear strong diagonal response represents very little smearing whereas a very broad diagonal response with many off-diagonal entries shows a large amount of smearing. From Fig. 5.12 it is clear that the amount of smearing is much greater in Pb–Pb (right hand figure) where there is a significant contribution from the underlying event compared to the smearing from detector effects alone in pp collisions (left hand figure).

The response matrices used to unfold the three observables z_{g}, R_{g} and n_{SD} in pp collisions are shown in Fig. 5.13 on the left whilst the response matrices used to smear the model predictions in Pb–Pb are shown on the right. The unfolding is applied in two dimensions ($p_{\mathrm{T,jet}}$ and *shape*) and the matrices shown represent the shape response for the range 40 $\leq p_{\mathrm{T,jet}}^{\mathrm{ch}} <$ 60 GeV/c.

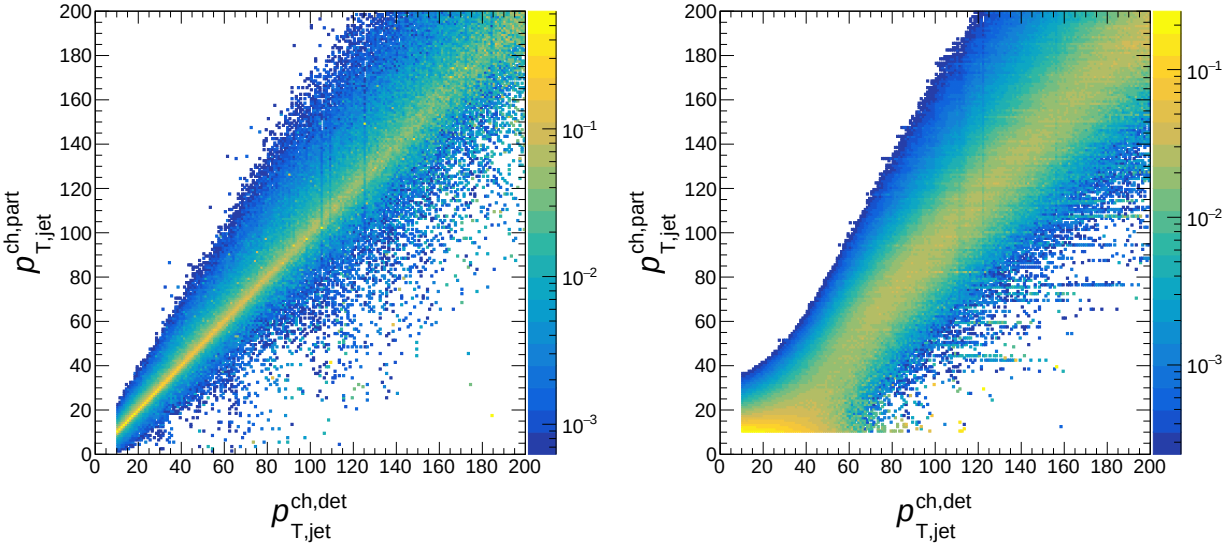

Figure 5.12: Detector (left) and embedding (right) response matrices for charged jet transverse momentum of jets generated using PYTHIA with detector effects modelled using GEANT 3.

5.4.2 Embedding

The response matrices for Pb–Pb collisions are constructed using an embedding procedure that replicates the effects of the underlying event on the jet population. The response matrix is constructed to map truth level simulations to the embedded level and PYTHIA jets are generated to perform this mapping. Jets identified in PYTHIA simulated events are passed through a simulation of the ALICE detector effects as with the pp response. A geometric matching is performed between the detector level jets and the truth level probes on an event by event basis. The detector level jets are then embedded into real Pb–Pb events selected from the 0–10% centrality interval - these combined events are referred to as *hybrid events*. A full jet finding is performed on the hybrid events and a geometric matching is again applied between the detector level and hybrid jets with the additional constraint that at least 50% of detector level $p_{\mathrm{T,jet}}^{\mathrm{ch}}$ is shared amongst the jet constituents that come from the PYTHIA embedded jet. By comparing the observables reconstructed from the sample of reconstructed

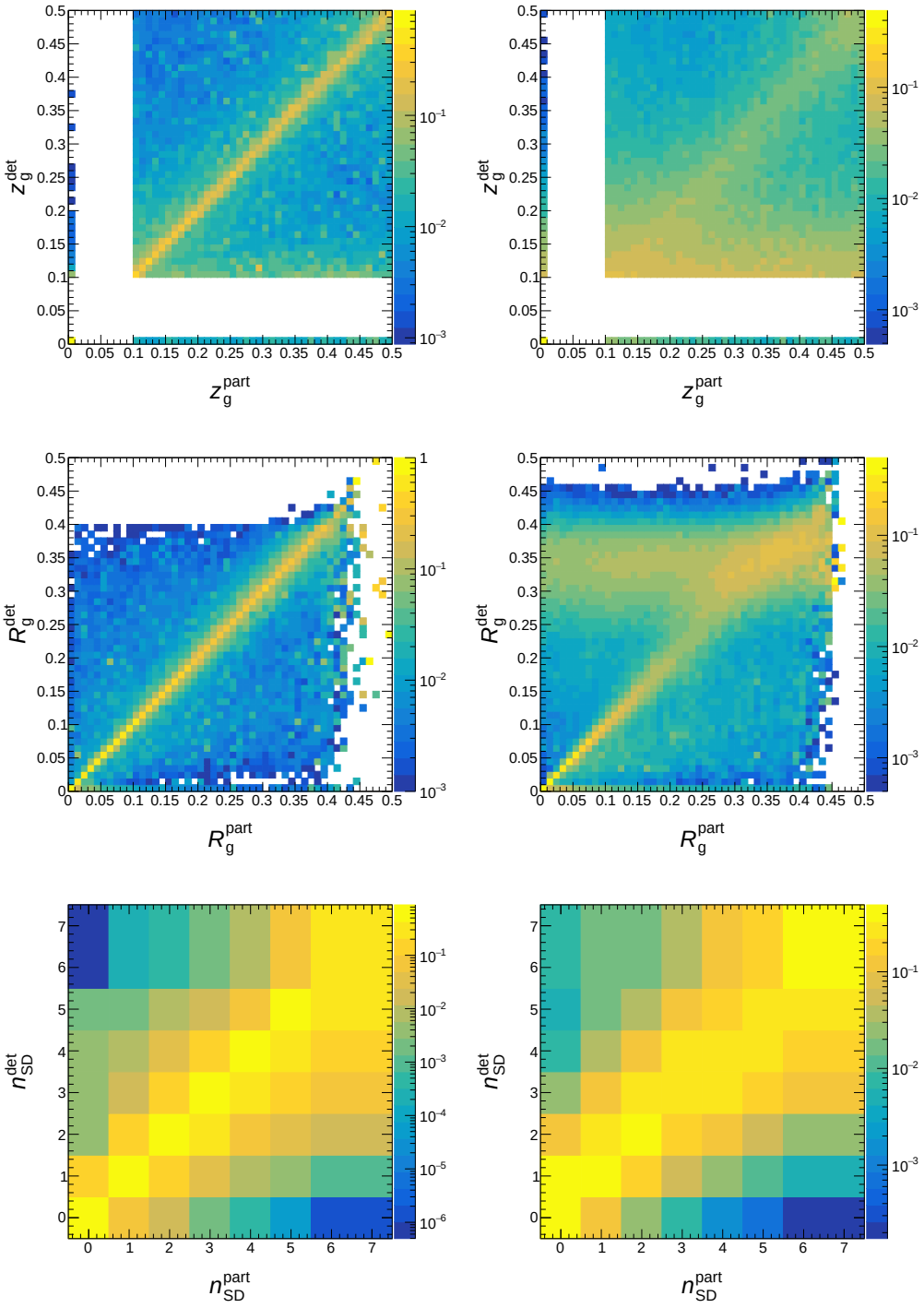

Figure 5.13: Detector (left) and embedding (right) response matrices for z_g, R_g and n_{SD} for jets generated using PYTHIA with detector effects modelled using GEANT 3.

embedded jets from the hybrid events to those for the truth level PYTHIA generated jets, one can construct multi-dimensional response matrices which characterise the modification of the jet observables due to the detector effects and background fluctuations arising from the underlying event.

5.4.3 Characterising the Response

The jet detector and background responses are used to quantify the Jet Energy Scale (JES) shift. The jet energy is modified by the detector inefficiencies and, for the case of Pb–Pb collisions, the presence of the underlying event fluctuations. Figure 5.14 shows the JES shift distribution due to detector effects for PYTHIA jets in three ranges of particle level jet transverse momentum. The distribution of JES shift is highly asymmetric because the efficiency of charged particle reconstruction dominates over any other detector effects leading to an average lower jet transverse momentum at detector level than particle level. To profile the JES shift in Pb–Pb collisions the detector level PYTHIA jets are embedded into real, central, Pb–Pb events. Figure 5.15 shows the distribution for embedded jets. It is clear that the distribution is much broader than in the case of detector effects only. The underlying event fluctuations can add a significant amount of transverse momentum to the jets that is not fully corrected for in the subtraction procedure. Due to the fluctuating nature of the underlying event it is also possible that the background subtraction procedure removes too much transverse momentum from the jets; this leads to the jets that have a negative energy scale shift. Figure 5.15 also shows how the width of the JES shift distribution changes as a function of $p_{\mathrm{T,jet}}^{\mathrm{ch}}$. At low jet transverse momentum, the background fluctuations dominate in the smearing of the jet energy while at high jet energies the detector effects dominate. This can be seen by the agreement in the width of the JES shift distribution in Fig. 5.15 (right) where the width for detector effects alone agrees with those from embedded jets at high particle level jet transverse momentum. The width of the JES shift distribution increases at

large $p_{\mathrm{T,jet}}^{\mathrm{ch,part}}$. This is because a high $p_{\mathrm{T,jet}}^{\mathrm{ch,part}}$ jet is more likely to contain a high p_{T} track, which means a larger shift in the JES is expected if this track is not reconstructed compared to a low p_{T} track. As the tracking efficiency is independent of the particle transverse momentum, it is expected that on average the fractional jet energy difference will be higher for larger $p_{\mathrm{T,jet}}^{\mathrm{ch,part}}$. In addition to this, the track momentum resolution is worse for tracks with large transverse momentum, this is due to difficulties in measuring the curvature in the applied magnetic field.

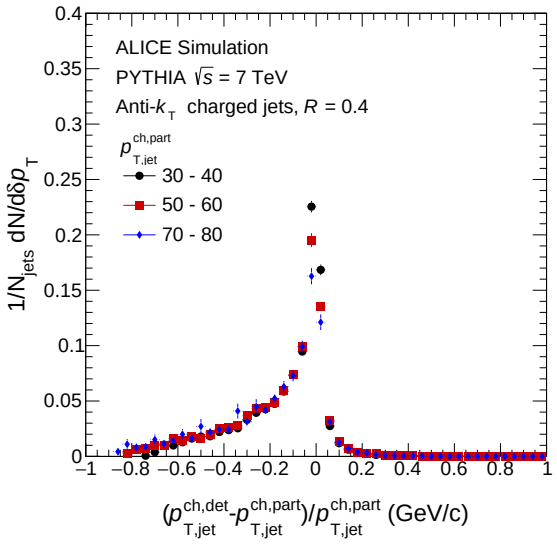

Figure 5.14: Jet energy shift for detector response of jets identified with anti-k_{T} clustering with $R = 0.4$ for a range of jet transverse momentum at particle level in simulated PYTHIA events at $\sqrt{s} = 7$ TeV.

The resolutions for the two jet shapes z_{g} and R_{g} are shown in Fig. 5.16. The distribution for n_{SD} is not shown because it takes integer values by definition so a continuous distribution of the residuals is not meaningful. The distributions for z_{g} and R_{g} in pp collisions show that there is strong correlation between the detector and particle level jet shapes; this agrees with the response matrices shown in Fig. 5.13. Comparing the two distributions one can observe that the resolution for the R_{g} observable is narrower and hence it is more robust to detector tracking efficiency effects. Figure 5.16 also shows the jet shape resolution distributions for

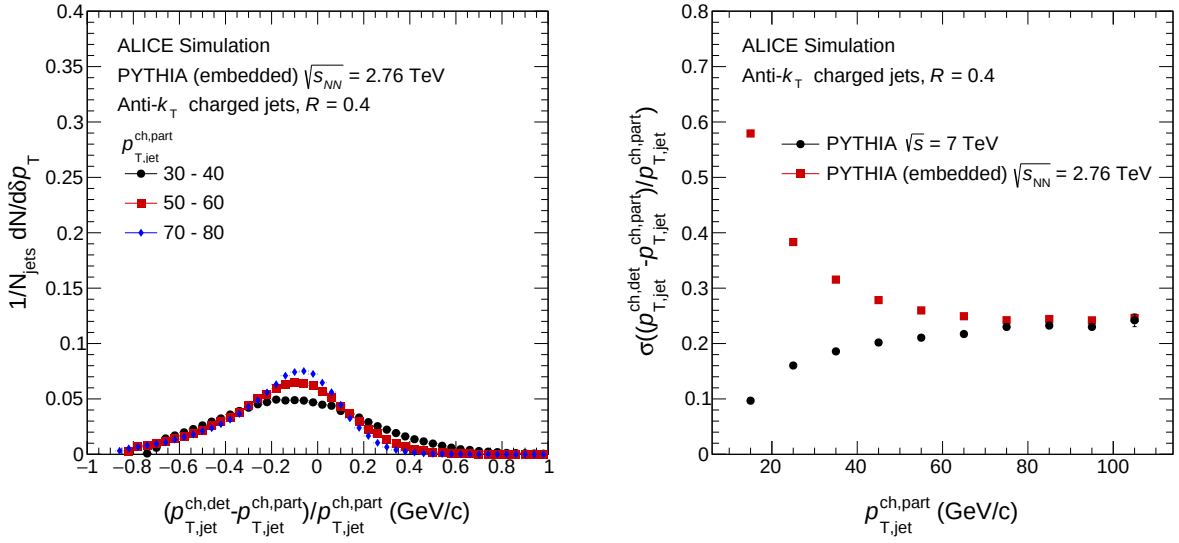

Figure 5.15: (left) Jet energy shift for detector and underlying event response of jets identified with anti$-k_{\mathrm{T}}$ clustering with $R = 0.4$ for a range of jet transverse momentum at particle level in PYTHIA+embedding events at $\sqrt{s_{\mathrm{NN}}} = 2.76$ TeV. (right) Average jet energy shift for full range of jet transverse momentum for detector only and detector + underlying event responses.

	pp	Pb–Pb
JES	$-17.19 \pm 0.19\%$	$-17.95 \pm 0.04\%$
z_{g}	$9.19 \pm 0.49\%$	$3.63 \pm 0.11\%$
R_{g}	$7.51 \pm 0.47\%$	$14.98 \pm 0.13\%$

Table 5.2: Average shift in observables due to underlying event and detector effects for jets in pp ($40 \leq p_{\mathrm{T,jet}}^{\mathrm{ch}} < 60$ GeV/c) and Pb–Pb ($80 \leq p_{\mathrm{T,jet}}^{\mathrm{ch}} < 120$ GeV/c) collisions.

Pb–Pb collisions where it can be seen that the resolution is much wider which is again what is seen in the response matrices in Fig. 5.13 where there are much stronger off diagonal components relative to the pp response matrices. The average shift in the JES as well as z_{g} and R_{g} are shown for pp and Pb–Pb collisions in Table 5.2. In the ranges studied in the two collisions systems the average JES shifts are very similar at approximately -17% whilst the observables z_{g} and R_{g} have more moderate average shifts of about 9% (3%) and 7% (15%) in pp (Pb–Pb) collisions respectively.

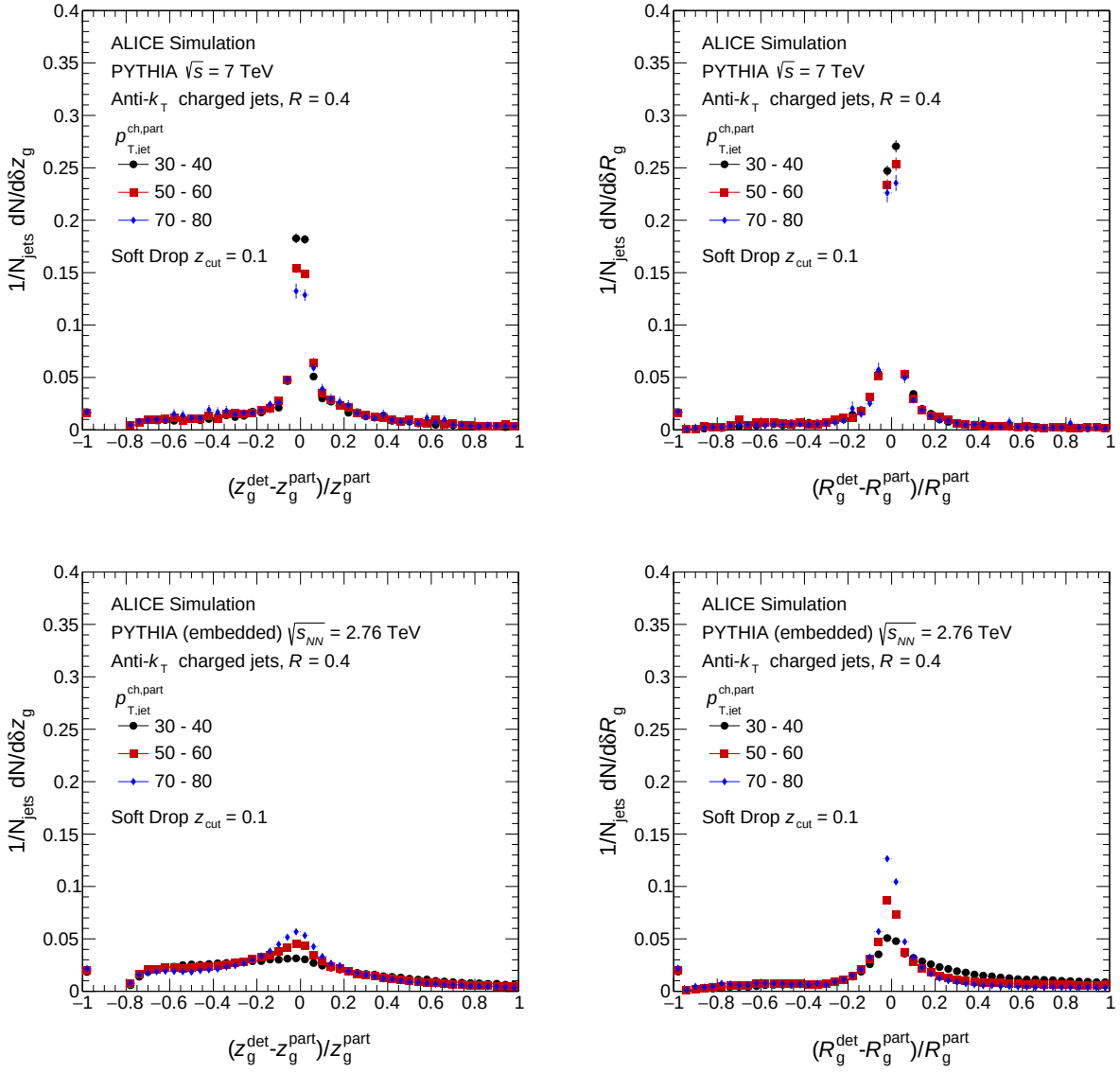

Figure 5.16: Jet shape resolution distributions for z_{g} and R_{g} for detector and underlying event response of PYTHIA jets identified with anti$-k_{\mathrm{T}}$ clustering with $R = 0.4$ for a range of jet transverse momentum at particle level.

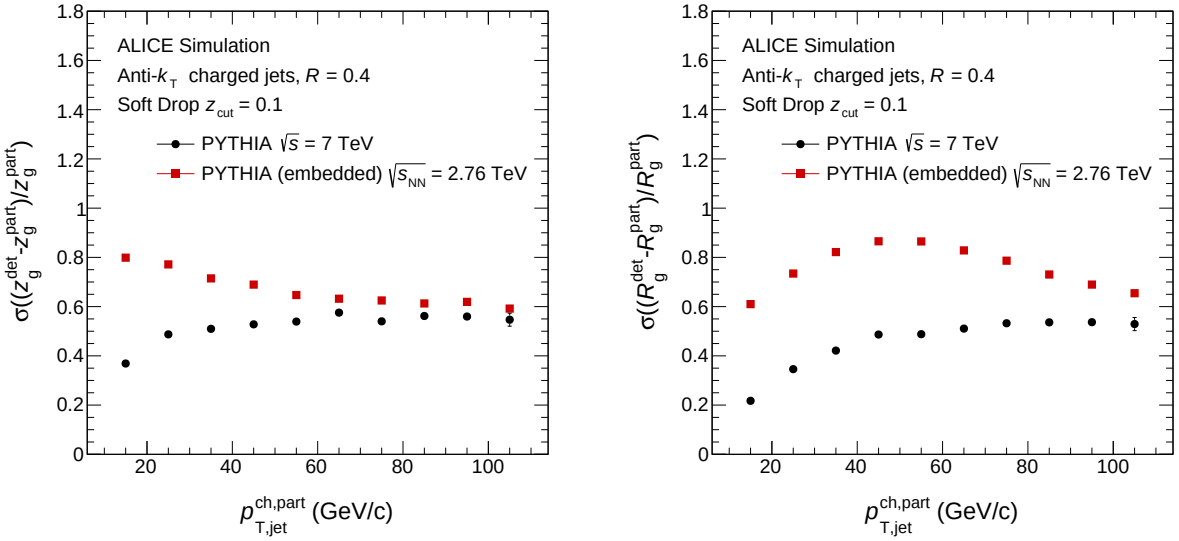

Figure 5.17: Average jet shape resolution of z_g and R_g in the full range of jet transverse momentum for jets reconstructed with anti$-k_T$ clustering with $R = 0.4$ from PYTHIA simulations with detector effects applied and embedded in central Pb–Pb events.

5.5 Raw Results

5.5.1 Lund Planes

Figure 5.18 shows the reconstructed Lund planes for jets reconstructed in pp and Pb–Pb collisions following the reconstruction procedures described above. These diagrams illustrate the first attempt to represent the phase space of intra-jet fragmentation using the Lund Plane prescription. It is clear from an initial consideration of the diagrams that binning has to be suitably broad to accommodate the limited statistics available in the current data sets. Significant differences are observed between the phase space diagrams for the two collision systems. The pp splittings look qualitatively very similar to the distributions shown in Section 3.1.2 which show the Lund Plane for PYTHIA simulated events. For Pb–Pb collisions, however, the phase space is populated in a very different way. The splittings appear to be localised much more to the left hand side of the diagram indicating that they are a lot broader. This is believed to be caused by the presence of the significant underlying

event in Pb–Pb collisions that is not possible to fully correct for. Figure 5.19 shows the Lund jet plane for PYTHIA jets embedded into real Pb–Pb events and it is clear that the density coverage is very similar to the Pb–Pb events which validates this assumption. The increase in splittings at large angles in Pb–Pb collisions is consistent with the effects seen in the R_{g} distributions shown in figure 5.20 where a large increase of splittings at large angles is observed in both Pb–Pb data and embedded PYTHIA relative to the vacuum reference distributions.

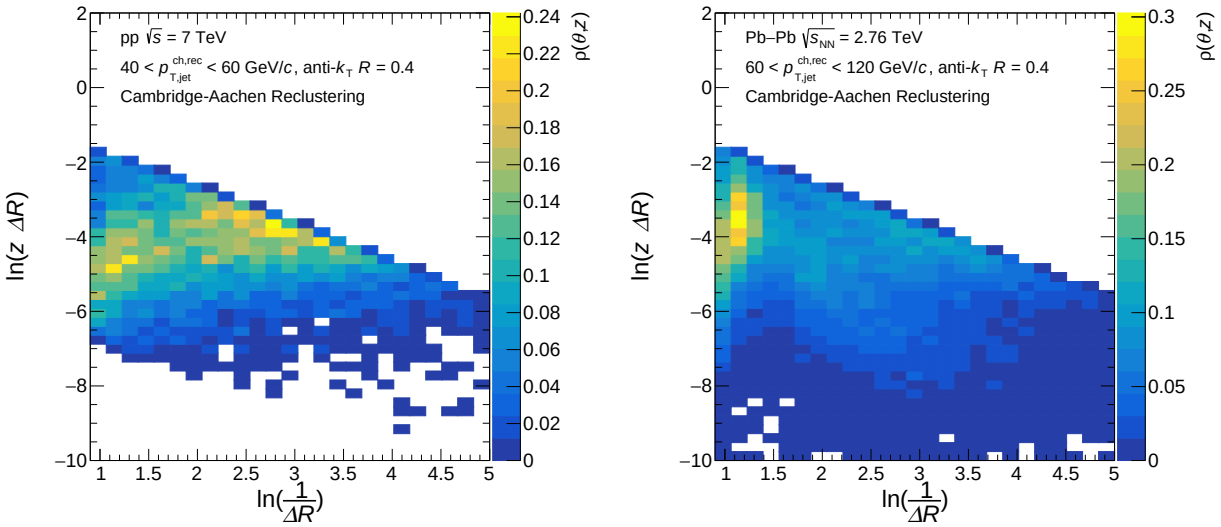

Figure 5.18: Lund planes populated with splittings identified with recursive declustering of jets in pp (left) and Pb–Pb (right) collisions at $\sqrt{s} = 7$ TeV and $\sqrt{s_{\mathrm{NN}}} = 2.76$ TeV respectively.

5.5.2 Jet Shapes

After identifying the population of jets to be analysed, the Soft Drop algorithm (section 3.1.3), is applied to calculate the two observables z_{g} and R_{g}. As previously discussed, these observables can be thought of as projections of the Lund Plane diagrams shown in Fig. 5.18. To measure the n_{SD} spectra, the grooming is iterated past the first splitting which satisfies the

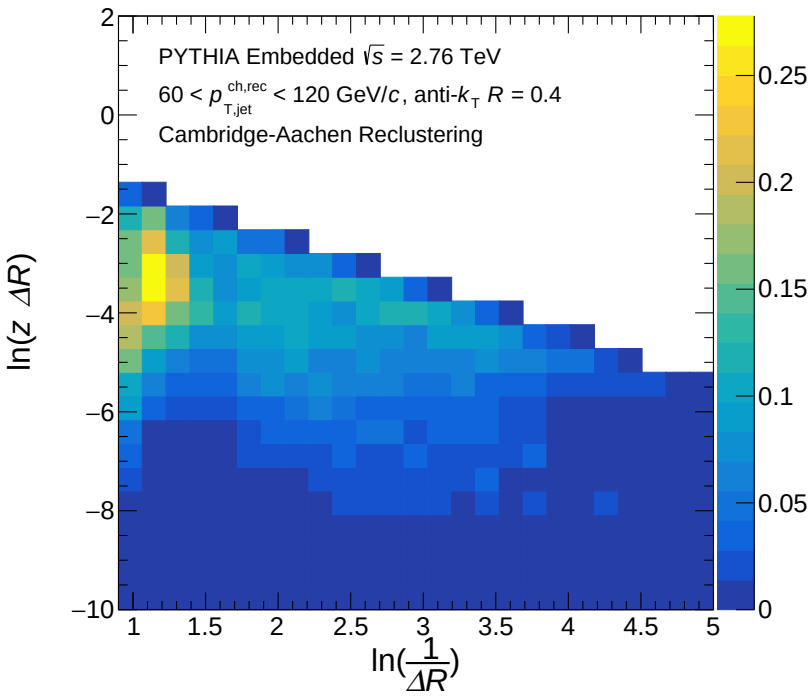

Figure 5.19: Lund plane for jets identified in PYTHIA simulated events at $\sqrt{s} = 2.76$ TeV embedded into real, $0-10\%$ centrality, Pb–Pb events.

grooming conditions in order to count the total number of hard splittings in the jet. The raw distributions for z_{g}, R_{g} and n_{SD} in the range $40 \leq p_{\mathrm{T,jet}}^{\mathrm{ch}} < 60$ GeV/c in pp collisions are shown in Fig. 5.20 (left) alongside the corresponding distributions for jets in the range $80 \leq p_{\mathrm{T,jet}}^{\mathrm{ch}} < 120$ GeV/c in Pb–Pb collisions (right). It can be seen from these figures that there are some differences in the shapes of the distributions between pp and Pb–Pb collisions, most notably in R_{g} where a "bump" arises in the distribution at large values. The fact that this feature is present in both the data and the embedded PYTHIA means that it can be concluded that it is induced by the presence of the underlying event. If it were a modification of the underlying jets then one would expect to see a significant difference between the data and the embedded PYTHIA distributions due to the fact that this behaviour is not observed in the PYTHIA jets in vacuum. It can also be seen that some differences are

observed between the pp data and the PYTHIA simulations for R_{g} and n_{SD}. However, these data are modified due to the detector effects of the ALICE detector system and hence must be corrected before being compared to simulation. This correction is performed using the Bayesian unfolding technique.

5.6 Bayesian Unfolding

In order to compare experimentally measured observables to predictions from phenomenological calculations, either the measured distributions have to be corrected to remove detector and background effects or the calculations have to be smeared by characterising the detector and background response. To correct the measured distributions a statistical approach can be taken and for measurements of pp data in this analysis the procedure used is Bayesian unfolding [181, 182] which is implemented using the RooUnfold framework [183]. The Bayesian unfolding procedure is based on Bayes' theorem which states that the probability of measuring a certain effect, E, due to a true cause, C_i, is given by

$$P(C_i|E_j) = \frac{P_0(E|C_i) \cdot P(C_i)}{\sum_{l=1}^{n_C} P_0(E_j|C_l) \cdot P(C_l)} \tag{5.2}$$

where $P(C_i)$ is the initial probability distribution of causes and the conditional probability of the $i-$th cause to produce the effect E is written as $P(E|C_i)$. Bayes' theorem can then be read as the probability that an observed effect is due to the $i-$th cause is proportional to the probability of that cause multiplied by the probability that the given cause produces the observed effect. $P(E|C_i)$ can be characterised by constructing a response matrix using detector simulations for the detector effect and an embedding procedure for the underlying event background; outlined in Section 5.4.1.

If one makes N_{obs} experimental observations then a distribution of effects is obtained, $n(E) \equiv \{n(E_1), n(E_2), ..., n(E_n)\}$. The expected number of events to be assigned to each

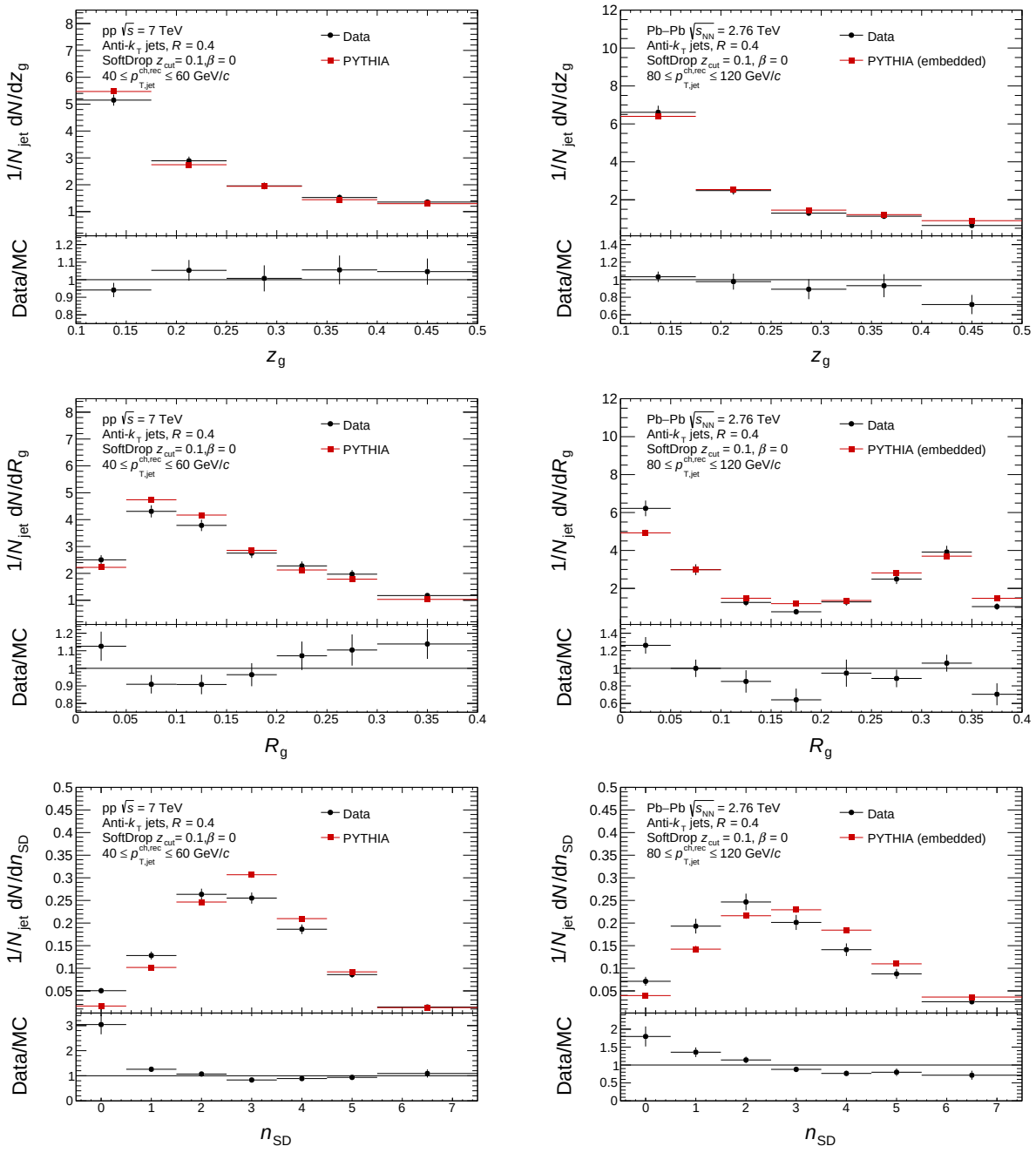

Figure 5.20: Raw distributions for z_{g}, R_{g} and n_{SD} for jets reconstructed in the transverse momentum range $40 \leq p_{\mathrm{T,jet}}^{\mathrm{ch}} < 60$ GeV/c in pp collisions at $\sqrt{s} = 7$ TeV (left) and $80 \leq p_{\mathrm{T,jet}}^{\mathrm{ch}} < 120$ GeV/c in Pb–Pb collisions at $\sqrt{s_{\mathrm{NN}}} = 2.76$ TeV (right) using the ALICE detector.

cause can then be calculated by using the conditional probability of the $j-$th effect, E_j, being caused by the $i-$th cause, $P(C_i|E_j)$, and summing over all observed effects:

$$\hat{n}(C_i) = \frac{1}{\epsilon_i} \sum_{j=1}^{n_E} n(E_j) \cdot P(C_i|E_j) \qquad \epsilon_i \neq 0 \tag{5.3}$$

where ϵ_i is the efficiency of detecting the cause C_i in any of the possible effects and $\hat{n}(C_i)$ is the distribution of the unfolded events. The final distribution, $\hat{P}(C)$, is obtained by simply normalising to the total number of true events, $\hat{N}_{true}$. The unfolded distribution will be somewhere between the initial distribution $P_0(C)$ and the true one and by proceeding iteratively one may be able to achieve convergence on the true distribution. The iterative procedure is applied as follows:

1. The a priori $P_0(C)$ distribution is chosen from best knowledge (in the case of this analysis using PYTHIA simulations)
2. Calculate $\hat{n}(C)$ from 5.3 and hence $\hat{P}(C)$
3. Compare $\hat{n}(C)$ and $n_0(C)$ and calculate a χ^2
4. Update $P_0(C)$ with the new unfolded distribution $\hat{P}(C)$ and $n_0(C)$ by $\hat{n}(C)$ and iterate again from step 2.

The number of iterations should be kept to as few as possible whilst minimising the differences between the true distribution and the unfolded one, so as to constrain the uncertainties induced by the unfolding procedure.

For the Pb–Pb analysis the unfolding procedure does not converge to a reliable and stable solution due to a combination of large off-diagonal elements in the response matrix and a lack of statistics in data. Therefore, the results are compared to an embedded vacuum reference and model comparisons are smeared using the same response that is constructed for unfolding - this process is described later in Section 5.7.

Statistics

Sufficient statistics are required in all bins used in the unfolding procedure in order to stabilise the process and produce a reliable unfolded distribution for comparison to particle level simulations or analytical calculations. The requirement that all bins in the two dimensions of shape and jet transverse momentum contain at least 10 counts is imposed and the binning is determined accordingly. The chosen binning boundaries are shown in Fig. 5.21 where the number of bin entries for each bin are shown. Note how the top right bin of the n_{SD} input statistics contains only 9 counts - this is not optimal but is accepted as binning in n_{SD} is very restricted and a single bin with fewer than 10 counts does not significantly effect the outcome of unfolding.

Ranges

The default raw data input ranges for unfolding are chosen as $0.0 \leq z_g^{rec} < 0.5$, $0.0 \leq R_g^{rec} < 0.4$ and $0 \leq n_{SD} < 8$ for the three shapes and all in the range $20 \leq p_{\mathrm{T,jet}}^{\mathrm{ch}} < 80$ GeV/c. At the unfolded level, the ranges are $0 \leq z_g^{part} < 0.5$, $0.0 \leq R_g^{part} < 0.4$ and $0 \leq n_{SD} < 8$ and $0 \leq p_{T,jet}^{part} < 160$ to allow for feed-in and feed-out.

Kinematic Efficiency Corrections

The cuts that are applied to the data must also be applied to the response matrix constructed to perform the unfolding. This means that the unfolding can successfully migrate counts within the detector level cut range as well as entries that exist outside the range at truth level and migrate into the range defined by the detector level cuts. The entries that cannot be corrected for are those that at truth level enter inside the detector level range but migrate outside due to detector effects as the response matrix does not contain the necessary information to do this. To overcome this, an efficiency correction is applied to the final unfolded distributions.

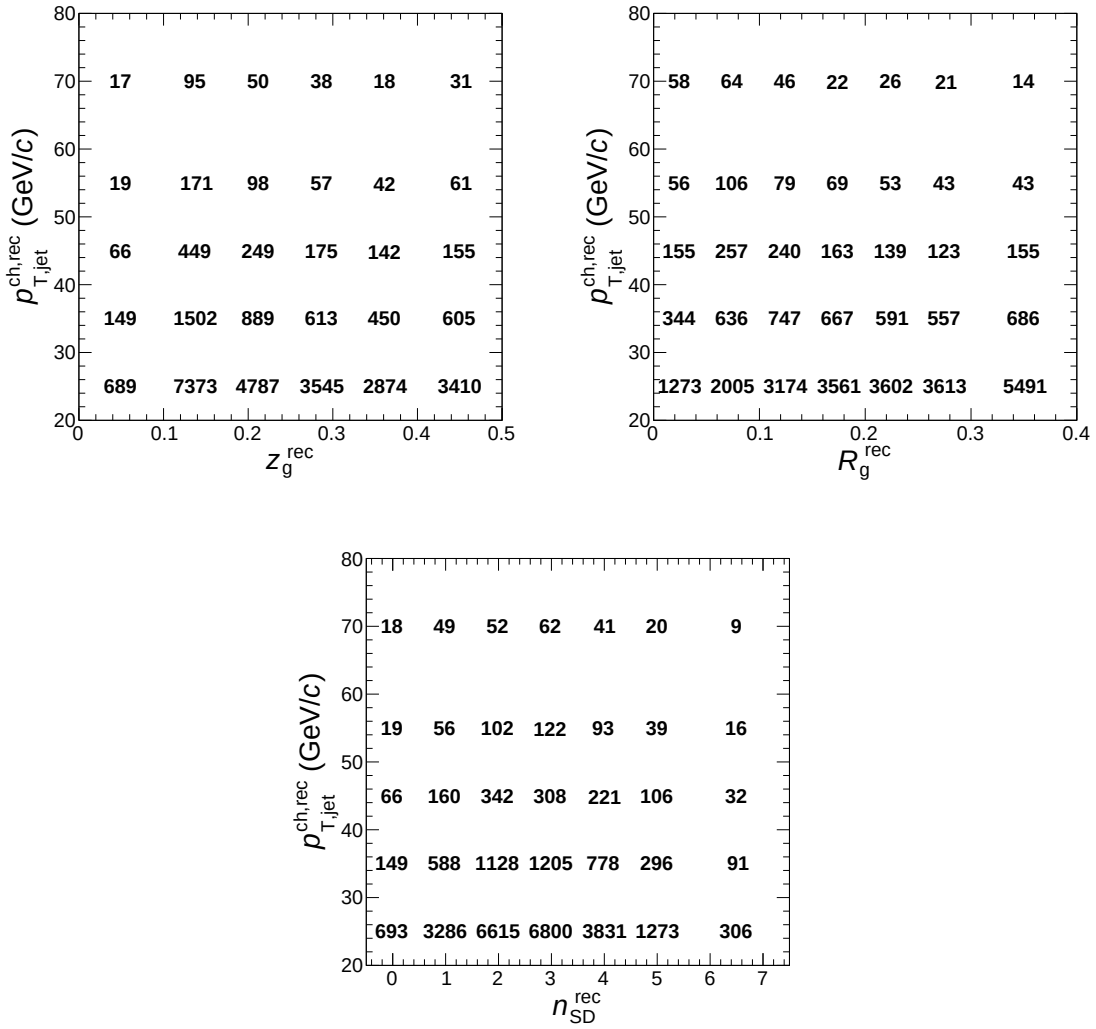

Figure 5.21: Statistics for input into unfolding of two dimensional measured distributions in shape and $p_{\mathrm{T,jet}}^{\mathrm{ch}}$ for z_{g}, R_{g} and n_{SD}.

In order to determine the kinematic efficiency corrections required to apply to the corrected distributions the raw input cuts applied to data are also applied to the detector level Monte Carlo simulations. The corresponding truth distributions with the cuts are then divided by the full truth distributions across the full range of the shape in bins of $p_{\mathrm{T,jet}}^{\mathrm{ch}}$. Figure 5.22 shows the resulting distributions after this scaling that are then used as the correction factors to apply to the corrected result. Note that this correction is purely MC-based

and thus should be kept as small as possible by reporting the unfolding range for which the correction is minimal in order to reduce potential biases. From Fig. 5.22, the range shown that requires the smallest correction whilst maintaining a good amount of statistics is $40 \leq p_{T,jet}^{part} < 60$ GeV/c. This range is therefore used as the reported transverse momentum interval for the corrected results in pp collisions throughout. Also note that the efficiency is rather flat versus the shape value. Since we are dealing with self-normalized observables, a flat efficiency correction has zero impact on the results. The efficiency correction at the boundaries can be very large as this is the region where detector smearing is most likely to migrate entries outside of the detector level range. This is very apparent in the efficiency corrections for the range $20 \leq p_{T,jet}^{part} < 40$ GeV/c where detector inefficiencies move a large number of jets to below the $p_{\mathrm{T,jet}}^{\mathrm{ch}} = 20$ GeV/c cut.

Unfolding Tests

The unfolding procedure is performed in iterations that should converge towards an agreeable solution. The number of iterations should be kept low enough so as be insensitive to any potential statistical fluctuations in the response but also high enough so as to not be too biased towards the shape of the unfolding prior. In order to choose an iteration for the final result the refolding tests and closure tests are considered. Figure 5.23 shows the unfolded results for z_{g}, R_{g} and n_{SD} for different iterations of unfolding. It is useful at this stage to study the unfolding iterations to ensure the solutions are not diverging in the latter iterations. The unfolded distributions show that the solution for all the observables is converging as one increases the iteration number.

Refolding Tests

A solution that is obtained using statistical unfolding from a well constructed response should be reversible if the procedure is sufficiently robust. In order to test this aspect of the unfold-

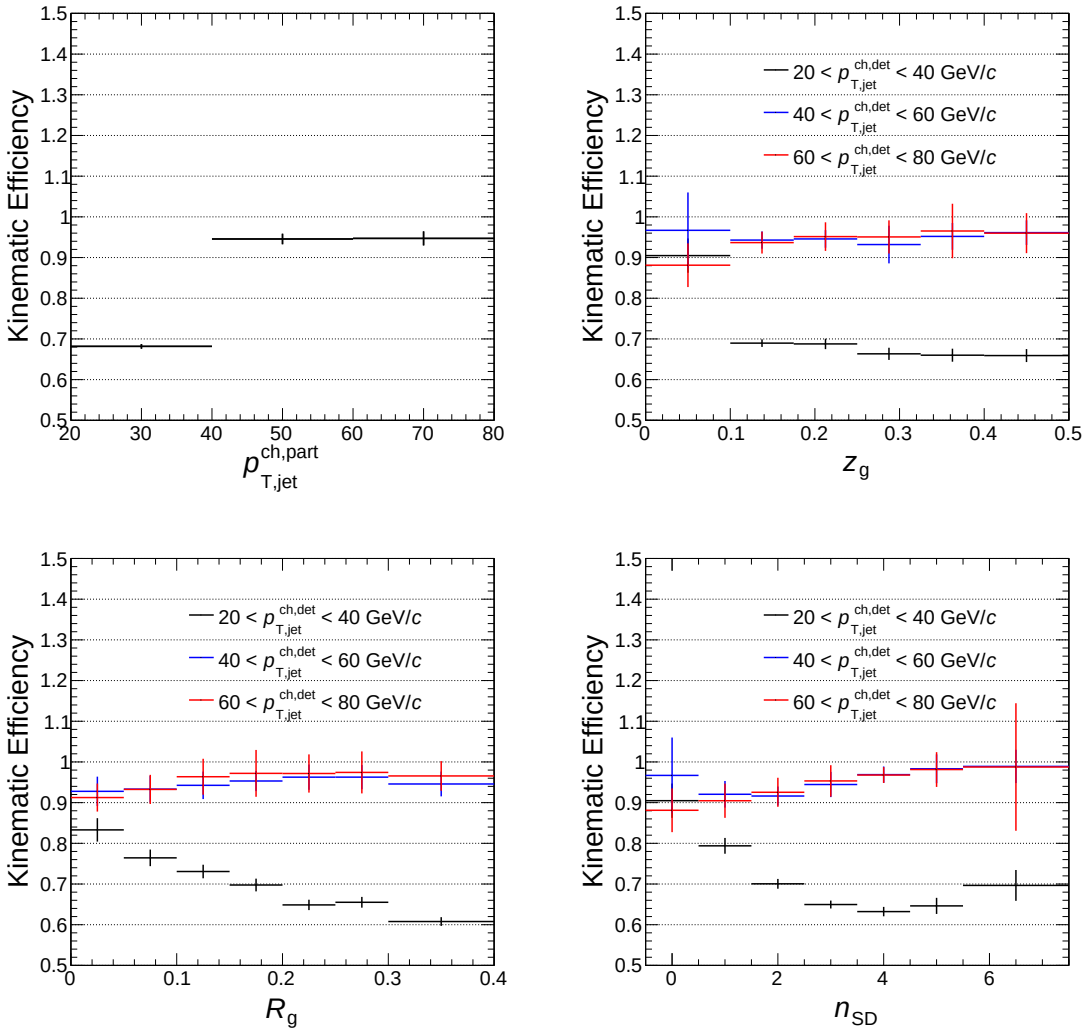

Figure 5.22: Kinematic efficiency correction factors to applied to unfolded solutions for $p_{\mathrm{T,jet}}^{\mathrm{ch}}$ spectrum (top left), z_{g} (top right) , R_{g} (bottom left) and n_{SD} (bottom right).

ing, refolding tests are performed. The refolding test is performed by taking the unfolded solutions and folding them back into the response matrix, the refolded distributions are then divided by the original input distribution. This test confirms whether the unfolding procedure is stable and not varying significantly due to statistical fluctuations in the response. In order to pass these tests the ratio distributions must be close to unity across the full data range. Figure 5.24 shows these folding tests for the pp response matrix used in the unfolding

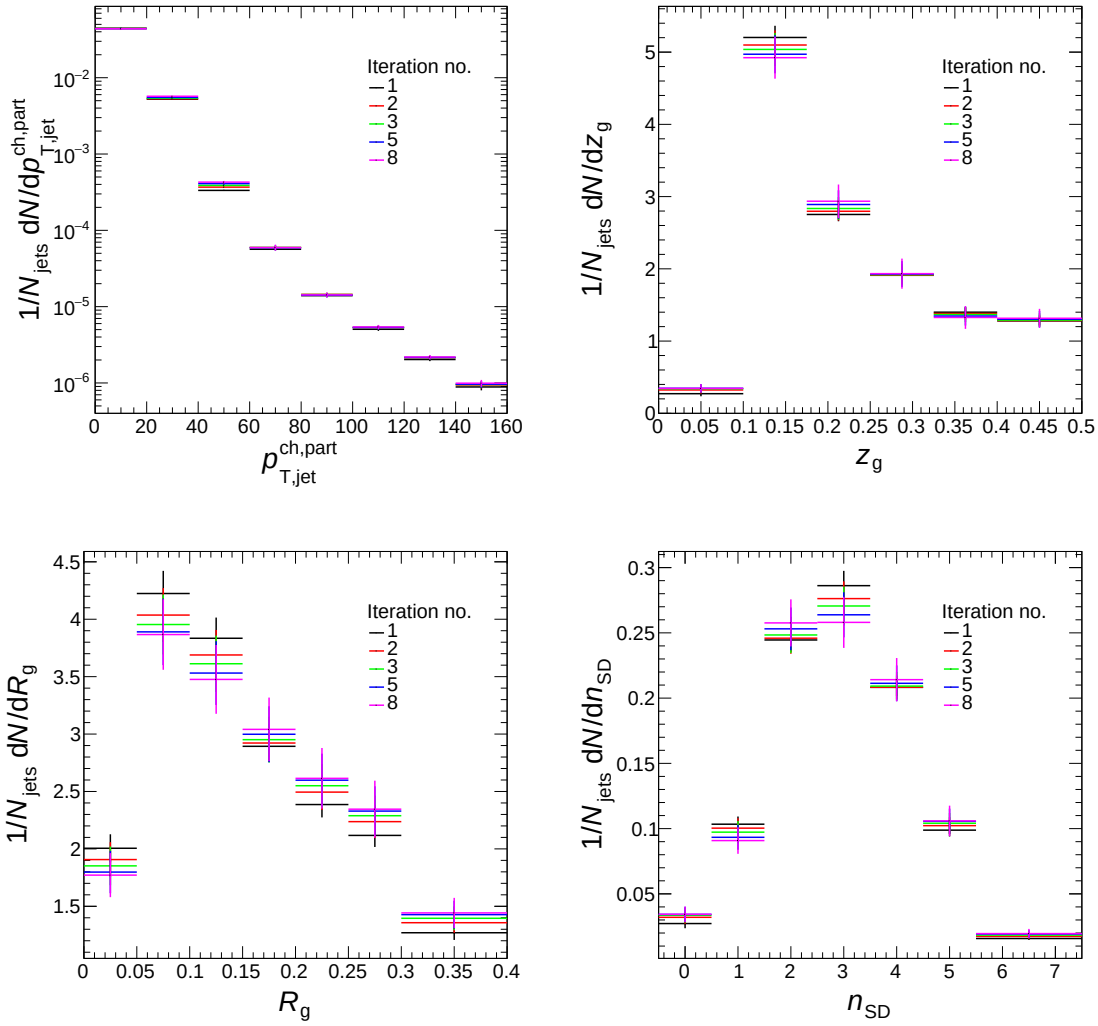

Figure 5.23: Unfolded distributions for $p_{\mathrm{T,jet}}^{\mathrm{ch}}$ spectrum (top left), z_{g} (top right), R_{g} (bottom left) and n_{SD} (bottom right) for $R = 0.4$ jets in pp collisions at $\sqrt{s} = 7$ TeV. For jet shape distributions, jets are selected in the range $40 \leq p_{\mathrm{T,jet}}^{\mathrm{ch}} < 60$ GeV/c.

procedure. It can be seen how the iterations quickly converge on unity after refolding and all iterations other than the first are within 10% across the full range of all shapes.

Closure Tests

In addition to testing the statistical stability of the unfolding, it is important to understand if the solution obtained is mathematically correct; in other words is the solution that the

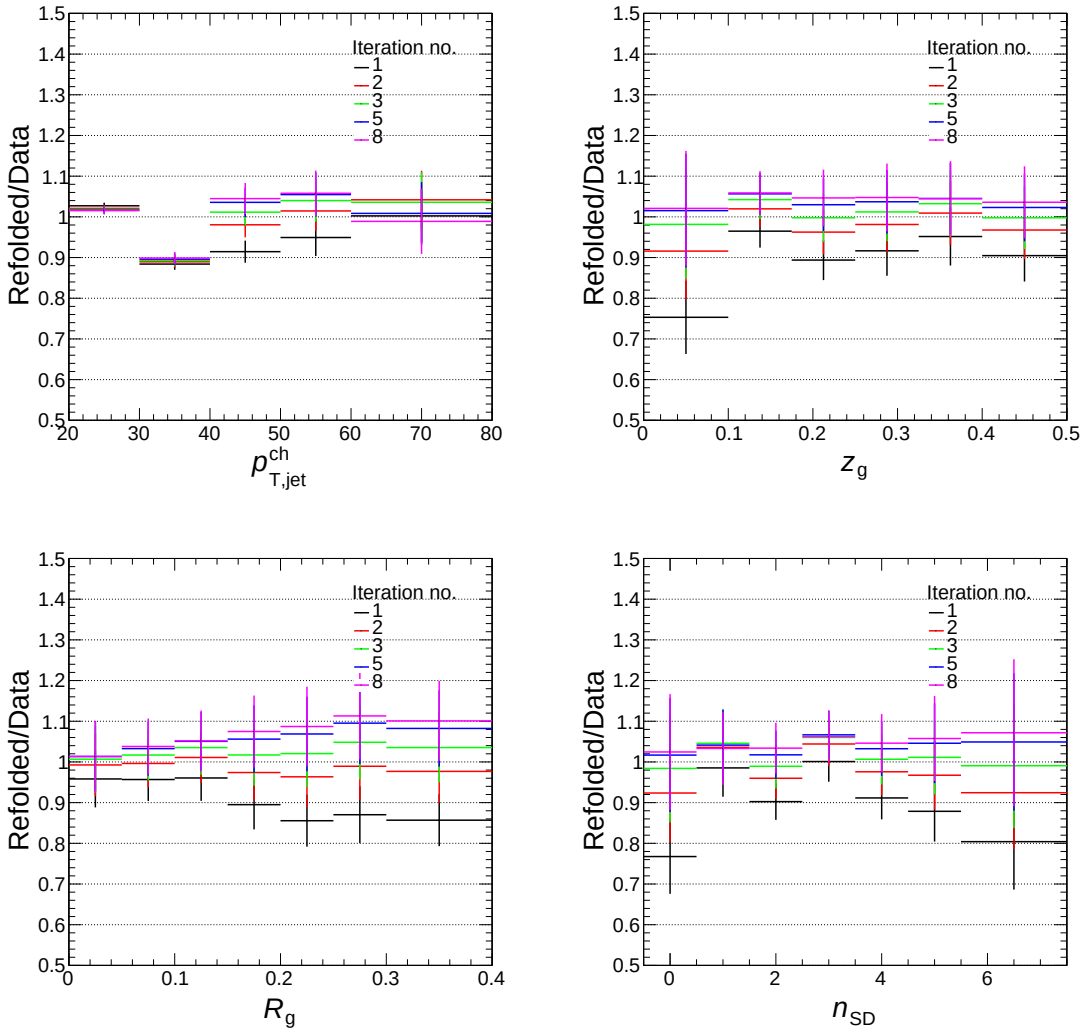

Figure 5.24: Refolding tests for $p_{\mathrm{T,jet}}^{\mathrm{ch}}$ spectrum (top left), z_{g} (top right), R_{g} (bottom left) and n_{SD} (bottom right) for $R = 0.4$ jets in pp collisions at $\sqrt{s} = 7$ TeV. For jet shape distributions, jets are selected in the range $40 \leq p_{\mathrm{T,jet}}^{\mathrm{ch}} < 60$ GeV/c.

unfolding converges on the correct one? To answer this question, a set of closure tests is performed. For the closure tests the Monte Carlo used to produce the response for unfolding is first divided into two sets; one set used as input to the unfolding (20%) while the remainder of the simulation is used to create the response as usual. The Monte Carlo input is then unfolded in the same way as the data and the ratio of the unfolded solution and the truth projection of the response is taken. If the unfolding process is converging on the correct solution then the

resulting ratio of the unfolded distribution and corresponding truth distributions should tend to unity. The closure tests were performed for each observable along with the corresponding $p_{\mathrm{T,jet}}^{\mathrm{ch}}$ closure test for each set of two dimensional solutions. The results of these closure test are shown in Figs. 5.25-5.27. It is shown that all three observables converge to within 10% of unity across their full range which indicates that the unfolding procedure is converging on the mathematically correct solution. The closure test for $p_{\mathrm{T,jet}}^{\mathrm{ch}}$ converges to within 20% in the range where input is provided ($20 \leq p_{\mathrm{T,jet}}^{\mathrm{ch}} < 80$ GeV/c) in all three cases which shows the solution is correct in both dimensions.

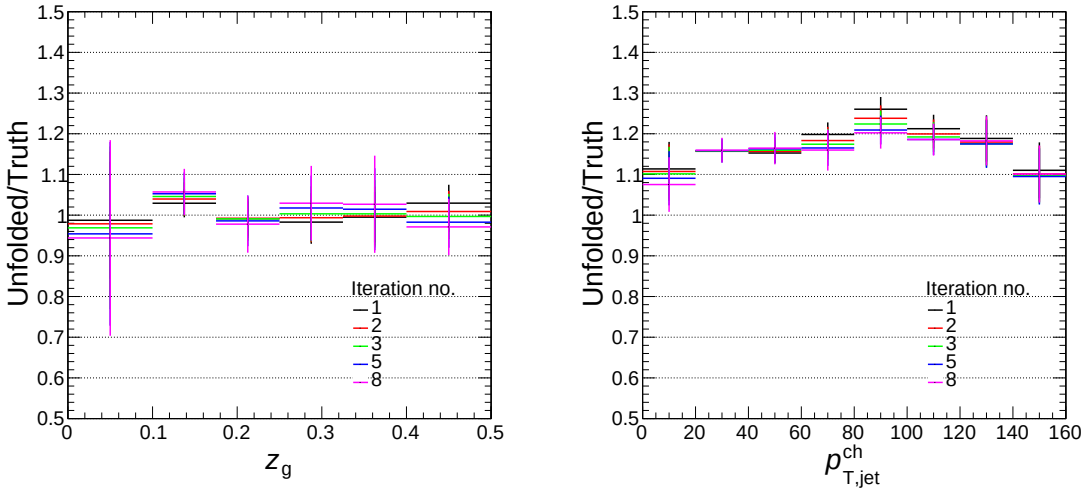

Figure 5.25: Closure tests in z_g and $p_{\mathrm{T,jet}}^{\mathrm{ch}}$for unfolding of z_g with pp data.

After performing the tests outlined in this section and studying the convergence of the solutions presented in Fig. 5.23 the iteration chosen as the final solution for each of the observables is shown in Table 5.3.

Correlation Matrices

A final check of the smoothness and stability of unfolding is to calculate the correlation between bins. Ideally in the iteration chosen for each solution we would like to see little correlation between far away bins. In order to quantify the correlation between bins the

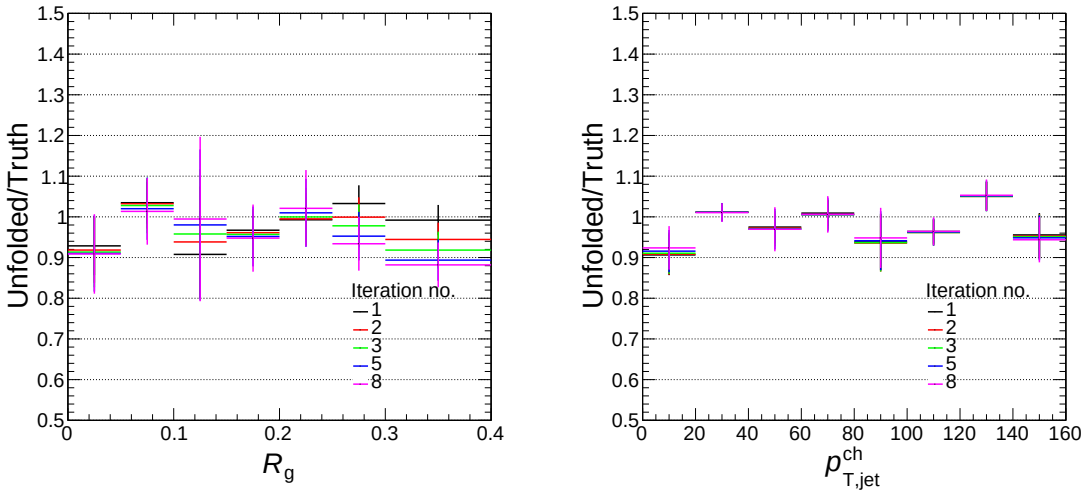

Figure 5.26: Closure tests in R_g and $p_{\mathrm{T,jet}}^{\mathrm{ch}}$for unfolding of R_g with pp data.

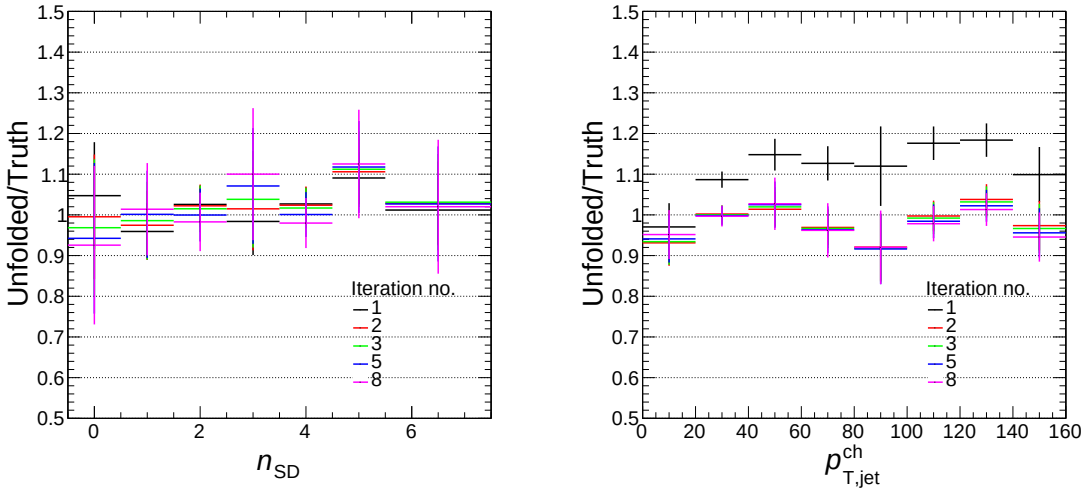

Figure 5.27: Closure tests in n_{SD} and $p_{\mathrm{T,jet}}^{\mathrm{ch}}$for unfolding of n_{SD} with pp data.

Shape	Iteration
z_{g}	4
R_{g}	5
n_{SD}	4

Table 5.3: Chosen unfolding iteration used for fully corrected measurement of z_{g}, R_{g} and n_{SD} in pp collisions at $\sqrt{s} = 7$ TeV.

Pearson correlation coefficients can be calculated bin-by-bin in both $p_{\mathrm{T,jet}}^{\mathrm{ch}}$ and shape. The Pearson coefficient is calculated as:

$$\rho_{X,Y} = \frac{\sigma_{X,Y}}{\sqrt{\sigma_{X,X}\sigma_{Y,Y}}}, \tag{5.4}$$

where $\sigma_{X,Y}$ is the covariance between, in general, two observables but in this case two bins of the same observable which is given by:

$$\sigma_{X,Y} = \frac{\sigma(x_i - \bar{x})(y_i - \bar{y})}{n-1}. \tag{5.5}$$

The resulting Pearson coefficient matrices for all three jet shapes are shown in Fig. 5.28. The Pearson coefficient matrices for the shapes have strong diagonal components. The corresponding matrix for $p_{\mathrm{T,jet}}^{\mathrm{ch}}$ shows that 40-60 GeV/c is the optimal bin to present the unfolding results as this is the bin with the smallest correlation with adjacent bins. Note that there is a strong correlation between bins in $p_{\mathrm{T,jet}}^{\mathrm{ch}}$ outside the range of data input. This can be explained by the resulting counts in these bins coming directly from the unfolding process itself making them all strongly correlated.

5.7 Folding

As previously mentioned, Bayesian unfolding could not be applied to the measurements in Pb–Pb because the procedure did not converge on a stable solution. This is caused by a combination of a lack of statistics and strong off diagonal elements in the response matrices. Therefore, in order to make a meaningful connection between the measurements and model predictions a folding approach is taken. This is essentially the reverse of the Bayesian unfolding of the data applied in pp, whereby the model predictions are smeared using the response matrices constructed from detector and embedding effects. Following the

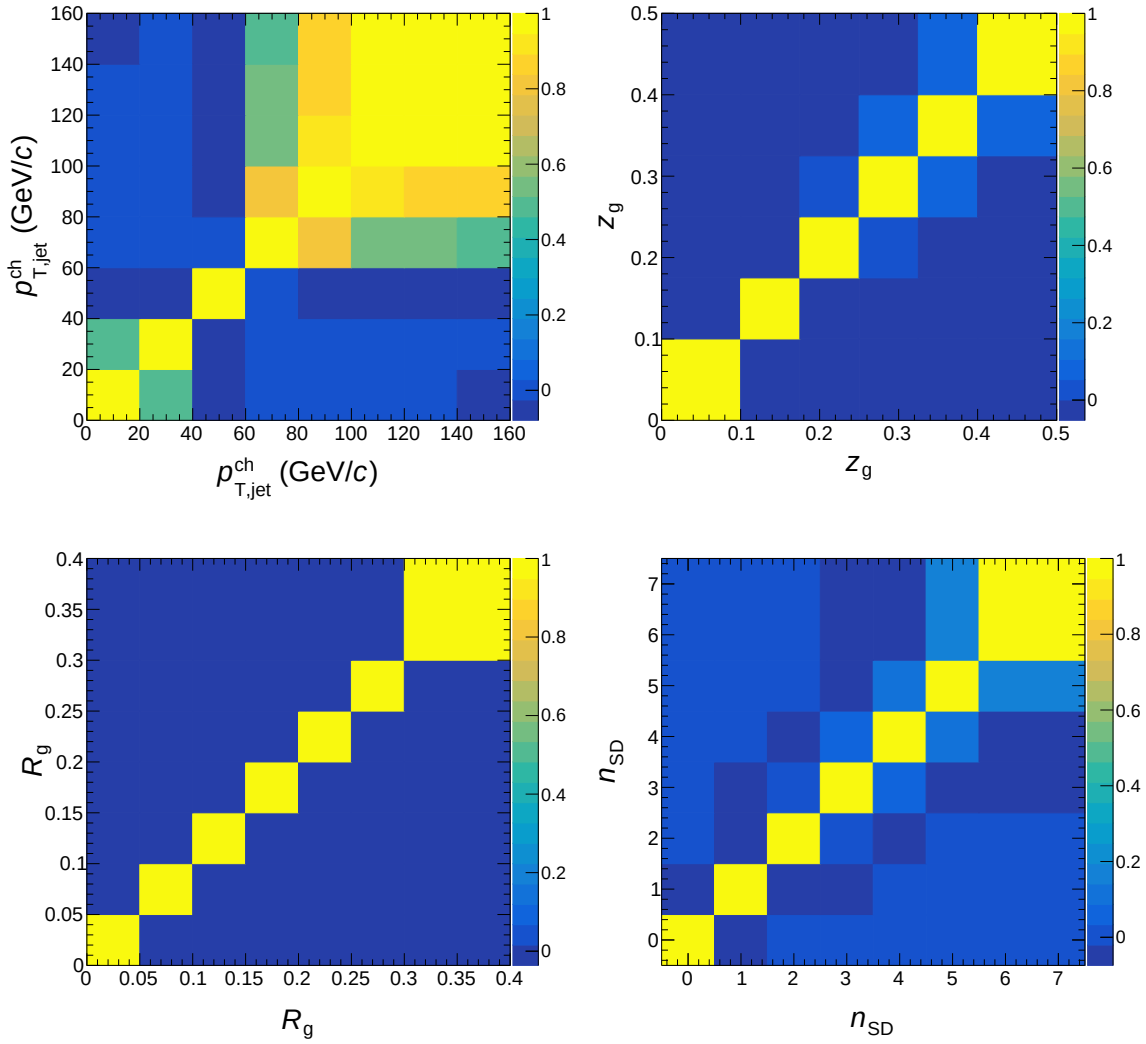

Figure 5.28: Pearson's coefficients for $p_{\mathrm{T,jet}}^{\mathrm{ch}}$, z_{g} (iteration 4), R_{g} (iteration 5) and n_{SD} (iteration 4) in the unfolded range of $40 \leq p_{\mathrm{T,jet}}^{\mathrm{ch}} < 60$ GeV/c.

embedding procedure outlined in Section 5.4.2, the response matrices shown in Fig. 5.13 were constructed. These response matrices show how the shapes are smeared in a selected range of $p_{\mathrm{T,jet}}^{\mathrm{ch}}$. In order to account for smearing in both shape and the significant smearing in $p_{\mathrm{T,jet}}^{\mathrm{ch}}$ that is expected from the presence of the underlying event a more complete matrix is required. This response is constructed by assigning a unique bin on each of the particle level and detector level axes $(part, det)$ for every two dimensional bin of $(p_{\mathrm{T,jet}}^{\mathrm{ch}}, shape)$ which

is then mapped to the corresponding bin on the other axis of the response. By constructing a response matrix this way it is possible to encode the information from a four dimensional response matrix in a simple two dimensional matrix.

In the case of z_{g}, the observable is studied differentially in R_{g} as well as $p_{\mathrm{T,jet}}^{\mathrm{ch}}$. Therefore, in order to replicate the detector level cuts applied on the data, the folding must be applied in three dimensions (z_{g}, R_{g}, $p_{\mathrm{T,jet}}^{\mathrm{ch}}$). The response matrix is constructed using the same simulations used to construct the Pb–Pb responses shown in Section 5.4.1. The entries are filled in a two dimensional matrix as with the two dimensional folding/unfolding with each bin corresponding to a unique bin in the six dimensional response. Once the two dimensional representation of the response matrix is constructed, it is normalised along the y-axis by:

$$C_{i,j} = \frac{c_{i,j}}{\sum_{j=1}^{N_x} c_{i,j}}, \tag{5.6}$$

where $C_{i,j}$ is the normalised bin content, $c_{i,j}$ is the bin content prior to normalisation and N_x is the number of bins along the x-axis of the response. The normalised response is then multiplied by the particle level distribution of the Monte-Carlo generator being smeared resulting in a smeared distribution in the three folded dimensions.

The effect of folding in three dimensions for JEWEL (with recoils) and Hybrid Model generations are shown in figures 5.29 and 5.30. It can be seen from these figures that the transverse momentum distribution is enhanced at low $p_{\mathrm{T,jet}}^{\mathrm{ch}}$ after smearing, an effect that is well understood to be due to the presence of combinatorial background. The other observables are varied slightly after smearing but the shape of the R_{g} distribution is modified in a particularly interesting way. The localised enhancement of splittings at large angles that was observed in the raw distribution of R_{g} in Pb–Pb collisions (Fig. 5.20) is also observed in the smeared model distributions. This is a reassuring confirmation that the folding procedure is incorporating the effects of the underlying event, that are encoded in the response matrix, on the smeared distributions.

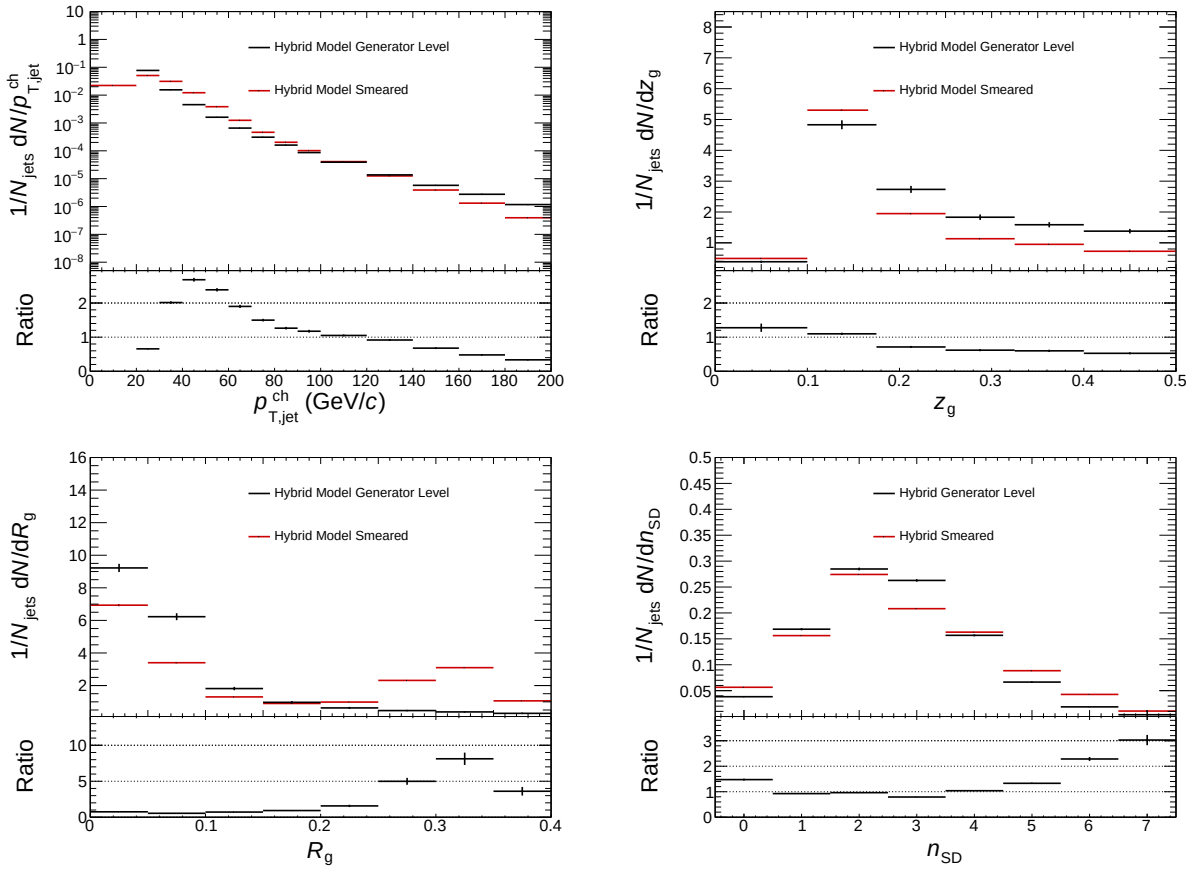

Figure 5.29: Effects of folding for Hybrid Model predictions of the $p_{\mathrm{T,jet}}^{\mathrm{ch}}$ spectrum and shape distributions for z_{g}, R_{g} and n_{SD} performed using a response matrix constructed from embedded PYTHIA jets.

5.8 Systematic Uncertainties

The systematic uncertainties attributed to the measurements are different for the two collision systems studied. For pp collisions the largest contribution to the uncertainties comes from selections made in the unfolding procedure, whilst in Pb–Pb collisions, where the jet sample is uncorrected, the systematic uncertainties arise from different sources.

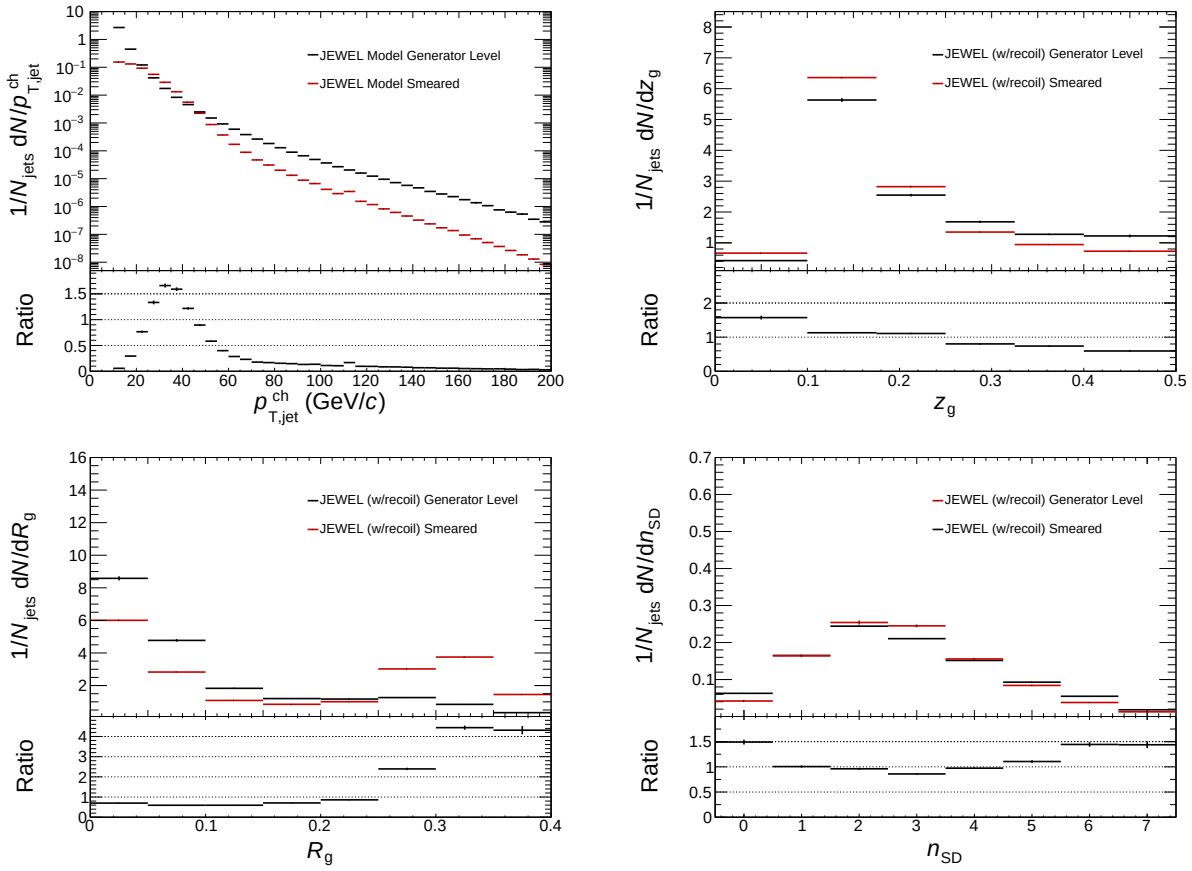

Figure 5.30: Effects of folding for JEWEL (with recoils) predictions of the $p_{\mathrm{T,jet}}^{\mathrm{ch}}$ spectrum and shape distributions for z_{g}, R_{g} and n_{SD} performed using a response matrix constructed from embedded PYTHIA jets.

5.8.1 pp

For pp collisions, the unfolding procedure introduces several sources of systematic uncertainty.

The following sources of systematic uncertainty are considered:

- Detector tracking efficiency uncertainty
- Number of iterations used in unfolding
- Variation of prior
- Variation of the unfolding range
- Modification of raw data binning

Tracking Efficiency Uncertainty

For the track selection applied to this analysis there is an uncertainty on the detector tracking efficiency of ±4%, determined by varying track quality cuts [145], which leads to an uncertainty on the jet energy scale. To estimate the uncertainty on the shape measurements due to the jet energy scale uncertainty of the ALICE detector, a response is produced by applying an artificial track rejection of 4%. The data are then unfolded using this new response and the deviation from the central values are taken as the systematic uncertainty. The calculated uncertainty is then symmetrised about the central values to reflect the fact that the efficiency may differ by 4% either side of the estimated value.

Choice of Iteration

The choice of iteration in the unfolding procedure is a relatively arbitrary selection and the senstivity to this choice is estimated by varying the iteration within the range where convergence is achieved. The default iterations chosen for z_g, R_g and n_{SD} unfolding were chosen to be $n_{iter} = 4$, $n_{iter} = 5$ and $n_{iter} = 4$, respectively. In order to measure the systematic uncertainty the unfolding was also performed with $n_{iter} \pm 2$. Again the deviation of these unfolded solutions from the central values above and below are taken. If the deviation from the two variations is in the same direction at any bin in shape then the variation with the greater deviation from the central value is taken and the other is ignored, otherwise the deviation either side of the central value is taken from the two contributing variations.

Unfolding Prior

The prior, i.e the a priori distribution used in the initial iteration of unfolding, was taken as the true distribution of the PYTHIA simulations used to construct the response matrix. In order to estimate the systematic uncertainty associated with unfolding prior a modification is applied by reweighting the response used in the unfolding procedure. The reweighting

Observable	Variation 1	Variation 2	Variation 3
z_{g}	$0.1 \leq z_{\mathrm{g}} \leq 0.5$	$10 \leq p_{\mathrm{T,jet}}^{\mathrm{ch}} < 80$ GeV/c	$20 \leq p_{\mathrm{T,jet}}^{\mathrm{ch}} < 90$ GeV/c
R_{g}	$0.0 \leq R_{\mathrm{g}} < 0.5$	$10 \leq p_{\mathrm{T,jet}}^{\mathrm{ch}} < 80$ GeV/c	$20 \leq p_{\mathrm{T,jet}}^{\mathrm{ch}} < 90$ GeV/c
n_{SD}	$0 \leq n_{\mathrm{SD}} < 9$	$10 \leq p_{\mathrm{T,jet}}^{\mathrm{ch}} < 80$ GeV/c	$20 \leq p_{\mathrm{T,jet}}^{\mathrm{ch}} < 90$ GeV/c

Table 5.4: Unfolding range modifications used to estimate the systematic uncertainty attributed to the ranges used in the unfolding procedure.

is estimated by taking the ratio of the 2-dimensionally unfolded data and the PYTHIA truth distribution. The result of this ratio is then applied to the event weight factor used when filling the detector response. This has the effect of modifying the shape of the prior distribution. Then the unfolding is performed using the new prior. The deviation of the new solution from the central values is taken as the uncertainty.

Unfolding Range

The default raw data input ranges for unfolding are chosen as $0.0 \leq z_{\mathrm{g}} < 0.5$, $0.0 \leq R_{\mathrm{g}} < 0.4$, $0.0 \leq n_{\mathrm{SD}} < 8$ for the three shapes and all in the range $20 \leq p_{\mathrm{T,jet}}^{\mathrm{ch}} < 80$ GeV/c. The sensitivity to these cuts is estimated by modifying the ranges as shown in Table 5.4. The unfolding is then performed with the varied cuts and compared to the default solutions. For each shape the variation with the biggest deviation from the default solution is taken.

Binning

Finally the choice of binning used to satisfy the statistics requirement has an effect on the unfolded solution. Therefore to test the uncertainty attributed to this selection the unfolding procedure is applied with the binning modified in the following ways:

- z_g Default binning: 0.1, 0.175, 0.25, 0.325, 0.4, 0.5
- z_g Modified binning: 0.1, 0.15, 0.2, 0.25, 0.3, 0.35, 0.4, 0.45, 0.5
- R_g Default binning: 0.0, 0.05, 0.1, 0.15, 0.2, 0.25, 0.3, 0.4

Shape	z_g		
Observable interval	0.1-0.175	0.25-0.325	0.4-0.5
Tracking	1.91%	0.21%	0.96%
Prior	$^{+0.00}_{-1.82}$%	$^{+0.63}_{-0.00}$%	$^{+1.63}_{-0.00}$%
Regularization	$^{+0.78}_{-0.55}$%	$^{+0.19}_{-0.25}$%	$^{+0.45}_{-0.49}$%
Truncation	$^{+2.17}_{-0.00}$%	$^{+1.83}_{-0.00}$%	$^{+2.36}_{-0.00}$%
Binning	0.54%	4.46%	1.25%
Total	$^{+3.05}_{-2.70}$%	$^{+4.87}_{-0.32}$%	$^{+3.05}_{-1.65}$%

Table 5.5: Relative systematic uncertainties on the measured jet shapes in pp collisions for three selected jet shape intervals in the jet $p_{\mathrm{T,jet}}^{\mathrm{ch}}$ range of 40–60 GeV/c.

- R_g Modified binning: 0.0, 0.1, 0.2, 0.3, 0.4

Note that there is no binning uncertainty associated with the n_{SD} measurement due to the integer nature of the observable.

Final Uncertainty

The contribution of each of the uncertainties is shown in figure 5.31 where the relative contributions can be seen compared together. To calculate the overall uncertainty the systematics are combined in quadrature. A summary of the systematic uncertainties for the pp results is also shown in Tables 5.5-5.7.

5.8.2 Pb–Pb

The systematic uncertainties for the Pb–Pb measurements are estimated using a different approach due to the fact that the results are presented at the uncorrected level and compared to a smeared PYTHIA ("vacuum") reference. For the Pb–Pb measurements, uncertainties are presented both on the data and the Monte Carlo simulations used for reference, unlike the pp systematic uncertainties which are evaluated entirely on the data. This is because the measurement in pp is compared directly to particle level simulations. In the Pb–Pb

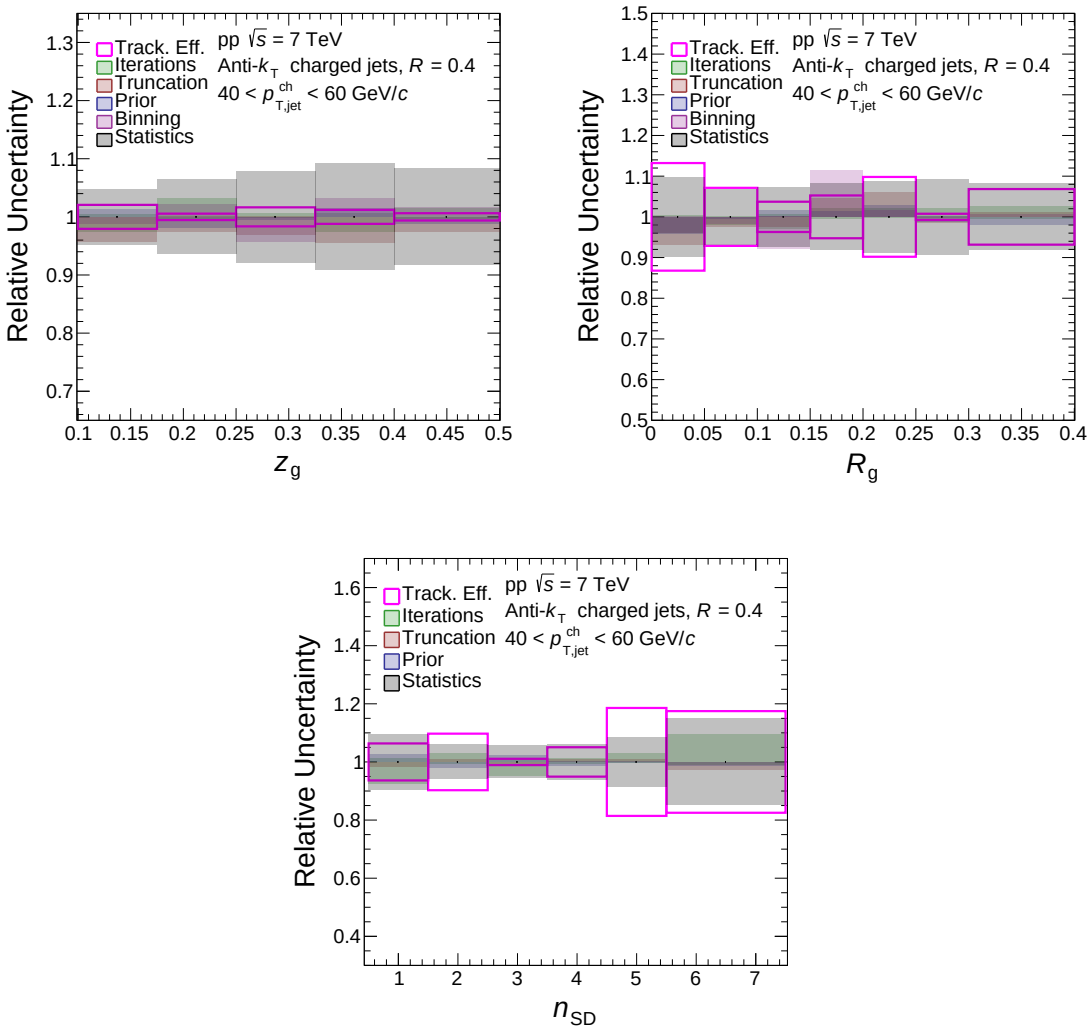

Figure 5.31: Components of the systematic uncertainties in pp.

measurements, the data are compared to a smeared approximation of the vacuum reference, the embedded PYTHIA distributions. These simulations have some small discrepancies when compared to the pp measurements and these differences are used to calculate a systematic uncertainty on the reference distributions. The systematic uncertainties on the Pb–Pb data and the reference are presented separately.

Shape	R_g		
Observable interval	0-0.05	0.15-0.2	0.3-0.4
Tracking	16.23%	7.64%	10.18%
Prior	$^{+4.33}_{-0.00}$%	$^{+0.00}_{-0.96}$%	$^{+0.65}_{-0.00}$%
Regularization	$^{+0.46}_{-0.29}$%	$^{+0.37}_{-0.46}$%	$^{+0.21}_{-0.33}$%
Truncation	$^{+6.78}_{-0.00}$%	$^{+0.00}_{-3.91}$%	$^{+0.00}_{-3.18}$%
Binning	3.81%	12.1%	0.02%
Total	$^{+18.51}_{-16.23}$%	$^{+7.65}_{-14.87}$%	$^{+10.21}_{-16.67}$%

Table 5.6: Relative systematic uncertainties on the measured jet shapes in pp collisions for three selected jet shape intervals in the jet $p_{\mathrm{T,jet}}^{\mathrm{ch}}$ range of 40–60 GeV/c.

Shape	n_{SD}		
Observable interval	0	3	6
Tracking	16.08%	1.15%	18.30%
Prior	$^{+0.68}_{-0.00}$%	$^{+0.00}_{-3.36}$%	$^{+3.35}_{-0.00}$%
Regularization	$^{+0.43}_{-1.43}$%	$^{+1.44}_{-1.09}$%	$^{+1.70}_{-2.98}$%
Truncation	$^{+0.0}_{-0.00}$%	$^{+0.00}_{-0.11}$%	$^{+4.37}_{-0.00}$%
Binning	N/A	N/A	N/A
Total	$^{+16.10}_{-16.15}$%	$^{+1.85}_{-3.72}$%	$^{+19.18}_{-18.54}$%

Table 5.7: Relative systematic uncertainties on the measured jet shapes in pp collisions for three selected jet shape intervals in the jet $p_{\mathrm{T,jet}}^{\mathrm{ch}}$ range of 40–60 GeV/c.

Tracking Efficiency

The first source of systematic uncertainty considered is, again, the jet energy scale uncertainty arising from variation of the tracking efficiency. To estimate the sensitivity to the jet energy scale uncertainty in Pb–Pb collisions, the cuts applied on the $p_{\mathrm{T,jet}}^{\mathrm{ch}}$ spectrum of the jet population are reduced by 4% and the deviations from the central values are symmetrised.

Angular Cut Resolution

Secondly, the Pb–Pb measurement of z_{g} is studied differentially in R_{g} in an attempt to scan the phase space as represented in the Lund Plane representation (see Section 3.1). To study differentially in the angular separation of the subjets a detector level cut of the aperture angle between the two reconstructed sub jets is applied. From Fig. 5.16, it can be seen that for embedded PYTHIA jets, the reconstruction of R_{g} has a resolution of about 10%. The sensitivity to this resolution is estimated by varying the cut on aperture angle of the splitting by 10%.

Vacuum Reference Discrepancy

Under ideal circumstances the vacuum reference would in fact be pp collisions of the same collision energy. In reality this is not possible with the current data available and so the measurements of z_{g}, R_{g} and n_{SD} in Pb–Pb collisions are compared to embedded PYTHIA simulations which are used as the vacuum reference. Whilst the results shown in Figs. 6.1-6.3 show a good agreement between the data and PYTHIA simulations, some discrepancies are apparent. The differences between the two distributions are taken and applied to the truth level via of the PYTHIA embedded simulations used in the Pb–Pb comparison by reweighting. The difference between the vacuum reference distributions with and without the reweighting is taken as the systematic uncertainty attributed to the discrepancy between pp data and Monte Carlo.

A summary of the systematic uncertainties for Pb–Pb collisions are shown in Tables 5.8 and 5.9.

Shape	z_{g}			z_{g} ($\Delta R > 0.1$)			z_{g} ($\Delta R > 0.2$)			z_{g} ($\Delta R < 0.1$)		
Shape interval	0.1-0.175	0.25-0.325	0.4-0.5	0.1-0.175	0.25-0.325	0.4-0.5	0.1-0.175	0.25-0.325	0.4-0.5	0.1-0.175	0.25-0.325	0.4-0.5
Data Systematics												
$p_{\mathrm{T,jet}}^{\mathrm{ch}}$ Resolution	1.15%	0.82%	6.30%	4.86%	2.77%	11.37%	6.32%	4.03%	13.65%	7.93%	0.90%	11.36%
ΔR Resolution	N/A	N/A	N/A	+2.27% −3.79%	+2.78% −0.00%	+10.00% −0.00 %	+1.90% −6.64%	+7.69% −3.85 %	+14.29% −0.00 %	+9.26% −5.56 %	+0.00% −2.44 %	+0.00% −2.86 %
Total Data	+1.15% −1.15 %	+0.82% −0.82 %	+6.30% −6.30 %	+5.37% −6.17 %	+3.92% −2.77 %	+15.14% −11.37 %	+6.60% −9.16 %	+8.68% −5.57 %	+19.76% −13.65 %	+12.19% −9.68 %	+0.90% −2.60 %	+11.36% −11.71 %
MC Systematics												
Reference	+3.55% −0.00 %	+2.02% −0.00 %	+0.00% −0.00 %	+0.00% −0.00 %	+12.41% −0.00 %	+10.08% −0.00 %	+18.06% −0.00 %	+24.92% −0.00 %	+29.41% −0.00 %	+0.00 % −14.81 %	+0.00 % −15.39 %	+0.00 % −12.40 %
Total MC	+3.55% −0.00 %	+2.02% −0.00 %	+0.00% −0.00 %	+0.00% −0.00 %	+12.41% −0.00 %	+10.08% −0.00 %	+18.06% −0.00 %	+24.92% −0.00 %	+29.41% −0.00 %	+0.00 % −14.81 %	+0.00 % −15.39 %	+0.00 % −12.40 %

Table 5.8: Relative systematic uncertainties on the measured jet shapes in Pb–Pb collisions for three selected jet shape intervals in the jet $p_{\mathrm{T,jet}}^{\mathrm{ch}}$ range of 80–120 GeV/c.

Shape	R_{g}			n_{SD}		
Observable interval	0.00-0.05	0.15-0.20	0.30-0.35	0	3	6
Tracking	9.52%	1.78%	13.92%	11.30%	7.82%	11.62%
Reference	$^{+0.36}_{-0.00}$%	$^{+0.00}_{-1.44}$%	$^{+0.00}_{-0.21}$%	$^{+30.09}_{-0.00}$%	$^{+0.00}_{-5.24}$%	$^{+5.30}_{-0.00}$%
Total	$^{+9.53}_{-9.52}$%	$^{+1.78}_{-2.51}$%	$^{+13.92}_{-13.92}$%	$^{+32.13}_{-11.30}$%	$^{+7.82}_{-8.14}$%	$^{+12.77}_{-11.62}$%

Table 5.9: Relative systematic uncertainties on R_{g} and n_{SD} in Pb-Pb collisions for three selected jet shape intervals in the jet $p_{\mathrm{T,jet}}^{\mathrm{ch}}$ range of 80–120 GeV/c.

Chapter 6

Results and Discussion

The aim of the previous chapter was to outline all of the analysis procedures employed to obtain a measurement for the three substructure observables, z_{g}, R_{g} and n_{SD}, in both pp and Pb–Pb collisions as well as certain relevant model predictions which are presented in this chapter. The substructure variables are described in detail in Section 3.2 and they relate to the momentum fraction (z_{g}) and opening angle (R_{g}) of the first hard splitting in the jet clustering history as well as the total number of such splittings that occur in the whole jet evolution (n_{SD}). In this section the final results are presented separately for pp and Pb–Pb. All measurements are performed on jets identified using the anti$-k_{\mathrm{T}}$ algorithm with a jet radius of $R = 0.4$. The Soft Drop grooming conditions used throughout are $z_{\mathrm{cut}} = 0.1$ and $\beta = 0$.

6.1 pp

For pp collisions, all measurements are made on unfolded jet samples in the range $40 \leq p_{\mathrm{T,jet}}^{\mathrm{ch}} < 60$ GeV/c in pp collisions at $\sqrt{s} = 7$ TeV measured with the ALICE detector. The measurements are compared to distributions obtained from both PYTHIA 6 and PYTHIA 8 simulations as well as PYTHIA + POWHEG jets which aim to model NLO effects.

6.1.1 Momentum Fraction z_{g}

Figure 6.1 shows the distribution for the momentum fraction of Soft Drop groomed jets, z_{g}, unfolded in the two dimensions of z_{g} and $p_{\mathrm{T,jet}}^{\mathrm{ch}}$ along with the corresponding model predictions. This plot shows how there is a higher probability of asymmetric splittings ($\sim$ 10/90% split of momentum) for the first hard splitting in the jet history. The lower panel displays the ratio of each of the Monte Carlo distributions to the data. The shaded box represents the systematic uncertainties on the measurement while the vertical error bars represent the statistical errors. A good agreement is observed between the unfolded data and all of the Monte Carlo distributions with all predictions agreeing with data within 10%. The distributions all, qualitatively at least, agree with the calculations from Ref. [152] made using first-principles QCD theory techniques.

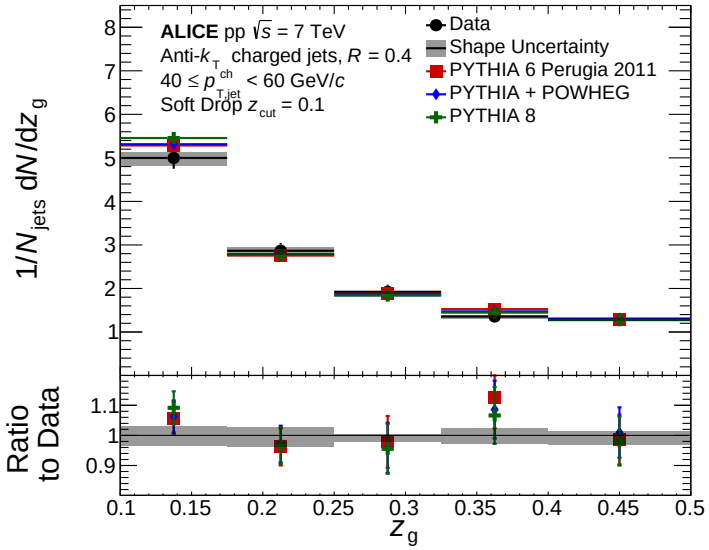

Figure 6.1: Fully corrected z_{g} distribution for $R = 0.4$ jets reconstructed in pp collisions at $\sqrt{s} = 7$ TeV using the ALICE detector in the range $40 \leq p_{\mathrm{T,jet}}^{\mathrm{ch}} < 60$ GeV/c with statistical and systematic uncertainties and compared to jets reconstructed from PYTHIA simulated events [1].

6.1.2 Groomed Radius R_{g}

The angular distribution of splittings identified with the Soft Drop algorithm, R_{g}, for pp collisions is shown in Fig. 6.2. In data, the distribution peaks at 0.05 – 0.1 before sharply falling off below 0.05. The steep fall off at the smallest values of R_{g}, corresponding to highly collimated splittings, also occurs in the Monte Carlo distributions. They continue to rise, however, and peak between 0.1 – 0.15. The first bin in this distribution also contains the small number of jets where no splitting was identified with Soft Drop. A full list of tagged rates (the fraction of jets with a splitting that satisfies Soft Drop) can be found in Table 6.1. The 0.1 – 0.15 bin has approximately a 20% disagreement between the central values of the data and all the Monte Carlo distributions, however after considering the combination of systematic and statistical uncertainties it is concluded that the distributions are consistent. The distribution of R_{g} is closely connected with the distribution of gluon radiation angles in the fragmentation process. This plot shows that the first hard gluon to be radiated in this process is more likely to at smaller angles with a decreasing probability for radiations up to $R_{\mathrm{g}} = 0.4$.

6.1.3 Number of Splittings n_{SD}

The final distribution for pp collisions is n_{SD} which is shown in Fig. 6.3. This constitutes the first measurement of n_{SD}, the total number of pairs of subjets in the clustering history with a momentum balance of $z_{\mathrm{g}} > 0.1$, for jets measured in pp collisions. This observable is closely related to the number of hard gluons that are radiated in the fragmentation part of jet production in vacuum. The distribution peaks at $n_{\mathrm{SD}} = 3$ and has a reasonably symmetric width with a slight skew to lower values of n_{SD}. Considering the ratio panel, which again displays the ratio of the Monte Carlo distributions to the data, it can be seen that the data and simulations agree well except at both extremes. The $n_{\mathrm{SD}} = 0$ bin represents jets where

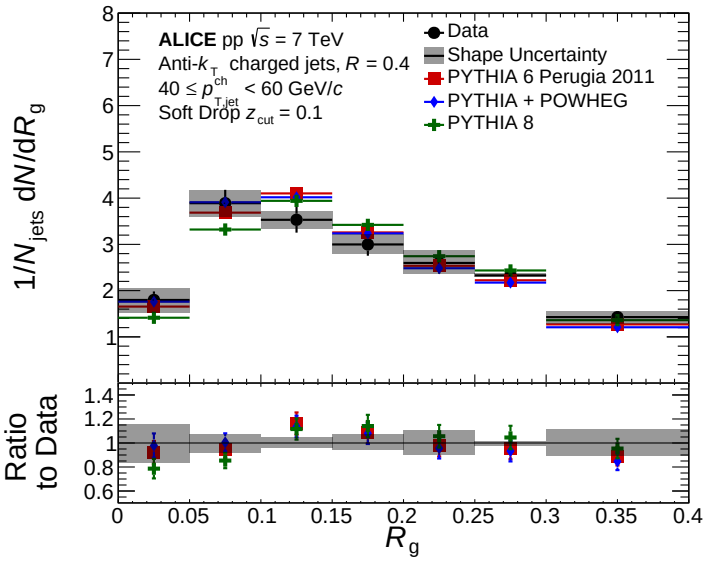

Figure 6.2: Fully corrected R_{g} distribution for $R = 0.4$ jets reconstructed in pp collisions at $\sqrt{s}$= 7 TeV using the ALICE detector in the range $40 \leq p_{\mathrm{T,jet}}^{\mathrm{ch}} < 60$ GeV/c with statistical and systematic uncertainties and compared to jets reconstructed from PYTHIA simulated events.

no splitting that satisfies Soft Drop is observed, this is a very small fraction of the overall jet sample (see Table 6.1). However, all of the simulations significantly underestimate the fraction of these untagged jets with the Monte Carlo generators all predicting less than 50% of the data. This disagreement between the models and the data indicates that the probability of zero semi-hard emissions in the jet evolution may not be particularly well modelled. This probability is closely related to the Sudakov Form Factor which is defined as the probability of emitting no resolvable radiation. A more detailed investigation into this zero emission probability is required before any reasonable conclusion may be drawn as to why there is such a disagreement. However, these first results offer an interesting new perspective on how these Monte Carlo generators model the evolution of the jet shower and how that compares to the data. At the other end of the scale, where $n_{\mathrm{SD}} \geq 6$, PYTHIA 6 predicts a lower rate than the data by about 30%. However, this disagreement is not observed when NLO effects are added to the PYTHIA parton shower using POWHEG or indeed when using PYTHIA 8

simulations.

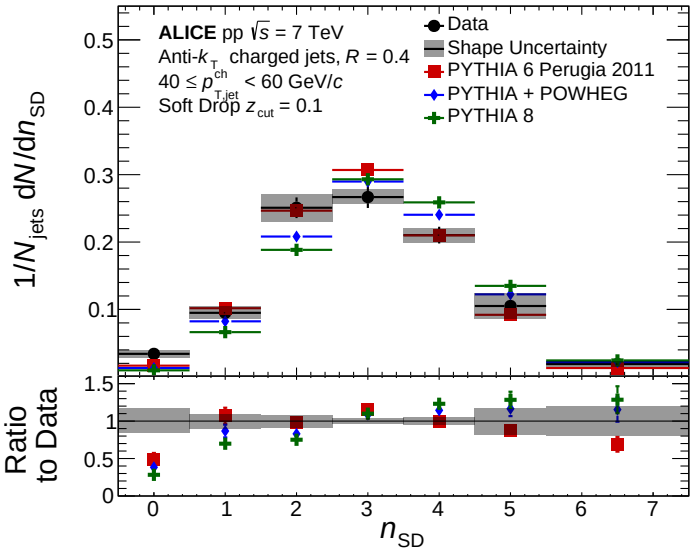

Figure 6.3: Fully corrected n_{SD} distribution for $R = 0.4$ jets reconstructed in pp collisions at $\sqrt{s} = 7$ TeV using the ALICE detector in the range $40 \leq p_{\mathrm{T,jet}}^{\mathrm{ch}} < 60$ GeV/c with statistical and systematic uncertainties and compared to jets reconstructed from PYTHIA simulated events [1].

6.2 Pb–Pb

The measurements in Pb–Pb are made on a constituent subtracted, uncorrected jet sample with comparisons made to smeared Monte Carlo predictions from JEWEL and the Hybrid Model with a PYTHIA embedded sample used as the vacuum reference. The pp distributions represent jets evolving in vacuum and the agreement observed between the pp data and PYTHIA simulations validate this approach. The measurements are made on jets reconstructed in the range $80 \leq p_{\mathrm{T,jet}}^{\mathrm{ch}} < 120$ GeV/c in Pb–Pb events from the 0–10% centrality interval in collisions at $\sqrt{s_{\mathrm{NN}}} = 2.76$ TeV. The $p_{\mathrm{T,jet}}^{\mathrm{ch}}$ range studied is chosen to reduce the contribution from combinatorial jets induced by the underlying event as discussed in Section 5.3.

6.2.1 Momentum Fraction z_{g}

The momentum fraction between two subjets identified using the Soft Drop grooming algorithm was studied differentially in opening angle for Pb–Pb. Figure 6.4 shows the distributions of z_{g} for 4 ranges in the opening angle with a cut on narrow separations ($\Delta R < 0.1$) shown on the left followed by an inclusive measurement ($\Delta R > 0.0$), then a cut that replicates that employed by CMS in Ref. [151] ($\Delta R > 0.1$) and finally a more extreme lower level cut ($\Delta R > 0.2$). These distributions represent the first differential measurement of z_{g} on the same jet population and demonstrate a clear dependence on the splitting opening angle. An important difference between the measurements shown in figure 6.4 and those of Refs. [151, 153] is that these distributions are all normalised by the total number of jets in the interval $80 \leq p_{\mathrm{T,jet}}^{\mathrm{ch}} < 120$ GeV/c (i.e all four curves are normalised by the same absolute value for each dataset) whereas previous measurements performed a self normalisation after applying additional cuts on the jet sample. The filled circles and shaded bands represent the data central values and systematic uncertainties, respectively, whilst the unfilled circles and hashed bands show the same for the embedded PYTHIA reference. The model predictions for JEWEL and the Hybrid model are shown as curves. All ratios are shown with respect to the PYTHIA reference where systematic uncertainties for the data are shown as shaded boxes and are the combination of the data and PYTHIA systematic uncertainties in quadrature. The systematic uncertainties on the model ratios are shown as the width of the curve and arise from the uncertainty in the PYTHIA distribution.

Starting from the inclusive measurement ($\Delta R > 0$) a significant suppression of the splittings is observed in the last bin ($0.4 \leq z_{\mathrm{g}} \leq 0.5$) of approximately 30% when comparing the data with the embedded PYTHIA. Both the smeared JEWEL and Hybrid predictions agree well with the embedded PYTHIA distributions and do not exhibit the same suppression of symmetric splittings ($z_{\mathrm{g}} \approx 0.5$) as the data. When the opening angle of the splittings are limited to $\Delta R > 0.1$ the modification observed is increased to around 60% in the last bin

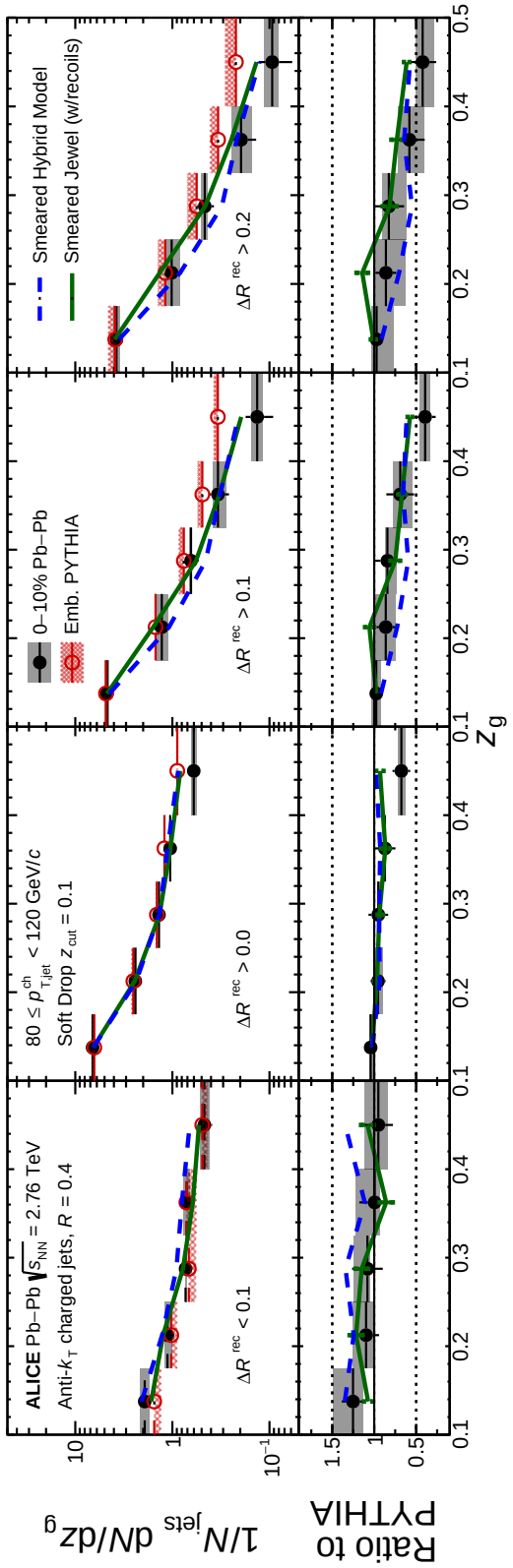

Figure 6.4: Distributions of z_g and corresponding ratios for Pb–Pb in the 0–10 % most central events and PYTHIA embedded jets in the range $80 \le p_{T,jet}^{ch} < 120$ GeV/c with several cuts on the splitting opening angle [1]. Comparisons to two jet quenching models JEWEL and the Hybrid Model are also shown as curves. Error bars represent statistical uncertainties on all distributions and the shaded and hashed areas in the top half of the plots represent the systematic uncertainties attributed to the data and PYTHIA reference respectively. Combined errors (in quadrature) in the ratio panel shown as shaded areas.

with a suppression also observed in the lower bins of z_{g} in data relative to the embedded PYTHIA. An important comparison to make at this stage is that all measurements of z_{g} are either consistent with the vacuum reference or suppressed. Because these distributions are not self normalised, as in previous analyses, their integrals are not the same and so an overall suppression across all bins can be observed. This is different from the behaviour observed in the measurement from Ref. [151] where the suppression of symmetric splittings was accompanied by a very slight enhancement of the most asymmetric (also most probable). By normalising by the total jet yield in the range of $p_{\mathrm{T,jet}}^{\mathrm{ch}}$ studied we see that in fact none of the splittings are enhanced at large angles and instead there is an overall suppression of jets in this region of phase space in data relative to the vacuum reference. Both of the model predictions show the same qualitative trend as the data, with more symmetric splittings ($z_{\mathrm{g}} \approx 0.5$) being suppressed. However, both models undervalue the level of suppression of the most symmetric splittings. Increasing the minimum opening angle to $\Delta R > 0.1$ does little to affect the shapes of the distributions or levels of suppression observed in the data and instead only seems to increase the errors as the statistics become more limited. In the narrow splitting angle limit ($\Delta R < 0.1$) the distributions of z_{g} in data are consistent with the PYTHIA reference within uncertainties. The JEWEL prediction also agrees with the vacuum distribution whilst the Hybrid model is consistently above the reference distribution.

Whilst one must take a cautious approach to drawing conclusions from such results, these measurements offer a unique and novel insight into the fragmentation process of jets in the presence of a colour charged medium. These measurements are in qualitative agreement with expectations from coherent and decoherent energy loss [154] where jets with a two pronged structure that is resolvable by the medium are expected to lose more energy and have their substructure modified relative to jets whose inner structure is not distinguishable and fragments as if in vacuum and loses energy to the medium as a single emitter. If the critical angle for the medium to resolve separate colour charges lies somewhere in the region

studied by these measurements this could offer an explanation for the differences observed in the collinear and wide angle limits respectively.

The role of the jet induced medium recoil is expected to enhance the probability of low z_{g} splittings as it promotes splittings that would initially fall below the Soft Drop threshold ($z_{\mathrm{cut}} = 0.1$) to just above and hence "push up" the low z_{g} bins. This effect is expected to occur mostly at large angles as there is an increased area assigned to the subleading prong and hence a higher chance of capturing more medium recoil - these effects have a similar effect on the observables as the uncorrelated background from the underlying event. The medium recoil is modelled in JEWEL which agrees with the data for z_{g} at large angles ($\Delta R > 0.1$) although it is believed that the effects of the uncorrelated underlying event dominate over those of the correlated medium recoil.

6.2.2 Groomed Radius R_{g}

Figure 6.5 shows the angular distribution of the subjets identified using the Soft Drop grooming algorithm, R_{g}, for Pb–Pb collisions in the centrality interval 0–10% at $\sqrt{s_{\mathrm{NN}}} = 2.76$ TeV. Overall the distribution exhibits two characteristics, a high probability of very collinear splittings (low R_{g}) which falls quickly towards larger values of R_{g} and a second peak in probability at large angles ($0.2 \leq R_{\mathrm{g}} < 0.4$) induced by the underlying event - this can be concluded from the fact it arises for PYTHIA jets once they have been embedded into the Pb–Pb events. This measurement shows that the most collimated splittings ($R_{\mathrm{g}} < 0.05$) appear to be enhanced in data relative to the embedded PYTHIA distribution, this is consistent with the slight enhancement across all bins of z_{g} observed in the $\Delta R < 0.1$ limit. This observation suggests that collinear radiation of gluons may be slightly enhanced in medium relative to vacuum. Splittings at angles larger than $R_{\mathrm{g}} = 0.1$ are generally suppressed relative to the vacuum reference, behaviour that is reproduced by both JEWEL and the Hybrid Model predictions. The enhancement of large angle splittings due to the underlying event is an effect that is

replicated in the model predictions after smearing with JEWEL predicting a larger number of splittings in this region which is expected due to the modelling of the correlated medium recoil.

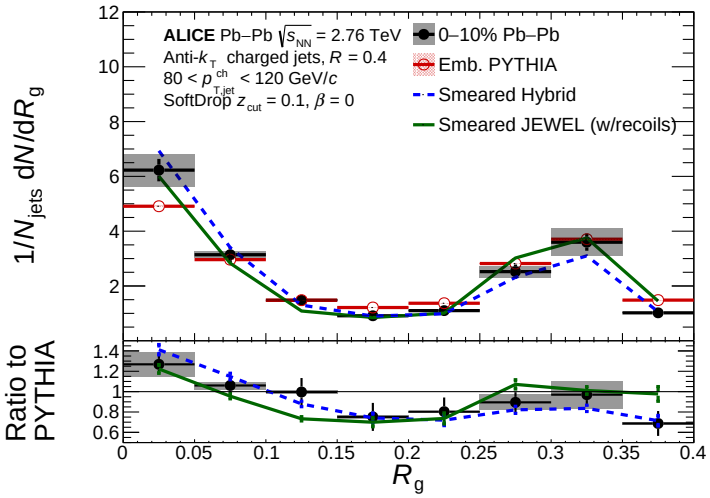

Figure 6.5: Distribution of R_g and corresponding ratios for Pb–Pb in the 0–10 % most central events and PYTHIA embedded jets in the range $80 \leq p_{T,jet}^{ch} < 120$ GeV/c with comparisons to two jet quenching models, JEWEL and the Hybrid model.

6.2.3 Number of Splittings n_{SD}

The distribution for the number of hard splittings in the iteratively declustered tree for jets in Pb–Pb collisions is shown in Fig. 6.6. The readers attention is first drawn to how the distribution for central Pb–Pb collisions is shifted to lower values of n_{SD} relative to the distribution for pp collisions shown in Fig. 6.3. The distribution in data is also shifted to lower values relative to the embedded PYTHIA reference with a significant increase in the number of untagged jets ($n_{SD} = 0$) and jets with one hard splitting and a suppression of jets with a large number of hard splittings. The data distribution is much better reproduced by the embedded PYTHIA distribution when only jets originating from initial quarks are considered - this is consistent with other findings of jet substructure [71]. Quark jets are expected to radiate fewer gluons and produce more collimated jets than gluon initiated jets [184] due to

their lower gluon emission probability which is proportional to the associated colour factor for gluon emission ($C_F = 4/3$ for quarks and $C_A = 3$ for gluons). Within errors the jet energy loss models JEWEL and the Hybrid model better reproduce the data compared to the embedded PYTHIA.

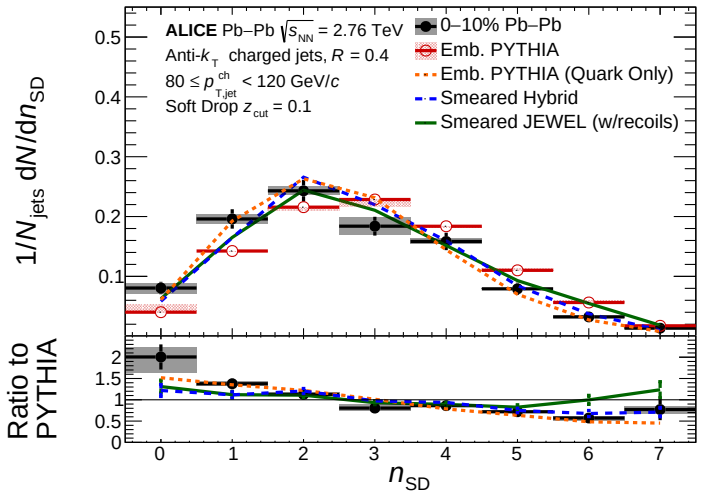

Figure 6.6: Distribution of n_{SD} and corresponding ratios for Pb–Pb in the 0–10 % most central events and PYTHIA embedded jets in the range $80 \le p_{\mathrm{T,jet}}^{\mathrm{ch}} < 120$ GeV/c with comparisons to two jet quenching models JEWEL and the Hybrid model [1].

	Tagged rate				
Dataset	Pb–Pb				pp
Angular Cut	$\Delta R < 0.1$	$\Delta R > 0.0$	$\Delta R > 0.1$	$\Delta R > 0.2$	$\Delta R > 0.0$
Data	$38.4 \pm 2.3(2.5)\%$	$92.1 \pm 3.5(0.9)\%$	$53.6 \pm 2.7(3.4)\%$	$41.8 \pm 2.4(3.6)\%$	$97.3 \pm 3.0(1.7)\%$
PYTHIA	34.6%	95.5%	60.2%	46.9%	98.6%
Hybrid	47.5%	93.4%	45.8%	35.0%	N/A
JEWEL	42.0%	93.0%	51.0%	40.0%	N/A

Table 6.1: Fraction of jets that pass the soft drop condition $z_{\text{cut}} = 0.1$ and $\beta = 0$ in the specified range of angular separation and in the transverse momentum range $40 \leq p_{\text{T,jet}}^{\text{ch}} < 60\,\text{GeV}/c$ for pp collisions and $80 \leq p_{\text{T,jet}}^{\text{ch}} < 120\,\text{GeV}/c$ for Pb–Pb collisions. Uncertainties on the data are written as statistical(systematic).

Conclusion

It has long been known that jets and high$-p_{\mathrm{T}}$ particles are suppressed in Pb–Pb collisions relative to pp and p-Pb collisions. It is commonly understood that this suppression occurs due to energy loss induced by the presence of a strongly-interacting, colour charge deconfined medium of quarks and gluons, the QGP. Despite this long held knowledge, the mechanisms by which a high energy particle traversing a QGP loses energy to the medium is far from well understood. Recently, the attention of both the experimental and theoretical communities has shifted to studying jets in a way that may shed a light on this elusive part of physics.

A novel approach to studying jet substructure using recursive declustering techniques in an attempt to access information about the partonic showering of jets in the presence of a colour deconfined medium has been presented. This approach, starting from a "map" in the kinematic phase space of splittings that occur in the jet evolution and selecting regions using grooming techniques, has been applied to data from pp and Pb–Pb collisions measured by the ALICE collaboration at $\sqrt{s} = 7$ TeV and $\sqrt{s_{\mathrm{NN}}} = 2.76$ TeV, respectively.

In pp collisions, the data have been presented in the range $40 \leq p_{\mathrm{T,jet}}^{\mathrm{ch}} < 60$ GeV/c using a jet clustering radius $R = 0.4$ with detector and background effects corrected for using the Bayesian unfolding procedure. The measurements are compared to model predictions from PYTHIA 6.4 and PYTHIA 8 as well as PYTHIA 6.4 with NLO calculations applied using the POWHEG method.

In the measurement of z_{g}, shown in Fig. 6.1, a steeply falling distribution is observed with

a good agreement between the data and predictions from Monte Carlo generators. The distribution for PYTHIA 8 has been shown in other work to be in agreement with first principle QCD calculations based on the DGLAP evolution equations [152]. The measurement of the angular distribution of the subjets resulting from the hard splittings of the jet, R_{g}, shown in Fig. 6.2, was also presented and a good agreement was observed between the data and generator predictions. The agreement observed between data, Monte Carlo and analytical prediction suggests that the features of jet fragmentation are reasonably well understood (at least in vacuum).

The first measurement of the number of hard splittings n_{SD} in the whole partonic shower of the jet identified by iterative declustering was also shown in Fig. 6.3. These measurements show that on average the number of splittings with a momentum fraction above 10% ($z > 0.1$) is 3 for a jet in pp collisions in the range $40 \leq p_{\mathrm{T,jet}}^{\mathrm{ch}} < 60$ GeV/c. The distribution is relatively broad with some jets exhibiting up to 6 or 7 hard splittings in vacuum. All of the Monte Carlo generators significantly under-predict the small fraction of jets that do not fragment in a hard way at all. PYTHIA 8 under-predicts this bin more than the other models considered. At large values of n_{SD} the PYTHIA 6.4 distribution is slightly below that of data but an agreement is recovered when applying NLO effects using the POWHEG method. This is consistent with an increase of hard outgoing particles included from the NLO Feynman diagrams.

In Pb–Pb collisions the first differential study of the momentum fraction z_{g} of Soft Drop groomed jets in opening angle was performed. A significant modification of the distribution in data was observed relative to the PYTHIA embedded distribution which was used as a vacuum reference. The momentum fraction of jets was most significantly modified at large angles where a net suppression of the number of splittings passing Soft Drop was also observed. The suppression of the most symmetric splittings ($z_{\mathrm{g}} \sim 0.5$) observed is qualitatively consistent with the measurements performed by CMS [151]. The model predictions from

JEWEL and the Hybrid Model have the same qualitative trend as the data when applying a minimum ΔR restriction but do not predict the suppression of symmetric splittings observed in data when no such restriction is applied and agree well with the distribution of the embedded PYTHIA jets. In the collinear region ($\Delta R < 0.1$) the Pb–Pb data agree with the vacuum reference within uncertainties with both JEWEL and Hybrid Model predictions qualitatively agreeing with the data. The measurement of the angular distribution of the splittings also displayed an enhancement of collinear splittings in Pb–Pb collisions relative to the vacuum reference with both models exhibiting the same behaviour.

The measurement of the number of hard splittings in Pb–Pb collisions showed that there is a slight shift towards lower values of n_{SD} in data relative to the vacuum reference. This is a novel measurement that provides new information about the hard fragmentation process of jets in the presence of the QGP.

The most striking observations from these measurements is the clear angular dependence of the modification of the z_{g} distribution in Pb–Pb collisions. It was proposed that after the initial observations of modifications of the z_{g} distribution that the contribution of the medium recoil could be responsible by promoting soft sub-leading subjets at wide angles above the Soft Drop threshold. However, in the measurement performed here an overall suppression of the large angle splittings is observed which is not consistent with the medium response picture. Alternative explanations for the modifications could include colour coherence effects where the medium modifies the internal structure of jets above some angular limit where it can resolve the individual components. This could certainly explain the angular dependence observed, but before any concrete conclusions can be drawn, a thorough model comparison would be required that goes beyond the comparisons performed in this work.

Future work

It is an exciting time to be involved in studying jets in heavy-ion collisions at ALICE. With all of the data already available from run 1 and run 2 of the LHC as well as the upcoming data from run 3 that will be collected with the significantly upgraded ALICE ITS there is still a huge amount to be done. It is hoped that the work presented in this thesis may act as a pedestal from which more comprehensive studies may be performed. With an increase of statistics at high $p_{\mathrm{T,jet}}^{\mathrm{ch}}$ expected from new data it is hoped that fully corrected measurements of substructure and groomed observables may be performed in Pb–Pb collisions. With fully corrected results it will be significantly easier to make comparisons with a wide range of Monte Carlo generators and analytical calculations which will lead to more concrete and meaningful conclusions. With larger data samples it will also be possible to do a more systematic scanning of the Lund Jet plane to study the phase space of jet splittings in a multi-dimensional way which may help highlight the role of medium induced modifications on jets in heavy-ion collisions. Additionally, further model comparisons could be performed to complement the measurements presented here in an attempt to understand in more detail the modifications that are observed. Specifically, comparisons of the Lund plane between data and the HERWIG event generator [185, 186] will help discern the discriminating power of these new tools for understanding jet substructure and QCD radiation in jets.

Appendix A

Publication: Exploration of jet substructure using iterative declustering in pp and Pb–Pb collisions at LHC energies

EUROPEAN ORGANIZATION FOR NUCLEAR RESEARCH

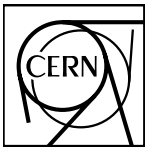

CERN-EP-2019-087
25 April 2019

Exploration of jet substructure using iterative declustering in pp and Pb–Pb collisions at LHC energies

ALICE Collaboration*

Abstract

The ALICE collaboration at the CERN LHC reports novel measurements of jet substructure in pp collisions at $\sqrt{s} = 7$ TeV and central Pb–Pb collisions at $\sqrt{s_{\rm NN}} = 2.76$ TeV. Jet substructure of track-based jets is explored via iterative declustering and grooming techniques. We present the measurement of the momentum sharing of two-prong substructure exposed via grooming, the $z_{\rm g}$, and its dependence on the opening angle, in both pp and Pb–Pb collisions. We also present the first measurement of the distribution of the number of branches obtained in the iterative declustering of the jet, which is interpreted as the number of its hard splittings. In Pb–Pb collisions, we observe a suppression of symmetric splittings at large opening angles and an enhancement of splittings at small opening angles relative to pp collisions, with no significant modification of the number of splittings. The results are compared to predictions from various Monte Carlo event generators to test the role of important concepts in the evolution of the jet in the medium such as color coherence.

*See Appendix A for the list of collaboration members

1 Introduction

The objective of the heavy-ion jet physics program at the LHC is to probe fundamental, microscopic properties of nuclear matter at high densities and temperatures. Jets provide well-calibrated probes of the dense medium created in heavy-ion collisions. In pp collisions, the production of jets and their substructure have been measured extensively and these measurements are well-reproduced by theoretical calculations based on perturbative QCD (pQCD) (see Refs. [1, 2] and citations therein). Jets are produced in high-momentum transfer processes, which occur on time scales much shorter than the formation time of the Quark-Gluon Plasma (QGP) generated in heavy-ion collisions; the production rates of jets in heavy-ion collisions can therefore be calculated accurately using the same pQCD approaches as for pp collisions, after taking into account the effects of nuclear geometry and nuclear modification of parton distribution functions (PDFs) [3].

Jets traversing the QGP will interact via elastic and radiative processes which modify the reconstructed jet cross section and structure relative to jets in vacuum ("jet quenching") [4]. Jet quenching effects have been extensively observed in nuclear collisions at RHIC and LHC in measurements of inclusive production and correlations of high-p_T hadrons and jets, including correlations of high-energy triggers (hadrons, photons, W and Z bosons, and jets) and reconstructed jets [5–8] as well as in the measurement of jet shapes [9–14]. Comparisons of these measurements to theoretical jet quenching calculations enable the determination of dynamical properties of the QGP, notably the transport parameter $\hat{q}$ [15].

More recently, the modification of the jet substructure due to jet quenching has been explored in heavy-ion collisions using tools developed for the measurement of jet substructure in pp collisions for QCD studies and Beyond Standard Model searches [2, 16]. A key tool is iterative declustering, which subdivides jets into branches or splittings that can be projected onto the phase space of such splittings, called the Lund plane [17–19]. While the splitting map contains kinematic information of all splittings, techniques like grooming [20, 21] can be applied to isolate a specific region of the splitting map according to different criteria such as mitigation of non-perturbative effects, enhancement of the jet quenching signal or simplification of perturbative calculations.

In this work we focus on Soft Drop (SD) grooming [21]. This technique selects the first splitting in the declustering process for which the subleading prong carries a fraction z of the momentum of the emitting prong larger than some value $z_{\rm cut}$, which in this analysis is set to $z_{\rm cut} = 0.1$. Note that this criterion selects a subset of the splittings. The grooming procedure removes soft radiation at large angles to expose a two-prong structure in the jet. The shared momentum fraction of those prongs is called $z_{\rm g}$, the groomed subjet momentum balance. The measurement of $z_{\rm g}$ in vacuum is closely related to the Altarelli-Parisi splitting functions [21].

Theoretical considerations of the in-medium modification of $z_{\rm g}$ can be found in [22–25]. A key physics ingredient in the theoretical calculations is color coherence[26]. This is the effect by which a color dipole cannot be resolved by the medium as two independent color charges if the opening angle of the dipole is small compared to a fundamental medium scale. If the dipole cannot be resolved, it will propagate through the medium as a single color charge. If color coherence is at work, there will be parts of the jet substructure that won't be resolved, leading to a reduced effective number of color charges and thus a reduced amount of energy loss in medium.

With the grooming technique we select a hard two-prong substructure. Then we inspect the dependence on the opening angle of the rate of such two-prong objects in medium relative to vacuum. We are interested in understanding whether large-angle splittings are more suppressed relative to vacuum than small-angle splittings, as one would expect if large-angle splittings are resolved by the medium and radiate in the medium incoherently. Previous measurements of $z_{\rm g}$ by the CMS collaboration [27] show a modification in central Pb–Pb collisions relative to the pp reference whilst measurements performed at RHIC by the STAR collaboration showed no modification [28]. Those measurements did not scan the ΔR

dependence and cover different intervals of the subleading prong energies that can bias towards different typical splitting formation times.

This work reports the measurement by the ALICE collaboration of z_g, the shared momentum fraction of two-prong substructure, its dependence on the opening angle and n_{SD}, the number of splittings satisfying the grooming condition obtained via the iterative declustering of the jet, in pp collisions at $\sqrt{s} = 7$ TeV and central (0–10%) Pb–Pb collisions at $\sqrt{s_{NN}} = 2.76$ TeV.

2 Data sets and event selection

A detailed description of the ALICE detector and its performance can be found in Refs. [29, 30]. The analysed pp data were collected during Run 1 of the LHC in 2010 with a collision centre-of-mass energy of $\sqrt{s} = 7$ TeV using a minimum bias (MB) trigger. The MB trigger configuration is the same as described in Ref. [31]. The data from heavy-ion collisions were recorded in 2011 at $\sqrt{s_{NN}} = 2.76$ TeV. This analysis uses the 0–10% most-central Pb–Pb collisions selected by the online trigger based on the hit multiplicity measured in the forward V0 detectors [32]. The datasets and event selection are identical to Refs. [5, 9]. After offline selection, the pp sample consists of 168 million events, while the Pb–Pb sample consists of 19 million events.

The analysis uses charged tracks reconstructed by the Inner Tracking System (ITS) [33] and Time Projection Chamber (TPC) [34] which both cover the full azimuth and pseudo-rapidity $|\eta| < 0.9$. Tracks are required to have transverse momentum $0.15 < p_T < 100$ GeV/c. The track selection is slightly different in the analysis of the 2010 and the 2011 data. The former uses a subclass of tracks with worse momentum resolution that is excluded from the latter [35].

In pp collisions, the tracking efficiency is approximately 80% for tracks with $p_T > 1$ GeV/c, decreasing to roughly 56% at $p_T = 0.15$ GeV/c, with a track momentum resolution of 1% for $p_T = 1$ GeV/c and 4.1% for $p_T = 40$ GeV/c [30, 31, 36]. In Pb–Pb collisions, the tracking efficiency is about 2 to 3% worse than in pp. The track p_T resolution is about 1% at $p_T = 1$ GeV/c and 2.5% for $p_T = 40$ GeV/c.

As a vacuum reference for the Pb–Pb measurements we use simulated pp collisions at $\sqrt{s} = 2.76$ TeV, calculated using PYTHIA 6.425 (Perugia Tune 2011) [27] and embedded into real central Pb–Pb events at the detector level, to take into account the smearing by the background fluctuations. We use the embedding of PYTHIA-generated events instead of the embedding of real pp data measured at $\sqrt{s} = 2.76$ TeV due to the limited size of the data sample. The PYTHIA MC describes well vacuum intrajet distributions [2]. In this paper, we validate the PYTHIA calculation by comparing it to jet substructure measurements in pp collisions at $\sqrt{s} = 7$ TeV.

3 Jet reconstruction

Jets are reconstructed from charged tracks using the anti-k_T algorithm [37] implemented in FastJet [38] with a jet resolution parameter of $R = 0.4$. The four-momenta of tracks are combined using the E-scheme recombination [38] where the pion mass is assumed for all reconstructed tracks. In order to ensure that all jet candidates are fully contained within the fiducial volume of the ALICE detector system, accepted jets were required to have their centroid constrained to $|\eta_{jet}| < 0.5$.

The jet finding efficiency is 100% in the measured kinematic ranges. The jet energy instrumental resolution is similar for pp and Pb–Pb collisions, varying from 15% at $p_{T,jet}^{ch} = 20$ GeV/c to 25% at $p_{T,jet}^{ch} = 100$ GeV/c. The Jet Energy Scale (JES) uncertainty is dominated by the tracking efficiency uncertainty which is 4%.

In pp collisions, no correction for the underlying event is applied. In Pb–Pb collisions, the jet energy is partially adjusted for the effects of uncorrelated background using the constituent subtraction

method [39]. Constituent subtraction corrects individual jet constituents by modifying their four-momentum. The momentum that is subtracted from the constituents is determined using the underlying event density, ρ, which is calculated by clustering the event into $R = 0.2$ jets using the k_{T} algorithm [40, 41] and taking the median jet p_{T} density in the event. The two leading k_{T} jets are removed before calculating the median, to suppress the contribution of true hard jets in the background estimation. The correction is applied such that the total momentum removed from the jet is equal to $\rho \times A_{\mathrm{j}}$, where A_{j} is the jet area. This background subtraction is applied both to the measured data and to the embedded PYTHIA reference.

4 Observables

Jet constituents are reclustered using the physical Cambridge/Aachen (CA) metric [42], leading to an angle-ordered shower. The declustering process consists of unwinding the clustering history step by step, always following the hardest branch. The first declustering step identifies the final subjet pair or branch that was merged. The second declustering step identifies the subjet pair that was merged into the leading subjet of the final step, etc. The coordinates of the subleading prong in the Lund Plane ($\log(z\Delta R)$, $\log(1/\Delta R)$) are registered at each declustering step, where z is the fraction of momentum carried by the subleading prong $z = \frac{\min(p_{\mathrm{T},1}, p_{\mathrm{T},2})}{p_{\mathrm{T},1}+p_{\mathrm{T},2}}$, with $p_{\mathrm{T},1}$ and $p_{\mathrm{T},2}$ being the momenta of the leading and subleading prongs, respectively, and ΔR the opening angle of the splitting.

The observable n_{SD} is obtained by counting the number of splittings in the declustering process that satisfy the Soft Drop selection $z > z_{\mathrm{cut}}$, $z_{\mathrm{cut}} = 0.1$. The observable z_{g} corresponds to the subjet momentum balance, z, of the first splitting satisfying the SD selection. Jets with $n_{\mathrm{SD}} = 0$ are labelled "untagged jets". The z_{g} distribution is absolutely normalised, including the untagged jets in the normalisation. This choice of normalisation, used here for the first time, provides crucial information for quantitative comparison of jet substructure measurements in Pb–Pb and pp collisions since it allows the results to be interpreted in terms of not only a change of shape in the distribution but also in terms of net enhancement/suppression of the yield of splittings satisfying the SD condition in a given jet transverse momentum range.

The tracking system enables the measurement of subjets with angular separation smaller than 0.1 radians and a scan of the z_{g} distribution in ranges of ΔR: $\Delta R < 0.1$, $\Delta R > 0.1$ and $\Delta R > 0.2$.

For data from pp collisions, the correction of the detector effects was performed via unfolding. The results are presented in the jet momentum interval of $40 < p_{\mathrm{T,jet}}^{\mathrm{ch}} < 60$ GeV/c, chosen to balance statistical precision and detector effects. In Pb–Pb collisions, the results are presented at detector-level, with the uncorrelated background subtracted on average from the jet p_{T} and from the substructure observable. The vacuum reference is thus smeared by background fluctuations and instrumental effects. The Pb–Pb results are presented in the jet momentum range of $80 < p_{\mathrm{T,jet}}^{\mathrm{ch}} < 120$ GeV/c, where uncorrelated background is negligible.

5 Corrections and systematic uncertainties

For data from pp collisions, the unfolding of instrumental effects is carried out using a four-dimensional response matrix that encodes the smearing of both jet $p_{\mathrm{T}}^{\mathrm{ch}}$ and the substructure observable (shape$^{\mathrm{part,ch}}$, $p_{\mathrm{T,jet}}^{\mathrm{part,ch}}$, shape$^{\mathrm{det,ch}}$, $p_{\mathrm{T,jet}}^{\mathrm{det,ch}}$), where "shape" denotes either z_{g} or n_{SD}. The upper index "part" refers to particle-level and "det" refers to detector-level quantities, obtained from simulations in which pp collisions are generated by PYTHIA (particle-level) and then passed through a GEANT3-based model [43] of the ALICE detector. We note that the particle-level jet finding is performed using the true particle masses so the unfolding corrects for the pion mass assumption at detector level.

To generate vacuum reference distributions for comparison to Pb–Pb results, which are not fully corrected, we superimpose detector-level PYTHIA events onto real Pb–Pb events. Consequently, no two-

Table 1: Relative systematic uncertainties on the measured distributions in pp collisions for three selected jet shape intervals in the jet $p_{\mathrm{T,jet}}^{\mathrm{ch}}$ interval of 40–60 GeV/c.

Observable	z_{g}			n_{SD}		
Interval	0.1–0.175	0.25–0.325	0.4–0.5	0	3	6
Tracking efficiency (%)	1.9	0.2	1.0	16.1	1.1	18.3
Prior (%)	$^{+0.0}_{-1.8}$	$^{+0.6}_{-0.0}$	$^{+1.6}_{-0.0}$	$^{+0.7}_{-0.0}$	$^{+0.0}_{-3.4}$	$^{+3.3}_{-0.0}$
Regularisation (%)	$^{+0.8}_{-0.5}$	$^{+0.2}_{-0.2}$	$^{+0.4}_{-0.5}$	$^{+0.4}_{-1.4}$	$^{+1.4}_{-1.1}$	$^{+1.7}_{-3.0}$
Truncation (%)	$^{+2.2}_{-0.0}$	$^{+1.8}_{-0.0}$	$^{+2.4}_{-0.0}$	$^{+0.0}_{-0.0}$	$^{+0.0}_{-0.1}$	$^{+4.4}_{-0.0}$
Binning (%)	0.5	4.5	1.2	N/A	N/A	N/A
Total (%)	$^{+3.0}_{-2.7}$	$^{+4.9}_{-0.3}$	$^{+3.0}_{-1.6}$	$^{+16.1}_{-16.1}$	$^{+1.8}_{-3.7}$	$^{+19.2}_{-18.5}$

Table 2: Relative systematic uncertainties on the measured distributions in Pb–Pb collisions for three selected jet shape intervals and one ΔR selection in the jet $p_{\mathrm{T,jet}}^{\mathrm{ch}}$ interval of 80–120 GeV/c.

Observable	$z_{\mathrm{g}}(\Delta R > 0.1)$			n_{SD}		
Interval	0.1–0.175	0.25–0.325	0.4–0.5	0	3	6
Tracking efficiency(%)	4.9	2.8	11.4	11.2	7.9	11.1
Angular cutoff (%)	$^{+2.3}_{-3.8}$	$^{+2.8}_{-0.0}$	$^{+10.0}_{-0.0}$	N/A	N/A	N/A
Reference (%)	$^{+0.0}_{-0.0}$	$^{+12.4}_{-0.0}$	$^{+10.1}_{-0.0}$	$^{+30.1}_{-0.0}$	$^{+0.0}_{-5.2}$	$^{+5.3}_{-0.0}$
Total (%)	$^{+5.4}_{-6.2}$	$^{+13.1}_{-2.8}$	$^{+18.2}_{-11.4}$	$^{+32.1}_{-11.2}$	$^{+7.9}_{-9.5}$	$^{+12.3}_{-11.1}$

track effects are present, however their impact in data is negligible due to the large required number of clusters per track. The matching of particle-level and embedded jets is performed as described in [9]. The matching efficiency is consistent with unity for jets with p_{T} above 30 GeV/c.

For pp collisions, Bayesian unfolding in two dimensions as implemented in the RooUnfold package [44] is used. The prior is the two-dimensional distribution ($p_{\mathrm{T,jet}}^{\mathrm{part,ch}}$, shape$^{\mathrm{part,ch}}$) generated with PYTHIA. The default number of iterations chosen for z_{g} and n_{SD} is 4, which corresponds to the first iteration for which the refolded distributions agree with the corresponding raw distributions within 5%. A closure test was also carried out, in which two statistically independent Monte Carlo (MC) samples are used to fill the response and the pseudo-data. For this test, the unfolded solution agrees with the MC truth distribution within statistical uncertainties.

Unfolding of the distributions was attempted for the Pb–Pb case, but no convergence on a mathematically consistent solution was obtained. The reason is that for Pb–Pb collisions data, the response is strongly non-diagonal due to the presence of sub-leading prongs at large angles that are not correlated to particle-level prongs. Strategies to suppress such uncorrelated secondary prongs are beyond the scope of this analysis.

The systematic uncertainties are determined by varying key aspects of the correction procedures for instrumental response and background fluctuations. The most significant components of the systematic uncertainties for z_{g} and n_{SD} are tabulated in Table 1 and 2. For pp collisions, the tracking efficiency uncertainty is $\pm 4\%$ [13]. The effect of this uncertainty on the substructure measurement is assessed by applying an additional track rejection of 4% at detector-level prior to jet finding. A new response is built and the unfolding is repeated, with the resulting variation in the unfolded solution symmetrised and taken as the systematic uncertainty. This is the largest contribution to the JES uncertainty. To estimate the regularisation uncertainty, the number of Bayesian iterations is varied by ± 1 with respect to the default

analysis value. The prior is varied by reweighting the response such that its particle-level projection matches the unfolded solution. The detector-level intervals in p_{T} and the substructure observables are modified to determine what in the table is referred to as truncation uncertainty. The uncertainty labelled "Binning" in the tables corresponds to a variation in binning of both p_{T} and substructure observables, subject to the constraint of at least 10 counts in the least populous bin to ensure the stability of the unfolding procedure.

In the case of Pb–Pb collisions, the evaluation of the uncertainty due to tracking efficiency is carried out similarly to the pp case. The z_{g} measurement is done differentially in ranges of ΔR. The limits of the ΔR ranges were varied by $\pm 10\%$, which corresponds approximately to the width of the distribution of the relative difference of particle-level and embedded-level ΔR in Pb–Pb collisions. The differences between PYTHIA and the unfolded pp distributions are taken into account when using PYTHIA as a reference for Pb–Pb measurements. This is done by reweighting the embedded PYTHIA reference so that its particle-level projection matches the unfolded pp $p_{\mathrm{T,jet}}$ vs z_{g} (or $p_{\mathrm{T,jet}}$ vs n_{SD}) correlation. The difference between the reference smeared with the default and the reweighted response is assigned as the corresponding uncertainty.

In both the pp and Pb–Pb analyses, the uncertainties are added in quadrature. All the contributions to the overall uncertainty produce changes in a given interval of the distribution that are strongly anti-correlated with changes in a different interval, i.e., they induce changes in the shape of the observable.

6 Results

Figures 1 and 2 show fully corrected distributions of z_{g} and n_{SD} measured in pp collisions at $\sqrt{s} = 7$ TeV for charged jets in the interval $40 < p_{\mathrm{T,jet}}^{\mathrm{ch}} < 60$ GeV/c. The results are compared to distributions obtained from PYTHIA 6 (Perugia Tune 2011), from PYTHIA 6 + POWHEG [45], to consider the impact of NLO effects, and from the newer PYTHIA 8 (Tune 4C) [46].

The z_{g} distribution is well-described within systematic and statistical uncertainties by all the MC generators considered. As discussed above, untagged jets contribute to the normalisation of the distributions. The untagged contribution is not shown in Fig. 1, due to the suppressed zero on the horizontal axis, but is shown in Fig. 2 in the bin representing $n_{\mathrm{SD}} = 0$. Table 3 shows the tagged fraction for data and simulations. For pp (rightmost column), the untagged fraction is about 2%. The Monte Carlo distributions in Fig. 2 disagree with the data in the tails of the distribution. They have a significantly lower fraction of jets with no splittings ($n_{\mathrm{SD}} = 0$) than observed in data. The addition of POWHEG corrections to PYTHIA 6 shifts the distribution towards a larger number of splittings, as expected from NLO corrections which introduce an additional hard parton in the final state.

Figure 3 shows z_{g} distributions measured in central Pb–Pb collisions for various ranges of angular separation ΔR. The results are presented in the uncorrected transverse momentum range $80 \leq p_{\mathrm{T,jet}}^{\mathrm{ch}} < 120$ GeV/c and compared to the distribution of PYTHIA jets embedded into real 0–10% central Pb–Pb events.

Figure 3 shows a larger difference between the measured Pb–Pb and embedded reference distributions for larger values of ΔR, indicating a relative suppression in the rate of symmetric splittings ($z_{\mathrm{g}} \approx 0.5$) in central Pb–Pb collisions. However, due to the steeply falling z_{g} distribution, the fraction of all jets that exhibit symmetric splittings is small, and this strong suppression corresponds to a suppression of only a few percent in the total rate of jets passing both the SD and angular cuts (c.f. Tab. 3). Conversely, in the small ΔR limit a small excess of splittings is observed in the data.

Figure 3 also shows comparisons to predictions from the JEWEL event generator [47] and Hybrid model [48] calculations. The JEWEL simulations include the medium response from jet-medium interactions [49]. The theoretical predictions must be smeared to account for the detector effects as well as fluc-

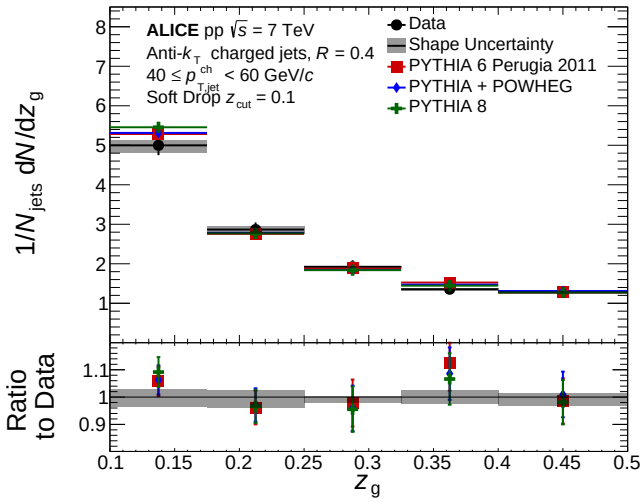

Fig. 1: Fully corrected z_g distribution in pp collisions for $40 \le p_{T,jet}^{ch} < 60$ GeV/c compared with predictions from PYTHIA simulations. The statistical uncertainties are shown as vertical bars and the systematic uncertainties are represented by a shaded area.

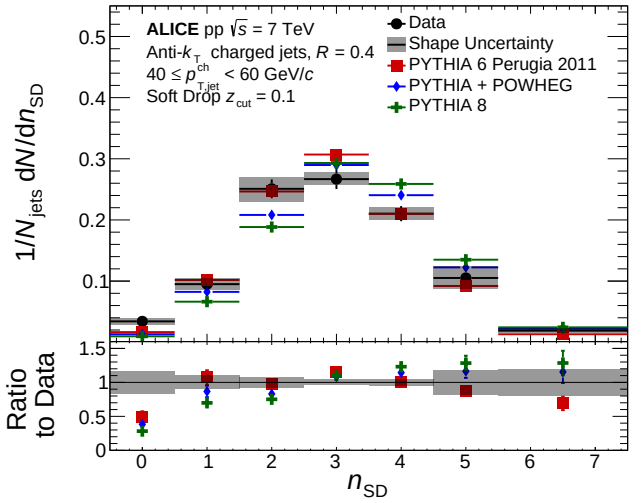

Fig. 2: Fully corrected n_{SD} distribution in pp collisions for $40 \le p_{T,jet}^{ch} < 60$ GeV/c, compared with predictions from PYTHIA simulations. The statistical uncertainties are shown as vertical bars and the systematic uncertainties are represented by a shaded area.

tuations due to uncorrelated background. This smearing is performed by constructing a 6-dimensional response matrix by superimposing PYTHIA events at detector level to real 0–10% central Pb–Pb events. The 6-dimensional matrix maps every embedded jet from a given bin of (z_g^{part}, ΔR^{part}, $p_{T,jet}^{part}$) to (z_g^{det}, ΔR^{det}, $p_{T,jet}^{det}$). The smearing of the distributions significantly modifies the predictions and is essential for quantitative comparison of the measurements and calculations.

The models capture the qualitative trends of the data, namely the enhancement of the number of small-angle splittings and the suppression of the large-angle symmetric splittings. The fraction of jets not passing the SD selection is similar in the models and data. However discrepancies are observed in the angular selection. For instance the number of SD splittings that pass the angular cut of $\Delta R > 0.2$ is the

Table 3: Fraction of jets that pass the Soft Drop condition $z_{\rm cut} = 0.1$ in the specified range of angular separation and in the transverse momentum range $40 \leq p_{\rm T,jet}^{\rm ch} < 60\,{\rm GeV}/c$ for pp and $80 \leq p_{\rm T,jet}^{\rm ch} < 120$ GeV/c for Pb–Pb collisions. Uncertainties on the data are written as statistical (systematic).

	Tagged rate (%)				
Dataset	Pb–Pb				pp
Angular Cut	$\Delta R < 0.1$	$\Delta R > 0.0$	$\Delta R > 0.1$	$\Delta R > 0.2$	$\Delta R > 0.2$
Data	$38.4 \pm 2.3(2.5)$	$92.1 \pm 3.5(0.9)$	$53.6 \pm 2.7(3.4)$	$41.8 \pm 2.4(3.6)$	$97.3 \pm 3.0(1.7)$
PYTHIA	34.6	95.5	60.2	46.9	98.6
Hybrid	47.5	93.4	45.8	35.0	N/A
JEWEL	42.0	93.0	51.0	40.0	N/A

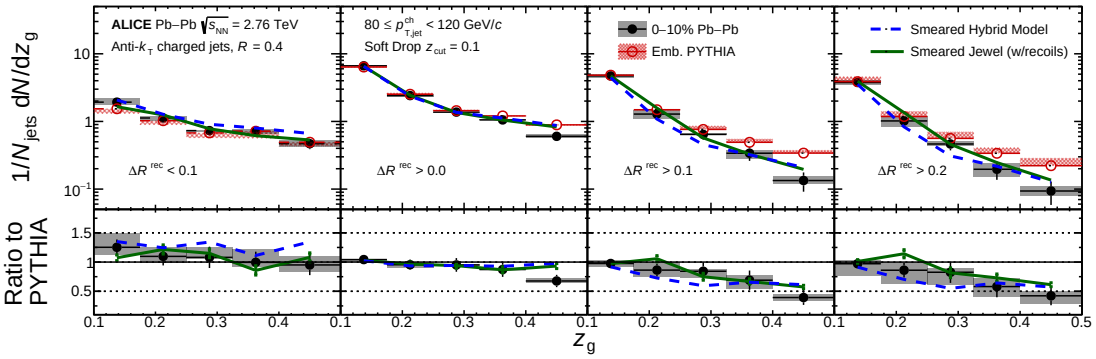

Fig. 3: Detector-level Pb–Pb distributions of $z_{\rm g}$ for $R = 0.4$ jets with varying minimum/maximum angular separation of subjets (ΔR) for jets in the range $80 \leq p_{\rm T,jet}^{\rm ch} < 120$ GeV/c. The systematic uncertainties are represented by the shaded area. The corresponding values for the embedded PYTHIA reference (open symbols), Hybrid model (dashed line) and JEWEL (solid line) are also shown in the plot. The lower plots show the ratios of data, Hybrid and JEWEL model to the embedded PYTHIA reference.

lowest in the case of the Hybrid model, pointing to a stronger incoherent quenching of the prongs.

The suppression of splittings at large opening angles is qualitatively expected from vacuum formation time and colour coherence arguments [24]. The wider the opening angle, the shorter the formation time of the splitting. This makes it more likely that the splitting propagates through, and is modified by, the medium. If coherence effects are at play in the medium then it is expected that splittings that are separated by more than the coherence angle will be more suppressed since they radiate energy independently.

Figure 4 shows the comparison of $n_{\rm SD}$ distributions from Pb–Pb measurements and the embedded PYTHIA reference. The data exhibit a shift towards lower number of splittings. The discrepancies between the distributions from PYTHIA and from pp collisions are incorporated as a part of the reference uncertainty via the reweighting procedure described above. The corresponding curves for the Hybrid model and JEWEL are also shown in the plot.

To explore the dependence of the $n_{\rm SD}$ distribution on the fragmentation pattern, we also show a calculation in which the pp reference distribution is based solely on light-quark fragmentation. Since the quark fragmentation is harder, we see that the number of splittings peaks at lower values, in line with what we observe in the data. The smeared JEWEL and Hybrid model calculation agree with the qualitative trend of the data.

The trends indicate that the larger the opening angle, the more suppressed the splittings are, and this

is qualitatively consistent with large-angle prongs being more resolved by the medium and thus more suppressed. The same process could lead to a reduction in the number of hard splittings as observed in Figure 4. However, it is worth noting that both the Hybrid and JEWEL models, in spite of their capturing of the general trends of the data, they do not incorporate the physics of color coherence and all the prongs in the jet lose energy incoherently. This points to a simpler interpretation of the results for instance in terms of formation times of the splittings and their interplay with the medium length. The vacuum formation time $t_f \approx \omega/k_T^2 \approx 1/(\omega\Delta R^2)$, with ω and k_T being the energy and relative transverse momentum of the radiated prong, is shorter for large-angle splittings, meaning that vacuum, large-angle splittings, will be produced mostly in the medium and their resulting prongs will be further modified by the medium. At large angles, the component of vacuum splittings that propagate in vacuum is less than at small angles, resulting in an enhanced contribution of medium-modifications compared to small-angle splittings.

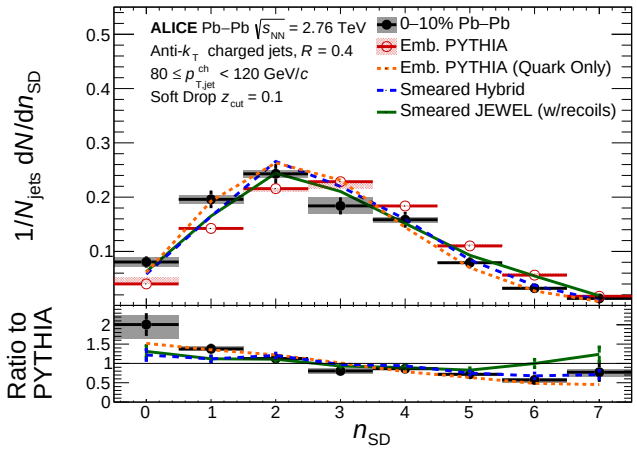

Fig. 4: The number of SD branches for jets reconstructed in Pb–Pb data are shown. The systematic uncertainties are represented by the shaded area. The datapoints are compared to jets found in PYTHIA events embedded into Pb–Pb events (open markers). The Hybrid model and JEWEL predictions correspond to the red (dashed) and blue (solid) lines. The lower panel shows the ratio of the n_{SD} distribution in data and the embedded PYTHIA reference (grey). The ratios of the Hybrid and JEWEL models to the embedded PYTHIA reference are also shown.

7 Summary

This Letter presents the measurement of jet substructure using iterative declustering techniques in pp and Pb–Pb collisions at the LHC. We report distributions of n_{SD}, the number of branches passing the soft drop selection, and z_g, the shared momentum fraction of the two-prong substructure selected by the mass drop condition, differentially in ranges of splitting opening angle.

Generally, good agreement between distributions for pp collisions and vacuum calculations is found except for the fraction of untagged jets, which is underestimated by the models. In Pb–Pb collisions, a suppression of the z_g distribution is observed at large angles relative to the vacuum reference whilst at low opening angles there is a hint of an enhancement. These observations are in qualitative agreement with the expected behaviour of two-prong objects in the case of coherent or decoherent energy loss [24] in the BMDPS-Z [50, 51] framework. However, the models that are compared to the data do not implement color coherence and yet they capture the qualitative trends of the data. This suggests that other effects might drive the observed behaviour, for instance the interplay between formation time of the splittings and medium length.

The number of splittings obtained by iteratively declustering the hardest branch in the jet, n_{SD}, is shifted

towards lower values in Pb–Pb relative to the vacuum reference. This suggests that medium-induced radiation does not create new splittings that pass the SD cut. On the contrary, there is a hint of fewer splittings passing the SD cut, pointing to a harder, more quark-like fragmentation in Pb–Pb compared to pp collisions, in qualitative agreement with the trends observed for other jet shapes [9].

With these measurements, we have explored a region of the Lund plane delimited by the Soft Drop cut $z > 0.1$. Other regions of the phase space of splittings will be scanned systematically in the future with larger data samples.

Acknowledgements

The ALICE Collaboration would like to thank all its engineers and technicians for their invaluable contributions to the construction of the experiment and the CERN accelerator teams for the outstanding performance of the LHC complex. The ALICE Collaboration gratefully acknowledges the resources and support provided by all Grid centres and the Worldwide LHC Computing Grid (WLCG) collaboration. The ALICE Collaboration acknowledges the following funding agencies for their support in building and running the ALICE detector: A. I. Alikhanyan National Science Laboratory (Yerevan Physics Institute) Foundation (ANSL), State Committee of Science and World Federation of Scientists (WFS), Armenia; Austrian Academy of Sciences, Austrian Science Fund (FWF): [M 2467-N36] and Nationalstiftung für Forschung, Technologie und Entwicklung, Austria; Ministry of Communications and High Technologies, National Nuclear Research Center, Azerbaijan; Conselho Nacional de Desenvolvimento Científico e Tecnológico (CNPq), Universidade Federal do Rio Grande do Sul (UFRGS), Financiadora de Estudos e Projetos (Finep) and Fundação de Amparo à Pesquisa do Estado de São Paulo (FAPESP), Brazil; Ministry of Science & Technology of China (MSTC), National Natural Science Foundation of China (NSFC) and Ministry of Education of China (MOEC) , China; Croatian Science Foundation and Ministry of Science and Education, Croatia; Centro de Aplicaciones Tecnológicas y Desarrollo Nuclear (CEADEN), Cubaenergía, Cuba; Ministry of Education, Youth and Sports of the Czech Republic, Czech Republic; The Danish Council for Independent Research — Natural Sciences, the Carlsberg Foundation and Danish National Research Foundation (DNRF), Denmark; Helsinki Institute of Physics (HIP), Finland; Commissariat à l'Energie Atomique (CEA), Institut National de Physique Nucléaire et de Physique des Particules (IN2P3) and Centre National de la Recherche Scientifique (CNRS) and Région des Pays de la Loire, France; Bundesministerium für Bildung und Forschung (BMBF) and GSI Helmholtzzentrum für Schwerionenforschung GmbH, Germany; General Secretariat for Research and Technology, Ministry of Education, Research and Religions, Greece; National Research, Development and Innovation Office, Hungary; Department of Atomic Energy Government of India (DAE), Department of Science and Technology, Government of India (DST), University Grants Commission, Government of India (UGC) and Council of Scientific and Industrial Research (CSIR), India; Indonesian Institute of Science, Indonesia; Centro Fermi - Museo Storico della Fisica e Centro Studi e Ricerche Enrico Fermi and Istituto Nazionale di Fisica Nucleare (INFN), Italy; Institute for Innovative Science and Technology , Nagasaki Institute of Applied Science (IIST), Japan Society for the Promotion of Science (JSPS) KAKENHI and Japanese Ministry of Education, Culture, Sports, Science and Technology (MEXT), Japan; Consejo Nacional de Ciencia (CONACYT) y Tecnología, through Fondo de Cooperación Internacional en Ciencia y Tecnología (FONCICYT) and Dirección General de Asuntos del Personal Academico (DGAPA), Mexico; Nederlandse Organisatie voor Wetenschappelijk Onderzoek (NWO), Netherlands; The Research Council of Norway, Norway; Commission on Science and Technology for Sustainable Development in the South (COMSATS), Pakistan; Pontificia Universidad Católica del Perú, Peru; Ministry of Science and Higher Education and National Science Centre, Poland; Korea Institute of Science and Technology Information and National Research Foundation of Korea (NRF), Republic of Korea; Ministry of Education and Scientific Research, Institute of Atomic Physics and Ministry of Research and Innovation and Institute of Atomic Physics, Romania; Joint Institute for Nuclear Research (JINR), Ministry of Education

and Science of the Russian Federation, National Research Centre Kurchatov Institute, Russian Science Foundation and Russian Foundation for Basic Research, Russia; Ministry of Education, Science, Research and Sport of the Slovak Republic, Slovakia; National Research Foundation of South Africa, South Africa; Swedish Research Council (VR) and Knut & Alice Wallenberg Foundation (KAW), Sweden; European Organization for Nuclear Research, Switzerland; National Science and Technology Development Agency (NSDTA), Suranaree University of Technology (SUT) and Office of the Higher Education Commission under NRU project of Thailand, Thailand; Turkish Atomic Energy Agency (TAEK), Turkey; National Academy of Sciences of Ukraine, Ukraine; Science and Technology Facilities Council (STFC), United Kingdom; National Science Foundation of the United States of America (NSF) and United States Department of Energy, Office of Nuclear Physics (DOE NP), United States of America.

References

[1] M. Dasgupta, F. A. Dreyer, G. P. Salam, and G. Soyez, "Inclusive jet spectrum for small-radius jets", *JHEP* **06** (2016) .

[2] L. Asquith *et al.*, "Jet Substructure at the Large Hadron Collider : Experimental Review",.

[3] K. J. Eskola, H. Paukkunen, and C. A. Salgado, "Nuclear PDFs at NLO - status report and review of the EPS09 results", *Nucl. Phys.* **A855** (2011) .

[4] A. Majumder and M. Van Leeuwen, "The Theory and Phenomenology of Perturbative QCD Based Jet Quenching", *Prog.Part.Nucl.Phys.* **A66** (2011) .

[5] **ALICE** Collaboration, J. Adam *et al.*, "Measurement of jet quenching with semi-inclusive hadron-jet distributions in central Pb–Pb collisions at $\sqrt{s_{\rm NN}} = 2.76$ TeV", *JHEP* **09** (2015) .

[6] **STAR** Collaboration, L. Adamczyk *et al.*, "Measurements of jet quenching with semi-inclusive hadron+jet distributions in Au+Au collisions at $\sqrt{s_{\rm NN}}$ = 200 GeV", *Phys. Rev.* **C96** no. 2, (2017) .

[7] **CMS** Collaboration, A. M. Sirunyan *et al.*, "Study of Jet Quenching with $Z+$jet Correlations in Pb–Pb and pp Collisions at $\sqrt{s_{\rm NN}} = 5.02$ TeV", *Phys. Rev. Lett.* **119** no. 8, (2017) .

[8] **ATLAS** Collaboration, M. Aaboud *et al.*, "Measurement of photonjet transverse momentum correlations in 5.02 TeV Pb + Pb and pp collisions with ATLAS", *Phys. Lett.* **B789** (2019) .

[9] **ALICE** Collaboration, S. Acharya *et al.*, "Medium modification of the shape of small-radius jets in central Pb–Pb collisions at $\sqrt{s_{\rm NN}} = 2.76$ TeV", *JHEP* **10** (2018) .

[10] **CMS** Collaboration, S. Chatrchyan *et al.*, "Modification of jet shapes in Pb–Pb collisions at $\sqrt{s_{\rm NN}} = 2.76$ TeV", *Phys. Lett.* **B730** (2014) .

[11] **CMS** Collaboration, A. M. Sirunyan *et al.*, "Observation of Medium-Induced Modifications of Jet Fragmentation in Pb-Pb Collisions at $\sqrt{s_{\rm NN}} = 5.02$ TeV Using Isolated Photon-Tagged Jets", *Phys. Rev. Lett.* **121** no. 24, (2018) .

[12] **ATLAS** Collaboration, M. Aaboud *et al.*, "Measurement of jet fragmentation in Pb+Pb and pp collisions at $\sqrt{s_{\rm NN}} = 2.76$ TeV with the ATLAS detector at the LHC", *Eur. Phys. J.* **C77** (2017) .

[13] **ALICE** Collaboration, S. Acharya *et al.*, "First measurement of jet mass in Pb–Pb and p–Pb collisions at the LHC", *Phys. Lett.* **B776** (2018) .

[14] **CMS** Collaboration, A. M. Sirunyan *et al.*, "Measurement of the groomed jet mass in PbPb and pp collisions at $\sqrt{s_{\rm NN}} = 5.02$ TeV", *JHEP* **10** (2018) .

[15] K. M. Burke, A. Buzzatti, N. Chang, C. Gale, M. Gyulassy, *et al.*, "Extracting jet transport coefficient from jet quenching at RHIC and LHC", *Phys.Rev.* **C90** (2014) .

[16] J. R. Andersen *et al.*, "Les Houches 2017: Physics at TeV Colliders Standard Model Working Group Report",.

[17] B. Andersson, G. Gustafson, L. Lonnblad, and U. Pettersson, "Coherence Effects in Deep Inelastic Scattering", *Z. Phys.* **C43** (1989) .

[18] F. A. Dreyer, G. P. Salam, and G. Soyez, "The Lund Jet Plane", *JHEP* **12** (2018) .

[19] H. Andrews *et al.*, "Novel tools and observables for jet physics in heavy-ion collisions",.

[20] M. Dasgupta, A. Fregoso, S. Marzani, and G. P. Salam, "Towards an understanding of jet substructure", *JHEP* **09** (2013) .

[21] A. J. Larkoski, S. Marzani, G. Soyez, and J. Thaler, "Soft Drop", *JHEP* **05** (2014) .

[22] G. Milhano, U. A. Wiedemann, and K. Zapp, "Sensitivity of jet substructure to jet-induced medium response", *Phys. Lett.* **B779** (2018) .

[23] F. D'Eramo, K. Rajagopal, and Y. Yin, "Molire scattering in quark-gluon plasma: finding point-like scatterers in a liquid", *JHEP* **01** (2019) .

[24] Y. Mehtar-Tani and K. Tywoniuk, "Groomed jets in heavy-ion collisions: sensitivity to medium-induced bremsstrahlung", *JHEP* **04** (2017) .

[25] N. Chang, S. Cao, and G. Qin, "Probing medium-induced jet splitting and energy loss in heavy-ion collisions", *Phys. Lett.* **B781** (2018) .

[26] J. Casalderrey-Solana, Y. Mehtar-Tani, C. A. Salgado, and K. Tywoniuk, "New picture of jet quenching dictated by color coherence", *Phys. Lett.* **B725** (2013) .

[27] **CMS** Collaboration, A. M. Sirunyan *et al.*, "Measurement of the Splitting Function in pp and Pb–Pb Collisions at $\sqrt{s_{\mathrm{NN}}} = 5.02$ TeV", *Phys. Rev. Lett.* **120** no. 14, (2018) .

[28] **STAR** Collaboration, K. Kauder *et al.*, "Measurement of the Shared Momentum Fraction z_{g} using Jet Reconstruction in p+p and Au+Au Collisions with STAR", *Nucl. Phys.* **A967** (2017) .

[29] **ALICE** Collaboration, K. Aamodt *et al.*, "The ALICE experiment at the CERN LHC", *JINST* **3** (2008) .

[30] **ALICE** Collaboration, B. Abelev *et al.*, "Performance of the ALICE Experiment at the CERN LHC", *Int.J.Mod.Phys.* **A29** (2014) .

[31] **ALICE** Collaboration, B. Abelev *et al.*, "Charged jet cross sections and properties in proton-proton collisions at $\sqrt{s} = 7$ TeV", *Phys. Rev.* **D91** (2015) .

[32] **ALICE** Collaboration, E. Abbas *et al.*, "Performance of the ALICE VZERO system", *JINST* **8** (2013) .

[33] **ALICE** Collaboration, K. Aamodt *et al.*, "Alignment of the ALICE Inner Tracking System with cosmic-ray tracks", *JINST* **5** (2010) .

[34] K. Aamodt *et al.*, "The ALICE TPC, a large 3-dimensional tracking device with fast readout for ultra-high multiplicity events", *Nucl. Instrum. Methods Phys. Res. A* **622** (Oct., 2010) .

[35] **ALICE** Collaboration, J. Adam *et al.*, "Measurement of jet suppression in central Pb–Pb collisions at $\sqrt{s_{\rm NN}} = 2.76$ TeV", *Phys.Lett* **B746** (2015) .

[36] **ALICE** Collaboration, B. Abelev *et al.*, "Centrality Dependence of Charged Particle Production at Large Transverse Momentum in Pb–Pb Collisions at $\sqrt{s_{\rm NN}} = 2.76$ TeV", *Phys.Lett.* **B720** (2013) .

[37] M. Cacciari, G. P. Salam, and G. Soyez, "The anti-k_t jet clustering algorithm", *JHEP* **04** (2008) .

[38] M. Cacciari, G. P. Salam, and G. Soyez, "FastJet User Manual", *Eur.Phys.J.* **C72** (2012) .

[39] P. Berta, M. Spousta, D. W. Miller, and R. Leitner, "Particle-level pileup subtraction for jets and jet shapes", *JHEP* **06** (2014) .

[40] S. Catani, Y. Dokshitzer, M. Seymour, and B. Webber, "Longitudinally-invariant k_t-clustering algorithms for hadron-hadron collisions", *Nuc. Phys. B* **406** no. 1, (1993) .

[41] M. Cacciari and G. P. Salam, "Dispelling the n3 myth for the k_t jet-finder", *Phys. Lett. B* **641** no. 1, (2006) .

[42] Yu.L.Dokshitzer, G.D.Leder, S.Moretti, and B.R.Webber, "Better Jet Clustering Algorithms", *JHEP* **08** (1997) .

[43] R. Brun, F. Bruyant, M. Maire, A.C. McPherson, and P. Zanarini, "GEANT3 User's Guide", *CERN Data Handling Division DD/EE/84-1* (1985) .

[44] RooUnfold `http://hepunx.rl.ac.uk/~adye/software/unfold/RooUnfold.html`.

[45] S. Frixione, P. Nason, and C. Oleari, "Matching NLO QCD computations with Parton Shower simulations: the POWHEG method", *JHEP* **0711** (2007) .

[46] T. Sjstrand, S. Ask, J. R. Christiansen, R. Corke, N. Desai, P. Ilten, S. Mrenna, S. Prestel, C. O. Rasmussen, and P. Z. Skands, "An Introduction to PYTHIA 8.2", *Comput. Phys. Commun.* **191** (2015) .

[47] K. Zapp, G. Ingelman, J. Rathsman, J. Stachel, and U. A. Wiedemann, "A Monte Carlo Model for 'Jet Quenching'", *Eur.Phys.J.* **C60** (2009) .

[48] J. Casalderrey-Solana, D. C. Gulhan, J. G. Milhano, D. Pablos, and K. Rajagopal, "Jet quenching within a hybrid strong/weak coupling approach", *Nucl. Phys.* **A931** (2014) .

[49] R. Kunnawalkam Elayavalli and K. C. Zapp, "Medium response in JEWEL and its impact on jet shape observables in heavy ion collisions", *JHEP* **07** (2017) .

[50] R.Baier, Yu.L.Dokshitzer, S. Peign, and D. Schiff, "Induced Gluon Radiation in a QCD Medium", *Phys. Lett.* **B345** (1994) .

[51] R. Baier, D. Schiff, and B. G. Zakharov, "Energy loss in perturbative QCD", *Ann. Rev. Nucl. Part. Sci.* **50** (2000) .

Bibliography

[1] **ALICE** Collaboration, S. Acharya *et al.*, "Exploration of jet substructure using iterative declustering in pp and Pb-Pb collisions at LHC energies", arXiv:1905.02512 [nucl-ex].

[2] H. A. Andrews *et al.*, "Novel tools and observables for jet physics in heavy-ion collisions", arXiv:1808.03689 [hep-ph].

[3] "Standard model", 2019. https://en.wikipedia.org/wiki/Standard_Model.

[4] S. Bethke, "World Summary of α_s (2012)", arXiv:1210.0325 [hep-ex]. [Nucl. Phys. Proc. Suppl.234,229(2013)].

[5] D. J. Gross and F. Wilczek, "Ultraviolet behavior of non-abelian gauge theories", *Phys. Rev. Lett.* **30** (Jun, 1973) . https://link.aps.org/doi/10.1103/PhysRevLett.30.1343.

[6] H. D. Politzer, "Reliable perturbative results for strong interactions?", *Phys. Rev. Lett.* **30** (Jun, 1973) . https://link.aps.org/doi/10.1103/PhysRevLett.30.1346.

[7] N. K. Nielsen, "ASYMPTOTIC FREEDOM AS A SPIN EFFECT", *Am. J. Phys.* **49** (1981) .

[8] J. C. Collins and M. J. Perry, "Superdense Matter: Neutrons Or Asymptotically Free Quarks?", *Phys. Rev. Lett.* **34** (1975) .

[9] "The Frontiers of Nuclear Science, A Long Range Plan", arXiv:0809.3137 [nucl-ex].

[10] F. Karsch, E. Laermann, and A. Peikert, "Quark mass and flavor dependence of the QCD phase transition", *Nucl. Phys.* **B605** (2001) , arXiv:hep-lat/0012023 [hep-lat].

[11] **CP-PACS** Collaboration, A. Ali Khan *et al.*, "Phase structure and critical temperature of two flavor QCD with renormalization group improved gauge action and clover improved Wilson quark action", *Phys. Rev.* **D63** (2000) , arXiv:hep-lat/0008011 [hep-lat].

[12] G. Martinez, "Advances in Quark Gluon Plasma", 2013. arXiv:1304.1452 [nucl-ex].

[13] F. Karsch, "Lattice QCD at high temperature and density", *Lect. Notes Phys.* **583** (2002) , arXiv:hep-lat/0106019 [hep-lat].

[14] M. Connors, C. Nattrass, R. Reed, and S. Salur, "Jet measurements in heavy ion physics", *Rev. Mod. Phys.* **90** (2018) , arXiv:1705.01974 [nucl-ex].

[15] **Particle Data Group** Collaboration, M. Tanabashi *et al.*, "Review of Particle Physics", *Phys. Rev.* **D98** no. 3, (2018) .

[16] J. Rafelski and B. Muller, "Strangeness Production in the Quark - Gluon Plasma", *Phys. Rev. Lett.* **48** (1982) . [Erratum: Phys. Rev. Lett.56,2334(1986)].

[17] T. Matsui and H. Satz, "J/ψ Suppression by Quark-Gluon Plasma Formation", *Phys. Lett.* **B178** (1986) .

[18] **ALICE** Collaboration, J. Adam *et al.*, "Multi-strange baryon production in p-Pb

collisions at $\sqrt{s_{\mathrm{NN}}} = 5.02$ TeV", *Phys. Lett.* **B758** (2016) , arXiv:1512.07227 [nucl-ex].

[19] **ALICE** Collaboration, J. Adam *et al.*, "Enhanced production of multi-strange hadrons in high-multiplicity proton-proton collisions", *Nature Phys.* **13** (2017) , arXiv:1606.07424 [nucl-ex].

[20] M. L. Miller, K. Reygers, S. J. Sanders, and P. Steinberg, "Glauber modeling in high energy nuclear collisions", *Ann.Rev.Nucl.Part.Sci.* **57** (2007) , arXiv:nucl-ex/0701025 [nucl-ex].

[21] **NA35** Collaboration, J. Bartke *et al.*, "Neutral strange particle production in sulphur sulphur and proton sulphur collisions at 200-GeV/nucleon", *Z. Phys.* **C48** (1990) .

[22] **WA85** Collaboration, S. Abatzis *et al.*, "Xi-, anti-xi-, Lambda and anti-Lambda production in sulphur - tungsten interactions at 200-GeV/c per nucleon", *Phys. Lett.* **B270** (1991) .

[23] **NA36** Collaboration, E. Andersen *et al.*, "Production of Lambda, Anti-lambda, and Xi-, Anti-xi+ particles in S + Pb collisions at 200-GeV/c per nucleon", *Phys. Lett.* **B327** (1994) .

[24] **NA49** Collaboration, P. G. Jones *et al.*, "Hadron yields and hadron spectra from the NA49 experiment", *Nucl. Phys.* **A610** (1996) .

[25] **WA97** Collaboration, E. Andersen *et al.*, "Strangeness enhancement at mid-rapidity in Pb Pb collisions at 158-A-GeV/c", *Phys. Lett.* **B449** (1999) .

[26] **WA97** Collaboration, E. Andersen *et al.*, "Enhancement of central Lambda, Xi and Omega yields in Pb - Pb collisions at 158 A-GeV/c", *Phys. Lett.* **B433** (1998) .

[27] **WA97** Collaboration, E. Andersen *et al.*, "Lambda, Xi and Omega production at mid-rapidity in Pb Pb and p Pb collisions at 158-A-GeV/c", *J. Phys.* **G25** (1999) .

[28] **NA50** Collaboration, M. Gonin *et al.*, "Anomalous J / psi suppression in Pb + Pb collisions at 158-A-GeV/c", *Nucl. Phys.* **A610** (1996) .

[29] **NA38** Collaboration, M. C. Abreu *et al.*, "Charmonia production in 450-GeV/c proton induced reactions", *Phys. Lett.* **B444** (1998) .

[30] **PHOBOS** Collaboration, B. B. Back *et al.*, "The PHOBOS perspective on discoveries at RHIC", *Nucl. Phys.* **A757** (2005) , arXiv:nucl-ex/0410022 [nucl-ex].

[31] **BRAHMS** Collaboration, I. Arsene *et al.*, "Quark gluon plasma and color glass condensate at RHIC? The Perspective from the BRAHMS experiment", *Nucl. Phys.* **A757** (2005) , arXiv:nucl-ex/0410020 [nucl-ex].

[32] **PHENIX** Collaboration, K. Adcox *et al.*, "Formation of dense partonic matter in relativistic nucleus-nucleus collisions at RHIC: Experimental evaluation by the PHENIX collaboration", *Nucl. Phys.* **A757** (2005) , arXiv:nucl-ex/0410003 [nucl-ex].

[33] **STAR** Collaboration, J. Adams *et al.*, "Experimental and theoretical challenges in the search for the quark gluon plasma: The STAR Collaboration's critical assessment of the evidence from RHIC collisions", *Nucl. Phys.* **A757** (2005) , arXiv:nucl-ex/0501009 [nucl-ex].

[34] **PHENIX** Collaboration, A. Adare *et al.*, "J/ψ Production vs Centrality, Transverse Momentum, and Rapidity in Au+Au Collisions at $\sqrt{s_{NN}} = 200$ GeV", *Phys. Rev. Lett.* **98** (2007) , arXiv:nucl-ex/0611020 [nucl-ex].

[35] **STAR** Collaboration, B. I. Abelev *et al.*, "Enhanced strange baryon production in Au + Au collisions compared to p + p at s(NN)**(1/2) = 200-GeV", *Phys. Rev.* **C77** (2008) , arXiv:0705.2511 [nucl-ex].

[36] **STAR** Collaboration, L. Adamczyk *et al.*, "J/ψ production at high transverse momenta in $p+p$ and Au+Au collisions at $\sqrt{s_{NN}} = 200$ GeV", *Phys. Lett.* **B722** (2013) , arXiv:1208.2736 [nucl-ex].

[37] **PHENIX Collaboration** Collaboration, K. Adcox *et al.*, "Suppression of hadrons with large transverse momentum in central $au + au$ collisions at $\sqrt{s_{\rm NN}} = 130$GeV", *Phys. Rev. Lett.* **88** (Dec, 2001) . https://link.aps.org/doi/10.1103/PhysRevLett.88.022301.

[38] **STAR Collaboration** Collaboration, C. Adler *et al.*, "Centrality dependence of high-p_T hadron suppression in Au + Au collisions at $\sqrt{s_{NN}} = 130$ GeV", *Phys. Rev. Lett.* **89** (Oct, 2002) . https://link.aps.org/doi/10.1103/PhysRevLett.89.202301.

[39] **STAR Collaboration** Collaboration, J. Adams *et al.*, "Transverse-momentum and collision-energy dependence of high-p_T hadron suppression in Au + Au collisions at ultrarelativistic energies", *Phys. Rev. Lett.* **91** (Oct, 2003) . https://link.aps.org/doi/10.1103/PhysRevLett.91.172302.

[40] **PHENIX Collaboration** Collaboration, S. S. Adler *et al.*, "High-p_T charged hadron suppression in Au + Au collisions at $\sqrt{s_{NN}} = 200$ GeV", *Phys. Rev. C* **69** (Mar, 2004) . https://link.aps.org/doi/10.1103/PhysRevC.69.034910.

[41] **STAR Collaboration** Collaboration, J. Adams *et al.*, "Evidence from d + Au measurements for final-state suppression of high-p_T hadrons in Au + Au collisions at

rhic", *Phys. Rev. Lett.* **91** (Aug, 2003) .
https://link.aps.org/doi/10.1103/PhysRevLett.91.072304.

[42] **STAR** Collaboration, K. H. Ackermann *et al.*, "Elliptic flow in Au + Au collisions at (S(NN))**(1/2) = 130 GeV", *Phys. Rev. Lett.* **86** (2001) , arXiv:nucl-ex/0009011 [nucl-ex].

[43] J.-Y. Ollitrault, "Anisotropy as a signature of transverse collective flow", *Phys. Rev. D* **46** (Jul, 1992) . https://link.aps.org/doi/10.1103/PhysRevD.46.229.

[44] O. S. Bruning, P. Collier, P. Lebrun, S. Myers, R. Ostojic, J. Poole, and P. Proudlock, "LHC Design Report Vol.1: The LHC Main Ring",.

[45] O. Bruning, P. Collier, P. Lebrun, S. Myers, R. Ostojic, J. Poole, and P. Proudlock, "LHC Design Report. 2. The LHC infrastructure and general services",.

[46] M. Benedikt, P. Collier, V. Mertens, J. Poole, and K. Schindl, "LHC Design Report. 3. The LHC injector chain",.

[47] **ALICE** Collaboration, K. Aamodt *et al.*, "The ALICE experiment at the CERN LHC", *JINST* **3** (2008) .

[48] **LHCb** Collaboration, A. A. Alves, Jr. *et al.*, "The LHCb Detector at the LHC", *JINST* **3** (2008) .

[49] **CMS** Collaboration, S. Chatrchyan *et al.*, "The CMS Experiment at the CERN LHC", *JINST* **3** (2008) .

[50] **ATLAS** Collaboration, G. Aad *et al.*, "The ATLAS Experiment at the CERN Large Hadron Collider", *JINST* **3** (2008) .

[51] **ALICE** Collaboration, B. Abelev *et al.*, "J/ψ suppression at forward rapidity in Pb-Pb collisions at $\sqrt{s_{NN}} = 2.76$ TeV", *Phys. Rev. Lett.* **109** (2012) , arXiv:1202.1383 [hep-ex].

[52] **CMS** Collaboration, S. Chatrchyan *et al.*, "Suppression of non-prompt J/ψ, prompt J/ψ, and Y(1S) in PbPb collisions at $\sqrt{s_{NN}} = 2.76$ TeV", *JHEP* **05** (2012) , arXiv:1201.5069 [nucl-ex].

[53] **ALICE** Collaboration, B. B. Abelev *et al.*, "K^0_S and Λ production in Pb-Pb collisions at $\sqrt{s_{NN}} = 2.76$ TeV", *Phys. Rev. Lett.* **111** (2013) , arXiv:1307.5530 [nucl-ex].

[54] **ALICE** Collaboration, B. B. Abelev *et al.*, "Multi-strange baryon production at mid-rapidity in Pb-Pb collisions at $\sqrt{s_{NN}} = 2.76$ TeV", *Phys. Lett.* **B728** (2014) , arXiv:1307.5543 [nucl-ex]. [Erratum: Phys. Lett.B734,409(2014)].

[55] M. Cacciari and G. P. Salam, "Dispelling the N^3 myth for the k_t jet-finder", *Phys. Lett.* **B641** (2006) , arXiv:hep-ph/0512210 [hep-ph].

[56] M. Cacciari, G. P. Salam, and G. Soyez, "The anti-k_t jet clustering algorithm", *JHEP* **04** (2008) , arXiv:0802.1189 [hep-ph].

[57] **ALICE** Collaboration, K. Aamodt *et al.*, "Suppression of Charged Particle Production at Large Transverse Momentum in Central Pb–Pb Collisions at $\sqrt{s_{\rm NN}} = 2.76$ TeV", *Phys.Lett.* **B696** (2011) , arXiv:1012.1004 [nucl-ex].

[58] **ATLAS** Collaboration, G. Aad *et al.*, "Observation of a Centrality-Dependent Dijet Asymmetry in Lead-Lead Collisions at $\sqrt{s_{\rm NN}} = 2.76$ TeV with the ATLAS Detector at the LHC", *Phys.Rev.Lett.* **105** (2010) , arXiv:1011.6182 [hep-ex].

[59] **CMS** Collaboration, S. Chatrchyan *et al.*, "Dependence on pseudorapidity and

centrality of charged hadron production in PbPb collisions at a nucleon-nucleon centre-of-mass energy of 2.76 TeV", *JHEP* **08** (2011) , arXiv:1107.4800 [nucl-ex].

[60] **CMS** Collaboration, S. Chatrchyan *et al.*, "Observation and studies of jet quenching in Pb–Pb collisions at nucleon-nucleon center-of-mass energy = 2.76 TeV", *Phys.Rev.* **C84** (2011) , arXiv:1102.1957 [nucl-ex].

[61] **ATLAS** Collaboration, G. Aad *et al.*, "Measurement of the jet radius and transverse momentum dependence of inclusive jet suppression in lead-lead collisions at $\sqrt{s_{\rm NN}} = 2.76$ TeV with the ATLAS detector", *Phys.Lett.* **B719** (2013) , arXiv:1208.1967 [hep-ex].

[62] **ALICE** Collaboration, B. Abelev *et al.*, "Measurement of charged jet suppression in Pb–Pb collisions at $\sqrt{s_{\rm NN}} = 2.76$ TeV", *JHEP* **03** (2014) , arXiv:1311.0633 [nucl-ex].

[63] **ALICE** Collaboration, J. Adam *et al.*, "Measurement of jet quenching with semi-inclusive hadron-jet distributions in central Pb–Pb collisions at $\sqrt{s_{\rm NN}} = 2.76$ TeV", *JHEP* **09** (2015) , arXiv:1506.03984 [nucl-ex].

[64] **ALICE** Collaboration, J. Adam *et al.*, "Measurement of jet suppression in central Pb–Pb collisions at $\sqrt{s_{\rm NN}} = 2.76$ TeV", *Phys.Lett* **B746** (2015) , arXiv:1502.01689 [nucl-ex].

[65] **CMS** Collaboration, V. Khachatryan *et al.*, "Measurement of inclusive jet cross sections in *pp* and PbPb collisions at $\sqrt{s_{NN}} = 2.76$ TeV", *Phys. Rev.* **C96** no. 1, (2017) , arXiv:1609.05383 [nucl-ex].

[66] **ATLAS** Collaboration, M. Aaboud *et al.*, "Measurement of the nuclear modification factor for inclusive jets in Pb+Pb collisions at $\sqrt{s_{\rm NN}} = 5.02$ TeV with the ATLAS detector", *Phys. Lett.* **B790** (2019) , arXiv:1805.05635 [nucl-ex].

[67] **ALICE** Collaboration, S. Acharya *et al.*, "Transverse momentum spectra and nuclear modification factors of charged particles in pp, p-Pb and Pb-Pb collisions at the LHC", *JHEP* **11** (2018) , arXiv:1802.09145 [nucl-ex].

[68] **CMS** Collaboration, S. Chatrchyan *et al.*, "Modification of jet shapes in PbPb collisions at $\sqrt{s_{\mathrm{NN}}} = 2.76$ TeV", *Phys.Lett.* **B730** (2014) , arXiv:1310.0878 [nucl-ex].

[69] **ATLAS** Collaboration, M. Aaboud *et al.*, "Measurement of jet fragmentation in Pb+Pb and *pp* collisions at $\sqrt{s_{\mathrm{NN}}} = 2.76$ TeV with the ATLAS detector at the LHC", *Eur. Phys. J.* **C77** (2017) , arXiv:1702.00674 [hep-ex].

[70] **CMS** Collaboration, A. M. Sirunyan *et al.*, "Observation of medium induced modifications of jet fragmentation in PbPb collisions using isolated-photon-tagged jets", arXiv:1801.04895 [hep-ex].

[71] **ALICE** Collaboration, S. Acharya *et al.*, "Medium modification of the shape of small-radius jets in central Pb-Pb collisions at $\sqrt{s_{\mathrm{NN}}} = 2.76\,\mathrm{TeV}$", *JHEP* **10** (2018) , arXiv:1807.06854 [nucl-ex].

[72] A. J. Larkoski, I. Moult, and B. Nachman, "Jet Substructure at the Large Hadron Collider: A Review of Recent Advances in Theory and Machine Learning",.

[73] J. R. Andersen *et al.*, "Les Houches 2017: Physics at TeV Colliders Standard Model Working Group Report",.

[74] L. Asquith *et al.*, "Jet Substructure at the Large Hadron Collider : Experimental Review",.

[75] J. C. Collins, D. E. Soper, and G. F. Sterman, "Factorization of Hard Processes in

QCD", *Adv. Ser. Direct. High Energy Phys.* **5** (1989) , arXiv:hep-ph/0409313 [hep-ph].

[76] J. I. Friedman and H. W. Kendall, "Deep inelastic electron scattering", *Ann. Rev. Nucl. Part. Sci.* **22** (1972) .

[77] V. N. Gribov and L. N. Lipatov, "Deep inelastic e p scattering in perturbation theory", *Sov. J. Nucl. Phys.* **15** (1972) . [Yad. Fiz.15,781(1972)].

[78] Y. L. Dokshitzer, "Calculation of the Structure Functions for Deep Inelastic Scattering and e+ e- Annihilation by Perturbation Theory in Quantum Chromodynamics.", *Sov. Phys. JETP* **46** (1977) . [Zh. Eksp. Teor. Fiz.73,1216(1977)].

[79] G. Altarelli and G. Parisi, "Asymptotic Freedom in Parton Language", *Nucl. Phys.* **B126** (1977) .

[80] A. Martin, W. Stirling, R. Thorne, and G. Watt, "Parton distributions for the LHC", *Eur.Phys.J.* **C63** (2009) , arXiv:0901.0002 [hep-ph].

[81] B. Foster, A. Martin, and M. Vincter, "Structure functions", 2019. http://pdg.lbl.gov/2011/reviews/rpp2011-rev-structure-functions.pdf.

[82] **ATLAS** Collaboration, G. Aad *et al.*, "Measurement of the jet fragmentation function and transverse profile in proton-proton collisions at a center-of-mass energy of 7 TeV with the ATLAS detector", *Eur. Phys. J.* **C71** (2011) , arXiv:1109.5816 [hep-ex].

[83] **STAR** Collaboration, J. Adams *et al.*, "Evidence from d + Au measurements for final state suppression of high p(T) hadrons in Au+Au collisions at RHIC", *Phys.Rev.Lett.* **91** (2003) , arXiv:nucl-ex/0306024 [nucl-ex].

[84] **STAR** Collaboration, J. Adams *et al.*, "Transverse momentum and collision energy dependence of high p_T hadron suppression in Au+Au collisions at ultrarelativistic energies", *Phys.Rev.Lett.* **91** (2003) , arXiv:nucl-ex/0305015 [nucl-ex].

[85] **PHENIX** Collaboration, S. S. Adler *et al.*, "Suppressed π^0 production at large transverse momentum in central Au+ Au collisions at $\sqrt{s_{\rm NN}} = 200$ GeV", *Phys. Rev. Lett.* **91** (2003) , arXiv:nucl-ex/0304022 [nucl-ex].

[86] D. d'Enterria, "Jet quenching", *Landolt-Bornstein* **23** (2010) , arXiv:0902.2011 [nucl-ex].

[87] J. D. Bjorken, "Energy Loss of Energetic Partons in Quark - Gluon Plasma: Possible Extinction of High p(t) Jets in Hadron - Hadron Collisions",.

[88] H. Bethe and W. Heitler, "On the Stopping of fast particles and on the creation of positive electrons", *Proc. Roy. Soc. Lond.* **A146** (1934) .

[89] L. D. Landau and I. Pomeranchuk, "Limits of applicability of the theory of bremsstrahlung electrons and pair production at high-energies", *Dokl. Akad. Nauk Ser. Fiz.* **92** (1953) .

[90] A. B. Migdal, "Bremsstrahlung and pair production in condensed media at high-energies", *Phys. Rev.* **103** (1956) .

[91] G. Salam, "Comparison of nuclear modification factor of fully reconstructed jets (anti-$k_{\rm t}$ r=0.2) with atlas (r scaled from 0.4 to 0.2) and cms in pb–pb 0–10% centrality class", 2019. https://alice-figure.web.cern.ch/node/14697.

[92] R. Baier, Y. L. Dokshitzer, A. H. Mueller, S. Peigne, and D. Schiff, "Radiative energy loss of high-energy quarks and gluons in a finite volume quark - gluon plasma", *Nucl. Phys.* **B483** (1997) , arXiv:hep-ph/9607355 [hep-ph].

[93] R. Baier, Y. L. Dokshitzer, A. H. Mueller, S. Peigne, and D. Schiff, "Radiative energy loss and p(T) broadening of high-energy partons in nuclei", *Nucl. Phys.* **B484** (1997) , arXiv:hep-ph/9608322 [hep-ph].

[94] B. G. Zakharov, "Fully quantum treatment of the Landau-Pomeranchuk-Migdal effect in QED and QCD", *JETP Lett.* **63** (1996) , arXiv:hep-ph/9607440 [hep-ph].

[95] B. G. Zakharov, "Radiative energy loss of high-energy quarks in finite size nuclear matter and quark - gluon plasma", *JETP Lett.* **65** (1997) , arXiv:hep-ph/9704255 [hep-ph].

[96] R. Baier, D. Schiff, and B. G. Zakharov, "Energy loss in perturbative QCD", *Ann. Rev. Nucl. Part. Sci.* **50** (2000) , arXiv:hep-ph/0002198 [hep-ph].

[97] M. Gyulassy, P. Levai, and I. Vitev, "Jet quenching in thin quark gluon plasmas. 1. Formalism", *Nucl. Phys.* **B571** (2000) , arXiv:hep-ph/9907461 [hep-ph].

[98] M. Gyulassy, P. Levai, and I. Vitev, "NonAbelian energy loss at finite opacity", *Phys. Rev. Lett.* **85** (2000) , arXiv:nucl-th/0005032 [nucl-th].

[99] M. Gyulassy, P. Levai, and I. Vitev, "Reaction operator approach to nonAbelian energy loss", *Nucl. Phys.* **B594** (2001) , arXiv:nucl-th/0006010 [nucl-th].

[100] U. A. Wiedemann, "Gluon radiation off hard quarks in a nuclear environment: Opacity expansion", *Nucl. Phys.* **B588** (2000) , arXiv:hep-ph/0005129 [hep-ph].

[101] M. Djordjevic and M. Gyulassy, "Heavy quark radiative energy loss in QCD matter", *Nucl. Phys.* **A733** (2004) , arXiv:nucl-th/0310076 [nucl-th].

[102] X.-f. Guo and X.-N. Wang, "Multiple scattering, parton energy loss and modified fragmentation functions in deeply inelastic e A scattering", *Phys. Rev. Lett.* **85** (2000) , arXiv:hep-ph/0005044 [hep-ph].

[103] P. B. Arnold, G. D. Moore, and L. G. Yaffe, "Transport coefficients in high temperature gauge theories. 1. Leading log results", *JHEP* **11** (2000) , arXiv:hep-ph/0010177 [hep-ph].

[104] P. B. Arnold, G. D. Moore, and L. G. Yaffe, "Photon emission from ultrarelativistic plasmas", *JHEP* **11** (2001) , arXiv:hep-ph/0109064 [hep-ph].

[105] S. Jeon and G. D. Moore, "Energy loss of leading partons in a thermal QCD medium", *Phys. Rev.* **C71** (2005) , arXiv:hep-ph/0309332 [hep-ph].

[106] **PHENIX** Collaboration, M. Shimomura, "High-p(T) pi0, eta, identified and inclusive charged hadron spectra from PHENIX", *Nucl. Phys.* **A774** (2006) , arXiv:nucl-ex/0510023 [nucl-ex].

[107] S. A. Bass, C. Gale, A. Majumder, C. Nonaka, G. Y. Qin, T. Renk, and J. Ruppert, "Systematic Comparison of Jet Energy-Loss Schemes in a 3D hydrodynamic medium", *J. Phys.* **G35** (2008) , arXiv:0805.3271 [nucl-th].

[108] Y. Mehtar-Tani, C. A. Salgado, and K. Tywoniuk, "Anti-angular ordering of gluon radiation in QCD media", *Phys. Rev. Lett.* **106** (2011) , arXiv:1009.2965 [hep-ph].

[109] J. Casalderrey-Solana, Y. Mehtar-Tani, C. A. Salgado, and K. Tywoniuk, "New picture of jet quenching dictated by color coherence", *Phys. Lett.* **B725** (2013) , arXiv:1210.7765 [hep-ph].

[110] Y. Mehtar-Tani and K. Tywoniuk, "Jet (de)coherence in Pb?Pb collisions at the LHC", *Phys. Lett.* **B744** (2015) , arXiv:1401.8293 [hep-ph].

[111] Y. L. Dokshitzer, V. A. Khoze, A. H. Mueller, and S. I. Troian, *Basics of perturbative QCD*. 1991.

[112] **ALICE** Collaboration, N. Zardoshti, "Investigating the Role of Coherence Effects on Jet Quenching in Pb–Pb Collisions at $\sqrt{s_{\rm NN}} = 2.76$ TeV using Jet Substructure", *Nucl. Phys.* **A967** (2017) , arXiv:1705.03383 [nucl-ex].

[113] S. D. Ellis and D. E. Soper, "Successive combination jet algorithm for hadron collisions", *Phys. Rev.* **D48** (1993) , arXiv:hep-ph/9305266 [hep-ph].

[114] Yu.L.Dokshitzer, G.D.Leder, S.Moretti, and B.R.Webber, "Better Jet Clustering Algorithms", *JHEP* **08** (1997) , arXiv:9707323 [hep-ph].

[115] G. P. Salam, "Towards Jetography", *Eur. Phys. J.* **C67** (2010) , arXiv:0906.1833 [hep-ph].

[116] G. Salam, "Gavin salam's web", 2019. https://gsalam.web.cern.ch/gsalam/.

[117] T. Sjöstrand, S. Mrenna, and P. Z. Skands, "PYTHIA 6.4 Physics and Manual", *JHEP* **05** (2006) , arXiv:hep-ph/0603175 [hep-ph].

[118] P. Z. Skands, "Tuning Monte Carlo Generators: The Perugia Tunes", *Phys.Rev.* **D82** (2010) , arXiv:1005.3457 [hep-ph].

[119] T. Sjöstrand, S. Ask, J. R. Christiansen, R. Corke, N. Desai, P. Ilten, S. Mrenna, S. Prestel, C. O. Rasmussen, and P. Z. Skands, "An Introduction to PYTHIA 8.2", *Comput. Phys. Commun.* **191** (2015) , arXiv:1410.3012 [hep-ph].

[120] B. Andersson, G. Gustafson, G. Ingelman, and T. Sjostrand, "Parton Fragmentation and String Dynamics", *Phys. Rept.* **97** (1983) .

[121] B. Andersson, "The Lund model", *Camb. Monogr. Part. Phys. Nucl. Phys. Cosmol.* **7** (1997) .

[122] S. Alioli, P. Nason, C. Oleari, and E. Re, "A general framework for implementing NLO calculations in shower Monte Carlo programs: the POWHEG BOX", *JHEP* **06** (2010) , arXiv:1002.2581 [hep-ph].

[123] P. Nason, "A New method for combining NLO QCD with shower Monte Carlo algorithms", *JHEP* **11** (2004) , arXiv:hep-ph/0409146 [hep-ph].

[124] S. Frixione, P. Nason, and C. Oleari, "Matching NLO QCD computations with Parton Shower simulations: the POWHEG method", *JHEP* **0711** (2007) , arXiv:0709.2092 [hep-ph].

[125] S. Aiola, "Fast monte carlo simulations for jet and heavy-flavor." https://github.com/aiola/alice-fast-simulation, 2018.

[126] K. Zapp, G. Ingelman, J. Rathsman, J. Stachel, and U. A. Wiedemann, "A Monte Carlo Model for 'Jet Quenching'", *Eur.Phys.J.* **C60** (2009) , arXiv:0804.3568 [hep-ph].

[127] K. C. Zapp, F. Krauss, and U. A. Wiedemann, "A perturbative framework for jet quenching", *JHEP* **03** (2013) , arXiv:1212.1599 [hep-ph].

[128] R. Kunnawalkam Elayavalli and K. C. Zapp, "Medium response in JEWEL and its impact on jet shape observables in heavy ion collisions", *JHEP* **07** (2017) , arXiv:1707.01539 [hep-ph].

[129] M. Van Leewuen *Private communication.* (2018) .

[130] J. Casalderrey-Solana, D. C. Gulhan, J. G. Milhano, D. Pablos, and K. Rajagopal, "A Hybrid Strong/Weak Coupling Approach to Jet Quenching", *JHEP* **10** (2014) , arXiv:1405.3864 [hep-ph]. [Erratum: JHEP09,175(2015)].

[131] J. Casalderrey-Solana, D. C. Gulhan, J. G. Milhano, D. Pablos, and K. Rajagopal, "Predictions for Boson-Jet Observables and Fragmentation Function Ratios from a Hybrid Strong/Weak Coupling Model for Jet Quenching", *JHEP* **03** (2016) , arXiv:1508.00815 [hep-ph].

[132] J. Casalderrey-Solana, D. Gulhan, G. Milhano, D. Pablos, and K. Rajagopal, "Angular Structure of Jet Quenching Within a Hybrid Strong/Weak Coupling Model", *JHEP* **03** (2017) , arXiv:1609.05842 [hep-ph].

[133] Z. Hulcher, D. Pablos, and K. Rajagopal, "Resolution Effects in the Hybrid Strong/Weak Coupling Model", *JHEP* **03** (2018) , arXiv:1707.05245 [hep-ph].

[134] P. M. Chesler and K. Rajagopal, "Jet quenching in strongly coupled plasma", *Phys. Rev.* **D90** no. 2, (2014) , arXiv:1402.6756 [hep-th].

[135] S. S. Gubser, D. R. Gulotta, S. S. Pufu, and F. D. Rocha, "Gluon energy loss in the gauge-string duality", *JHEP* **10** (2008) , arXiv:0803.1470 [hep-th].

[136] P. M. Chesler, K. Jensen, A. Karch, and L. G. Yaffe, "Light quark energy loss in strongly-coupled N = 4 supersymmetric Yang-Mills plasma", *Phys. Rev.* **D79** (2009) , arXiv:0810.1985 [hep-th].

[137] D. Pablos *Private communication.* (2018) .

[138] J. Thaler and K. Van Tilburg, "Identifying Boosted Objects with N-subjettiness", *JHEP* **03** (2011) , arXiv:1011.2268 [hep-ph].

[139] A. J. Larkoski, J. Thaler, and W. J. Waalewijn, "Gaining (Mutual) Information about Quark/Gluon Discrimination", *JHEP* **11** (2014) , arXiv:1408.3122 [hep-ph].

[140] J. G. Milhano and K. C. Zapp, "Origins of the di-jet asymmetry in heavy ion collisions", *Eur. Phys. J.* **C76** no. 5, (2016) , arXiv:1512.08107 [hep-ph].

[141] K. Rajagopal, A. V. Sadofyev, and W. van der Schee, "Evolution of the jet opening angle distribution in holographic plasma", *Phys. Rev. Lett.* **116** no. 21, (2016) , arXiv:1602.04187 [nucl-th].

[142] **ATLAS** Collaboration, G. Aad *et al.*, "Measurement of inclusive jet charged-particle fragmentation functions in Pb+Pb collisions at $\sqrt{s_{NN}} = 2.76$ TeV with the ATLAS detector", *Phys. Lett.* **B739** (2014) , arXiv:1406.2979 [hep-ex].

[143] **CMS** Collaboration, S. Chatrchyan *et al.*, "Measurement of jet fragmentation in PbPb and pp collisions at $\sqrt{s_{\mathrm{NN}}} = 2.76$ TeV", *Phys. Rev.* **C90** (2014) , arXiv:1406.0932 [nucl-ex].

[144] **CMS** Collaboration, V. Khachatryan *et al.*, "Decomposing transverse momentum balance contributions for quenched jets in PbPb collisions at $\sqrt{s_{\mathrm{N\,N}}} = 2.76$ TeV", *JHEP* **11** (2016) , arXiv:1609.02466 [nucl-ex].

[145] **ALICE** Collaboration, S. Acharya *et al.*, "First measurement of jet mass in Pb–Pb and p–Pb collisions at the LHC", *Phys. Lett.* **B776** (2018) , arXiv:1702.00804 [nucl-ex].

[146] F. A. Dreyer, G. P. Salam, and G. Soyez, "The Lund Jet Plane", arXiv:1807.04758 [hep-ph].

[147] H. A. Bethe, "Molière's theory of multiple scattering", *Phys. Rev.* **89** (Mar, 1953) . https://link.aps.org/doi/10.1103/PhysRev.89.1256.

[148] A. J. Larkoski, S. Marzani, G. Soyez, and J. Thaler, "Soft Drop", *JHEP* **05** (2014) , arXiv:1402.2657 [hep-ph].

[149] J. M. Butterworth, A. R. Davison, M. Rubin, and G. P. Salam, "Jet substructure as a

new Higgs search channel at the LHC", *Phys. Rev. Lett.* **100** (2008) , arXiv:0802.2470 [hep-ph].

[150] M. Dasgupta, A. Fregoso, S. Marzani, and G. P. Salam, "Towards an understanding of jet substructure", *JHEP* **09** (2013) , arXiv:1307.0007 [hep-ph].

[151] **CMS** Collaboration, A. M. Sirunyan *et al.*, "Measurement of the Splitting Function in *pp* and Pb-Pb Collisions at $\sqrt{s_{\mathrm{NN}}} = 5.02$ TeV", *Phys. Rev. Lett.* **120** no. 14, (2018) , arXiv:1708.09429 [nucl-ex].

[152] A. Tripathee, W. Xue, A. Larkoski, S. Marzani, and J. Thaler, "Jet Substructure Studies with CMS Open Data", *Phys. Rev.* **D96** no. 7, (2017) , arXiv:1704.05842 [hep-ph].

[153] **STAR** Collaboration, K. Kauder, "Measurement of the Shared Momentum Fraction z_{g} using Jet Reconstruction in p+p and Au+Au Collisions with STAR", *Nucl. Phys.* **A967** (2017) , arXiv:1704.03046 [nucl-ex].

[154] Y. Mehtar-Tani and K. Tywoniuk, "Groomed jets in heavy-ion collisions: sensitivity to medium-induced bremsstrahlung", *JHEP* **04** (2017) , arXiv:1610.08930 [hep-ph].

[155] Y.-T. Chien and I. Vitev, "Probing the hardest branching within jets in heavy-ion collisions", *Phys. Rev. Lett.* **119** (Sep, 2017) . https://link.aps.org/doi/10.1103/PhysRevLett.119.112301.

[156] J. G. Milhano, U. A. Wiedemann, and K. C. Zapp, "Sensitivity of jet substructure to jet-induced medium response", arXiv:1707.04142 [hep-ph].

[157] N.-B. Chang, S. Cao, and G.-Y. Qin, "Probing medium-induced jet splitting and

energy loss in heavy-ion collisions", *Phys. Lett.* **B781** (2018) , arXiv:1707.03767 [hep-ph].

[158] E. Ciapala *et al.*, "Commissioning of the 400MHz LHC RF System", in *Particle accelerator. Proceedings, 11th European Conference, EPAC 2008, Genoa, Italy, June 23-27, 2008*. 2008. http://weblib.cern.ch/abstract?CERN-LHC-PROJECT-REPORT-1147.

[159] R. Garoby, "Upgrade issues for the cern accelerator complex",.

[160] D. Czerwinski, A. Deloff, K. Karpio, S. Kozak, L. Lukaszek, H. Malinowski, T. Siemiarczuk, G. Stefanek, L. Tykarski, and G. Wilk, *Alice Technical Design Report of the High Momentum Particle Identification Detector*. 09, 1998.

[161] **ALICE** Collaboration, P. Cortese *et al.*, "ALICE electromagnetic calorimeter technical design report",.

[162] **ALICE** Collaboration, K. Aamodt *et al.*, "Centrality dependence of the charged-particle multiplicity density at mid-rapidity in Pb-Pb collisions at $\sqrt{s_{NN}} = 2.76$ TeV", *Phys. Rev. Lett.* **106** (2011) , arXiv:1012.1657 [nucl-ex].

[163] **ALICE** Collaboration, G. Dellacasa *et al.*, "ALICE technical design report of the inner tracking system (ITS)",.

[164] **ALICE** Collaboration, K. Aamodt *et al.*, "Alignment of the ALICE Inner Tracking System with cosmic-ray tracks", *JINST* **5** (2010) , arXiv:1001.0502 [physics.ins-det].

[165] D. Nouais, S. Beol?, M. Bondila, V. Bonvicini, P. Cerello, E. Crescio, P. Giubellino, M. Idzik, A. Kolozhvari, S. Kouchpil, E. Torres, M. Martinez, G. Mazza, S. Piano, C. Piemonte, A. Rashevsky, L. Riccati, A. Rivetti, F. Tosello, W. Trzaska, A. Vacchi,

and R. Wheadon, "The alice silicon drift detector system", *Nuclear Instruments and Methods in Physics Research Section A: Accelerators, Spectrometers, Detectors and Associated Equipment* **501** no. 1, (2003) . http://www.sciencedirect.com/science/article/pii/S016890020202020X. Proceedings of the 10th International Workshop on Vertex Detectors.

[166] K. Aamodt *et al.*, "The ALICE TPC, a large 3-dimensional tracking device with fast readout for ultra-high multiplicity events", *Nuclear Instruments and Methods in Physics Research A* **622** (Oct., 2010) , arXiv:1001.1950 [physics.ins-det].

[167] **ALICE** Collaboration, E. Abbas *et al.*, "Performance of the ALICE VZERO system", *JINST* **8** (2013) , arXiv:1306.3130 [nucl-ex].

[168] R. Brun, F. Bruyant, M. Maire, A.C. McPherson, and P. Zanarini, "GEANT3 User's Guide", *CERN Data Handling Division DD/EE/84-1* (1985) .

[169] **ALICE Collaboration** Collaboration, C. W. Fabjan, L. Jirdén, V. Lindestruth, L. Riccati, D. Rorich, P. Van de Vyvre, O. Villalobos Baillie, and H. de Groot, *ALICE trigger data-acquisition high-level trigger and control system: Technical Design Report*. Technical Design Report ALICE. CERN, Geneva, 2004. https://cds.cern.ch/record/684651.

[170] **ALICE** Collaboration, B. Abelev *et al.*, "Measurement of inelastic, single- and double-diffraction cross sections in proton–proton collisions at the LHC with ALICE", *Eur. Phys. J.* **C73** no. 6, (2013) , arXiv:1208.4968 [hep-ex].

[171] **ALICE** Collaboration, J. Adam *et al.*, "Jet-like correlations with neutral pion triggers in pp and central Pb?Pb collisions at 2.76 TeV", *Phys. Lett.* **B763** (2016) , arXiv:1608.07201 [nucl-ex].

[172] M. Ivanov, I. Belikov, P. Hristov, and K. ?afa?ík, "Track reconstruction in high density environment", *Nuclear Instruments and Methods in Physics Research Section A-accelerators Spectrometers Detectors and Associated Equipment - NUCL INSTRUM METH PHYS RES A* **566** (10, 2006) .

[173] Y. Belikov, M. Ivanov, K. Safarik, and J. Bracinik, "TPC tracking and particle identification in high density environment", *eConf* **C0303241** (2003) , arXiv:physics/0306108 [physics].

[174] **ALICE** Collaboration, B. Abelev *et al.*, "Performance of the ALICE Experiment at the CERN LHC", *Int.J.Mod.Phys.* **A29** (2014) , arXiv:1402.4476 [nucl-ex].

[175] R. Fruhwirth, "Application of Kalman filtering to track and vertex fitting", *Nucl.Instrum.Meth.* **A262** (1987) .

[176] A. Collaboration, "Hybrid tracks", 2019. https://twiki.cern.ch/twiki/bin/view/ALICE/HybridTracks.

[177] R. Glauber, "Cross sections in deuterium at high energies", *Physical Review - PHYS REV X* **100** (10, 1955) .

[178] **ALICE** Collaboration, B. Abelev *et al.*, "Centrality determination of Pb-Pb collisions at $\sqrt{s_{NN}} = 2.76$ TeV with ALICE", *Phys. Rev.* **C88** no. 4, (2013) , arXiv:1301.4361 [nucl-ex].

[179] M. Cacciari, G. P. Salam, and G. Soyez, "FastJet User Manual", *Eur.Phys.J.* **C72** (2012) , arXiv:1111.6097 [hep-ph].

[180] P. Berta, M. Spousta, D. W. Miller, and R. Leitner, "Particle-level pileup subtraction for jets and jet shapes", *JHEP* **06** (2014) , arXiv:1403.3108 [hep-ex].

[181] G. D'Agostini, "A multidimensional unfolding method based on Bayes' theorem", *Nucl.Instrum.Meth.* **A362** (1995) .

[182] G. D'Agostini, "Improved iterative Bayesian unfolding", *ArXiv e-prints* (Oct., 2010) , arXiv:1010.0632 [physics.data-an].

[183] RooUnfold http://hepunx.rl.ac.uk/~adye/software/unfold/RooUnfold.html.

[184] M. Spousta and B. Cole, "Interpreting single jet measurements in Pb+Pb collisions at the LHC", *Eur. Phys. J.* **C76** (2016) , arXiv:1504.05169 [hep-ph].

[185] G. Corcella, I. G. Knowles, G. Marchesini, S. Moretti, K. Odagiri, P. Richardson, M. H. Seymour, and B. R. Webber, "HERWIG 6: An Event generator for hadron emission reactions with interfering gluons (including supersymmetric processes)", *JHEP* **01** (2001) , arXiv:hep-ph/0011363 [hep-ph].

[186] M. Bahr *et al.*, "Herwig++ Physics and Manual", *Eur. Phys. J.* **C58** (2008) , arXiv:0803.0883 [hep-ph].